

BROADBAND MICROSTRIP ANTENNAS USING COUPLED RESONATORS

A Thesis Submitted
In Partial Fulfilment of the Requirements
for the Degree of
DOCTOR OF PHILOSOPHY

By
GIRISH KUMAR

to the
DEPARTMENT OF ELECTRICAL ENGINEERING
INDIAN INSTITUTE OF TECHNOLOGY KANPUR
NOVEMBER, 1982

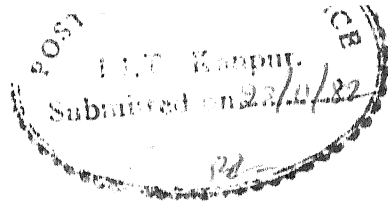
4 JUN 1984

CENTRAL LIBRARY

Acc. No. A 82704

82704

EE-1982-D-KUM-880



CERTIFICATE

This is to certify that the work reported in this thesis entitled 'BROADBAND MICROSTRIP ANTENNAS USING COUPLED RESONATORS' by Mr. Girish Kumar has been carried out under my supervision and has not been submitted elsewhere for a degree.

(K.C. Gupta)
Professor

Department of Electrical Engineering
Indian Institute of Technology
Kanpur - 208016

... has been approved
... of the Dept. of
... (Ph.D.)
... with the
... of the Indian
... of Technology - Kanpur
Date: 2/5/1983 BR.

ACKNOWLEDGEMENTS

With profound sense of gratitude, I express my indebtedness to Professor K.C. Gupta for providing an exemplary guidance and encouragement throughout the course of this work. I am proud of my association with him which in itself has been a source of learning not only in academic environment but also otherwise. I sincerely feel that no words are adequate to acknowledge his contributions.

I am grateful to Dr. R. Raghuram for the keen interest shown in the work.

I am also thankful to Dr. Rakesh Chadha and Shri P.C. Sharma for the fruitful and interesting discussions throughout. I take this opportunity to thank my friends for providing me with splendid company, untiring help and much needed moral support during my stay here.

The co-operation and help from Shri S.K. Kolay and Shri V.S. Yadav in fabricating numerous antennas used in the present investigation, are thankfully acknowledged.

I express my sincere thanks to Shri C.M. Abraham for the efficient typing and painstaking efforts in bringing this thesis to its present form.

Thanks are also due to Shri J.C. Verma for neat drawings, Shri R.S. Shukla for electronic stencil cutting and Shri Triveni Tiwari and Shri Gangaram for careful cyclostyling.

Finally, I wish to put on record my sense of regard to my parents for their blessings but for which it would not have been possible to undertake this work.

Girish Kumar

LIST OF CONTENTS

LIST OF FIGURES	x
SYNOPSIS	xix
Chapter One INTRODUCTION	1
1.1 MICROSTRIP ANTENNAS	1
1.1.1 Special features of microstrip patch antennas	1
1.1.2 Methods of analyzing microstrip antennas	5
1.1.3 Bandwidth of microstrip antennas	9
1.2 CONFIGURATIONS FOR IMPROVING THE BANDWIDTH	12
1.2.1 Diagonal fed nearly square patch antennas	12
1.2.2 Trapezoidal shaped microstrip antenna	12
1.2.3 Short-circuit quarter wavelength parasitic elements coupled to the radiating edges of rectangular patch antenna	14
1.2.4 Parasitic strips placed parallel to the non-radiating edges of square patch antenna	15
1.2.5 Log-periodic microstrip antenna	15
1.2.6 Quasi-log-periodic microstrip antenna	17
1.3 PRESENT INVESTIGATIONS	18

Chapter Two		
GREEN'S FUNCTION APPROACH, SEGMENTATION METHOD, AND RECTANGULAR PATCH ANTENNAS		24
2.1	GREEN'S FUNCTION APPROACH	24
2.2	SEGMENTATION METHOD	27
2.3	RADIATION PATTERN CALCULATIONS	30
2.4	RECTANGULAR PATCH ANTENNAS (RPA)	33
	2.4.1 Analysis	34
	2.4.2 Bandwidth	36
	2.4.3 Radiation pattern	44
2.5	DISCUSSION	47
Chapter Three		
RADIATING EDGES GAP COUPLED MICROSTRIP ANTENNAS(REGCOMA)		48
3.1	MULTIPLE RESONATOR STRUCTURES	48
3.2	MODELLING OF THE COUPLING GAPS	52
3.3	REGCOMA WITH IDENTICAL PARASITIC ELEMENTS	54
	3.3.1 Analysis	54
	3.3.2 Effect of the antenna parameters on performance	57
	3.3.3 Initial experiments	62
	3.3.4 Modification of the values of the gap capacitances	67
	3.3.5 Optimization for broader bandwidth	70
3.4	REGCOMA WITH PARASITIC ELEMENTS OF DIFFERENT LENGTHS	76
	3.4.1 Introduction	76
	3.4.2 Effect of the lengths of the parasitic elements	78
	3.4.3 Effect of the gap-widths	79
	3.4.4 Experiments	79
	3.4.5 Voltage distribution and radiation pattern	82

3.5	REGCOMA ON THICKER SUBSTRATE	89
3.6	DISCUSSION	94

Chapter Four

NON-RADIATING EDGES GAP COUPLED AND FOUR EDGES GAP COUPLED MICROSTRIP ANTENNAS	96
--	----

4.1	NEGCOMA WITH IDENTICAL PARASITIC ELEMENTS	96
4.1.1	Analysis	96
4.1.2	Effect of antenna parameters on performance	98
4.1.3	Experiments	107
4.2	NEGCOMA WITH PARASITIC ELEMENTS OF DIFFERENT LENGTHS	110
4.2.1	Effect of antenna parameters	113
4.2.2	Experiment	116
4.3	NEGCOMA ON THICKER SUBSTRATE	119
4.3.1	Identical parasitic elements	120
4.3.2	Parasitic elements of different lengths	123
4.4	FOUR EDGES GAP COUPLED MICROSTRIP ANTENNAS (FEGCOMA)	132
4.4.1	Introduction	132
4.4.2	Analysis	132
4.4.3	Experiments and optimization	136
4.5	DISCUSSION	146

Chapter Five		
RADIATING EDGES DIRECTLY COUPLED MICROSTRIP ANTENNAS (REDCOMA)		148
5.1	ANALYSIS	148
5.2	EFFECT OF ANTENNA PARAMETERS ON PERFORMANCE	150
5.2.1	Lengths of the parasitic elements	151
5.2.2	Length and width of the connecting strips	154
5.2.3	Feed-point location	154
5.3	EXPERIMENTS AND OPTIMIZATION	158
5.4	DISCUSSION	166
Chapter Six		
NON-RADIATING EDGES DIRECTLY COUPLED AND FOUR EDGES DIRECTLY COUPLED MICROSTRIP ANTENNAS		167
6.1	NON- RADIATING EDGES DIRECTLY COUPLED MICROSTRIP ANTENNAS (NEDCOMA)	167
6.1.1	Analysis	167
6.1.2	Effect of antenna parameters on the input impedance	169
6.1.3	Experiments	177
6.1.4	Radiation pattern	181
6.2	FOUR EDGES DIRECTLY COUPLED MICROSTRIP ANTENNAS (FEDCOMA)	186
6.2.1	Analysis	186
6.2.2	Optimization and experiment	188
6.2.3	Radiation pattern	193
6.3	DISCUSSION	196

Chapter Seven	
CONCLUDING REMARKS	198
7.1	SALIENT RESULTS 198
7.1.1	General approach 198
7.1.2	Gap-coupled antennas 199
7.1.3	Directly coupled antennas 201
7.1.4	Comparison 202
7.2	FURTHER INVESTIGATIONS 203
7.2.1	Unsymmetrical four edges coupled antennas 203
7.2.2	Mixed (gap and direct) coupling in microstrip antennas 203
7.2.3	Arrays of broadband microstrip antennas 204
7.2.4	Coupled trapezoidal microstrip antennas 208
7.2.5	Gap coupled planar microwave circuits 210
Appendix A	
MEASUREMENT OF DIELECTRIC CONSTANT	212
Appendix B	
EVALUATION OF GAP CAPACITANCES	214
REFERENCES	217

LIST OF FIGURES

Figure No.	Caption	Page
1.1	Microstrip antenna configuration	2
1.2	Various types of microstrip antennas	3
1.3	A rectangular patch antenna modelled as transmission line	6
1.4	Some broadband microstrip antenna configurations	13
1.5	(a) Log-periodic and (b) Quasi-log-periodic microstrip antenna configurations	16
1.6	Various gap coupled microstrip antenna structures : (a) Radiating edges gap coupled microstrip antenna (b) Non-radiating edges gap coupled microstrip antenna (c) Four edges gap coupled microstrip antenna	20
1.7	Various directly coupled microstrip antenna configurations: (a) Radiating edges directly coupled microstrip antenna (b) Non-radiating edges directly coupled microstrip antenna (c) Four edges directly coupled microstrip antenna	21
2.1	Procedure to analyze microstrip antennas by Green's function approach	26
2.2	Segmentation for analyzing the loaded multi-port network model of Fig. 2.1	29
2.3	(a) Orientation of electric field and magnetic current vectors (b) Co-ordinate system	32
2.4	(a) Rectangular patch antenna and (b) its segmented network	35
2.5	Input impedance loci of RPA for three different feed-point locations	38

Figure No.	Caption	Page
2.6	VSWR variation with frequency of RPA for three different feed-point locations	39
2.7	VSWR variation with frequency for three different widths of RPA	39
2.8	Theoretical and experimental variations of VSWR with frequency of RPA with width (a) $W = 2.0$ cm and $W = 4.0$ cm	41
2.9	VSWR variation with frequency of RPA for two different substrate thicknesses	43
2.10	Theoretical and experimental variations of VSWR of RPA for $h = 0.159$ cm	43
2.11	Theoretical and experimental values of (a) E_θ in $\varphi = 0^\circ$ plane and (b) E_φ in $\varphi = 90^\circ$ plane of RPA shown in Fig. 2.10 (inset)	45
2.12	Experimental set-up for radiation pattern measurement	46
3.1	(a) Rectangular resonator, (b) its lumped representation, and (c) resonance curve; (d) Gap coupled resonators, (e) their lumped representation and (f) resonance curve	49
3.2	(a) Directly coupled resonators and (b) their lumped representation	51
3.3	(a) A gap coupled microstrip antenna and representation of gap by multi-terminal capacitive π -network, (b) Practical gap model	53
3.4	(a) REGCOMA with identical parasitic elements (b) magnetic wall boundary, (c) even-mode half section and (d) its segmented network	55
3.5	Input impedance loci of REGCOMA for three different values of length l_1 of the parasitic elements	59
3.6	Input impedance loci of REGCOMA for three values of gap-widths	61
3.7	Input impedance loci of REGCOMA for three different feed-point locations	63

Figure No.	Caption	Page
3.8	Theoretical and experimental input impedance loci of REGCOMA for $S_1 = 0.1$ cm	64
3.9	Theoretical and experimental input impedance loci of REGCOMA for $S_1 = 0.165$ cm	64
3.10	Experimental variations of VSWR with frequency of REGCOMA for two values of gap-widths	65
3.11	Input impedance loci of REGCOMA for three different coefficients of capacitance C_g	68
3.12	Input impedance loci of REGCOMA for three values of capacitance coefficient C_{ci}	69
3.13	Theoretical and experimental variations of VSWR with frequency of REGCOMA shown in Fig. 3.8 (inset)	71
3.14	Theoretical and experimental variations of VSWR with frequency of REGCOMA shown in Fig. 3.9 (inset)	72
3.15	Theoretical and experimental (a) input impedance loci and (b) VSWR versus frequency of REGCOMA	74
3.16	Input impedance locus for the modified dimensions of REGCOMA with identical parasitic elements	75
3.17	Input impedance loci of REGCOMA for three combinations of the lengths l_1 and l_2 of the parasitic elements	77
3.18	Input impedance loci of REGCOMA for three combinations of the gap-widths S_1 and S_2	80
3.19	Theoretical and experimental (a) input impedance loci and (b) variations of VSWR with frequency of REGCOMA	81
3.20	Photograph of the REGCOMA fabricated on $h = 0.159$ cm thick substrate with $\epsilon_r = 2.55$	83

Figure No.	Caption	Page
3.21	Normalized values of (a) real and (b) (b) imaginary parts of the voltage along the periphery of REGCOMA at three frequencies	84
3.22	Theoretical values of (a) E_θ in $\phi = 0^\circ$ plane and (b) E_ϕ in $\phi = 90^\circ$ plane of REGCOMA shown in Fig. 3.20	86
3.23	(a) Experimental E_θ in $\phi = 0^\circ$ plane and (b) theoretical and experimental E_ϕ in $\phi = 90^\circ$ plane of the REGCOMA shown in photograph 3.20	88
3.24	Experimental (a) input impedance locus and (b) VSWR variation with frequency of REGCOMA	90
3.25	Theoretical and experimental (a) input impedance loci and (b) variations of VSWR with frequency of REGCOMA	92
3.26	Photograph of the REGCOMA fabricated on the substrate having thickness $h = 0.318$ cm and $\epsilon_r = 2.55$	93
4.1	(a) NEGCOMA with identical parasitic elements and its (b) even-mode half section and (c) segmented network	97
4.2	Input impedance loci of NEGCOMA for three different values of gap-width S_1	100
4.3	Input impedance loci of NEGCOMA for three different values of coupling coefficient C_{cg}	102
4.4	Input impedance loci of NEGCOMA for three different values of coupling coefficient C_{ci}	103
4.5	Input impedance loci of NEGCOMA for three values of length l_1 of parasitic element	105
4.6	Input impedance loci of NEGCOMA for three locations of the feed-point	106
4.7	(a) NEGCOMA with identical parasitic elements and its (b) theoretical and experimental input impedance loci	108

Figure No.	Caption	Page
4.8	(a) Theoretical and experimental input impedance loci and (b) experimental VSWR variation with frequency of NEGCOMA	109
4.9	(a) NEGCOMA with parasitic elements of different lengths and (b) its segmented network	112
4.10	Input impedance loci of NEGCOMA for three different combinations of gapwidths S_1 and S_2	114
4.11	Impedance loci of NEGCOMA for three different combinations of lengths l_1 and l_2 of parasitic elements	115
4.12	(a) Theoretical and experimental input impedance loci and (b) experimental VSWR variation with frequency of NEGCOMA	117
4.13	Photograph of the NEGCOMA fabricated on the substrate having thickness $h = 0.159$ cm and $\epsilon_r = 2.55$	118
4.14	Input impedance loci of NEGCOMA for two values of length l_1 of parasitic element	121
4.15	(a) Theoretical and experimental input impedance loci and (b) experimental VSWR variation with frequency of NEGCOMA	122
4.16	Input impedance loci of NEGCOMA for two combinations of lengths l_1 and l_2 of parasitic elements	124
4.17	Photograph of the NEGCOMA fabricated on $h = 0.318$ cm thick substrate with $\epsilon_r = 2.55$	125
4.18	(a) Theoretical and experimental input impedance loci and (b) experimental VSWR variation with frequency of NEGCOMA	126
4.19	Real and imaginary parts of the voltage distribution along the periphery of the NEGCOMA at different frequencies	128
4.20	Theoretical values of radiation fields of NEGCOMA shown in Fig. 4.17	129

Figure No.	Caption	Page
4.21	Experimental values of radiation fields of NEGCOMA shown in Fig. 4.17	131
4.22	(a) Four edges gap coupled microstrip antenna (FEGCOMA), (b) its even mode half section (for $l_1 = l_4$ and $S_1 = S_4$) and (c) segmented network	133
4.23	Theoretical input impedance locus of FEGCOMA	135
4.24	(a) FEGCOMA and (b) its experimental input impedance locus	137
4.25	(a) FEGCOMA with $S_1 = 0.02$ cm and (b) its experimental input ¹ impedance locus	139
4.26	FEGCOMA fabricated on the substrate with $h = 0.318$ cm and $\epsilon_r = 2.55$	141
4.27	(a) FEGCOMA with $l_1 = 2.4$ cm and (b) its experimental input impedance locus	142
4.28	Experimental variation of VSWR with frequency of FEGCOMA shown in Fig. 4.27	143
4.29	Experimental values of radiation fields of FEGCOMA shown in Fig. 4.26	145
5.1	(a) Radiating edges directly coupled microstrip antenna (REDCOMA), (b) even-mode half section, and (c) segmented network	149
5.2	Input impedance loci of REDCOMA for two values of length l_1 of parasitic element	152
5.3	Input impedance loci of REDCOMA for two values of length l_2 of parasitic element	153
5.4	Input impedance loci of REDCOMA for different values of length l_c of connecting strips	155
5.5	Input impedance loci of REDCOMA for two different widths w_c of connecting strips	156
5.6	Input impedance loci of REDCOMA for two different feed-point locations	157

Figure No.	Caption	Page
5.7	(a) REDCOMA and (b) its theoretical and experimental input impedance loci	159
5.8	(a) Experimental input impedance locus and (b) VSWR variation with frequency of REDCOMA shown in (inset)	160
5.9	Photograph of the fabricated REDCOMA	161
5.10	Theoretical values of (a) E_θ (in $\phi = 0^\circ$ plane) and (b) E_ϕ (in $\phi = 90^\circ$ plane) for REDCOMA shown in Fig. 5.9	163
5.11	(a) Experimental values of E_θ (in $\phi = 0^\circ$ plane) and (b) theoretical and experimental values of E_ϕ (in $\phi = 90^\circ$ plane) for REDCOMA shown in Fig. 5.9	165
6.1	(a) Non-radiating edges directly coupled micro-strip antenna (NEDCOMA) and (b) its segmented network	168
6.2	Input impedance loci of NEDCOMA for two different values of length l_1 of parasitic element	171
6.3	Input impedance loci of NEDCOMA for two values of length l_2 of parasitic element	172
6.4	Input impedance loci of NEDCOMA for two different values of length l_c of connecting strips	174
6.5	Input impedance loci of NEDCOMA for two values of width w_c of the connecting strips	175
6.6	Input impedance loci of NEDCOMA for two different locations 'b' of the connecting strips	176
6.7	Input impedance loci of NEDCOMA for two different values of feed-point location 'a'	178
6.8	Input impedance locus of NEDCOMA shown in inset	179

Figure No.	Caption	Page
6.9	(a) Theoretical and experimental input impedance loci and (b) experimental VSWR variation with frequency of NEDCOMA	180
6.10	Photograph of the NEDCOMA configuration	182
6.11	Theoretical values of E_{θ} in $\varphi = 0^{\circ}$ plane and E_{φ} in $\varphi = 90^{\circ}$ plane of NEDCOMA shown in photograph 6.10	183
6.12	Experimental values of E_{θ} in $\varphi = 0^{\circ}$ plane and E_{φ} in $\varphi = 90^{\circ}$ plane of NEDCOMA shown in photograph 6.10	185
6.13	(a) Four edges directly coupled microstrip antennas (FEDCOMA) and (b) segmented network of even-mode half section of FEDCOMA	187
6.14	(a) FEDCOMA and (b) its theoretical and experimental input impedance loci	190
6.15	Experimental VSWR variation with frequency of FEDCOMA shown in Fig. 6.14(a)	191
6.16	Photograph of the FEDCOMA	192
6.17	Theoretical values of (a) E_{θ} in $\varphi = 0^{\circ}$ plane and (b) E_{φ} in $\varphi = 90^{\circ}$ plane of FEDCOMA shown in photograph 6.16	194
6.18	Experimental values of (a) E_{θ} in $\varphi = 0^{\circ}$ plane and (b) E_{φ} in $\varphi = 90^{\circ}$ plane of FEDCOMA shown in photograph 6.16	195
7.1	Segmentation for analysis of a microstrip antenna with mixed coupled resonators along the radiating edges	205
7.2	Series-fed arrays of (a) REGCOMA's and (b) NEDCOMA's	206
7.3	A corporate-fed array of NEDCOMA's	207

Figure No.	Caption	Page
7.4	(a) REGCOMA, (b) NEGCOMA and (c) FEDCOMA realized with trapezoidal structures	209
7.5	(a) Band stop filter using gap coupled triangular resonators and (b) its segmented network	211
A.1	A stripline half-wave resonator with upper plane removed	213
B.1	Asymmetric microstrip coupled line and its (a) even-mode capacitances and (b) odd-mode capacitances	215
B.2	Representation of gap by capacitive π -network	215

SYNOPSIS

BROADBAND MICROSTRIP ANTENNAS USING COUPLED RESONATORS

A Thesis Submitted
In Partial Fulfilment of the Requirements
for the Degree of
DOCTOR OF PHILOSOPHY

by
Girish Kumar
Department of Electrical Engineering
Indian Institute of Technology
Kanpur 208016.
August, 1982.

Microstrip antennas usually employ two-dimensional microstrip-like resonator structures. They are light in weight, have small volume and low-profile planar configurations which can be made conformal. The major shortcoming of these antennas is their narrow bandwidth. A commonly used definition for bandwidth is the frequency range over which input VSWR is less than two. A rectangular patch antenna has a bandwidth of the order of 4 percent at 3 GHz (substrate thickness $h = 0.318$ cm and $\epsilon_r = 2.55$). Bandwidth of the antenna can be increased proportionately either by increasing the substrate thickness or by reducing the dielectric constant. However, the increase in substrate thickness is generally limited by excitation of surface waves and there are practical limitations in

decreasing the value of dielectric constant. Thus, the bandwidth realized is not sufficient for many purposes.

A few configurations for improving the bandwidth have been reported in the literature. An improvement of 20 percent in the bandwidth has been obtained by using trapezoidal structures instead of commonly employed rectangular structures. The bandwidth of the antenna can be nearly doubled by placing quarter wavelength short circuit parasitic elements adjacent to the radiating edges of rectangular patch element or by placing parasitic strips parallel to the non-radiating edges of a patch antenna. Single feed has been used in these antenna structures. The bandwidth of the antenna can be increased manyfolds by employing multi-fed microstrip antenna arrays in log-periodic or quasi-log-periodic configuration.

In the present thesis, various configurations yielding broader bandwidth, from single fed antennas are proposed. These are : radiating edges coupled, non-radiating edges coupled, and four edges coupled microstrip antennas. The mechanism of the coupling between the resonators can be either gap coupling (two resonators being placed in close vicinity) or direct coupling (two resonators are connected by a short line section). These antenna structures are analyzed and optimized using Green's function approach with segmentation method. In segmentation method,

a structure is divided into segments for which impedance Green's functions are known. In gap coupled configurations, the gap between the coupled resonators is modelled as a capacitive π -network. The value of these capacitances is calculated by using formulas available for asymmetric coupled microstrip lines. This capacitive network model for the gap becomes one of the segments in the segmentation procedure. All series capacitances are shunted by conductances to account for the radiation from the gap. Based on these designs, extensive experiments have been carried out around 3 GHz frequency by fabricating more than fifty antennas on polystyrene substrate ($\epsilon_r = 2.55$).

In radiating edges gap coupled microstrip antennas, two resonators of slightly different lengths (approximately half wavelength) and widths equal to that of rectangular patch antenna, are placed adjacent to the radiating edges of rectangular patch element. Lengths of the parasitic elements, gap-width between the resonators, and location of the feed-point are optimized to yield maximum bandwidth. The bandwidth of the antenna obtained experimentally is 330 MHz (= 10 percent) for $h = 0.159$ cm and 510 MHz (= 16.9 percent) for $h = 0.318$ cm, which is 4.2 times the bandwidth of rectangular patch antenna (BW = 121 MHz).

In the non-radiating edges gap coupled antennas, two resonators of different lengths (nearly half wavelength) are gap coupled to the non-radiating edges of rectangular element. The experimental bandwidth of the antenna is 225 MHz for $h = 0.159$ cm. and 480 MHz for $h = 0.318$ cm. In this configuration, the gap-width between the resonators is found to be much smaller (~ 0.2 to 0.3 mm) than that of radiating edges gap coupled antennas. Because, in the non-radiating edges coupled case, field varies along the coupled edges, so coupling will be less for any specified gap-width as compared to the radiating edges coupled case where the field is nearly uniform along the coupled edges.

Four edges gap coupled antennas consist of four parasitic elements which are gap coupled to all the four edges of a rectangular patch element. The lengths of the parasitic elements placed along the non-radiating edges are taken equal. Experimental bandwidth of the antenna is 815 MHz ($= 25.8$ percent) for $h = 0.318$ cm, which is 6.7 times the bandwidth of rectangular patch antenna.

In radiating edges directly coupled antennas, two resonators of different lengths are directly coupled to the radiating edges of rectangular patch element through a short microstripline section. The parameters optimized are : lengths of the parasitic elements, location of the

feed-point, length and width of the connecting strip. Bandwidth of the antenna is 550 MHz (= 17.1 percent) for $h = 0.318$ cm.

In case of non-radiating edges directly coupled and four edges directly coupled antennas, additional resonators are directly coupled to non-radiating edges and all the four edges of rectangular patch element respectively. In the latter case, the resonators placed along the non-radiating edges are of equal lengths. As the field varies along the non-radiating edges, the coupling will be more if the connecting strip is located at higher field point. So, the locations of the connecting strips along the non-radiating edges become additional design parameters along with the other parameters of the radiating edges directly coupled antennas. Experimental bandwidths of the two antennas are 600 MHz (= 18.2 percent) and 810 MHz (= 24 percent) respectively for $h = 0.318$ cm.

A comparative study of these antenna structures points out that the four edges gap coupled and directly coupled antennas yield largest bandwidth. These designs help in overcoming the narrow bandwidth limitations of microstrip antennas.

CHAPTER ONE

INTRODUCTION

1.1 MICROSTRIP ANTENNAS

The concept of microstrip antennas was first proposed by Deschamps [1] in 1953. But the most extensive work and practical applications of microstrip antennas have been reported only during the last decade [2] - [33].

The simplest configuration of microstrip antenna is shown in Fig. 1.1. It consists of a radiating patch (of any geometry) on one side of a dielectric substrate, backed by a ground plane on the other side. However, a large variety of microstrip antennas is available. These include patch antennas, travelling wave antennas, slot antennas, and dipole antennas [2] - [33], as shown in Fig. 1.2. In this thesis, investigations are confined to microstrip patch antennas. These patch antennas are two-dimensional resonator structures. These structures have dimensions comparable to the wavelength (typically $\lambda/2$) in the two directions but the third dimension (i.e. the thickness of the substrate) is much smaller than the wavelength [34].

1.1.1 Special features of microstrip patch antennas

Microstrip patch antennas have numerous advantages over the conventional microwave antennas [30]. The main advantages are :

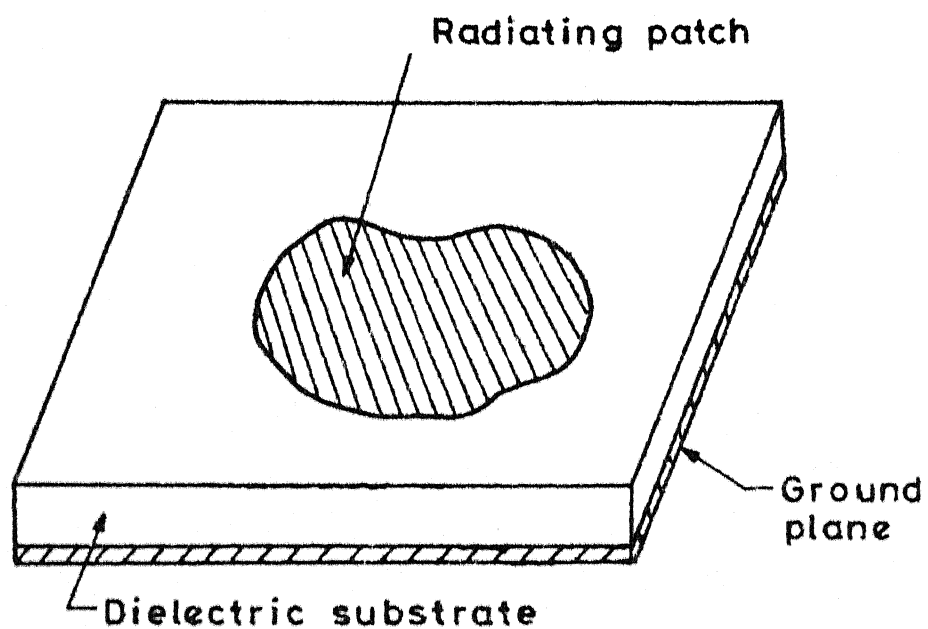
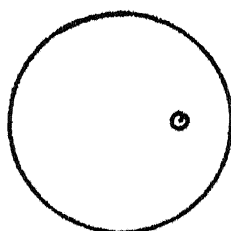
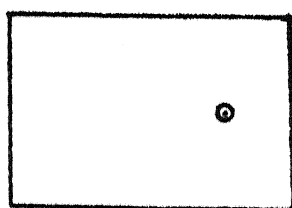
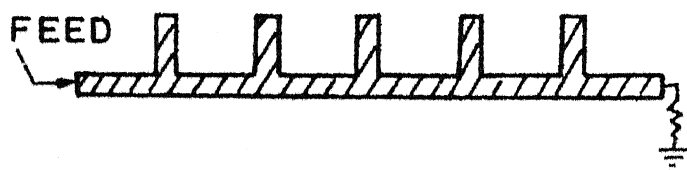


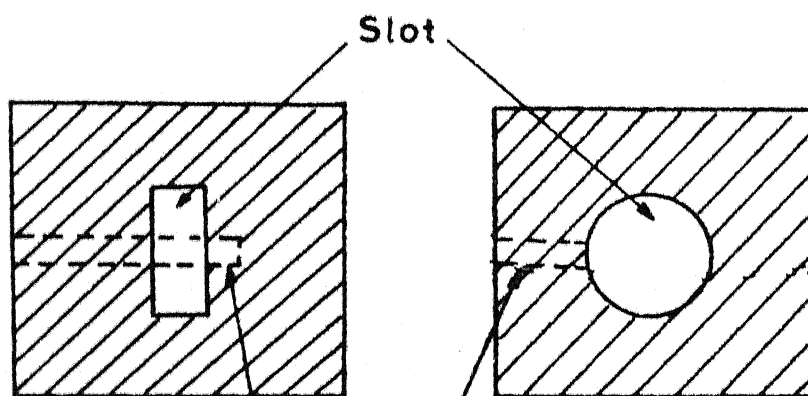
Fig.1.1 Microstrip antenna configuration



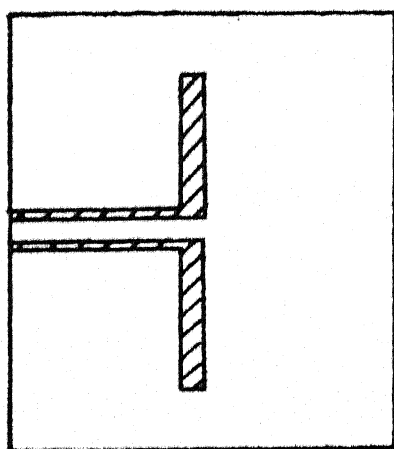
(a) Patch antenna



(b) Travelling wave antenna



(c) Slot antenna



(d) Dipole antenna

Fig.1.2 Various types of microstrip antennas

- i) Microstrip antennas are light in weight, have small volume and low-profile planar configurations which can be made conformal.
- ii) The antennas can be made paper thin, and therefore can be mounted conveniently on missiles, rockets, and satellites without perturbing the aerodynamic behaviour of the host vehicles.
- iii) Microstrip antennas are compatible with microwave integrated circuits so that solid state devices like oscillators, amplifiers, modulators, mixers, switches, variable attenuators, phase shifters, etc. can be fabricated on the antenna substrate itself.
- iv) Both linear and circular polarizations (left or right handed) are obtainable.
- v) Dual frequency and multiple frequency antennas can be easily designed.
- vi) Feed lines and matching networks are fabricated simultaneously alongwith the antenna structure.

Microstrip patch antennas also have a few disadvantages compared to the conventional microwave antennas. These are as follows :

- i) The major shortcoming of these antennas is their relatively narrow bandwidth (typically 1 percent to 5 percent).

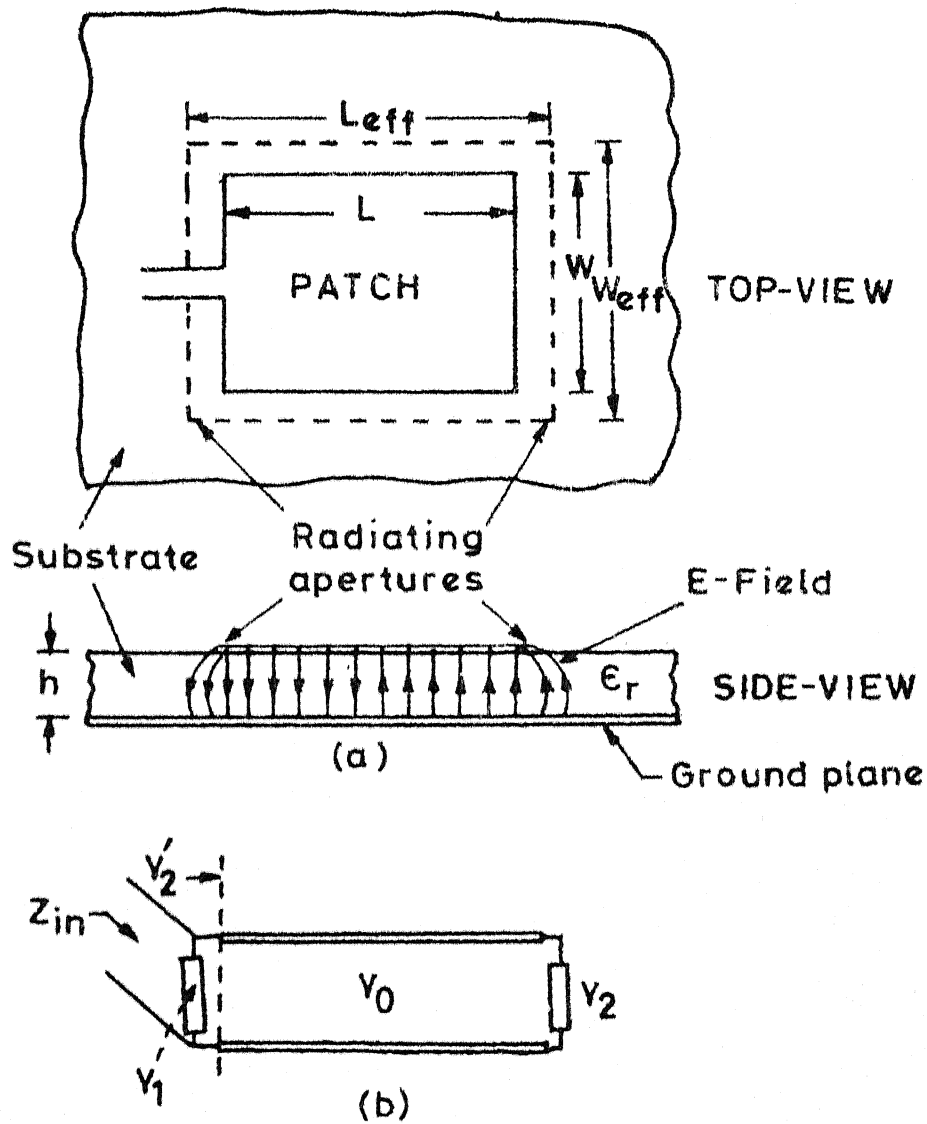
- ii) Surface waves may be excited along the antenna substrate, resulting in radiation in undesired directions. These surface waves produce excessive mutual coupling between the elements in the antenna arrays.

Because of the notable advantages of microstrip antennas over the conventional antennas, microstrip antennas have been developed for several applications, e.g., satellite communications, doppler radars, altimeters, missile telemetry, weapon fusing, phased array radars, satellite navigation receivers, biomedical applicators, etc.

1.1.2 Methods of analyzing microstrip antennas

Various methods for analyzing microstrip patch antennas have been proposed in the literature. Some of these methods are applicable only for the antennas with simple geometries, whereas others (the numerical techniques) have been used for analyzing complicated geometries also.

The simplest of all the methods is transmission line model, but it is applicable only to rectangular (or square) patch antennas. In this technique, the patch is modelled as a transmission line, with no transverse field variation [3], [30], [31]. The radiating edges of length W are considered as narrow slots radiating into half space as shown in Fig. 1.3. The effective length L_{eff} of the rectangle, after taking into account the open-end fringing fields, is chosen equal to half a wavelength ($\lambda_0/2\sqrt{\epsilon_r}$), which



Transmission line model

Fig.1-3 A rectangular patch antenna modelled as transmission line

makes the two parallel radiating slots to be excited with equal voltages but 180° out of phase [30]. The slot admittance [35], input impedance and resonant frequency are evaluated from the slot width and the effective dimensions of the patch [3], [30]. The input impedance is calculated by referring the admittance of the slots to the location of the feed-point as illustrated in Fig. 1.3(b). The radiation characteristics are obtained by considering the field distribution along the radiating edges to be uniform.

In the modal-expansion method, the radiating patch is viewed as a resonator with magnetic walls [22] - [26],[31]. The field in the cavity is expanded in series of corresponding eigen functions. The effect of radiation and other losses is represented in terms of either increased effective loss-tangent [22] or by employing impedance boundary conditions at the walls [23]. This method can be used for analyzing the shapes for which eigen functions are available [22],[23].

When a patch antenna is of a simple shape, impedance Green's functions [34],[36] are used for analysis. Green's functions are available for various simple shapes, like rectangle [34], circle [37], equilateral triangle, right-angled isosceles triangle, and 30° - 60° right angled triangle [38], circular sectors, annular sectors and annular rings [39],[40]. In this approach, the antenna structure is

modelled as a multiport network, and its impedance matrix is evaluated using Green's functions. In more general situations, when the antenna structure can be considered as combination of simple shapes, or if it can be considered as obtained by removal of one or more regular shapes from a larger segment (which is either a regular shape or combination of regular shapes), segmentation [36],[40] - [45] or desegmentation method [45] - [47] can be used for calculating Z-matrix of the multiport network. The ports of this multiport network are loaded with radiation conductance to account for the radiation from the antenna. The input impedance and voltage distribution along the periphery of the antenna (from which radiation characteristics are evaluated) are obtained from the Z-matrix of the loaded network. Details of the Green's function approach and segmentation method are described in Chapter Two.

For the analysis of arbitrary shaped planar antennas, numerical methods such as finite element method [23],[31] and method of moments [48],[49] are available. In the finite element method, the interior and exterior regions of the microstrip antenna are mathematically decoupled through the use of an equivalent aperture admittance as boundary conditions. The interior electric field satisfies the inhomogeneous wave equation alongwith the impedance boundary conditions on the perimeter walls, and these equations are solved as variational problem [31]. For analysis,

the antenna geometry is divided into several segments. Certain basis functions are used for each segment to solve the variational problem and the boundary conditions are imposed locally along the edges of the segment. The solution is obtained numerically.

In the method of moments, the electric surface currents flowing over the microstrip patch and ground planes, and the magnetic surface currents flowing over the magnetic wall are obtained from the Richmond's reaction method [48], [49]. Using boundary conditions for the surface currents, the reaction integral equation is solved by the method of moments. By selecting suitable expansion functions for electric surface currents, and electric test sources for magnetic currents, the reaction integral equation reduces to simultaneous linear equations. The coefficients of these equations give the elements of the impedance matrix.

Another approach is the spectral domain analysis [50] - [55]. The formulation of the method [54] is based on the spectral domain immittance matrix, which is derived from the spectral domain equivalent circuits. Galerkin's method is used to obtain the solution. In case of circular disk antenna, the full wave analysis has been carried out using Hankel transform [55].

1.1.3 Bandwidth of microstrip antennas

Depending upon system objectives, the bandwidth of an

antenna is limited either by its radiation characteristics (like beamwidth, axial ratio in case of circularly polarized antennas, etc.), or by its input VSWR characteristics. In case of microstrip patch antennas, the resonant behaviour causes the bandwidth to be limited by input VSWR. For such antennas, bandwidth is usually specified [30] as the frequency range over which the input VSWR is less than two. A typical bandwidth of a rectangular patch antenna is of the order of 2 percent at 3 GHz frequency (substrate thickness $h = 0.159$ cm, $\epsilon_r = 2.55$).

The input impedance characteristics of microstrip patch antennas can be understood by viewing them as resonators. The frequency range over which a resonator can be matched to an input transmission line is related to its Q-factor. The higher the Q-factor, the lower is the input matching bandwidth. Thus the input impedance matching bandwidth can be increased by increasing the losses in the resonators. Resonators for microstrip antennas experience four types of losses: (i) conductor losses in the patch and the ground plane, (ii) dielectric losses in the substrate dielectric material, (iii) losses due to the surface waves excited on the substrate, and (iv) losses because of the radiation of electromagnetic energy. Highest antennas efficiencies are obtained when conductor, dielectric, and surface wave losses (i, ii and iii) are negligible as compared to the radiation loss (iv). Thus any attempts of increasing the antenna bandwidth should increase radiated power for a specific energy storage in the resonator.

For single resonator microstrip patch antennas, power radiated from the fringing fields at the periphery of the antenna depends upon several parameters. If the thickness of the dielectric substrate is increased, the fringing field and the radiated power increase. The antenna bandwidth is found to increase linearly with the substrate thickness. However, for thicker substrate, the power loss due to the excitation of surface wave increases and put an upper limit on the thickness of the substrate that can be used at a given operating frequency. Decrease in the dielectric constant of the substrate increases the fringing field. So, radiated power and hence the bandwidth increase correspondingly. Therefore, low dielectric constant substrates are used for microstrip antennas. Percentage bandwidth is found to increase linearly with frequency. With increase in the frequency, the resonant length of the antenna and hence the energy storage decreases, consequently the bandwidth increases. Also the bandwidth increases with increase in the width W of the radiating edge of the rectangular patch. As the width increases, the radiated power and energy storage in the resonator increase. The increase in the radiated power is more than the increase in the energy storage, so the bandwidth increases slightly. But for larger widths, higher order modes may get excited causing field distortions. Thus, the bandwidth of the rectangular patch antenna is limited and is not sufficient for many applications.

1.2 CONFIGURATIONS FOR IMPROVING THE BANDWIDTH

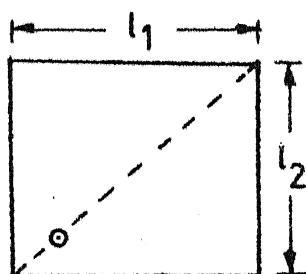
Various configurations have been reported in the literature to improve the bandwidth of the antenna by modifying the basic rectangular element. Some of these configurations are described in this section.

1.2.1 Diagonal fed nearly square patch antennas

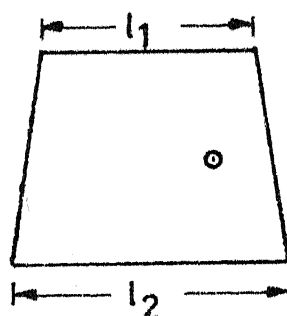
The bandwidth of the microstrip antennas can be increased by coupling the two-spatially orthogonal modes in rectangular resonators [56]. For a nearly square patch of dimensions l_1 and l_2 (shown in Fig. 1.4(a)), two modes are resonant at nearby frequencies f_1 and f_2 . The antenna is fed along the diagonal so that the input signal can be coupled to any one of the two modes. By optimum selection of lengths l_1 and l_2 , and feed-point location, VSWR bandwidth of the antenna can be increased to more than twice that of a single patch. The main disadvantage of this design is that the direction of polarization gets shifted by 90° , when the frequency of operation is changed from f_1 to f_2 [44].

1.2.2 Trapezoidal shaped microstrip antenna

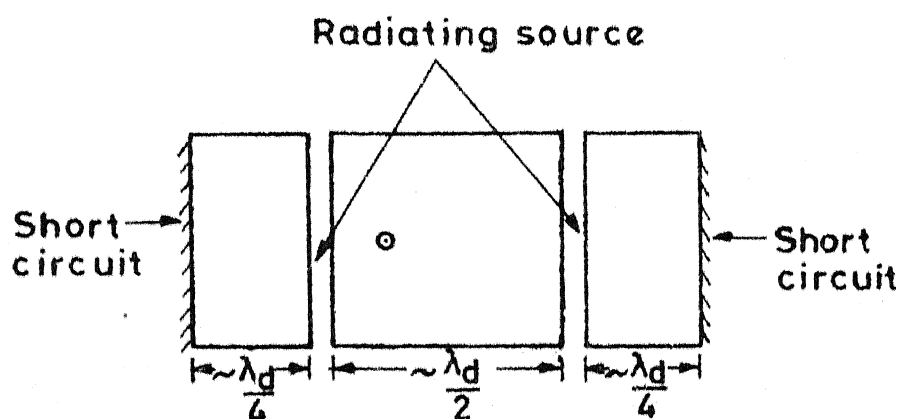
The bandwidth of microstrip antennas can be increased by using trapezoidal structures instead of commonly employed rectangular structures [57]. A trapezoidal shaped antenna of length l_1 at one edge and length l_2 at the other parallel edge is shown in Fig. 1.4(b). It is expected that a portion



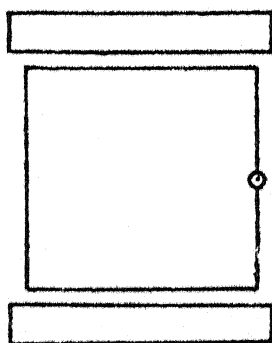
(a) Nearly square



(b) Trapezoidal



(c) Parasitic elements coupled to radiating edges



(d) Parasitic strips placed parallel to non radiating edges

Fig.14 Some broadband microstrip antenna configurations

of the width nearer to smaller side will be resonant at higher frequency and nearer to larger side will be resonant at lower frequency. However, because of tight coupling between these two resonances, one gets a single resonant frequency instead of multiple resonance behaviour. About 20 percent improvement in the bandwidth has been reported on the basis of initial experiments, when the difference between the lengths l_1 and l_2 is small [57], [44].

1.2.3 Short-circuit quarter wavelength parasitic elements coupled to the radiating edges of rectangular patch antenna

It has been reported that by coupling the short-circuit parasitic elements to the radiating edges of the rectangular patch antenna (as shown in Fig. 1.4(c)), the bandwidth of the antenna can be approximately doubled [58]. This phenomenon can be explained in terms of antiphase resonance condition between the driven patch and the parasitic element, which makes the radiated power to be four times that of the individual patch. However, the stored energy is only doubled, and since the bandwidth of the antenna is proportional to the ratio of radiated power and stored energy, it becomes nearly double that of the single patch element.

1.2.4 Parasitic strips placed parallel to the non-radiating edges of square patch antenna

By placing narrow parasitic strips parallel to the non-radiating edges of square patch antenna, as depicted in Fig. 1.4(d), matching to 50 ohms feed-line and bandwidth of the antenna can be improved [59],[31]. The parasitic strips are taken slightly longer than the patch, and the separation between the strips and patch should be 2.5 to 3 times the substrate thickness to yield best performance [59]. The bandwidth of the antenna is found to be more than twice that of corresponding single patch element [60].

1.2.5 Log-periodic microstrip antenna

The bandwidth of the microstrip antennas can be increased manifolds by employing multi-fed microstrip antenna arrays in log-periodic and semi-log-periodic configurations.

In log-periodic microstrip antenna configuration (depicted in Fig. 1.5(a)), broader bandwidth is obtained by series feeding a linear array of microstrip patch resonators, whose size and spacing increase in the log-periodic manner [61]. At lower frequencies, patches of larger sizes are excited, and form an active region. As the frequency increases, this active region moves along the array (i.e., towards the patches of smaller sizes). An array of 9-elements, using electromagnetic coupling between the feed

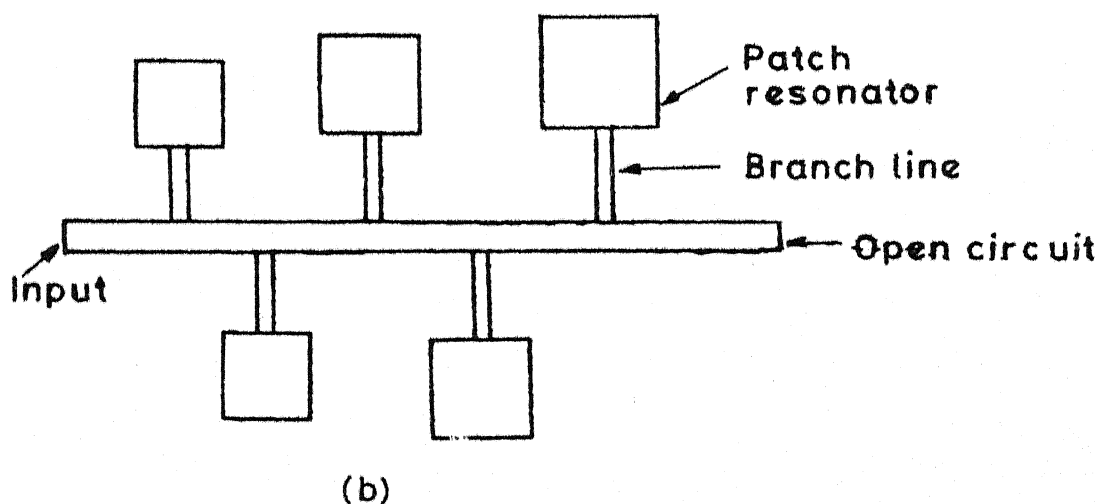
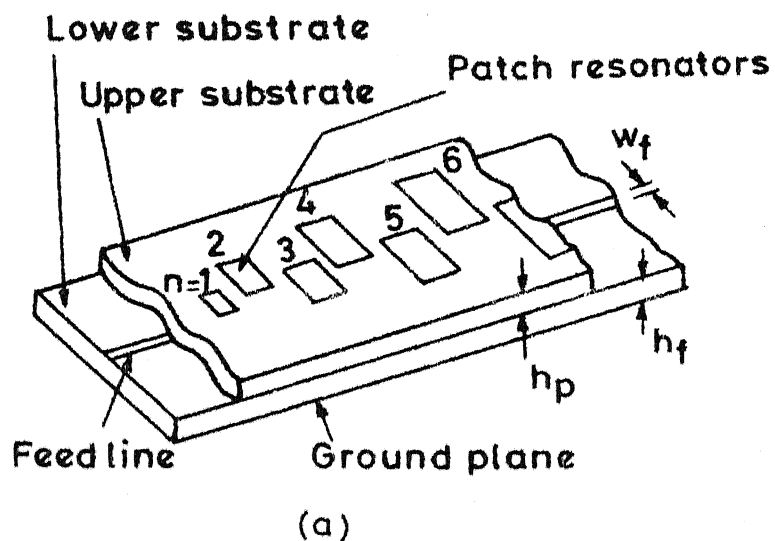


Fig.1-5 (a) Log-periodic and (b) Quasi-log-periodic microstrip antenna configurations

line and the overlaid resonators, yields a bandwidth of the order of 30 percent at nearly 8.9 GHz centre frequency [61].

1.2.6 Quasi-log-periodic microstrip antenna

A lay-out of the quasi-log-periodic antenna is shown in Fig. 1.5(b). In this configuration, the patch resonators are scaled log-periodically, and they are directly fed by microstrip line in one-layer structure instead of two-layer structure in case of log-periodic microstrip antenna [62]. The branch-lines are designed as quarter-wave transformers, which transform the resonant input impedance of the corresponding patch resonators to 50 ohms. An experimental bandwidth of 22 percent is obtained for VSWR < 2.6 at nearly 3 GHz frequency, which is nearly ten times the bandwidth of single element.

The bandwidth of the antenna can also be increased by using multilayer structures [63] or by using arrays of stagger-tuned resonators [64]. For a two layer structure, a bandwidth of 13 percent is obtained when a 3.9 mm x 3.9 mm patch on alumina ceramic substrate ($h = 0.625$ mm and $\epsilon_r = 9.8$) is covered by an 8 mm x 8 mm x 1.59 mm polyguide substrate ($\epsilon_r = 2.32$), which then serves as a matching transformer to free space [31], [63]. A bandwidth of 18 percent can be obtained by using three layers.

1.3 PRESENT INVESTIGATIONS

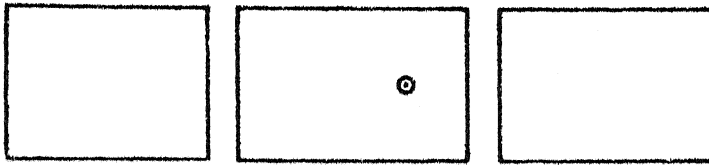
The investigations reported in this thesis are aimed at the development of the various microstrip antenna configurations to yield broader bandwidth. These antenna configurations have been designed, analyzed and optimized using the Green's function approach and the segmentation method, described in Section 1.1.2.

A detailed review of the Green's function approach and the segmentation method is presented in Chapter Two. In this approach, the antenna configuration is considered as a multiport network, which is obtained by dividing the periphery of the antenna into a finite number of ports. Z-matrix for this multiport network is calculated by employing an appropriate Green's function. For more complicated shapes, segmentation method is used, which involves breaking up of the antenna configuration into segments for which Green's functions are known. To account for the radiated power from the antenna, the ports of the multiport network are loaded with radiation conductances. The Z-matrix of the loaded multiport network yields input impedance and voltage distribution along the periphery, which in turn, is used to calculate radiation characteristics of the antenna. This approach has been used for analyzing rectangular patch antenna. Effects of changing the width of the rectangular element and substrate thickness on the bandwidth of the antenna

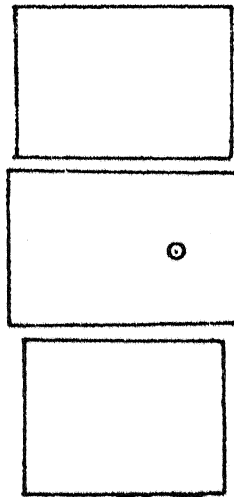
are studied. Experiments have been carried out for two different values of width of the rectangle and for two different substrate thicknesses. The experimental results are found to be in good agreement with the theoretical results.

In the next four chapters, six types of broadband microstrip antennas, which are developed during the present investigations, are analyzed and optimized using the Green's function approach and the segmentation method. These antenna configurations are : radiating edges coupled, non-radiating edges coupled and four edges coupled microstrip antennas. Both gap coupling and direct coupling between the resonators are considered separately for these three configurations as depicted in Figs. 1.6 and 1.7. These antenna structures consist of multiple resonators of slightly different lengths. So, at any specified frequency, one resonator gets excited, and at nearby frequencies, other resonators are excited, thereby yielding broader bandwidth.

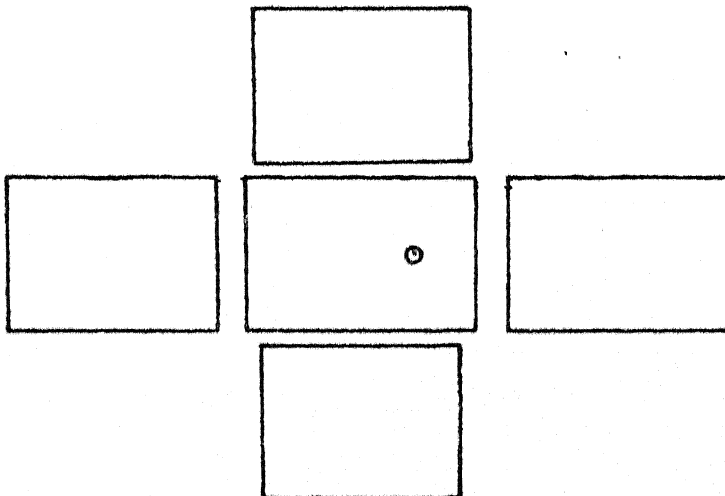
The details of the investigations carried out on radiating edges gap coupled microstrip antennas are described in Chapter Three. In this structure two resonators are placed adjacent to the radiating edges of the rectangular patch element. The gap between the resonators is modelled as a capacitive π -network. This capacitive network model becomes one of the segments in the segmentation procedure. The effect



(a) Radiating edges gap coupled microstrip antenna

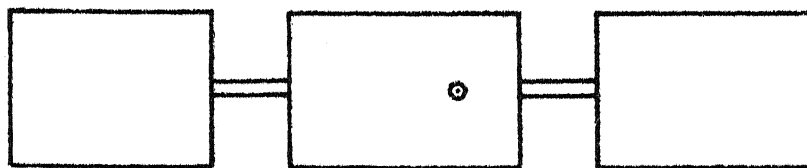


(b) Non-radiating edges gap coupled microstrip antenna

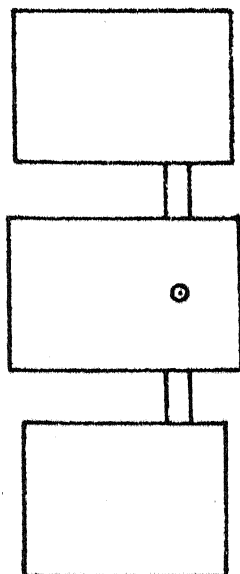


(c) Four edges gap coupled microstrip antenna

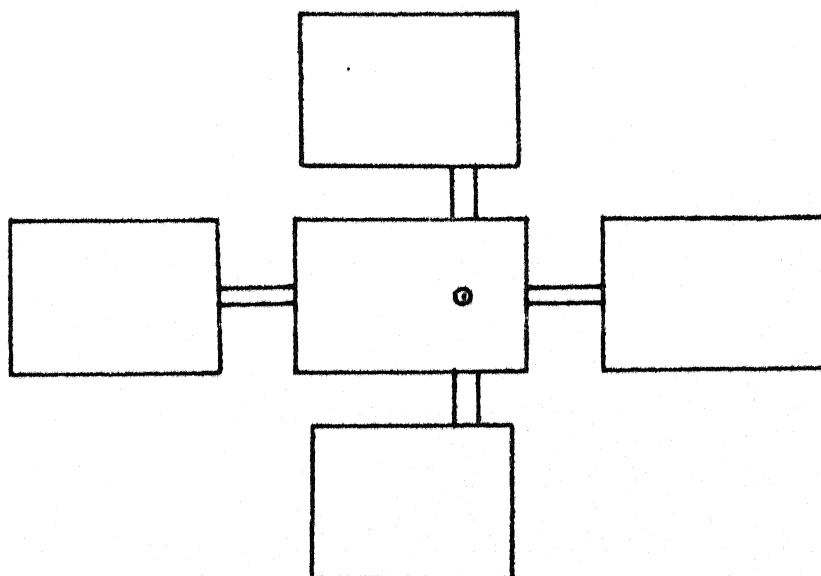
Fig.1-6 Various gap coupled microstrip antenna structures



(a) Radiating edges directly coupled microstrip antenna



(b) Non-radiating edges directly coupled microstrip antenna



(c) Four edges directly coupled microstrip antenna

Fig.17 Various directly coupled microstrip antenna configurations

of the various antenna parameters (like lengths of the parasitic elements, gap between the resonators, and feed-point location) on the input impedance locus is studied. Experiments have been performed to study some of these effects. A broader bandwidth is obtained by optimizing the above parameters, and has been verified experimentally. Radiation pattern for the optimum design is calculated and measured.

Chapter Four deals with the analysis, design and optimization of non-radiating edges gap coupled and four edges gap coupled microstrip antennas. In these two configurations, the additional resonators are gap coupled to the non-radiating edges and all the four edges of rectangular patch element respectively. The effect on the input impedance locus due to change in the antenna parameters (such as, lengths of the parasitic elements, gaps between the patch and parasitic elements, and location of the feed-point) is investigated. These parameters are then optimized to yield wider bandwidth and based on these designs, experiments have been carried out.

Analysis and design of radiating-edges directly coupled microstrip antennas are reported in Chapter Five, and that of non-radiating edges directly coupled and four edges directly coupled microstrip antennas are contained in Chapter Six. In these three antenna structures, parasitic

resonators are directly coupled to the radiating edges, non-radiating edges and all the four edges of rectangular patch element respectively, through short sections of microstrip line. The effect of varying the antenna parameters (lengths of the parasitic elements, connecting strips dimensions, and locations of the connecting strips and feed point) on the input impedance locus are observed. The results obtained from these observations are utilized for performing the experiments to get broader bandwidth.

The Seventh and the concluding chapter discusses the significant results reported in the thesis and gives suggestions for further extension of this work.

CHAPTER TWO

GREEN'S FUNCTION APPROACH, SEGMENTATION METHOD, AND RECTANGULAR PATCH ANTENNAS

Green's function approach [34] is a useful technique for analyzing two-dimensional planar circuits. This approach is basically applicable to simple shapes for which Green's functions are available. However, by using segmentation method, this technique has been extended to analyze two-dimensional components, which can be considered as combination of simple shapes [40] - [42]. Recently, this technique has been used for analyzing planar microstrip antennas also [36], [43] - [45]. As this approach has been used for the investigations reported in this thesis, a brief review of the method is presented in the following section.

2.1 GREEN'S FUNCTION APPROACH

The problem of analyzing microstrip antennas can be divided into two parts. Firstly, for a given location of the feed-point, one calculates the voltage distribution along the periphery of the antenna. This voltage distribution can then be expressed as an equivalent magnetic current distribution and the far fields are calculated using Kirchhoff-Huygen's formula. For calculating the voltage along the periphery of the antenna, the Green's function approach is

employed. Green's functions are available for rectangles [34], circles [37], equilateral triangles, right-angled isosceles triangles, 30° - 60° right-angled triangles [38], circular sectors, annular sectors and annular rings [39], [40].

The procedure for analyzing microstrip antennas is illustrated in Fig. 2.1. For the analysis purpose, an equivalent network model of the antenna is considered. To obtain this model, the physical boundary of the antenna structure is extended outward to account for the open-end fringing fields [30],[65], and a magnetic wall is considered to exist at this boundary. This magnetic wall boundary is divided into several sections of finite widths and each section is considered as a port of the multiport network. The width of these ports is selected such that the variation of the field along this part of the periphery is small. So, the number of ports considered along any edge depends upon the field variation along that edge. These ports along the periphery of the antenna alongwith the feed-port (or ports) constitute a multiport network model of the antenna. The impedance matrix of this multiport network model is obtained by using an appropriate Green's function. The diagonal element Z_{ii} of the impedance matrix gives the input impedance at the i th port. The poles of the input impedance yield the

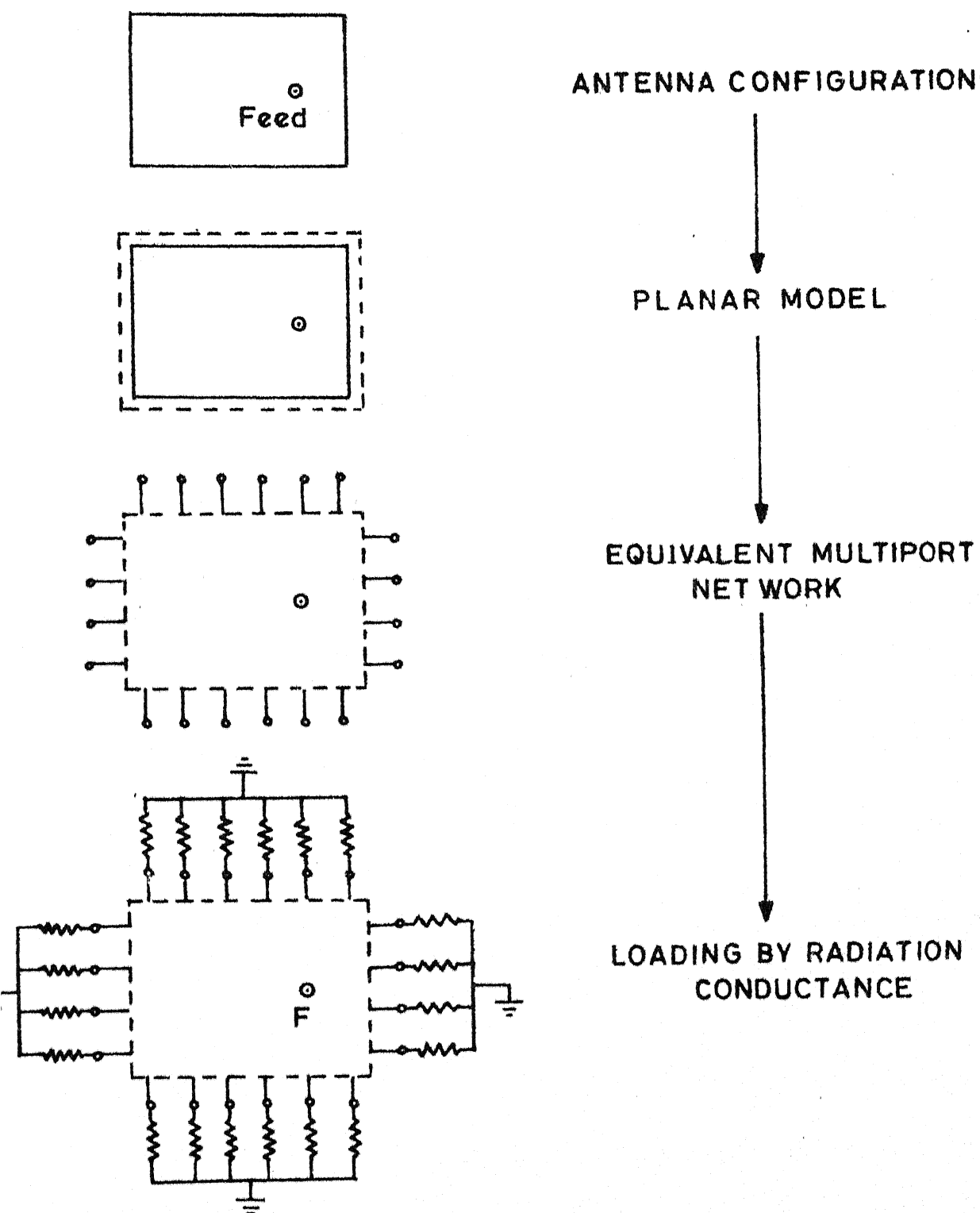


Fig.21 Procedure to analyze microstrip antennas by Green's function approach

resonance frequencies of the planar structure. The element Z_{ij} gives the voltage at the i th port for a unit input current excitation at the j th port.

The ports along the periphery of the multiport network are terminated with conductances [18],[30],[66] to account for the radiated power from the antenna, as shown in Fig. 2.1. The values of the radiation conductances which terminate the ports are calculated as follows :

- i) The radiation conductance for each of the four sides of the planar model of Fig. 2.1 is calculated; ii) this radiation conductance is distributed to each of the ports along the periphery, the values being proportional to the portwidths; iii) the conductances thus obtained are considered to be connected at the mid-points of the respective ports.

The next step involves (i) finding the input impedance of the loaded equivalent multiport network at the feed-point F , and ii) calculating the voltages at the various ports on the periphery of the loaded network. For this purpose segmentation method is used.

2.2 SEGMENTATION METHOD

Consider an example of loaded equivalent network model of rectangular patch antenna shown in Fig. 2.1. The multiport network representing the planar element is considered as one segment (α) and radiation conductance multiport network (β) as

another segment as illustrated in Fig. 2.2. The entries in the Z-matrix of the β -segment are all zeros except the diagonal elements Z_{ii} , which are equal to inverse of the radiation conductances of the corresponding i-ports. The Z-matrix of the loaded network is calculated from the Z-matrices of the individual sub-components using segmentation method as follows [42],[45] :

Z-matrices of the individual sub-components are expressed in a single matrix equation after regrouping the connected ports (denoted by subscripts c and d) and external port/ports (denoted by a subscript p) separately [42]. This yields

$$\begin{bmatrix} \underline{v}_p \\ \underline{v}_c \\ \underline{v}_d \end{bmatrix} = \begin{bmatrix} \underline{Z}_{pp} & \underline{Z}_{pc} & \underline{Z}_{pd} \\ \underline{Z}_{cp} & \underline{Z}_{cc} & \underline{Z}_{cd} \\ \underline{Z}_{dp} & \underline{Z}_{dc} & \underline{Z}_{dd} \end{bmatrix} \begin{bmatrix} \underline{i}_p \\ \underline{i}_c \\ \underline{i}_d \end{bmatrix} \quad (2.1)$$

where the bar (-) below the letters indicates a matrix or a multi-dimensional vector. The interconnections can be expressed as

$$\underline{v}_c = \underline{v}_d, \quad \underline{i}_c = -\underline{i}_d \quad (2.2)$$

Substituting (2.2) in (2.1) and eliminating \underline{v}_p , \underline{v}_c and \underline{i}_d , one gets

$$\underline{i}_c = \underline{Z}'_{cp} \underline{i}_p \quad (2.3)$$

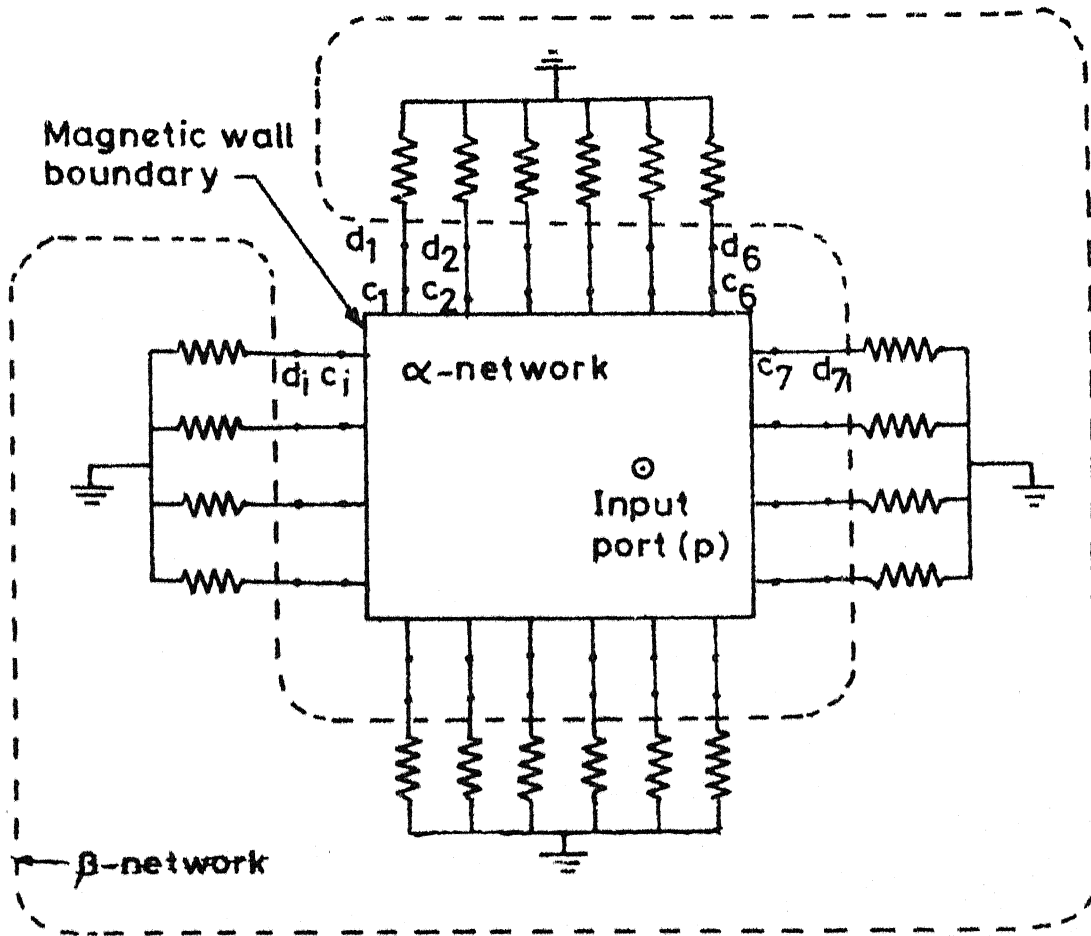


Fig.2-2 Segmentation for analyzing the loaded multiport network model of Fig.2.1

where

$$\underline{Z}'_{cp} = (\underline{Z}_{cc} - \underline{Z}_{cd} - \underline{Z}_{dc} + \underline{Z}_{dd})^{-1} (\underline{Z}_{dp} - \underline{Z}_{cp}) \quad (2.4)$$

Substituting (2.3) into the first equation of (2.1) and using $\underline{i}_c = -\underline{i}_d$, the Z-matrix for the overall network is obtained as

$$\underline{Z}_p = \underline{Z}_{pp} + (\underline{Z}_{pc} - \underline{Z}_{pd})\underline{Z}'_{cp} \quad (2.5)$$

For a single external p-port, \underline{Z}_p directly yields the input impedance of the antenna. For more than one external p-ports, the diagonal elements Z_{ii} of the impedance matrix \underline{Z}_p give the input impedances at the i-ports.

Voltages $\underline{v}_c (= \underline{v}_d)$ at the connected c-ports can be obtained by substituting (2.3) into the second equation of (2.1) as

$$\underline{v}_c = [\underline{Z}_{cp} + (\underline{Z}_{cc} - \underline{Z}_{cd})\underline{Z}'_{cp}]\underline{i}_p \quad (2.6)$$

The radiation pattern of the antenna is calculated from the voltage distribution along the periphery as described in the following section [45].

2.3 RADIATION PATTERN CALCULATIONS

The voltage at any port along the periphery, given by (2.6), can be expressed as equivalent Huygen's magnetic current source [22],

$$\underline{K}' = -2(\hat{n} \times \hat{z})E_z \quad (2.7)$$

where \bar{K}' is the surface magnetic current density, \hat{n} is the outward unit vector normal to the magnetic wall, \hat{z} is the unit vector along z-axis, and E_z is the electric field at the respective port location directed along z-axis. The relative orientation of the vectors \bar{K}' , \hat{n} and \bar{E}_z are shown in Fig. 2.3(a). The image of the magnetic current with respect to the ground plane is accounted by introducing a factor of 2 in (2.7). In the case of planar microstrip antennas, the thickness of the substrate is generally small and therefore the field E_z is assumed to be constant along the z-direction, thus (2.7) becomes

$$\bar{K} = 2(\hat{n} \times \hat{z})V_z \quad (2.8)$$

where \bar{K} represents the equivalent magnetic line current source which is obtained by integrating (2.7) over the thickness of the substrate, and V_z is the voltage at the corresponding port location. The electric vector potential for the magnetic current, given by (2.8), can be expressed as

$$\bar{F}(\bar{r}) = \epsilon_0 \int_c \frac{\bar{K}(\bar{r}')}{4\pi|\bar{r}-\bar{r}'|} e^{-jk_0|\bar{r}-\bar{r}'|} dl(\bar{r}') \quad (2.9)$$

where \bar{r} and \bar{r}' are the distance vectors of the field point and source point respectively as shown in Fig. 2.3(b). The integral is performed along the periphery of the antenna. As the voltage is nearly uniform over a port width, (2.9) reduces to

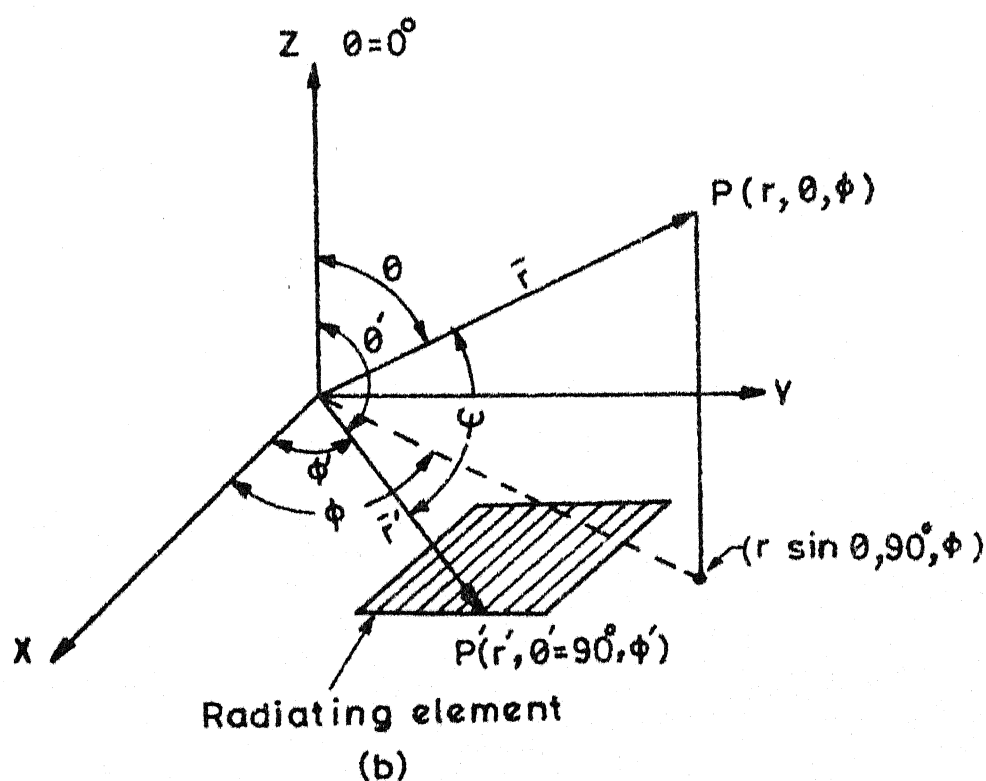
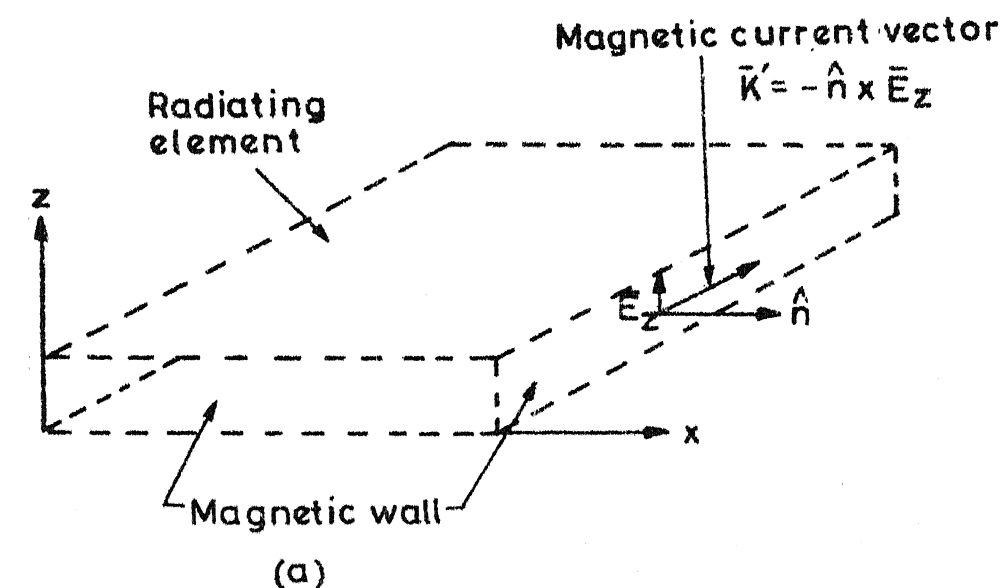


Fig.2.3(a) Orientation of electric field and magnetic current vectors
(b) Co-ordinate system

$$\bar{F}(\bar{r}) = \frac{\epsilon_0}{4\pi} \sum_{i=1}^m \bar{K}_i(\bar{r}') \int_{c_i} \frac{1}{|\bar{r}-\bar{r}'|} e^{-jk_0|\bar{r}-\bar{r}'|} dl(\bar{r}') \quad (2.10)$$

where m is the number of ports considered on the periphery of the antenna. The integration is thus performed over each portwidth and summed up to evaluate the electric vector potential. The far fields at a distance \bar{r} from the origin are obtained as

$$\bar{E}_\theta = -jk_0(\bar{F}_X \sin\varphi - \bar{F}_Y \cos\varphi) \quad (2.11a)$$

$$\bar{E}_\varphi = -jk_0(\bar{F}_X \cos\varphi + \bar{F}_Y \sin\varphi) \cos\theta \quad (2.11b)$$

where \bar{F}_X and \bar{F}_Y are x and y components of the electric vector potential $\bar{F}(\bar{r})$. The two radiation fields \bar{E}_θ and \bar{E}_φ are in space-quadrature, and after calculating their amplitudes and phases from (2.11), the polarization pattern can be evaluated in any direction and plane.

2.4 RECTANGULAR PATCH ANTENNAS (RPA)

In this section, Green's function approach and segmentation method are used to analyze and design rectangular patch antennas (RPA). The effects of changing some of the parameters on the bandwidth of RPA are studied, which will be useful for the analysis and design of the various antenna structures (for improving the bandwidth of the antenna), discussed in Chapters Three to Six. For the comparison of the bandwidth obtained in the cases of various antennas structures described in the later chapters with the bandwidth of RPA, these studies are necessary.

2.4.1 Analysis

A rectangular patch antenna with a co-axial feed is shown in Fig. 2.4(a). The analysis method discussed above is used for analyzing RPA. The magnetic wall boundary, obtained by extending the physical boundary of the antenna outward to account for the fringing fields at the open-ends [65], is divided into several ports as shown in Fig. 2.4(b). The widths of these ports are considered such that the field variation along each portwidth is small. It is noted that six ports are needed along the non-radiating edges (as the field varies sinusoidally along the length), and only two ports are needed along the radiating edges (as the field is nearly uniform along the width) for the analysis. By considering these many ports, the input VSWR obtained is correct upto three decimal places. If more number of ports are considered, accuracy will be better but the computation time required for analysis increases. The ports of the multiport network are terminated with the conductances to account for the radiated power [66]. Z-matrix of the loaded multiport network model is calculated from the Z-matrices of the two segments (namely, planar model of the rectangular element and radiation conductance network) by using (2.5).

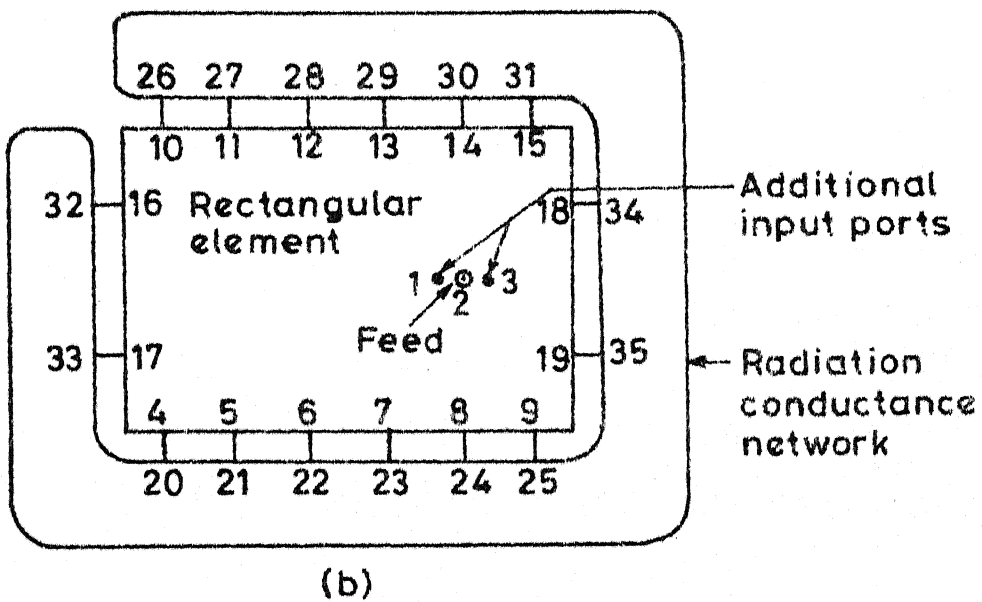
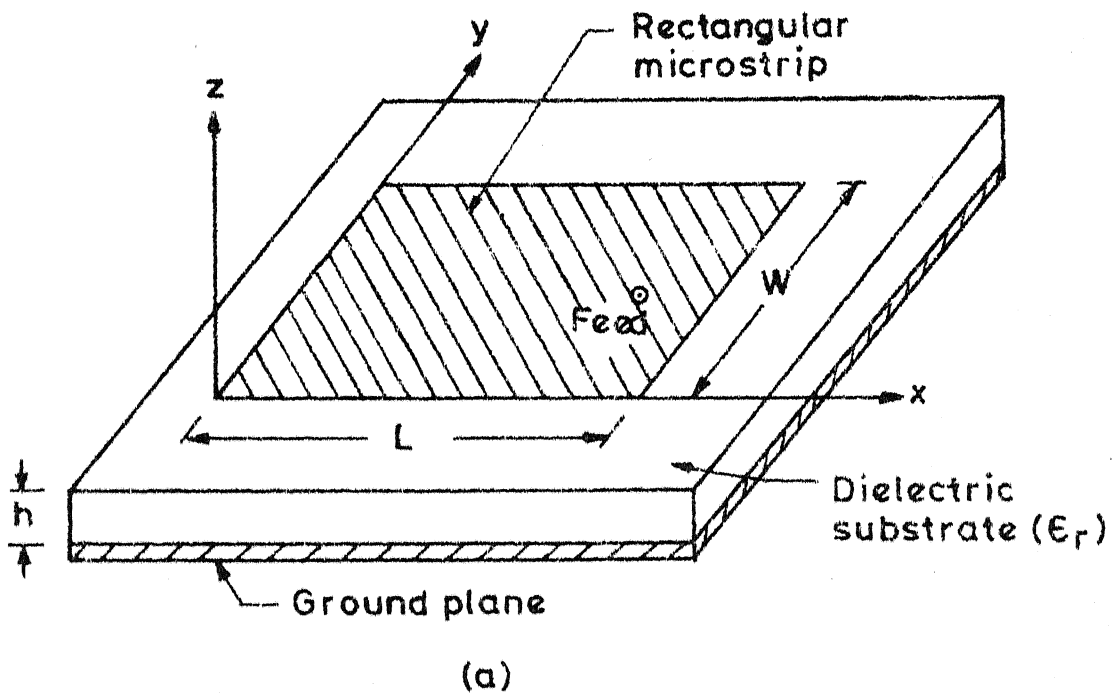


Fig.2.4(a) Rectangular patch antenna and
(b) its segmented network

In order to select a feed-point location for which the input impedance is 50 ohms, the analysis is carried out with various possible locations of the feed-points considered as external ports in the antenna configuration shown in Fig. 2.4(b). The widths of the feed-ports are taken equal to the diameter of the pin of co-axial feed line or equal to the width of the feed-line in case of microstrip feed. The Z-matrix is evaluated with respect to these external ports. The diagonal elements of the Z-matrix give input impedances at the feed-locations. For a unit current excitation at the feed-port, the voltage distribution along the periphery is obtained from (2.6). The electric vector potential is calculated using (2.10) and the far fields are evaluated from (2.11).

2.4.2 Bandwidth

For a RPA, the bandwidth is limited by input VSWR and it may be defined as the frequency range for which VSWR remains less than two. The VSWR is calculated from the input impedance at the feed-point locations. The effects of some of the parameters of RPA (like feed-point location, width of the rectangle, and substrate thickness), on the bandwidth of the antenna are discussed below.

Effect of feed-point location

For three different feed-point locations with patch dimensions : $L = 2.9$ cm and $W = 4.0$ cm, and substrate parameters:

$h = 0.318$ cm and $\epsilon_r = 2.55$, the input impedance loci and variation of VSWR with frequency are plotted in Figs. 2.5 and 2.6 respectively. As the feed-point location 'a' decreases from 0.86 cm to 0.65 cm (i.e. the feed-point location is shifted towards the nearer edge of the rectangle), the impedance locus shifts towards the right side of the Smith chart, and the bandwidth of the antenna increases from 100 MHz to 123 MHz. Because by shifting the feed-point location near to the edge, the value of the field increases, so the input impedance increases. This results in shifting the impedance locus towards the right side of the Smith chart. For $a = 0.65$ cm, the impedance plot crosses the VSWR = 2 circle along the diameter, so the bandwidth is maximum, but the input impedance is not matched to 50 ohms line at any frequency.

Effect of width

Variation of VSWR with frequency for three different widths ($W = 2.0, 3.0$ and 4.0 cm) of a RPA with length $L = 2.9$ cm, $\epsilon_r = 2.55$ and $h = 0.318$ cm, is plotted in Fig. 2.7. The feed-point locations to match input impedance to 50 ohms at centre frequency, are found to be different for the three cases. From the VSWR plots, it is noted that with increase in the width of the RPA from 2.0 cm to 4.0 cm, centre frequency decreases from 2.99 GHz to 2.91 GHz, and the bandwidth of the antenna increases from 97.5 MHz (= 3.25 percent) to 115 MHz (= 3.95 percent).

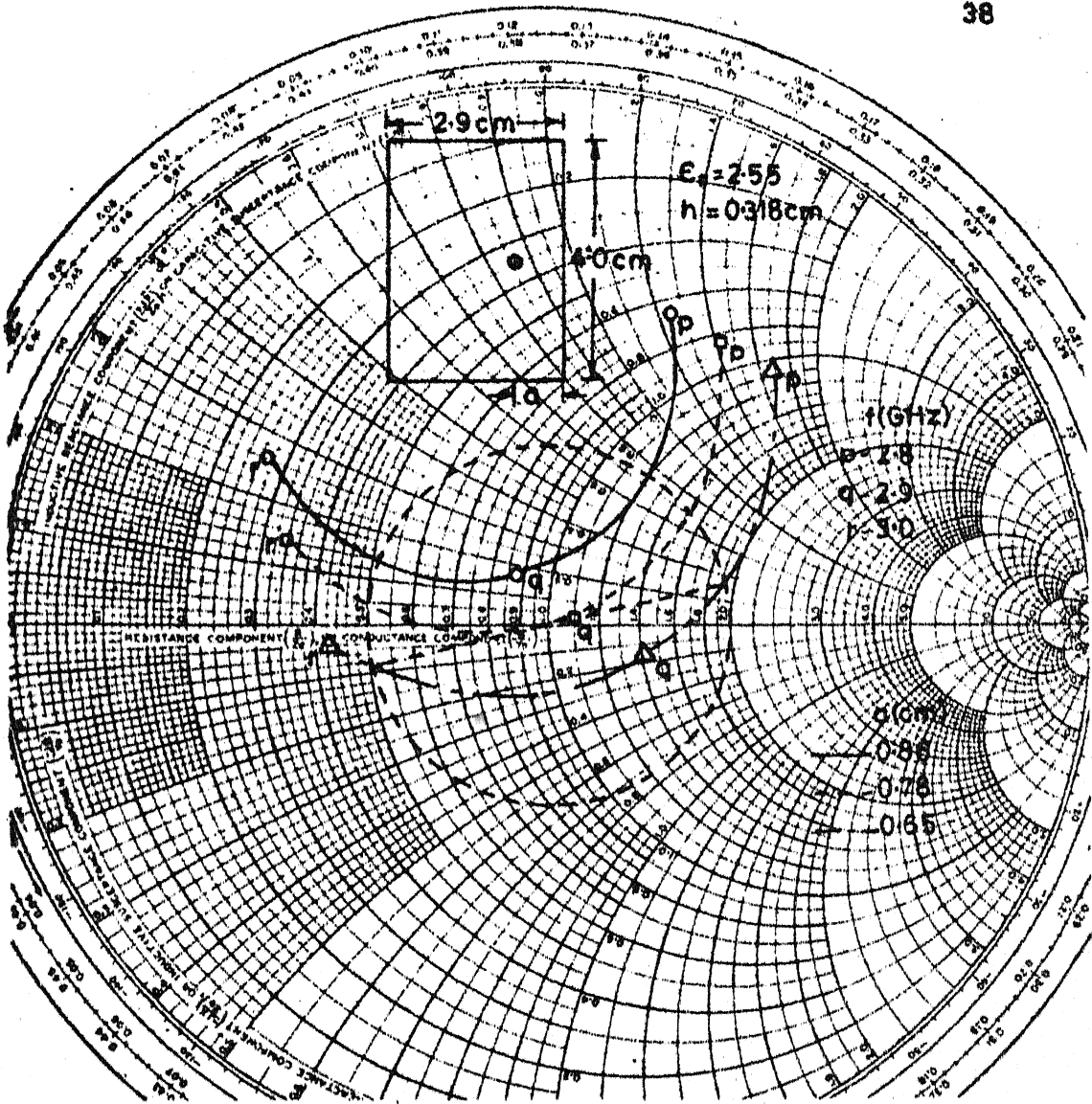


Fig. 2.5 Input impedance loci of RPA for three different feed-point locations

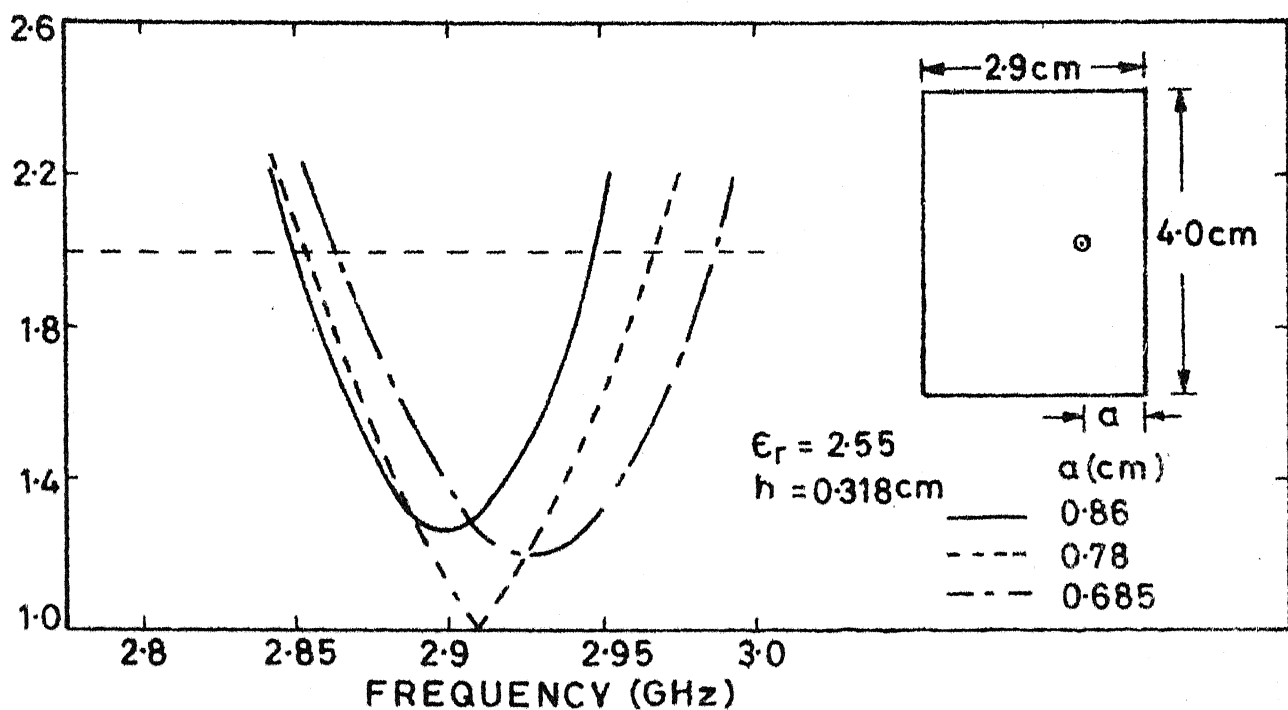


Fig. 2.6 VSWR variation with frequency of RPA for three different feed-point locations

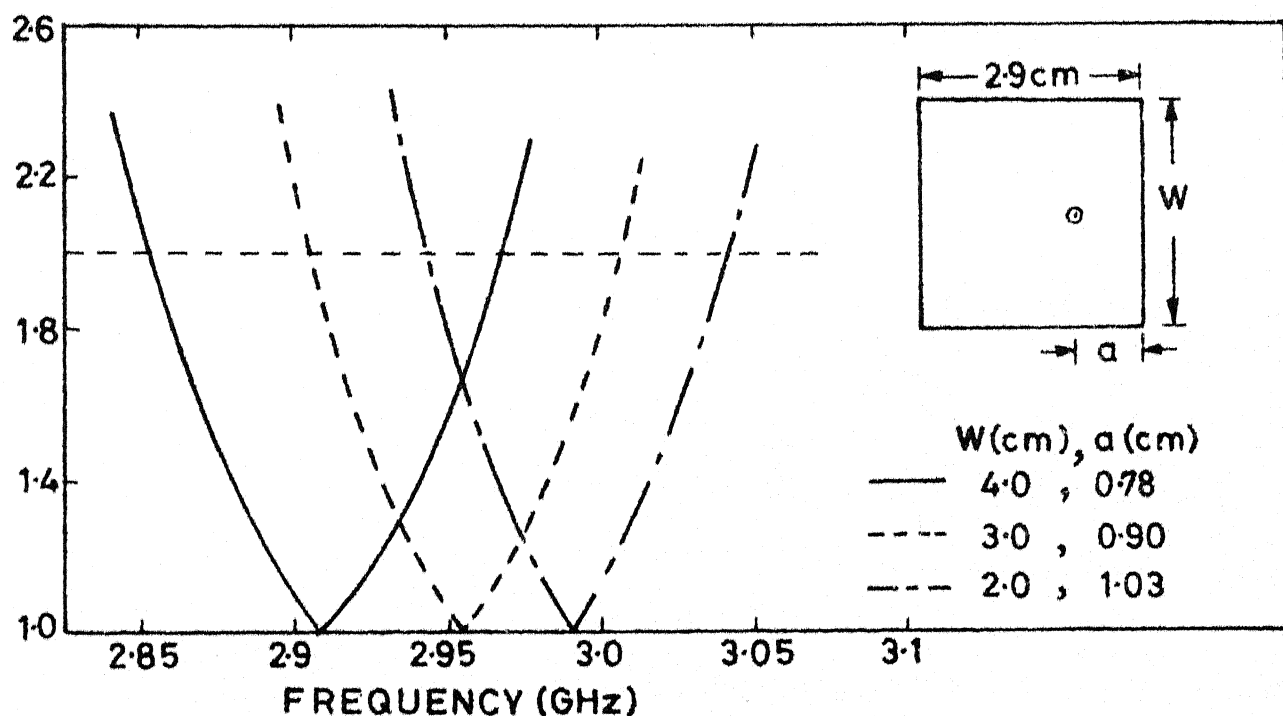
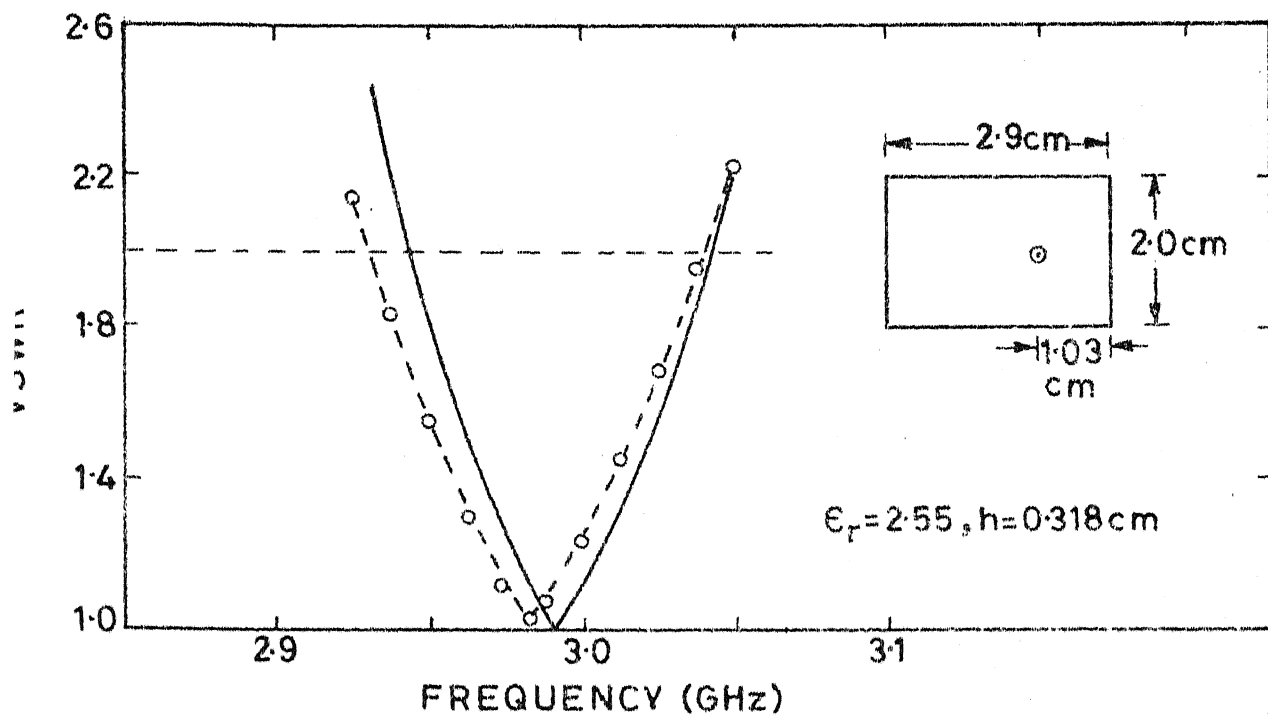


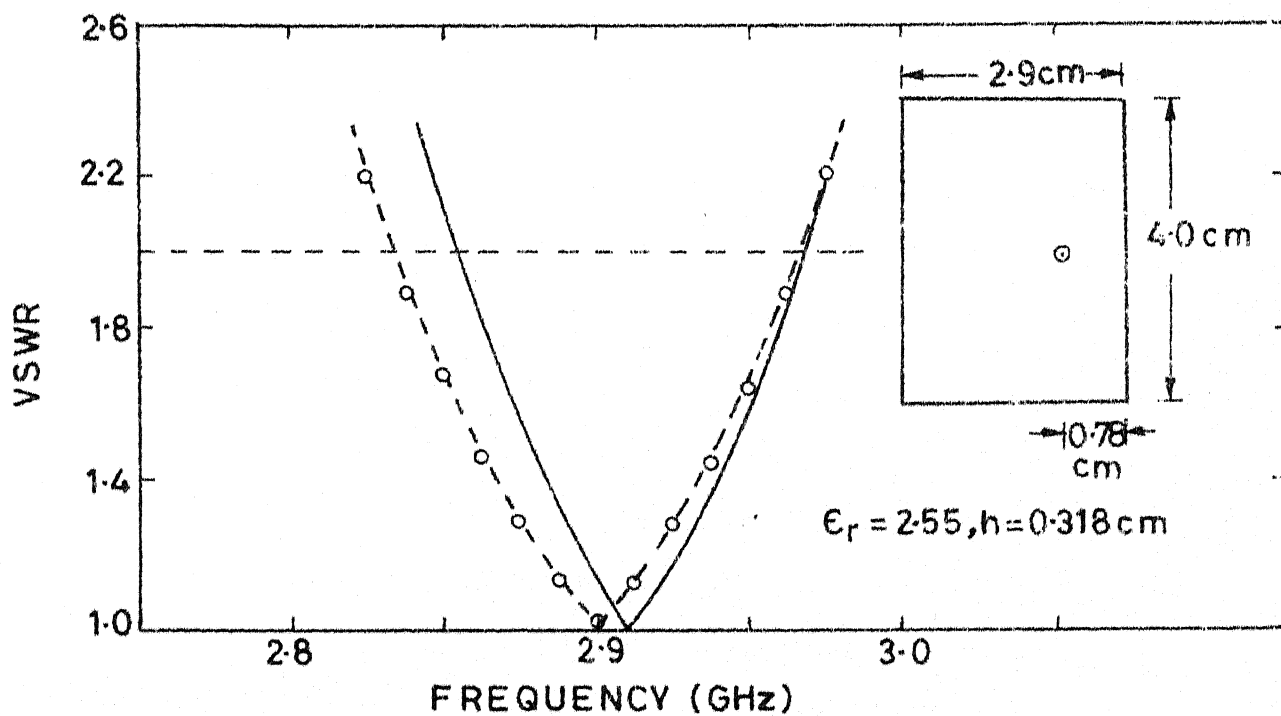
Fig. 2.7 VSWR variation with frequency for three different widths of RPA

When the width is increased, the value of effective dielectric constant and extension in the length increases. Both of these changes result in the decrease of centre frequency. With increase in the width, the value of radiation conductance increases, which increases the radiated power. This decreases the quality factor and hence the bandwidth is increased.

Experiments have been performed on RPA with two different widths ($W = 2.0$ cm and 4.0 cm). Polystyrene substrates of 0.318 cm thickness have been used for carrying out the experiments. The measured values of ϵ_r of the substrates are found to be 2.55 . The measurement method used is described in Appendix A. Experimental variations of VSWR with frequency for the two widths are plotted in Figs. 2.8(a) and (b) respectively. For comparison, theoretical values of VSWR versus frequency are also plotted in these figures. The experimental values of centre frequency are in close agreement with the theoretically predicted values. The measured bandwidths of RPA for $W = 2.0$ cm and $W = 4.0$ cm are 109 MHz and 133 MHz respectively, which are slightly greater than the theoretical values. This is due to the fact that conductor losses, dielectric losses, and losses due to the surface wave propagation are ignored in the analysis.



(a)



(b)

Fig.28 Theoretical (—) and experimental (---) variations of VSWR with frequency of RPA with width (a) $W = 2.0$ cm and (b) $W = 4.0$ cm

Effect of substrate thickness

For a RPA with patch dimensions ($L = 2.9$ cm and $W = 4.0$ cm), variations of VSWR with frequency for two different substrate thicknesses ($h = 0.159$ cm and 0.318 cm) are plotted in Fig. 2.9. The value of ϵ_r for the two substrates is taken as 2.55. The locations of the feed-point for the two cases to obtain unity VSWR at centre frequency, are found to be different. From these plots, it is observed that as the substrate thickness increases from 0.159 cm to 0.318 cm, the centre frequency decreases from 3.023 GHz to 2.91 GHz, and the bandwidth of the antenna increases from 59.4 MHz to 115 MHz. With increase in the substrate thickness, the extension in the length (to account for the open-end fringing fields) increases. Thus the effective length of the RPA increases, resulting in decrease of the centre frequency. When the substrate thickness increases, quality factor decreases, and therefore the bandwidth increases.

Experiment has been carried out on RPA with substrate thickness $h = 0.159$ cm. Other dimensions of the antenna are depicted in Fig. 2.10 (inset). Theoretical and experimental variations of VSWR are plotted in Fig. 2.10. The measured bandwidth of the RPA is 62 MHz (2.05 percent, centre frequency $f_0 = 3.021$ GHz), which is slightly more than the theoretical value ($BW = 59.4$ MHz).

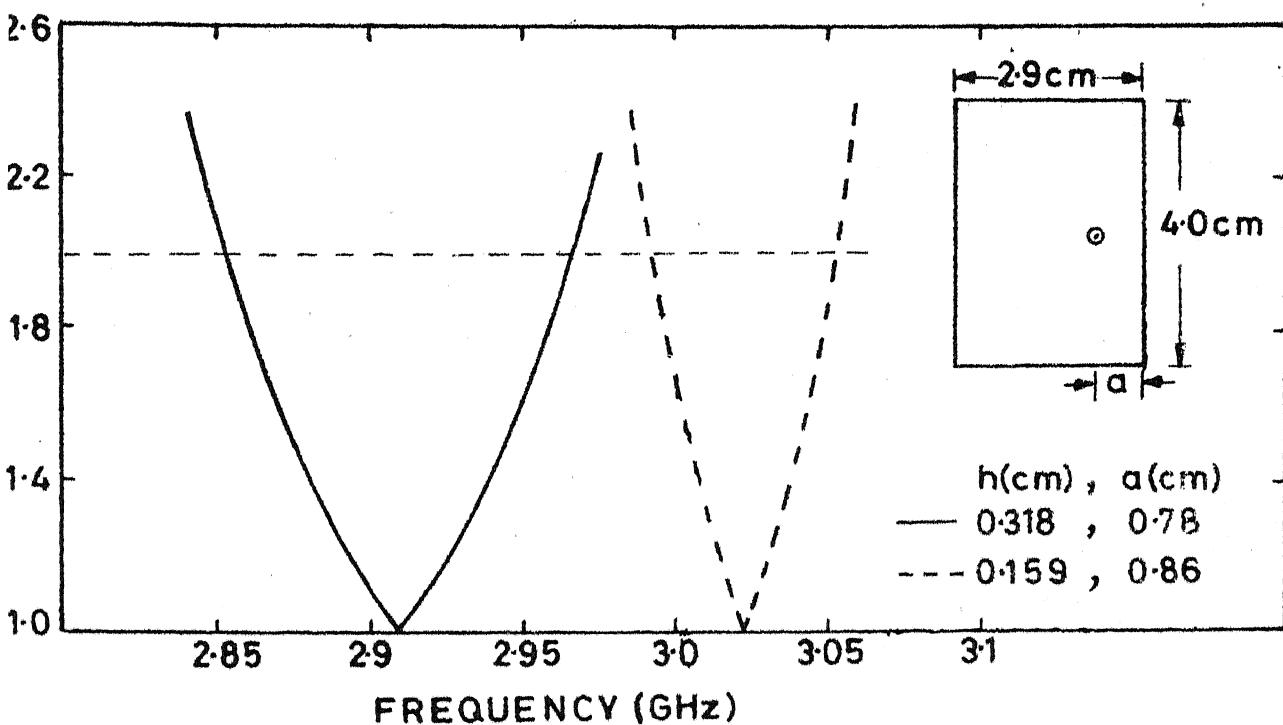


Fig. 2-9 VSWR variation with frequency of RPA for two different substrate thicknesses

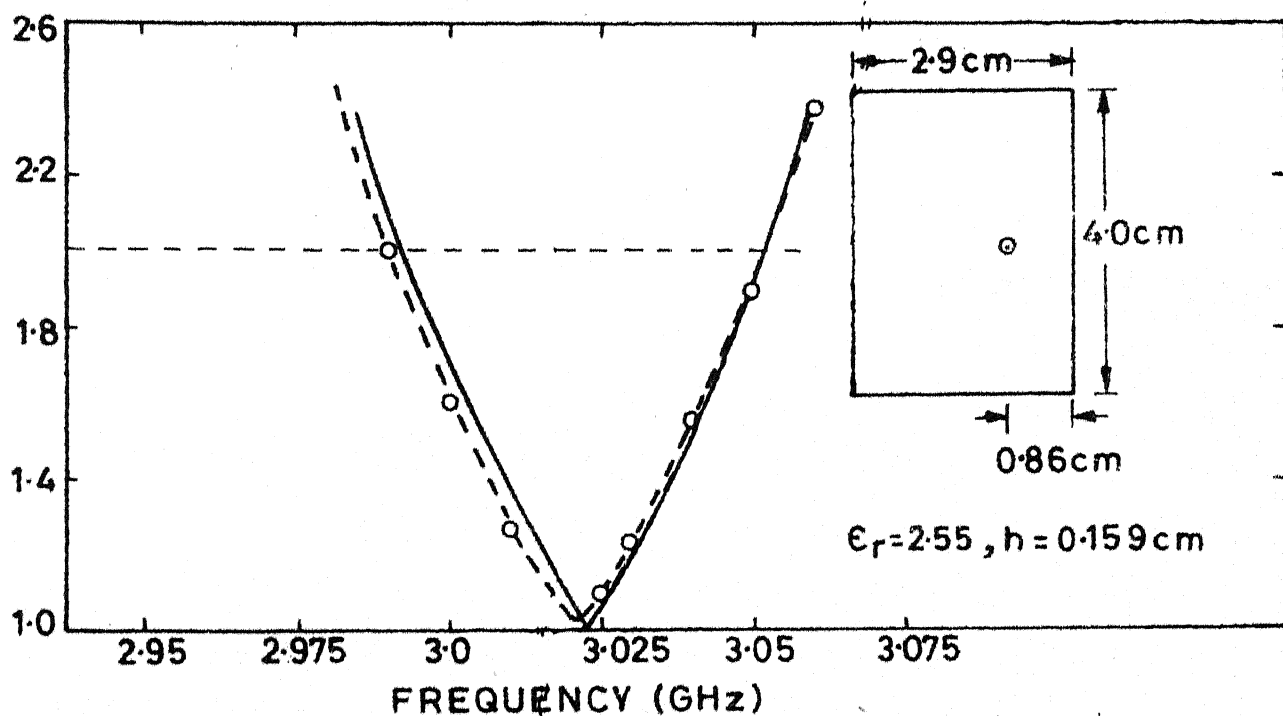


Fig. 2-10 Theoretical (—) and experimental (- - -) variations of VSWR of RPA for $h=0.159\text{ cm}$

2.4.3 Radiation pattern

Radiation pattern of the RPA shown in Fig. 2.10, is calculated in both $\varphi = 0^\circ$ and $\varphi = 90^\circ$ planes at centre frequency by using (2.11). It is noted that only E_θ component of the radiation field is present in $\varphi = 0^\circ$ plane, and only E_φ component is present in $\varphi = 90^\circ$ plane. E_θ in $\varphi = 0^\circ$ plane and E_φ in $\varphi = 90^\circ$ plane are plotted in Figs. 2.11(a) and (b) respectively. The values of the 3-db beamwidth in $\varphi = 0^\circ$ and $\varphi = 90^\circ$ planes are 100° and 72° respectively.

Radiation pattern of the above antenna is measured in both $\varphi = 0^\circ$ and $\varphi = 90^\circ$ planes. Experimental set-up for measuring the field components E_θ and E_φ in a plane, is shown in Fig. 2.12. To measure the fields in the orthogonal plane, the antenna is turned by 90° . The measured values of E_θ in $\varphi = 0^\circ$ plane and E_φ in $\varphi = 90^\circ$ plane are also plotted in Figs. 2.11(a) and (b) respectively. The values of the 3-db beamwidth in $\varphi = 0^\circ$ and $\varphi = 90^\circ$ planes are 82° and 56° . These experimental values of beamwidth are somewhat smaller than the theoretical values. For E_θ component of the radiation field in $\varphi = 0^\circ$ plane, the experimental values are much less than the theoretical values for $\theta > 60^\circ$. Such discrepancy has been observed by other investigators also [16], [45]. This decrease in the value of E_θ may be due to i) the excitation of surface

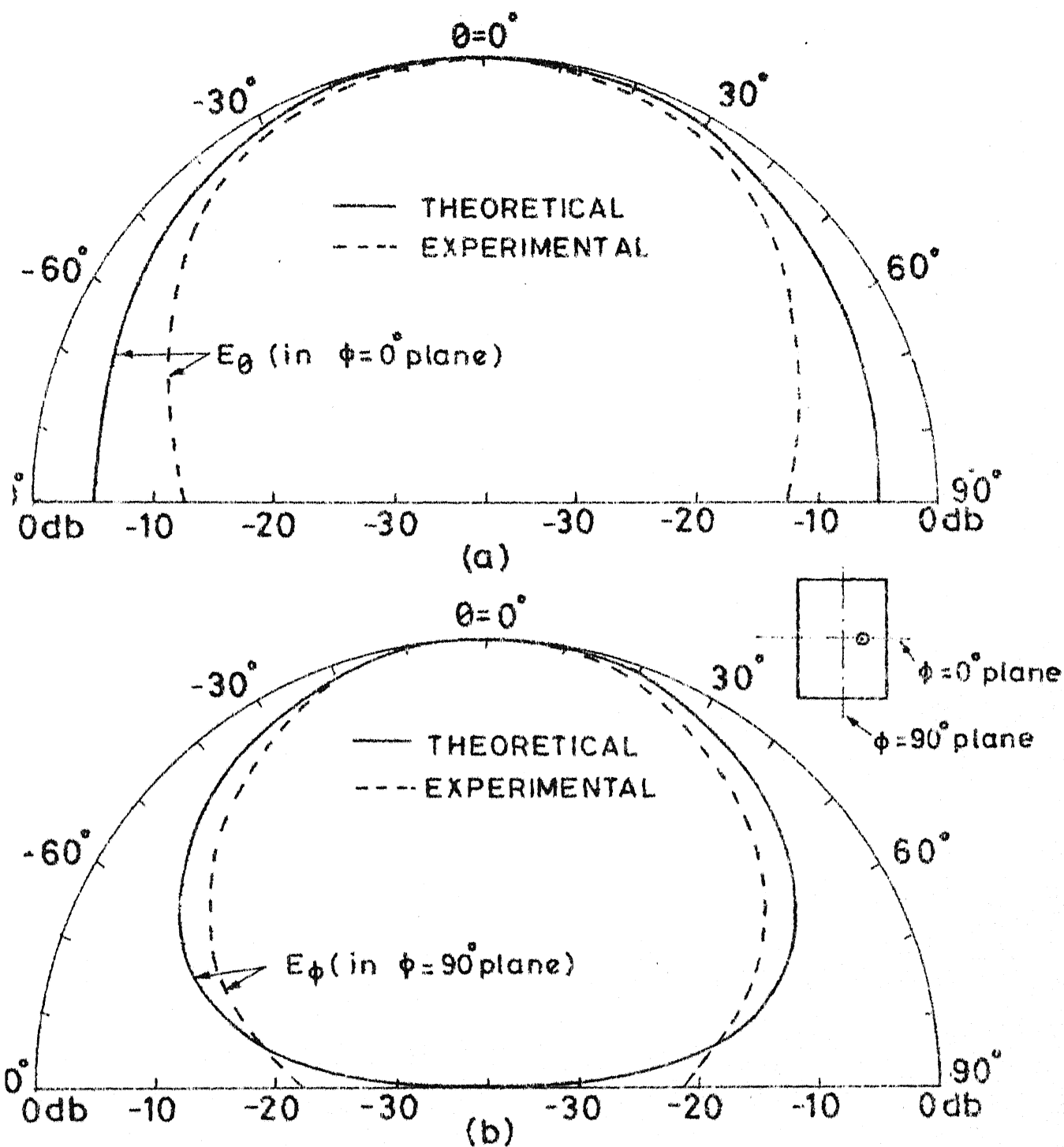


Fig.2.11 Theoretical and experimental values of
 (a) E_θ in $\phi = 0^\circ$ plane and (b) E_ϕ in $\phi = 90^\circ$ plane
 of RPA shown in Fig. 2.10 (inset)

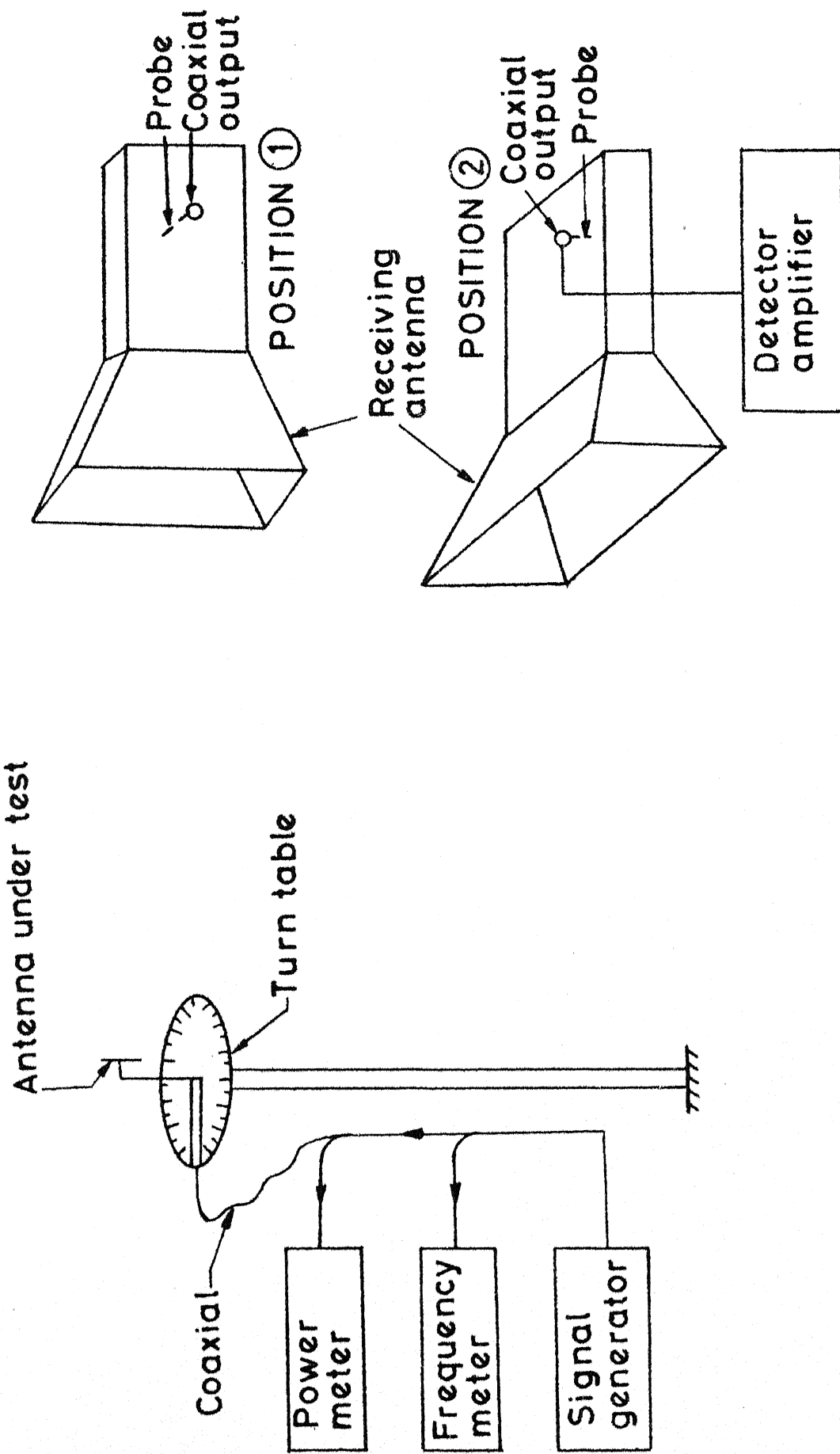


Fig.2.12 Experimental setup for radiation pattern measurement

waves which cause flow of power along the substrate surface and ii) because of the presence of finite ground plane.

When the width of the RPA decreases (from $W = 4.0$ cm to 2.0 cm), 3-db beamwidth in $\phi = 90^\circ$ plane increases slightly, but in $\phi = 0^\circ$ plane, it remains unaltered. With the increase in substrate thickness (from $h = 0.159$ cm to 0.318 cm), there is no appreciable change in the beamwidths in the two planes.

2.5 DISCUSSION

The Green's function approach and the segmentation method described in this chapter are used later in Chapters Three to Six for analyzing gap coupled and directly coupled microstrip antennas. Results for the bandwidth of RPA reported in Section 2.4 serve as a reference for evaluating the performance of wideband microstrip antennas discussed in the later chapters of this thesis.

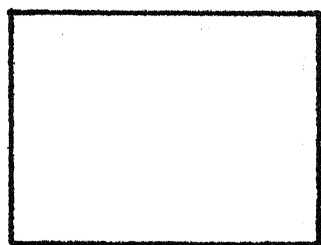
CHAPTER THREE

RADIATING EDGES GAP COUPLED MICROSTRIP ANTENNAS (REGCOMA)

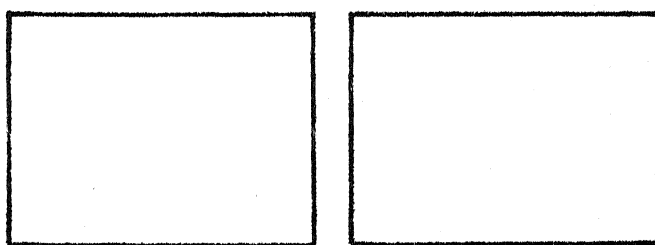
In this chapter, the investigations carried out on radiating edges gap coupled microstrip antenna (REGCOMA) are reported. The antenna has been analyzed using Green's function approach and segmentation method described in Chapter Two. The coupling gaps between the coupled resonators are modelled as capacitive π -networks. The values of these capacitances are calculated from the formulas available for asymmetric coupled microstrip lines [67]. All the series capacitances in the capacitive π -network are shunted by conductances, to account for the radiation from the gap. This π -network model of the gap becomes one of the segments in the segmentation procedure. The REGCOMA has been optimized to give maximum bandwidth.

3.1 MULTIPLE RESONATOR STRUCTURES

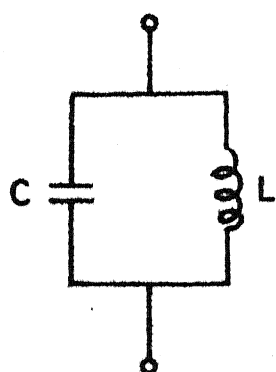
Radiating edges gap coupled microstrip antennas (REGCOMA) consist of multiple resonators. At some frequency, one resonator will be resonant and at nearby frequencies, other resonators will be resonant, thereby yielding a broader bandwidth. To explain this consider an example of a rectangular resonator and two gap coupled resonators, shown in Figs. 3.1(a) and (d) respectively. The rectangular resonator is



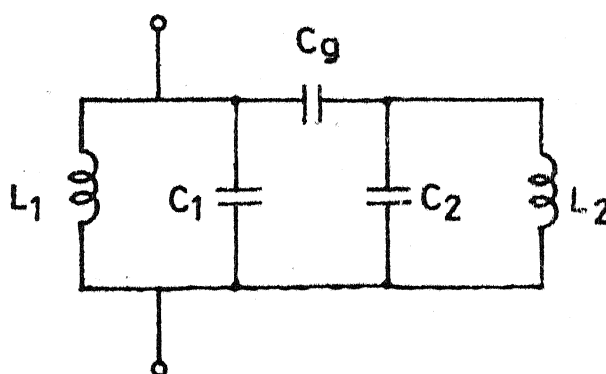
(a)



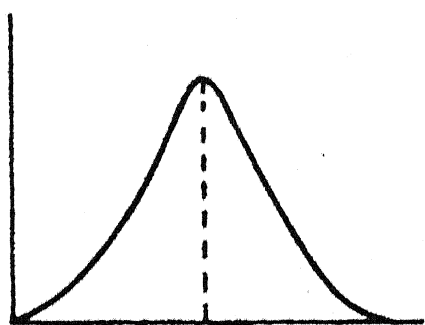
(d)



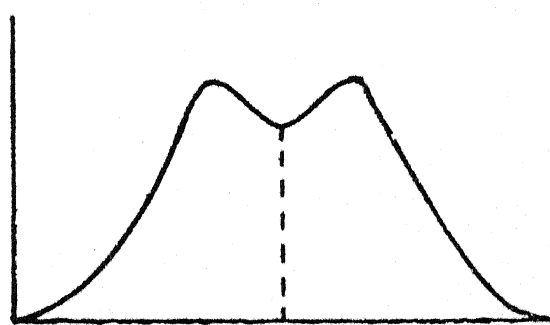
(b)



(e)



(c)

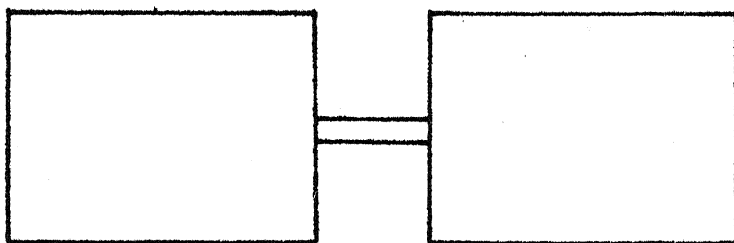


(f)

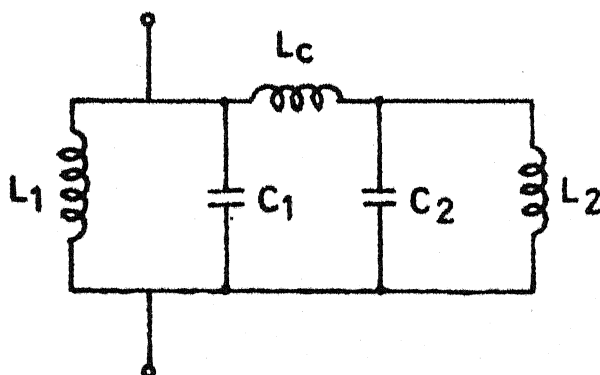
Fig.3-1 (a) Rectangular resonator, (b) its lumped representation, and (c) resonance curve; (d) Gap coupled resonators, (e) their lumped representation and (f) resonance curve

represented by a parallel resonant LC circuit (Fig. 3.1(b)), and its resonance curve (i.e. impedance versus frequency response) is shown in Fig. 3.1(c). The coupled resonators can be represented by two resonant parallel LC circuits connected by a capacitance as depicted in Fig. 3.1(e). The resultant resonance curve may have a hump in the resonance curve for the over coupled case, as shown in Fig. 3.1(f). It can be noted from the two resonance curves that the coupled resonators have larger bandwidth as compared to the single resonator. So, by choosing the proper coupling between the resonators, the bandwidth of the antenna can be increased.

The mechanism of the coupling between the resonators can be either gap coupling or direct coupling. Two resonators which are directly coupled through a short section of micro-strip line, are shown in Fig. 3.2. These directly coupled resonators are represented in a similar way as the gap coupled resonators, by two parallel resonant circuits. The only difference is that these resonant circuits are now connected by an inductance instead of a capacitance. In this case also, the resonance curve can have a hump by choosing the proper coupling between the resonators. Thus the directly coupled antennas will also yield broader bandwidth than the single rectangular patch antenna. If more than two resonators are coupled, then the resonance curve will



(a)



(b)

Fig.32 (a) Directly coupled resonators and
(b) their lumped representation

have multiple humps, so the bandwidth of the antenna will further increase.

The various wide-band antenna structures studied in this thesis are shown in Figs. 1.6 and 1.7. The structures shown in Fig. 1.6 are radiating edges gap coupled, non-radiating edges gap coupled, and four edges gap coupled microstrip antennas. Fig. 1.7 shows radiating edges directly coupled, non-radiating edges directly coupled and four edges directly coupled microstrip antennas. These antenna structures work on the multiple resonance principle.

3.2 MODELLING OF THE COUPLING GAPS

A gap coupled microstrip antenna with two resonators is shown in Fig. 3.3(a). The coupling gap between the coupled resonators is modelled by a multi-terminal network as shown in Fig. 3.3(a). Capacitances C_1 , C_2 and C_g constitute the capacitive π -network representing the gap capacitances. The values of these gap capacitances are obtained using the formulas for asymmetric coupled microstrip line [67]. The expressions for calculating these capacitances are given in Appendix B. The number of π -subnetworks in each gap model is equal to the number of sections into which the coupled edges are divided for analysis by segmentation method. In order to account for the radiation from the gap, all the series capacitances C_g are shunted by conductances as shown in Fig. 3.3(b). The values of these

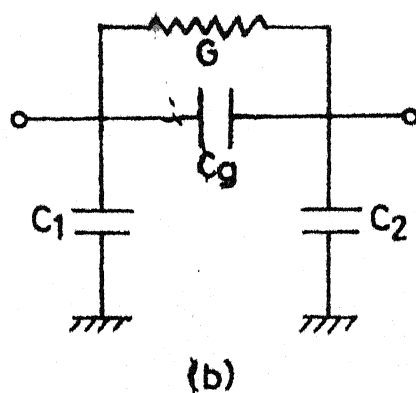
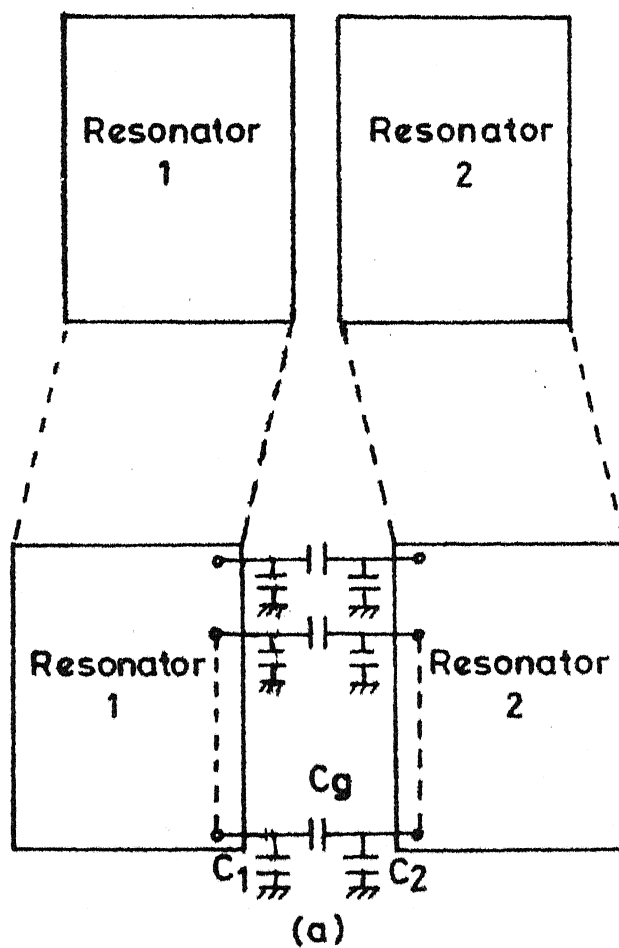


Fig.33(a) A gap coupled microstrip antenna and representation of gap by multi-terminal capacitive π -network
 (b) Practical gap model

conductances are obtained by dividing the radiation conductance of the coupled edge by the number of ports considered along that edge. This π -network model of the gap is considered as one of the segments in the segmentation method discussed in Section 2.2. In the segmentation method, impedance matrix for the gap circuit is required, and is calculated as

$$\underline{Z} = \frac{1}{Z_1 + Z_2 + Z_g} \begin{bmatrix} (Z_2 + Z_g)Z_1 & Z_1 Z_2 \\ Z_1 Z_2 & (Z_1 + Z_g)Z_2 \end{bmatrix} \quad (3.1)$$

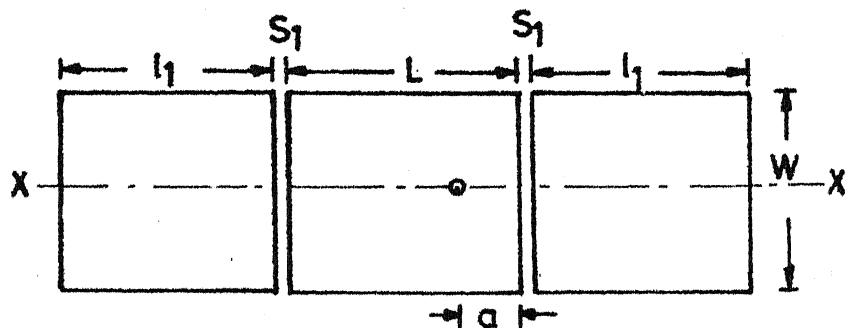
where

$$Z_1 = \frac{1}{j\omega C_1}, \quad Z_2 = \frac{1}{j\omega C_2}, \quad \text{and} \quad Z_g = \frac{1}{G + j\omega C_g} \quad (3.2)$$

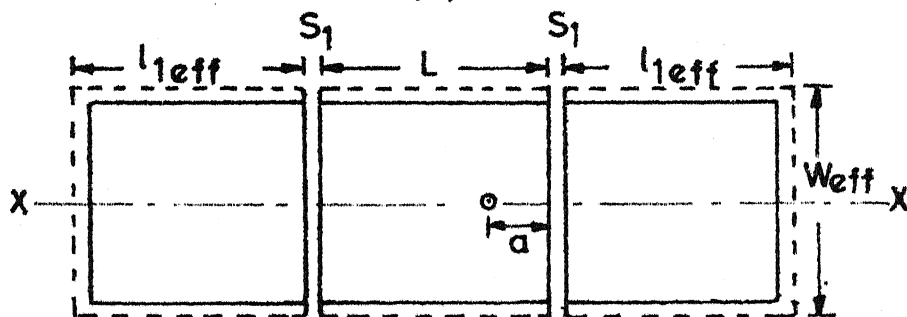
3.3 REGCOMA WITH IDENTICAL PARASITIC ELEMENTS

3.3.1 Analysis

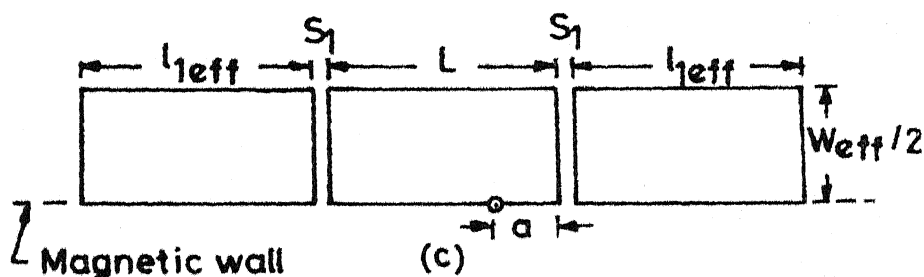
In radiating edges directly coupled microstrip antennas (REGCOMA), two rectangular resonators are placed adjacent to the radiating edges of the rectangular patch antenna. In this section, these resonators are considered identical as shown in Fig. 3.4(a). The analysis and design of REGCOMA with parasitic elements of different lengths are discussed later in this chapter. The length l_1 of the identical resonators is taken nearly equal to half wavelength, and width of these resonators is taken equal to the width of the central rectangular patch. The central patch is excited by a co-axial feed, and the feed-point is chosen along XX,



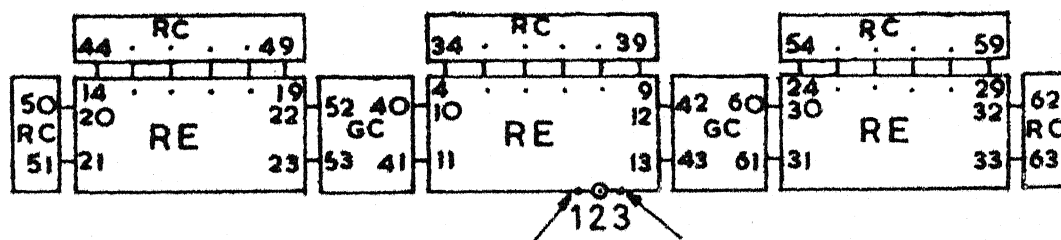
(a)



(b)



(c)



Additional ports

(d)

RC (Radiation conductance network)

GC (Gap-circuit)

RE (Rectangular element)

Fig. 3-4(a) REGCOMA with identical parasitic elements, (b) magnetic wall boundary, (c) even-mode half section and (d) its segmented network

the axis of symmetry. With such an excitation, the field is roughly sinusoidal along the length and is nearly uniform along the width of the various resonators. As only the central resonator is excited, the additional resonators are termed as parasitic elements.

REGCOMA has been analyzed using the Green's function approach and the segmentation method described in Chapter Two. The physical boundary of the antenna is extended outward to account for the open-end fringing fields, and a magnetic wall boundary is considered to exist at this location. However, along the gap, the magnetic wall is located at the physical boundary itself as shown in Fig. 3.4(b), because the fringing fields along the gap are taken care of in the gap modelling by the capacitances C_1 and C_2 . Since the antenna structure and the feeding arrangement are symmetrical with respect to axis XX, fields will have even symmetry about this axis and it is sufficient to analyze only half of the structure with a magnetic wall at XX. This procedure reduces the computational time to half. Even-mode half section of REGCOMA is shown in Fig. 3.4(c). The characteristic impedance of the co-axial feed line is taken as 100 ohms instead of 50 ohms for analysis.

To apply segmentation method for analysis, even-mode half section of REGCOMA is divided into various segments as depicted in Fig. 3.4(d). These segments are - three

rectangular elements, two gap-circuits, and five radiation conductance networks. The periphery of the antenna is divided into 63 ports with connected $c(=d)$ ports equal to 30 ports and 3 external p -ports. Since the field varies along the non-radiating edges and is nearly uniform along the radiating edges, a larger number of ports (i.e. six) are considered along the non-radiating edges as compared to the number of ports (i.e. two) taken along the radiating edges, so that the variation of the field over any port-width is small. Three external ports are considered to evaluate input impedances at the various locations of the feed-point. The Z -matrix of the overall circuit is evaluated from the Z -matrices of the individual segments by using (2.5). The diagonal elements of the Z -matrix give input impedances at the feed-point locations. The voltage distribution along the periphery is obtained from (2.6), and the radiation pattern of the antenna is calculated using (2.11).

3.3.2 Effect of the antenna parameters on performance

For a given patch dimensions ($L = 2.7$ cm and $W = 3.9$ cm) and substrate specifications ($\epsilon_r = 2.55$ and $h = 0.159$ cm), the various parameters of REGCOMA which have optimized to yield maximum bandwidth are : length l_1 of the parasitic element, gap-width S_1 between the two resonators, and the feed-point location 'a'. The widths of the parasitic elements are taken equal to the width of the central rectangular patch,

and have not been taken as variables to be optimized to yield broader bandwidth. Because the resonance behaviour of the parasitic element is governed by its length and not by its width. So by choosing the width of the parasitic element different than that of the central rectangular patch, the bandwidth of the REGCOMA will not change much. Moreover, the coupling between the resonators will vary with the width of the parasitic element, and the modelling of the gap will become complicated. Effects of the above three parameters on the input impedance of the antenna are discussed separately in this section.

Length l_1 of the parasitic element

The input impedance loci of REGCOMA for three different values of length l_1 of the parasitic element, with gap-width $S_1 = 0.4$ cm and feed-point location 'a' = 0.38 cm, are plotted on the Smith Chart as shown in Fig. 3.5. From these plots, the following may be noted. The presence of the identical parasitic elements introduce, as a result of interaction, a loop in the input impedance locus. With decrease in the length l_1 from 2.7 cm to 2.6 cm, the loop in the impedance locus shifts downward and towards the left side of the Smith chart. Also, the frequency corresponding to the minimum VSWR increases as the length decreases. Except for the loop, the impedance loci for three different lengths l_1 follow the same pattern as the impedance locus of RPA shown in Fig. 2.5. When the length l_1 of the parasitic

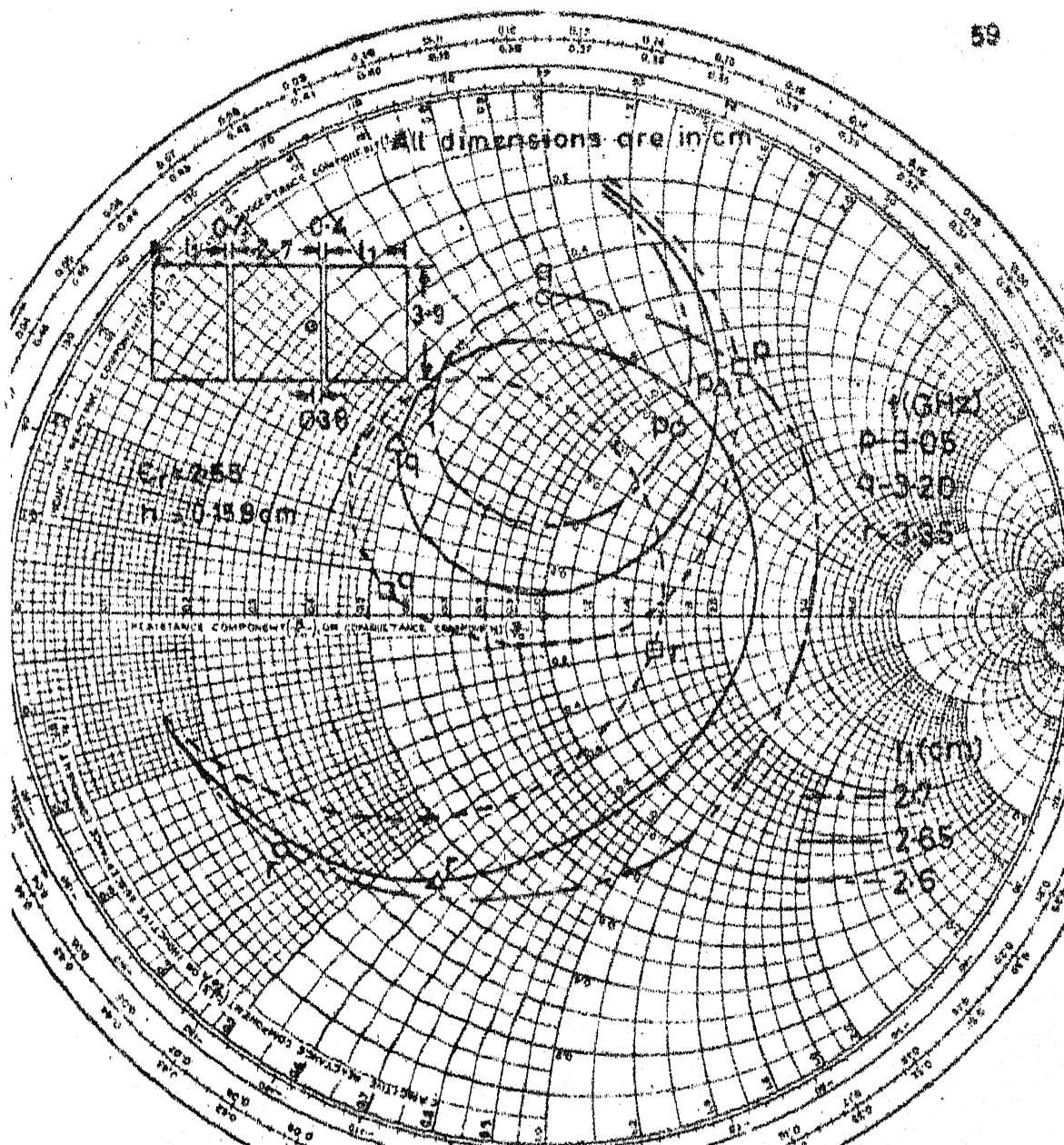


Fig. 3.5 Input impedance loci of REGCOMA for three different values of length l_1 of the parasitic elements

element decreases, its resonance frequency increases, so the loop is formed at the higher frequency point on the impedance locus of the RPA. With increase in the frequency the point corresponding to the input impedance of RPA moves downward and towards the left side of the Smith chart. Therefore, the loop in the impedance locus of REGCOMA also shifts downward and towards the left side with decrease in length l_1 .

Gap-width S_1 between the resonators

Input impedance loci of REGCOMA for three different values of gap-widths ($S_1 = 0.2, 0.4$ and 0.6 cm) are plotted in Fig. 3.6. The other dimensions of the antenna are depicted in Fig. 3.6 (inset). With increase in the gap-width from $S_1 = 0.2$ cm to 0.6 cm, the size of the loop in the impedance locus decreases and the frequency corresponding to the minimum VSWR increases. As the gap-width increases, the interaction between the resonators decreases, and hence the size of the loop decreases. As the gap-width is increased further, the size of the loop will go on decreasing, and for a large gap-width, the loop will disappear and the impedance locus of REGCOMA will become similar to that of RPA.

Location of the feed-point

For three different locations of feed-point ($a = 0.485, 0.38$ and 0.215 cm) with length $l_1 = 2.65$ cm and gap-width

Fig.3.6 Input impedance loci of REGCOMA for three values of gap-widths

$S_1 = 0.4$ cm, input impedance loci are plotted in Fig.3.7. From these plots, the following conclusion may be drawn. When the location of the feed-point is shifted towards the nearer edge of the central rectangular patch (i.e. from $a = 0.485$ cm to 0.215 cm), impedance locus shifts towards the right side of the Smith chart. However, the shape of the impedance locus remains unaltered. Similar shift in the impedance locus has been observed for the RPA shown in Fig. 2.5.

3.3.3 Initial experiments

To study the effect of gap-width on the antenna performance experimentally, REGCOMA's have been fabricated for two different gap-widths ($S_1 = 0.1$ cm and 0.25 cm) with length $l_1 = 2.65$ cm. For the two cases, the input impedance loci are plotted in Figs. 3.8 and 3.9 respectively, and the variations of VSWR with frequency are shown in Fig. 3.10. From these plots, the following may be observed. The size of the loop in the impedance locus decreases with increase in the gap-width. Two minima occur in the VSWR plot of REGCOMA, while only one minimum in the VSWR plot has been observed in the case of RPA. The second minimum in the VSWR plot is due to the presence of the loop in the impedance locus. With increase in the gap-width, the two minima shift towards each other, and the magnitude of the ripple (i.e. the difference between the minimum and maximum values of VSWR) decreases.

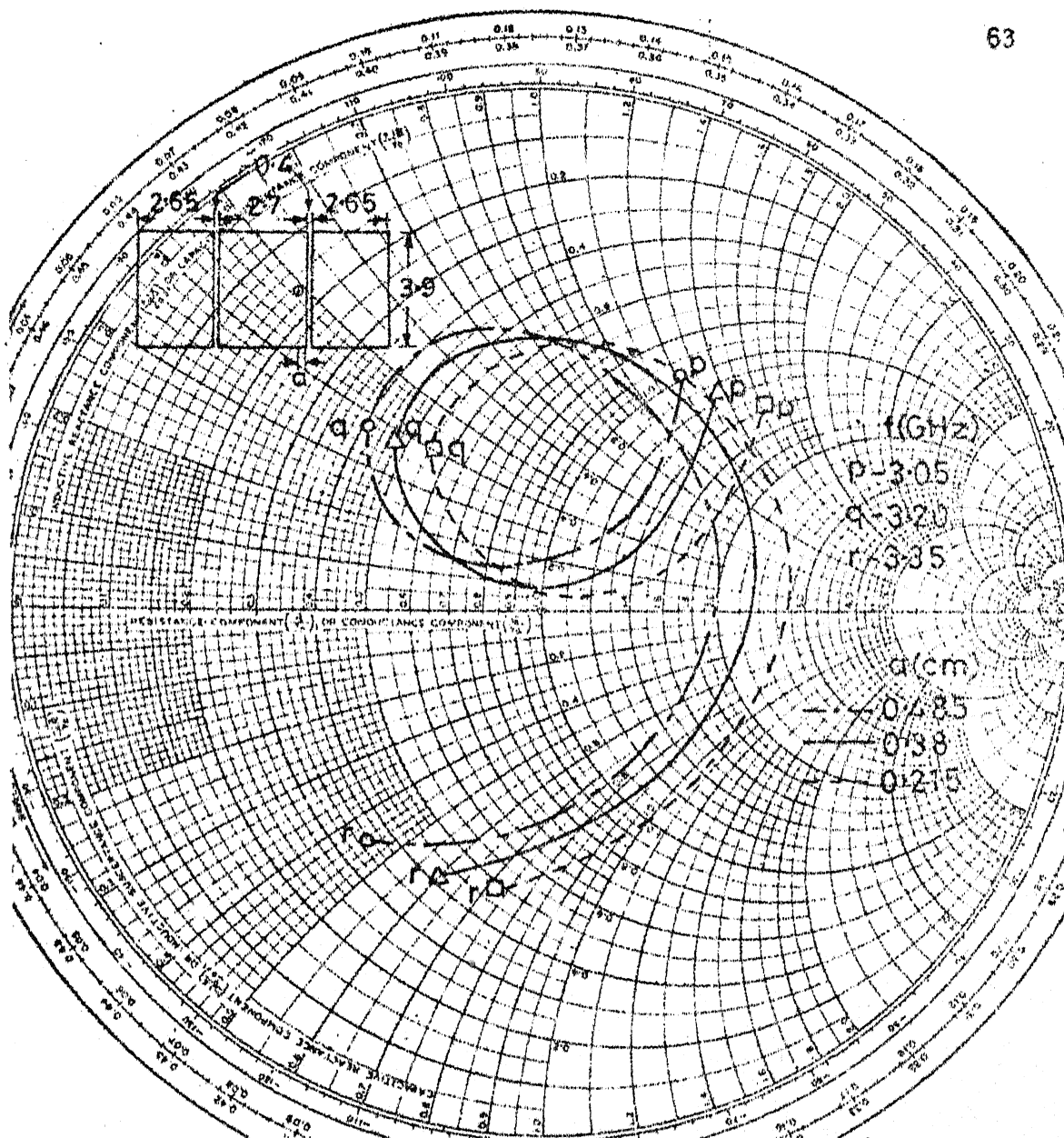


Fig.37 Input impedance loci of REGCOMA for three different feed-point locations

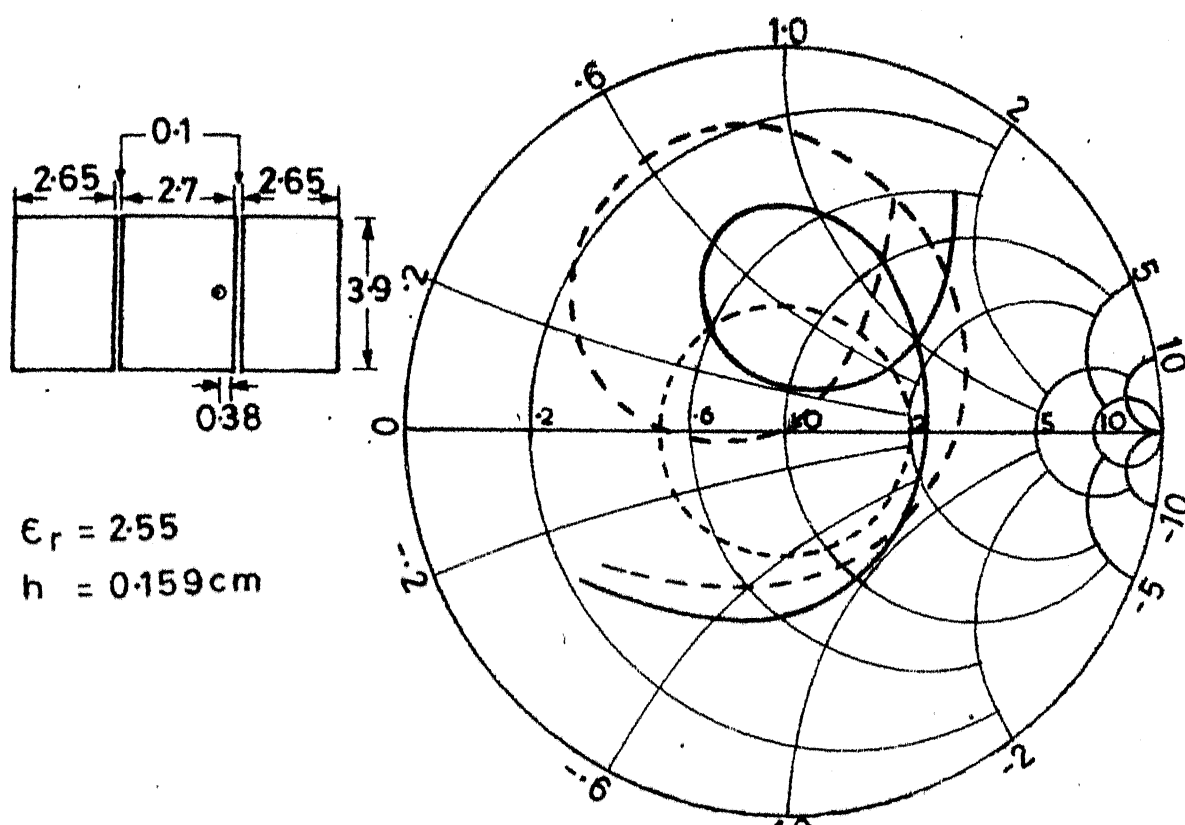


Fig.38 Theoretical (---) and experimental (—) input impedance loci of REGCOMA for $S_1=0.1 \text{ cm}$

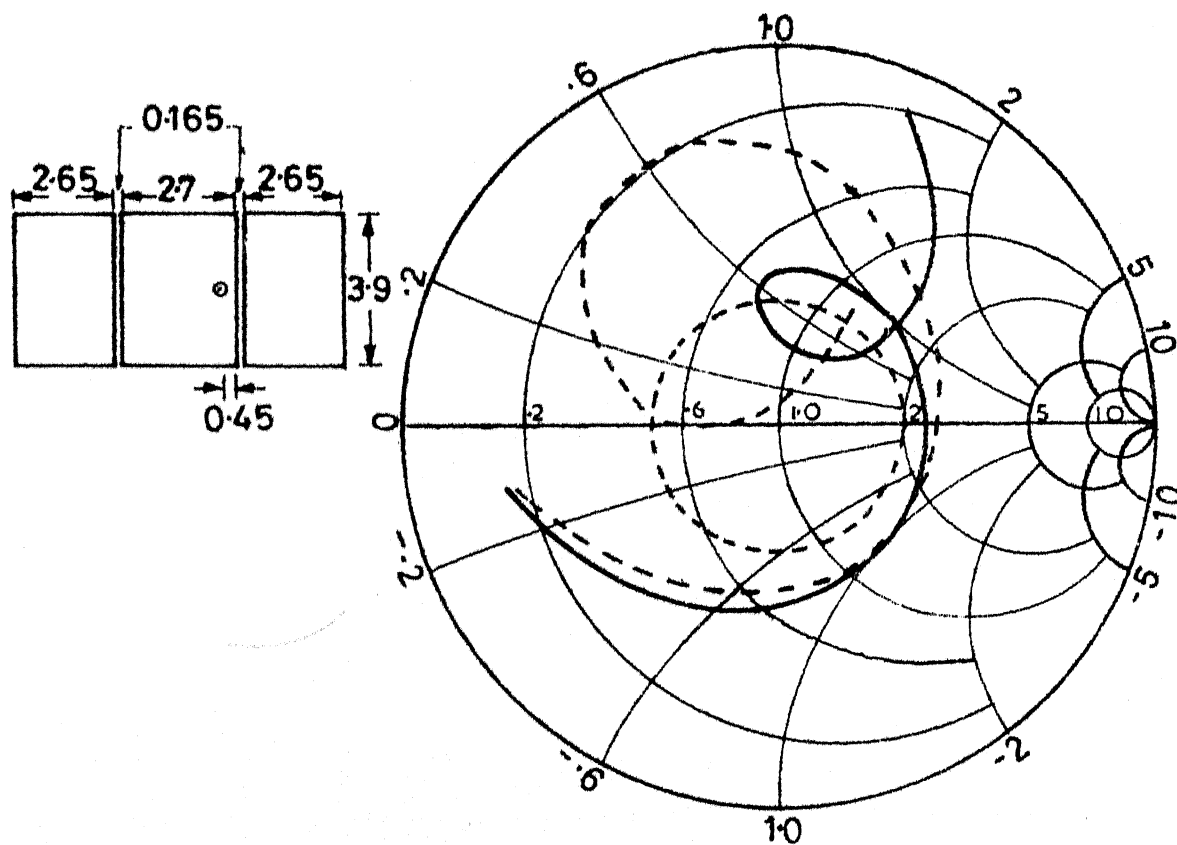


Fig.3.9 Theoretical (---) and experimental (—) input impedance loci of REGCOMA for $S_1=0.165 \text{ cm}$

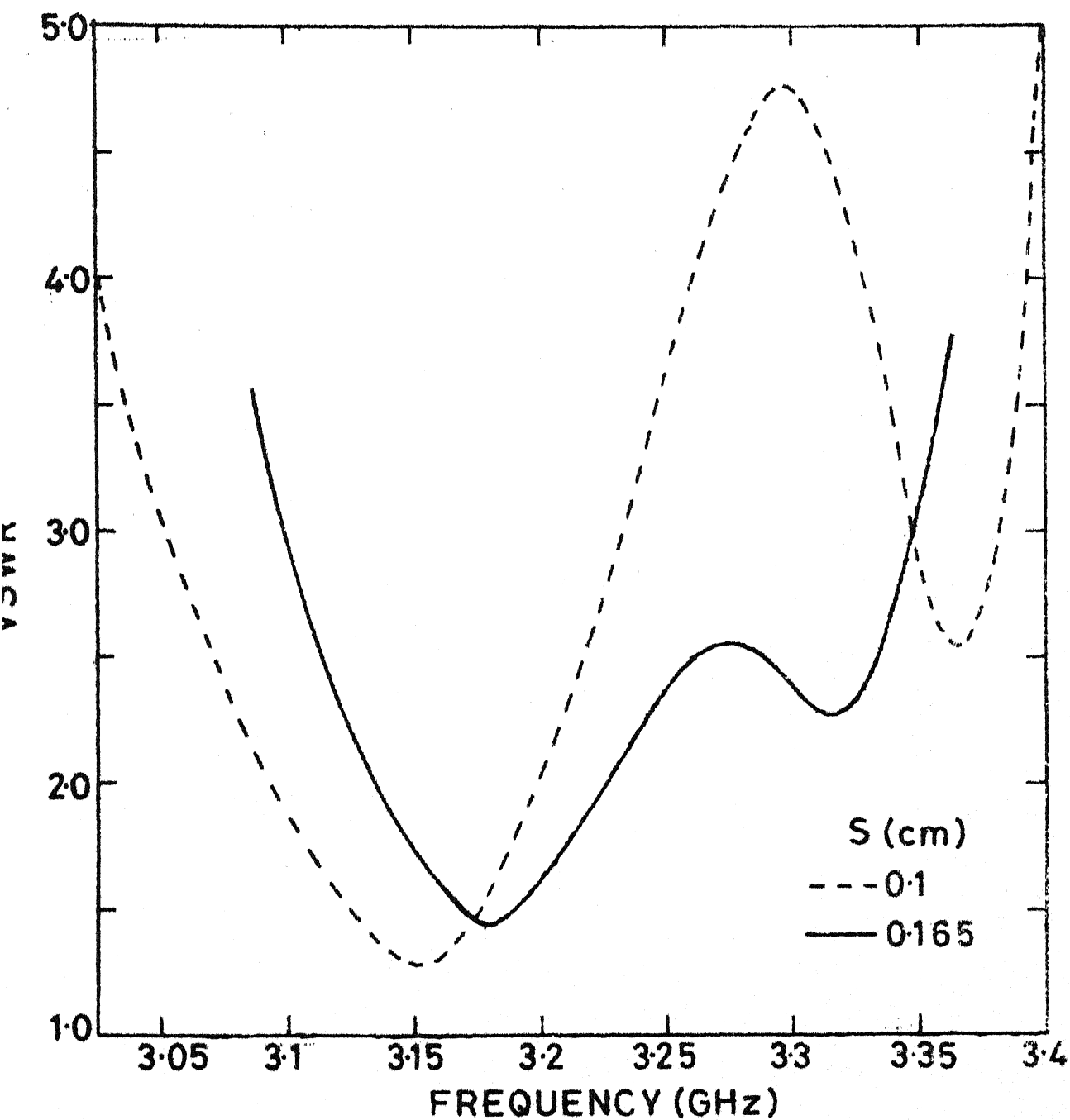


Fig. 3.10 Experimental variations of VSWR with frequency of REGCOMA for two values of gap-widths

For comparison, theoretical input impedance loci for the two cases are also plotted in Figs. 3.8 and 3.9. It may be noted that the size of the loop in the theoretical impedance loci is much larger than the size of the loop in the experimental impedance loci. This discrepancy may be due to the reason that the values of the gap capacitances considered in the gap modelling (Fig. 3.3) are not accurate. These capacitances (C_1 , C_2 and C_g) are calculated from the formulas for asymmetric coupled microstrip lines, which may not be correct for radiating gaps in the planar circuits. Also, these capacitance formulas are derived from quasi-static calculations, and they are not accurate at higher frequencies. For any specified value of gap-width, the coupling between the resonators will decrease with increase in frequency. This implies that a gap-width will act as an effectively larger gap at higher frequencies. In terms of coupling capacitances, the values of the capacitances C_1 and C_2 should be increased and the value of the capacitance C_g should be decreased at higher frequencies. Thus, the formulas for evaluating the values of the capacitances are modified for the analysis of the antenna structures, such that the theoretical results match with the experimental results.

3.3.4 Modification of the values of the gap capacitances

Firstly, the effects of changing the values of the gap capacitances (C_1, C_2 and C_g) on the input impedance locus of REGCOMA are studied. For this purpose, the same dimensions have been taken for which experiment has been performed for $S = 0.1$ cm (i.e. $l_1 = 2.65$ cm and $a = 0.38$ cm). The values of the capacitances obtained from the capacitance formulas are multiplied by a non-zero real number, and then effects of changing these coefficients are studied. Input impedance loci for three different coefficients of capacitance C_g ($C_{cg} = 1.0, 0.8$ and 0.6) and for unity coefficients of capacitances C_1 and C_2 ($C_{c1} = C_{c2} = 1.0$) are plotted in Fig. 3.11. It may be noted from the impedance plot that when the value of the C_{cg} decreases from 1.0 to 0.6, the size of the loop reduces and the frequency corresponding to minimum VSWR increases. Theoretical impedance locus corresponding to $C_{cg} = 0.6$ is nearly similar to the experimental locus shown in Fig. 3.8.

Input impedance loci for three different coefficients of C_1 and C_2 ($C_{ci} = 1.0, 1.2$ and 1.4 , where $i=1,2$) with $C_{cg}=0.6$ are plotted in Fig. 3.12. The coefficients for the capacitances C_1 and C_2 are taken equal because their values are nearly equal. From the impedance plot it may be observed that with increase in the value of C_{ci} from 1.0 to 1.4, the loop in the impedance locus shifts downward and the frequency for minimum

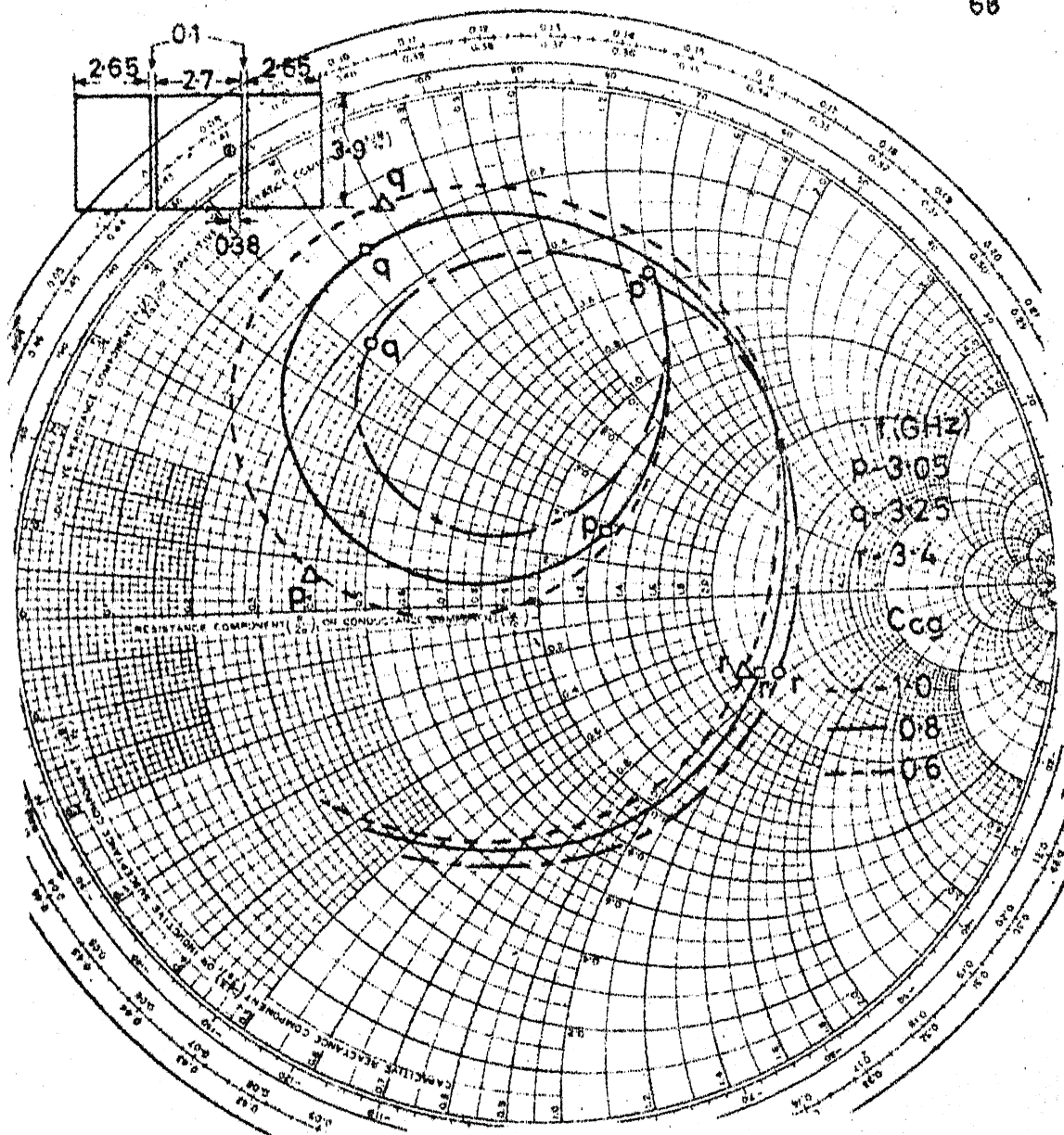


Fig.3.11. Input impedance loci of REGCOMA for three different coefficients of capacitance C_g ..

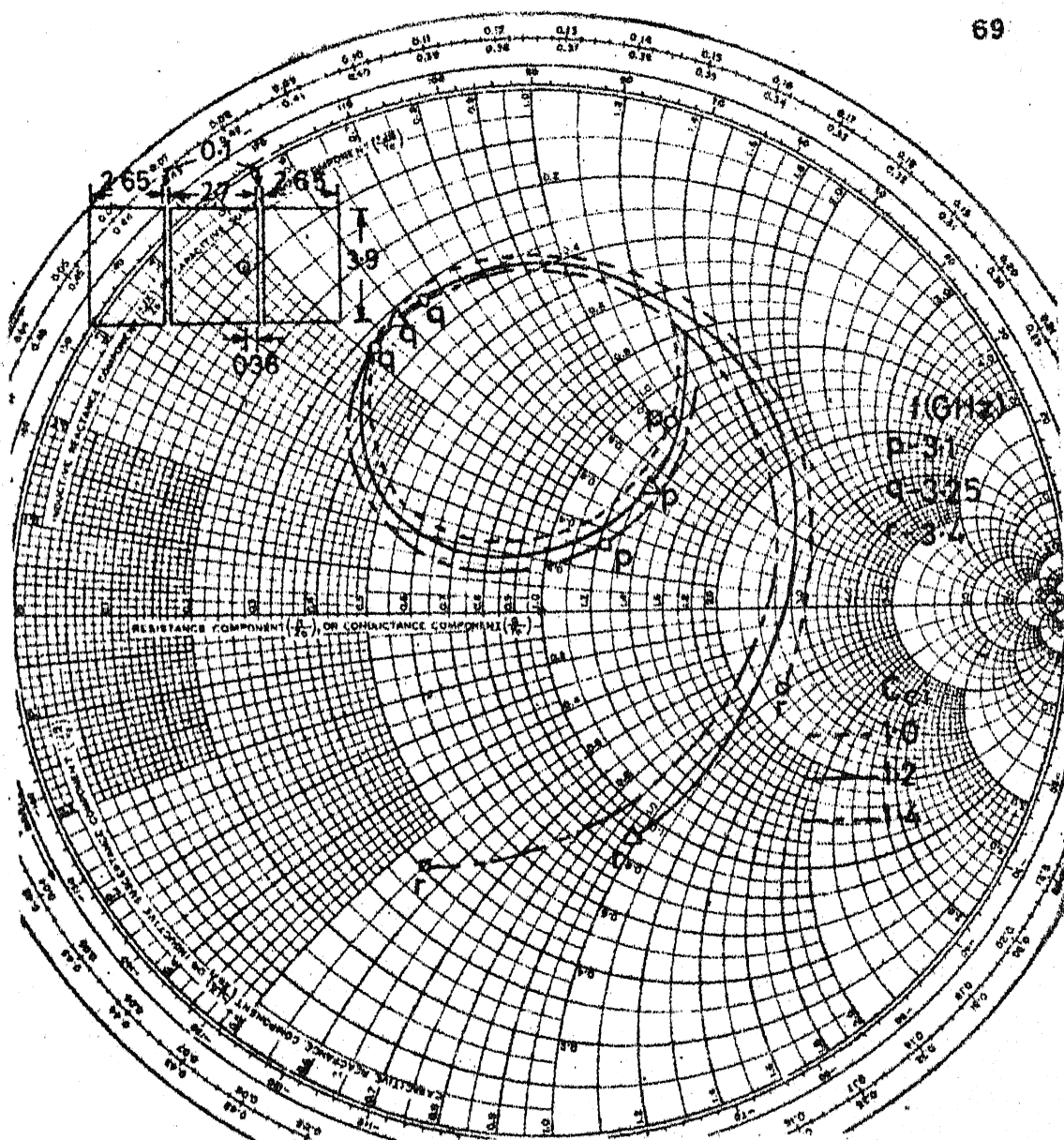


Fig.3.12 Input Impedance loci of REGCOMA for three values of capacitance coefficient C_{ci}

VSWR decreases. The combined effect of decreasing C_{cg} and increasing C_{ci} is equivalent to that of increasing the value of the gap-width between the resonators, because when the gap-width increases, the values of the capacitances C_1 and C_2 increase, while the value of capacitance C_g decreases.

The values of the capacitance coefficients C_{ci} and C_{cg} for the two gap widths ($S_1 = 0.1$ cm and 0.165 cm) on which experiments have been performed, are found by iterative method to match theoretical results with the experimental results. These coefficients are modified by knowing the effects of changing the capacitances on the impedance locus, and are found to be : $C_{ci} = 1.25$ and $C_{cg} = 0.55$ for $S_1 = 0.1$ cm, and $C_{ci} = 1.25$ and $C_{cg} = 0.44$ for $S_1 = 0.165$ cm.

For these modified values of gap capacitances, VSWR variations with frequency for the two cases are plotted in Figs. 3.13 and 3.14. Experimental results are also plotted in these figures. It may be noted that by changing the capacitance values, good agreement between theoretical and experimental results is obtained.

3.3.5 Optimization for broader bandwidth

After studying the effect of changing the gap-width between the resonators on the input impedance locus of the antenna experimentally, and modifying the gap-capacitances,

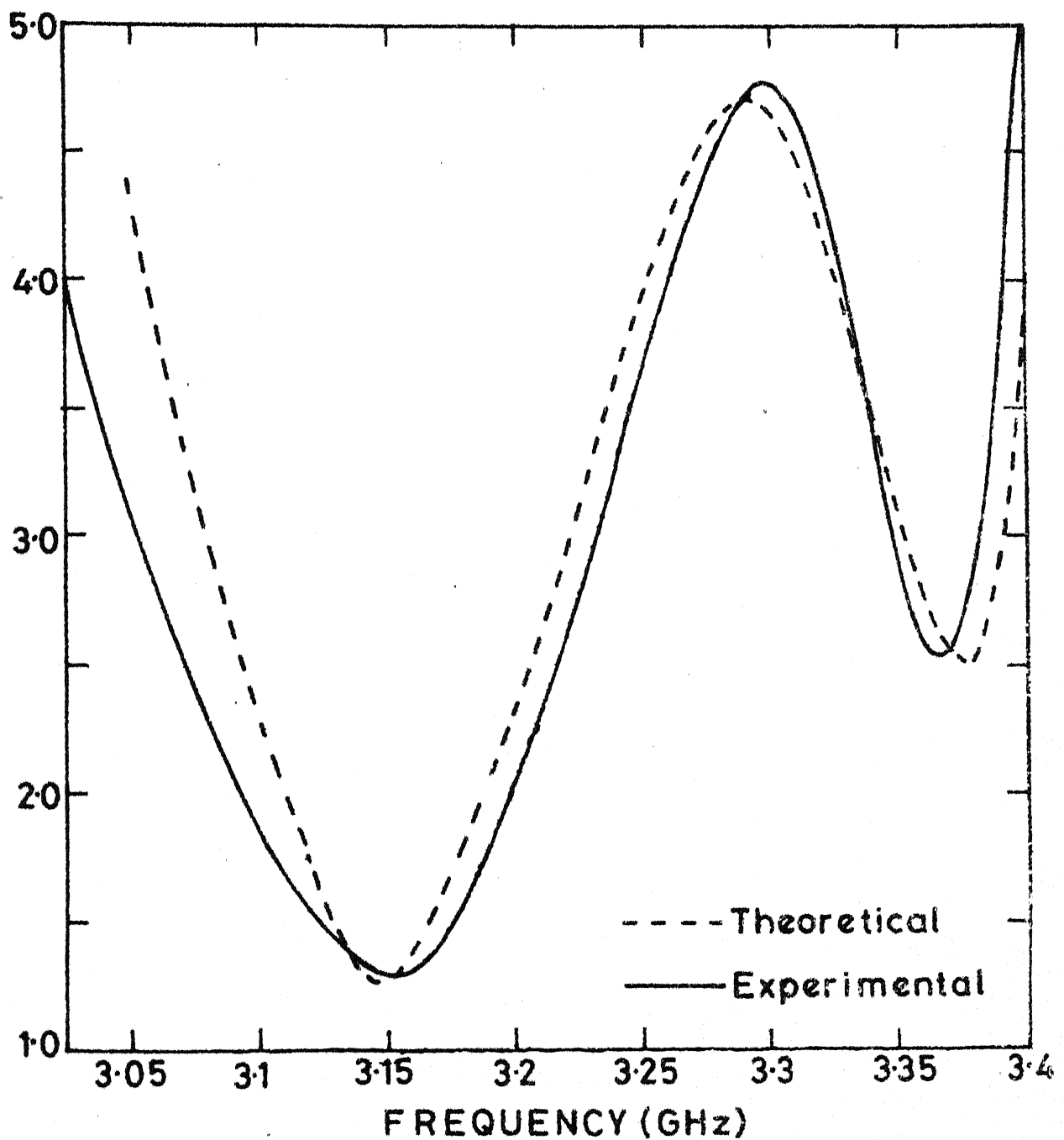


Fig.3.13 Theoretical and experimental variations of VSWR with frequency of REGCOMA shown in Fig.3.8(inset)

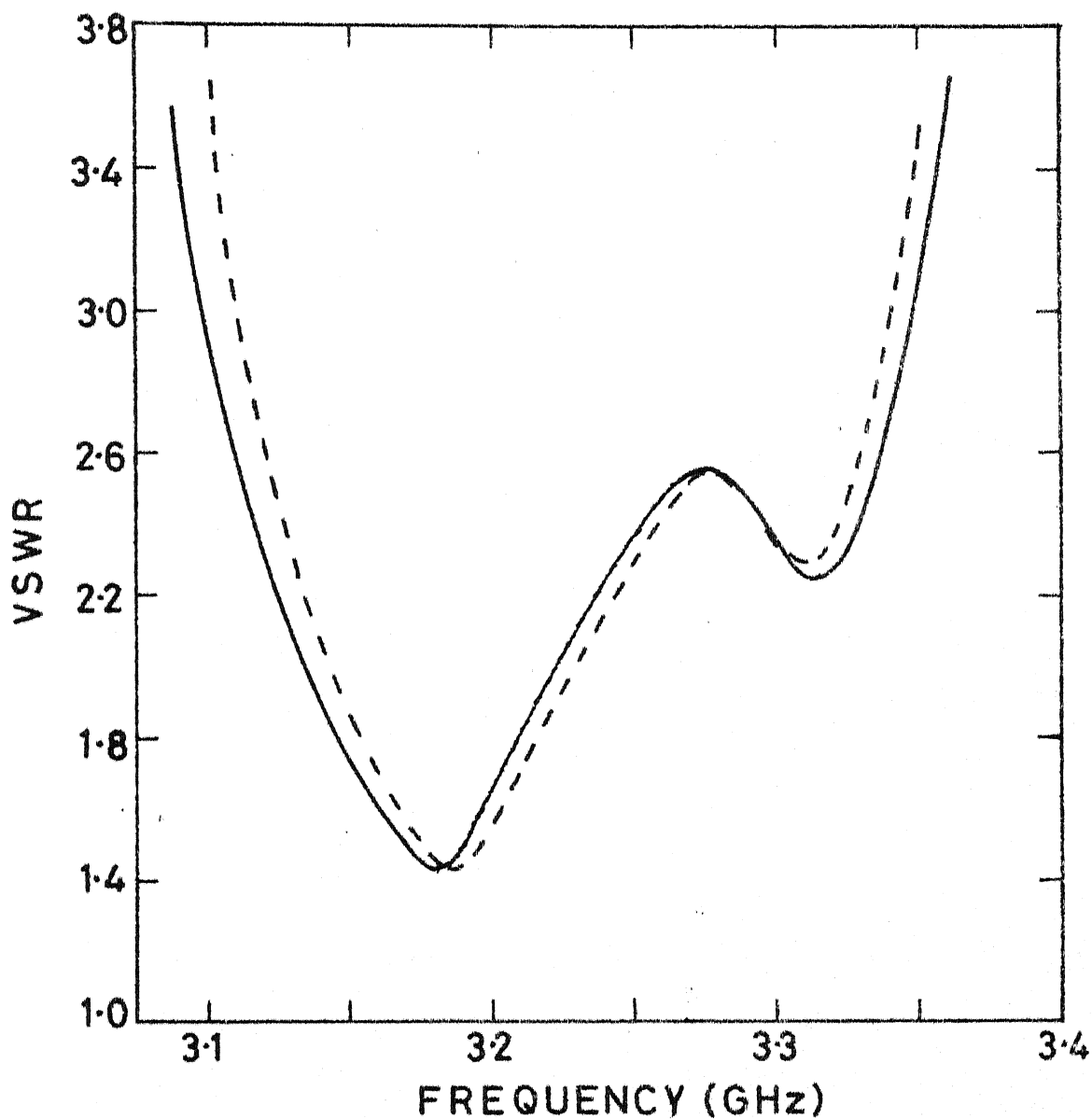


Fig.3.14 Theoretical (---) and experimental (—) variations of VSWR with frequency of REGCOMA shown in Fig.3.9 (inset)

bandwidth of the antenna is optimized. For the REGCOMA shown in Fig. 3.15 (inset), the theoretical input impedance locus and VSWR variation with frequency are plotted in Figs. 3.15(a) and (b) respectively. The modified values of the gap-capacitances are used for the analysis. The loop in the impedance locus is inside the $VSWR = 2$ circle and the bandwidth of the antenna is 207 MHz (6.3 percent, centre frequency $f_0 = 3.27$ GHz), which is 3.45 times the theoretical bandwidth of RPA ($BW = 60$ MHz). Experiment has been performed on this REGCOMA, and measured input impedance locus and variation of VSWR with frequency are also plotted in Fig. 3.15. Theoretical results agree with the experimental results, which shows the validity of the modified gap formulas. The experimental bandwidth is 225 MHz, which is slightly more than the theoretical value, because the dielectric loss, conductors loss and losses due to the surface wave propagation are ignored in the analysis.

The bandwidth of the REGCOMA (shown in Fig. 3.15) can be further improved by decreasing the length l_1 of the parasitic element, which will shift the loop in the impedance locus downward, and by reducing the gap-width S_1 , which will increase the size of the loop. The dimensions of the REGCOMA with reduced length l_1 and gap-width S_1 , and its input impedance locus are shown in Fig. 3.16. The bandwidth of the antenna is 257 MHz (7.7 percent, $f_0 = 3.345$ GHz), which is

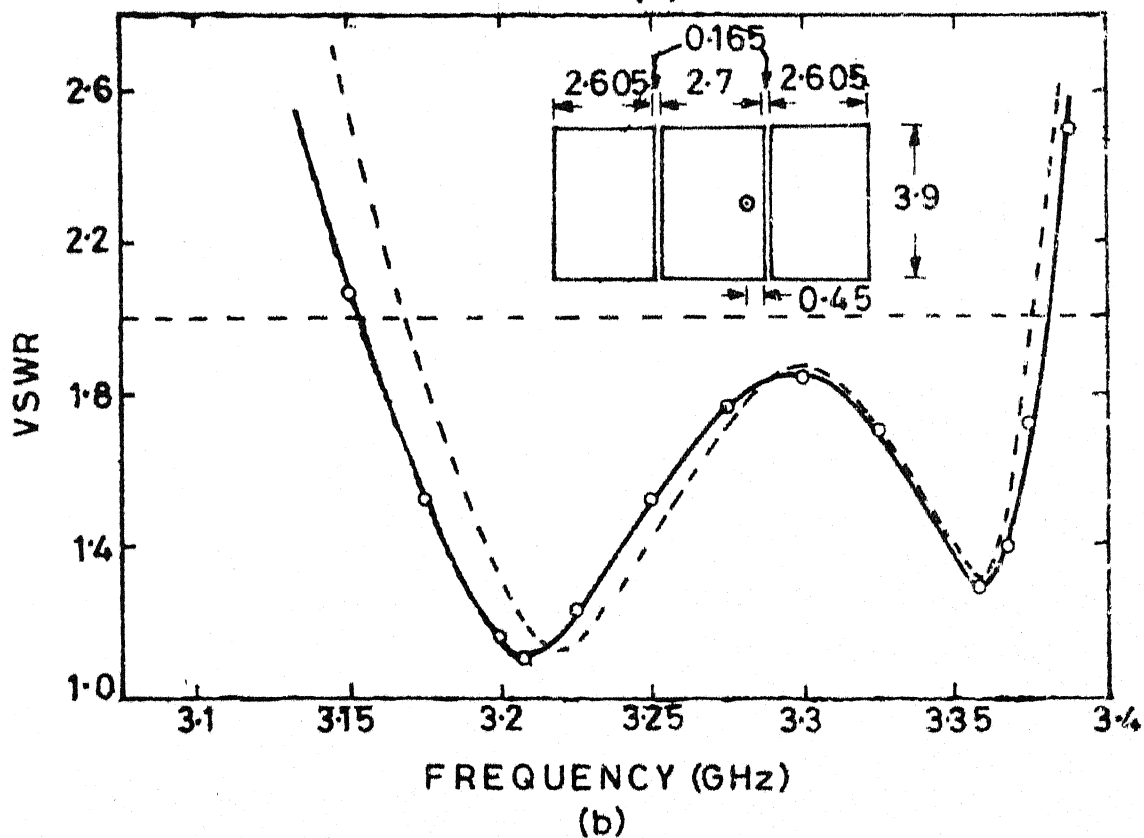
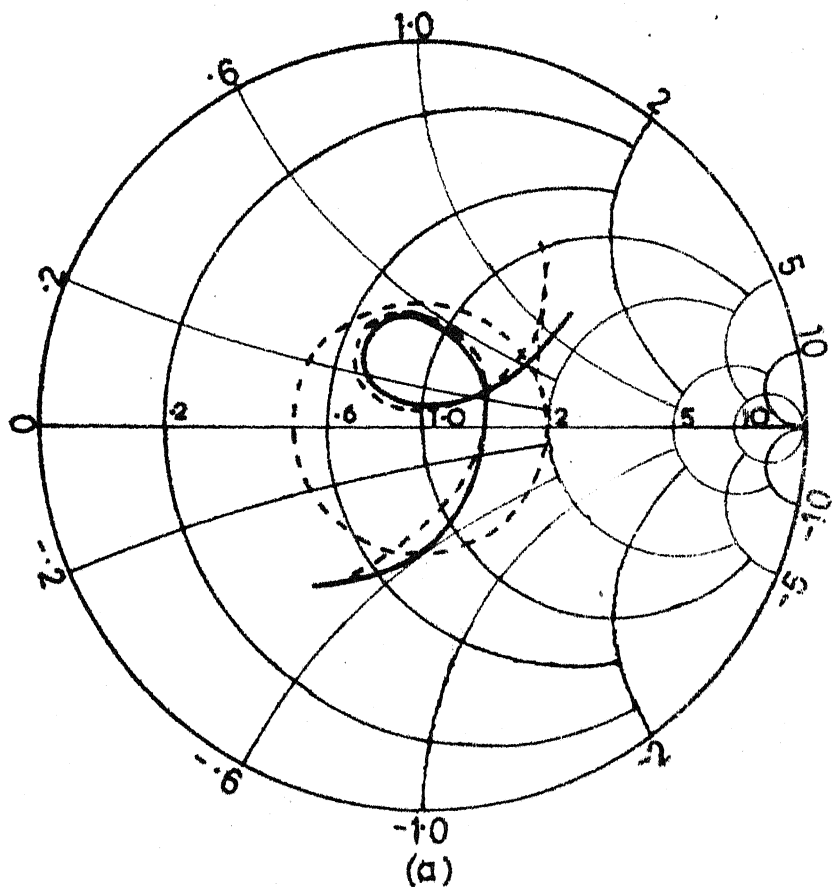


Fig.3.15 Theoretical (---) and experimental (—)
(a) input impedance loci and (b) VSWR
versus frequency of REGCOMA

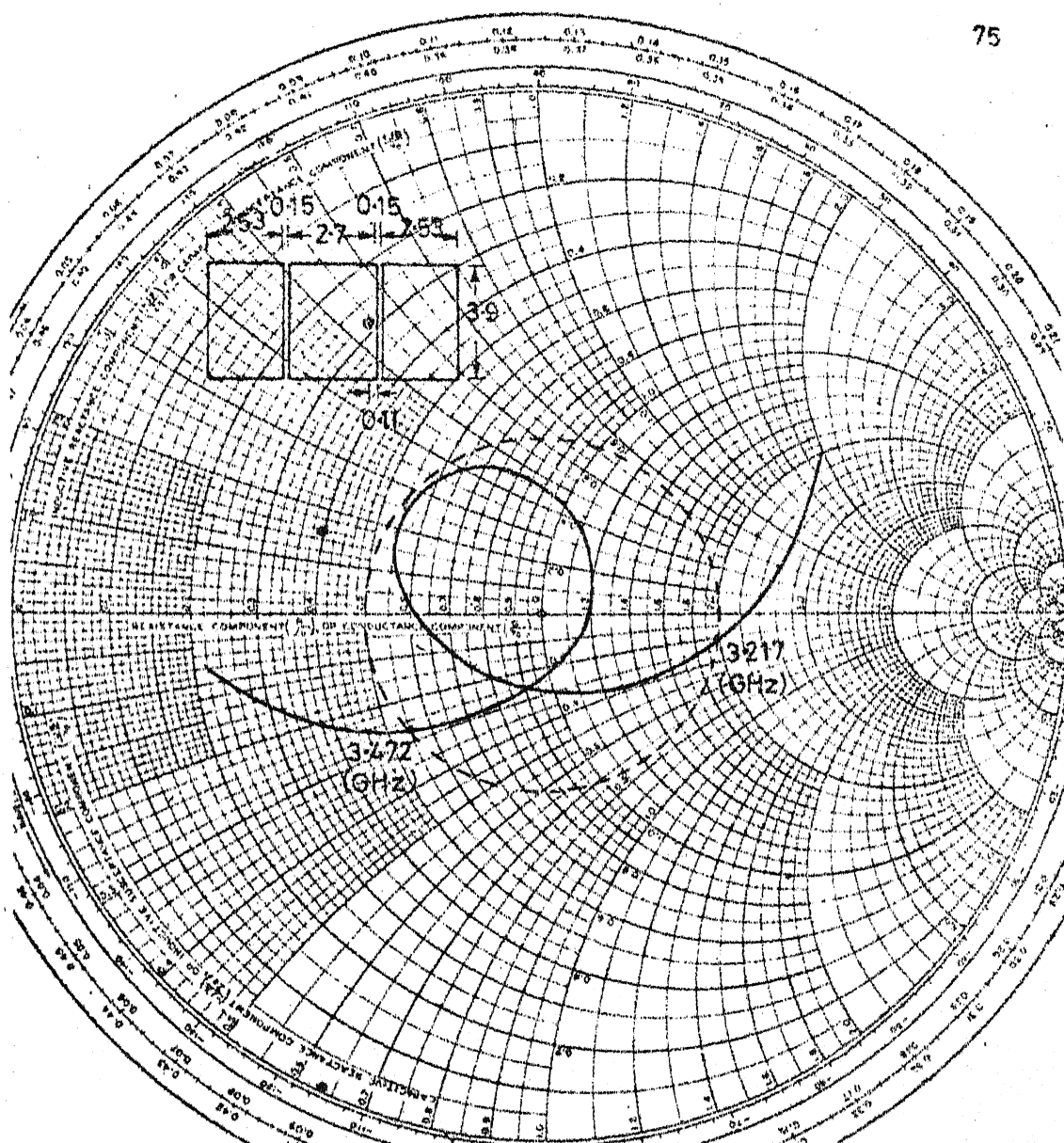


Fig.3-16 Input impedance locus for the modified dimensions of REGCOMA with identical parasitic elements

50 MHz more than the bandwidth of the REGCOMA shown in Fig. 3.15. Thus, the experimental bandwidth is likely to be even more.

3.4 REGCOMA WITH PARASITIC ELEMENTS OF DIFFERENT LENGTHS

3.4.1 Introduction

In the previous section, REGCOMA with identical parasitic elements has been discussed. The gap-widths between the central patch and the parasitic elements were taken equal. In this case, the central patch was resonant at one frequency and at nearby frequency, parasitic elements were resonant. When the lengths of the parasitic elements are different, their resonant frequencies will be different. Therefore, each parasitic element will form a separate loop in the impedance locus, resulting in two loops in the impedance locus, whereas only one loop was present when the parasitic elements were of equal lengths.

The REGCOMA with parasitic elements of different lengths l_1 and l_2 is shown in Fig. 3.17 (inset). The gap-widths S_1 and S_2 between the central patch and the parasitic elements need not be equal. The antenna has been analyzed using the procedure described in Section 3.3.1. The effects of changing the lengths l_1 and l_2 of the parasitic elements and the gap-widths S_1 and S_2 on the input impedance locus of the antenna are described in this section. These

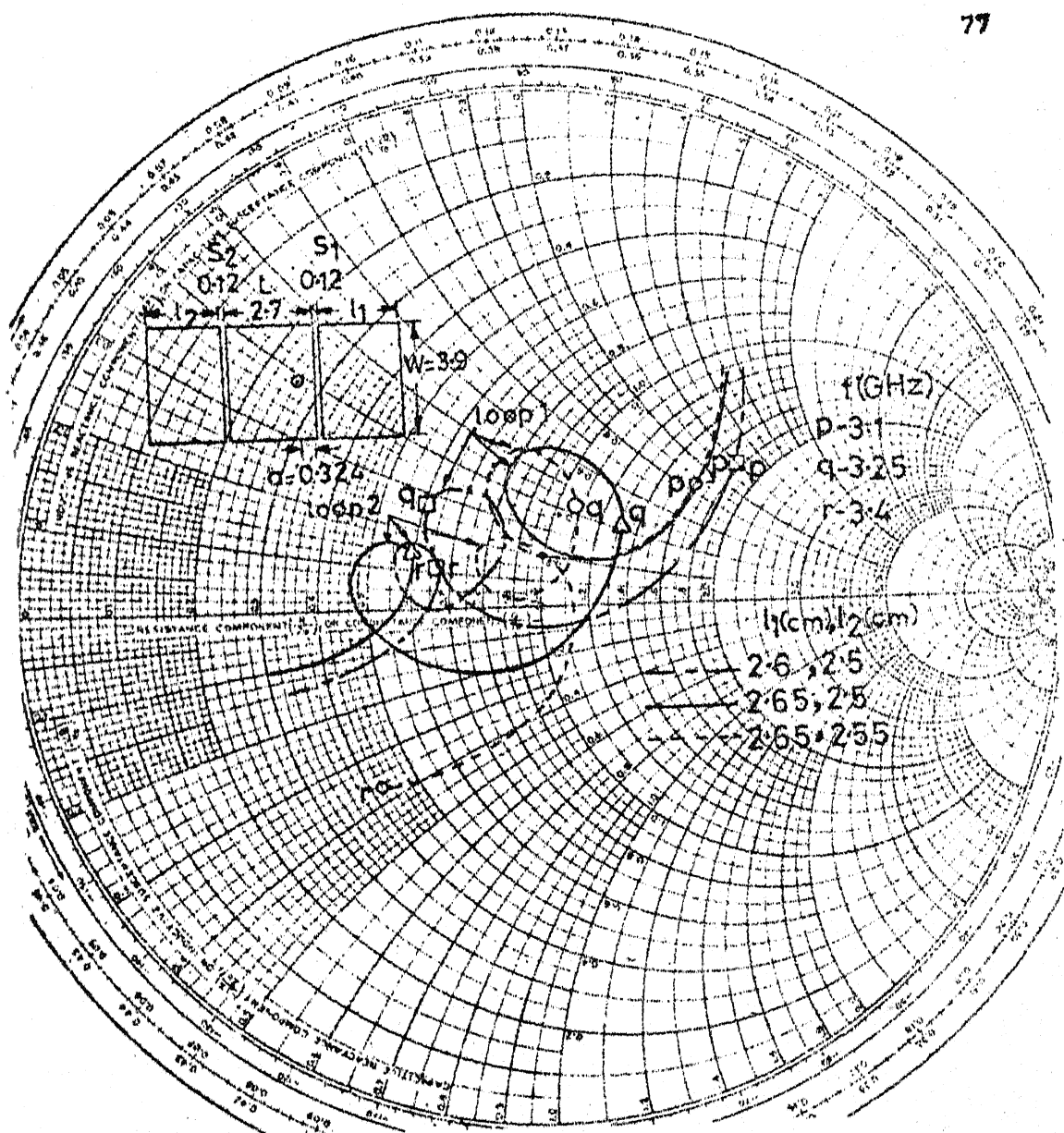


Fig.3.17 Input impedance loci of REGCOMA for three combinations of the lengths l_1 and l_2 of the parasitic elements

informations are used for optimizing the antenna to yield broader bandwidth.

3.4.2 Effect of the lengths of the parasitic elements

Input impedance loci of REGCOMA for three different combinations of the lengths l_1 and l_2 ($= (2.6, 2.5)$, $(2.65, 2.5)$ and $(2.65, 2.55)$ cm) of the parasitic elements, with S_1 and S_2 equal to 0.12 cm and feed-point location ' a ' = 0.324 cm, are plotted in Fig. 3.17. From these plots the following conclusion may be drawn. Two loops are present in each impedance locus as predicted in Section 3.4.1. Loops 1 and 2 correspond to the parasitic elements with larger and smaller lengths (l_1 and l_2) respectively. When the length l_1 is increased from 2.6 cm to 2.65 cm, while l_2 remains equal to 2.5 cm (i.e. the difference between the lengths l_1 and l_2 is increased), loop 1 shifts upward and towards the right side of the Smith chart and loop 2 shifts downward and towards the left side of the Smith chart, thereby increasing the separation between the two loops. For increase in the length l_2 from 2.5 cm to 2.55 cm, with $l_1 = 2.65$ cm (i.e. the difference between the two lengths l_1 and l_2 decreases), loop 1 moves downward and loop 2 moves upward, and the two loops came closer to each other. As the difference between the two lengths decreases, the two loops will come nearer and nearer, and will finally merge into a single loop when the two lengths

are equal. When both the lengths l_1 and l_2 are increased from (2.6, 2.5) cm to (2.65, 2.55) cm, both the loops in the impedance locus shift upward and towards the right side of the Smith chart.

3.4.3 Effect of the gap-widths

Input impedance loci for three combinations of the gap-widths S_1 and S_2 ($= (0.12, 0.12)$, $(0.12, 0.165)$, and $(0.165, 0.165)$ cm) are plotted in Fig. 3.18. Other dimensions of the REGCOMA are shown in Fig. 3.18 (inset). Size of the loop 1 (or 2) is mainly affected by the change in gap-width S_1 (or S_2) and is slightly affected by gap-width S_2 (or S_1). With increase in the gap-width S_1 and/or S_2 , the size of the loop 1 and/or loop 2 decreases and the two loops shift apart.

3.4.4 Experiments

After studying the effects of the lengths l_1 and l_2 , and gap-widths S_1 and S_2 on the input impedance locus, the dimensions of the antenna are selected such that the two loops in the impedance locus are inside the $VSWR = 2$ circle, thereby yielding wider bandwidth. For the REGCOMA shown in Fig. 3.19 (inset), theoretical input impedance locus and variation of $VSWR$ with frequency are plotted in Figs. 3.19(a) and (b) respectively. The two loops in the impedance locus are inside the $VSWR = 2$ circle, and the bandwidth of the antenna is 294 MHz (8.9 percent, $f_0 = 3.305$ GHz). For the analysis,

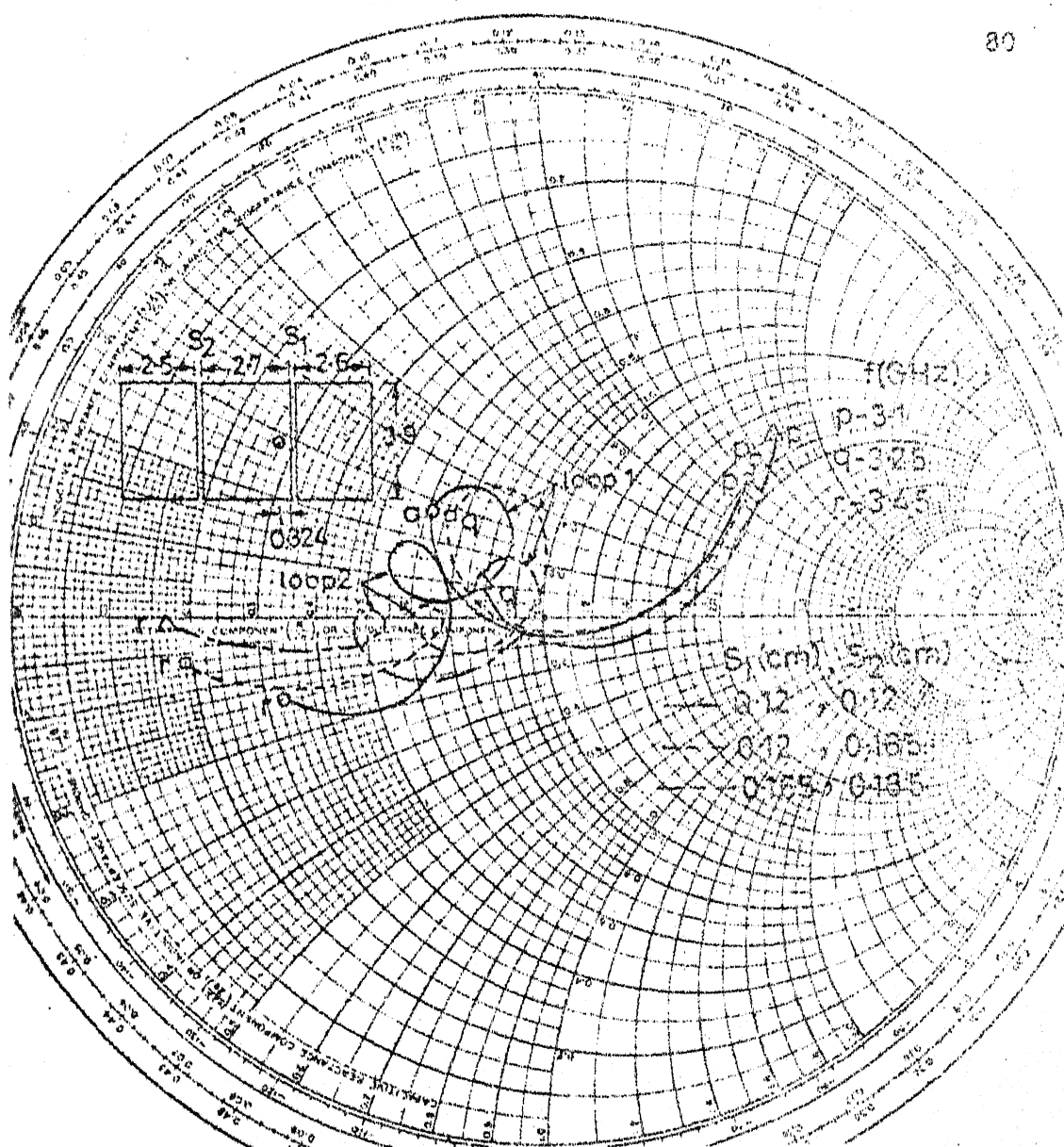


Fig.3-18 Input impedance loci of REGCOMA for three combinations of the gap-widths S_1 and S_2

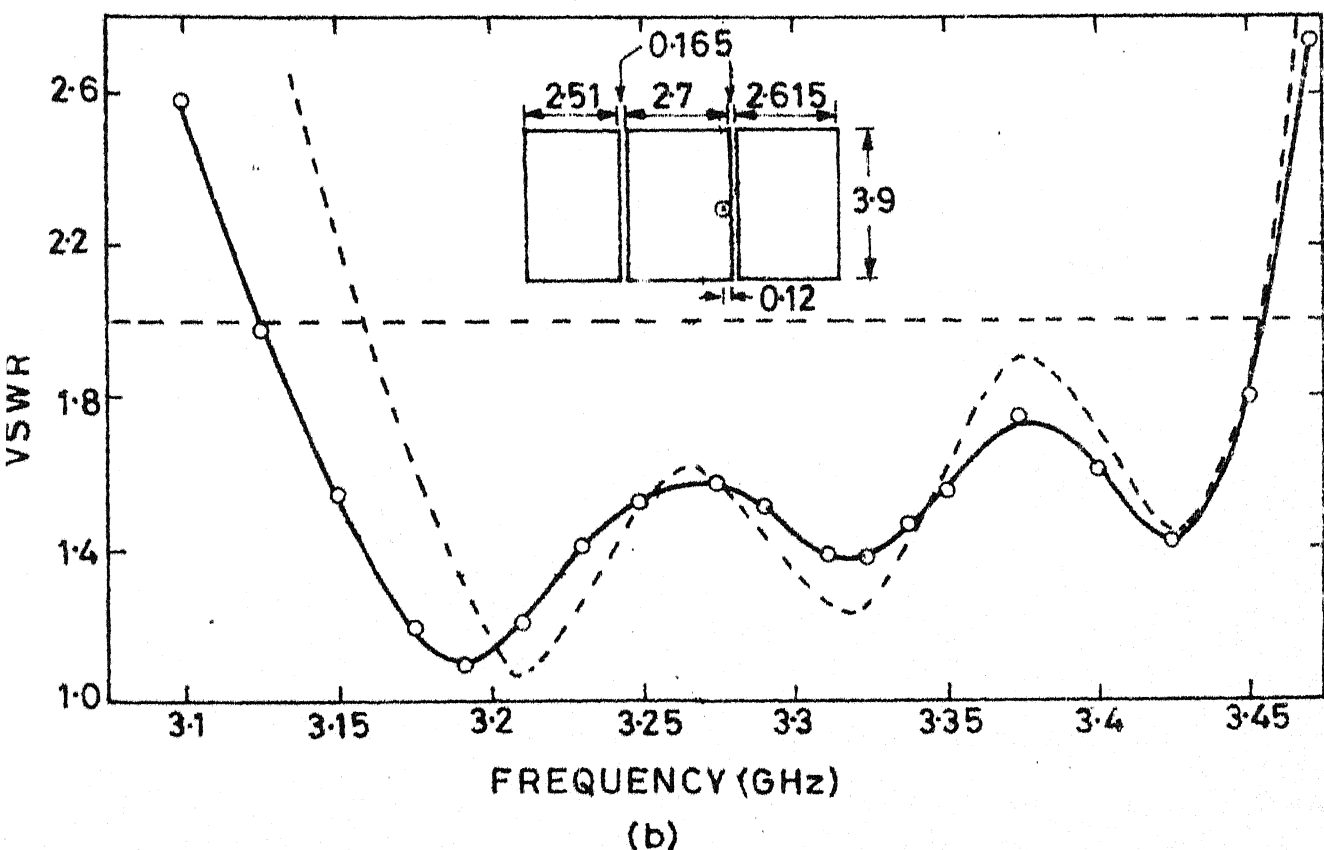
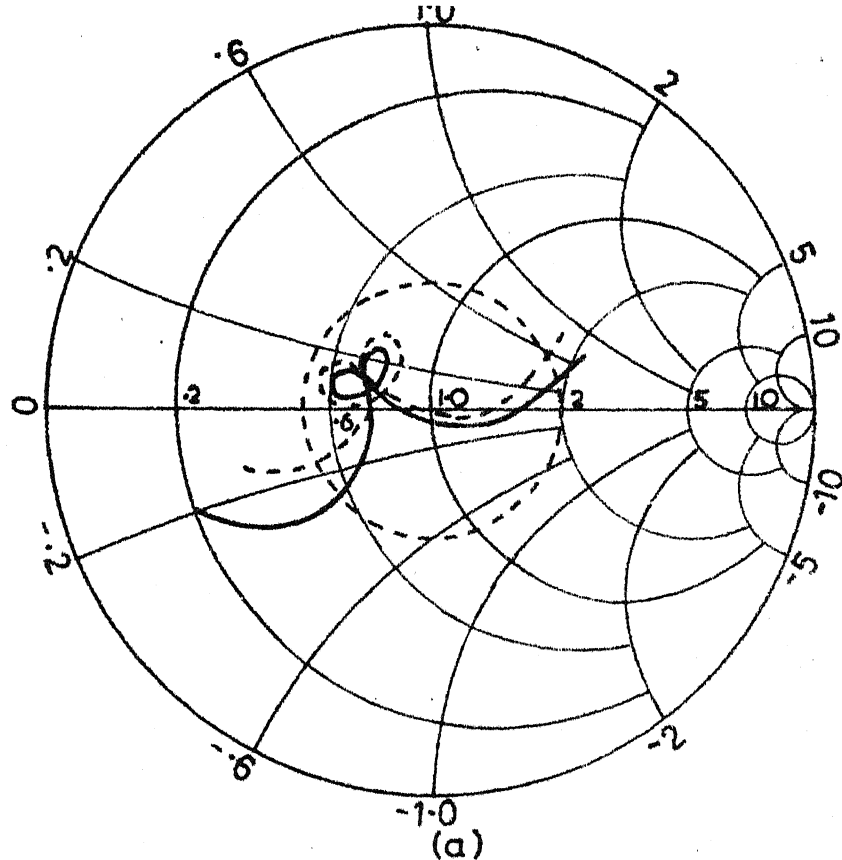


Fig.3.19 Theoretical (----) and experimental (—)(a) input impedance loci and (b) variations of VSWR with frequency of REGCQMA

the values of the capacitance coefficients are taken as :

$C_{ci} = 1.25$ and $C_{cg} = 0.52$ for $S_1 = 0.13$ cm, and $C_{ci} = 1.25$ and $C_{cg} = 0.49$ for $S_2 = 0.105$ cm. These values are interpolated from the values given in Section 3.3.4.

Experiment has been carried out on the above REGCOMA, and the photograph of the fabricated antenna is shown in Fig. 3.20. Experimental input impedance locus and VSWR versus frequency are also plotted in Fig. 3.19. Theoretical results are in acceptable agreement with the experimental results. The measured bandwidth of the antenna is 331 MHz (10 percent, $f_0 = 3.29$ GHz), which is 5.3 times the experimental bandwidth of RPA (BW = 62 MHz).

3.4.5 Voltage distribution and radiation pattern

Radiation pattern of the REGCOMA shown in Fig. 3.19 (inset), is evaluated from the voltage distribution along the periphery of the antenna by using (2.11). The voltage distribution along the periphery of the antenna is obtained from (2.6). Normalized values of the real and imaginary parts of the voltage are plotted at three frequencies in Fig. 3.21. From the voltage plots, the following may be observed. The voltage along the radiating edges of the REGCOMA is almost uniform and it varies nearly sinusoidally along the non-radiating edges. With the change in the frequency, the voltage distribution along the periphery changes and the voltage across the gap (i.e. the difference between the voltages along the coupled radiating edges) also varies.

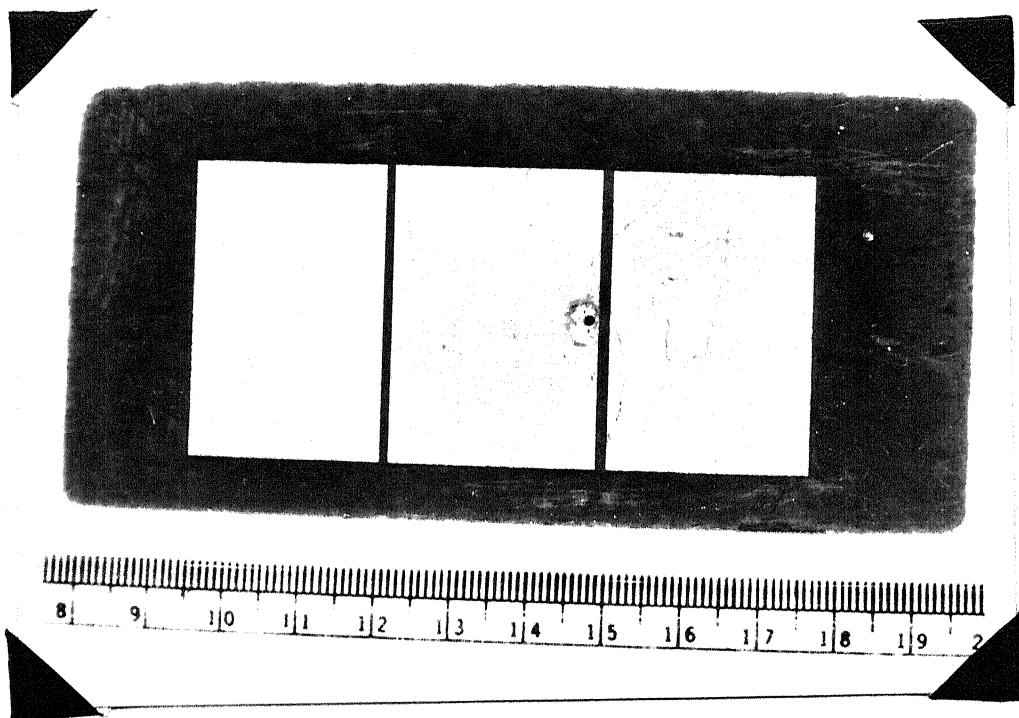


Fig. 3.20 Photograph of the REGCOMA fabricated on
 $h = 0.159$ cm thick substrate with $\epsilon_r = 2.55$

Since the voltage distribution along the periphery of the antenna varies with frequency, it is expected that the radiation pattern of the antenna will also vary with frequency. Radiation pattern is calculated in both $\varphi = 0^\circ$ and $\varphi = 90^\circ$ planes at several frequencies covering the entire bandwidth of the antenna. It is noted that only E_θ component of the radiation field is present in $\varphi = 0^\circ$ plane and only E_φ component is present in $\varphi = 90^\circ$ plane. E_θ in $\varphi = 0^\circ$ plane is plotted at three different frequencies in Fig. 3.22(a). From these plots, the following may be noted. The radiation field is not symmetrical with $\theta = 0^\circ$ axis, and the direction of maximum radiation varies from $\theta = 0^\circ$ to $\theta = 20^\circ$ as the frequency increases from 3.19 GHz to 3.39 GHz. 3-db beamwidth in $\varphi = 0^\circ$ plane at the three frequencies $f = 3.19, 3.29$ and 3.39 GHz is $60^\circ, 55^\circ$ and 99° respectively. A minimum occurs in E_θ at $f = 3.29$ GHz along $\theta = -40^\circ$, and its level is 23.5 db below the maximum level. E_φ component of the radiation field in $\varphi = 90^\circ$ plane is plotted at $f = 3.2$ GHz in Fig. 3.22(b). At other frequencies for which VSWR remains less than two, there is no appreciable change in the value of E_φ . 3-db beamwidth in $\varphi = 90^\circ$ plane is 74° .

Radiation pattern of the antenna is measured in both $\varphi = 0^\circ$ and $\varphi = 90^\circ$ planes at the various frequencies of interest. E_θ in $\varphi = 0^\circ$ plane is plotted at three frequencies

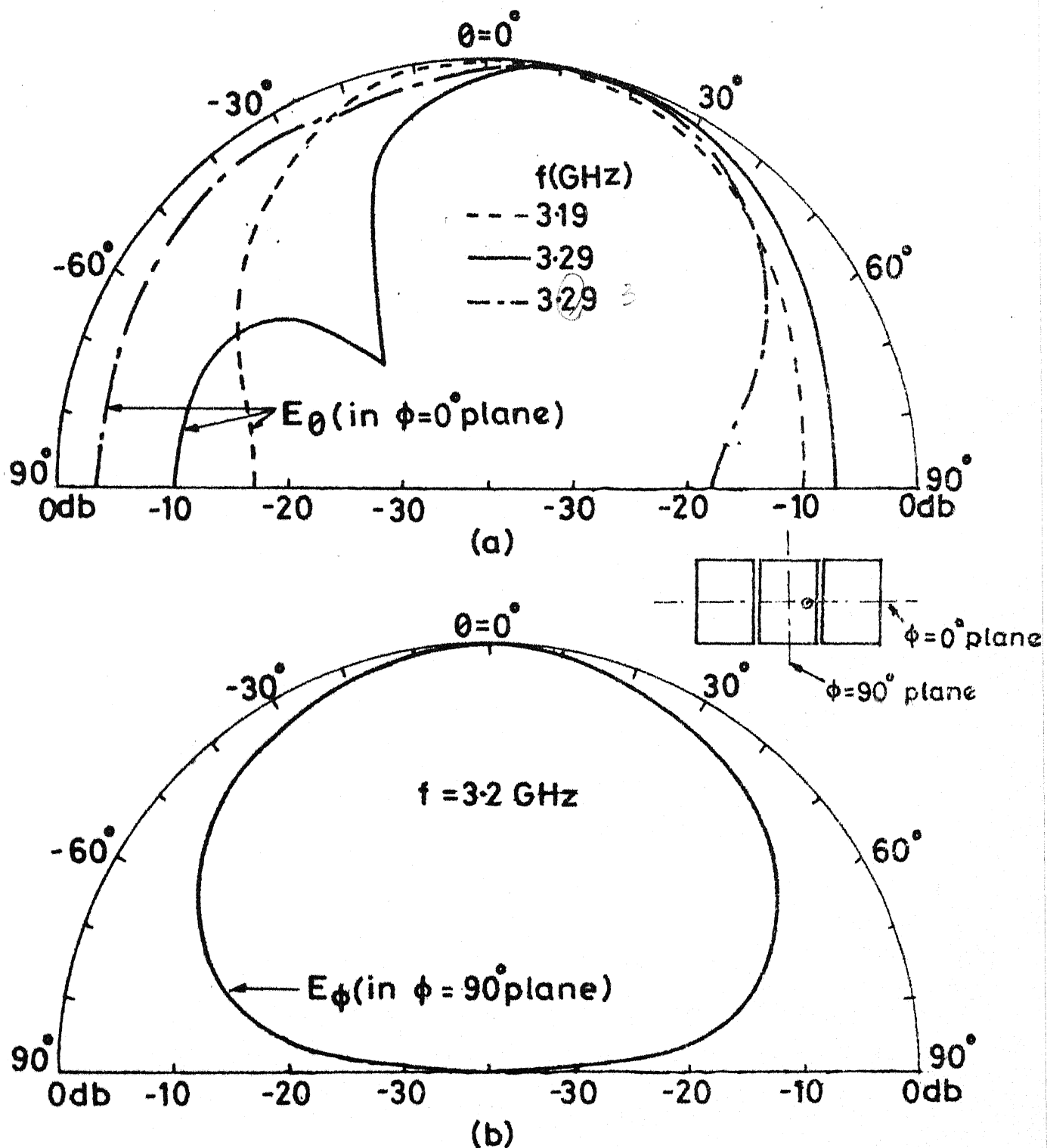


Fig.3.22 Theoretical values of (a) E_θ in $\phi = 0^\circ$ plane and (b) E_ϕ in $\phi = 90^\circ$ plane of REGCOMA shown in Fig.3.20

in Fig. 3.23(a). The direction of maximum radiation varies between $\theta = 0^\circ$ and $\theta = 10^\circ$ in the frequency range of 3.2 GHz to 3.405 GHz. 3-dB beamwidth in $\varphi = 0^\circ$ plane fluctuates between 33° and 48° as the frequency increases from 3.2 GHz to 3.405 GHz. The level of minimum in E_θ at $f = 3.2$ GHz is 15.5 dB below the corresponding maximum level. E_φ in $\varphi = 90^\circ$ plane is plotted at $f = 3.2$ GHz in Fig. 3.23(b). For comparison, theoretical E_φ in $\varphi = 90^\circ$ plane is also plotted in this figure. The experimental 3-dB beamwidth in $\varphi = 90^\circ$ plane is 68° , which is somewhat smaller than the theoretical value. The experimental values of the 3-dB beamwidth in the two planes ($\varphi = 0^\circ$ and 90°) are found to be smaller than the theoretical values as observed in the case of RPA (Fig. 2.10). This discrepancy may be due to the excitation of surface waves and because of the presence of finite ground plane [45].

Thus, the bandwidth of the RPA has been increased by using REGCOMA structure, but E_θ component of the radiation field in $\varphi = 0^\circ$ plane varies with frequency. The bandwidth of the REGCOMA shown in Fig. 3.19 (inset) can be further increased by reducing the gap-widths S_1 and S_2 , which will increase the size of the loops in the impedance locus of Fig. 3.19(a), and by decreasing the length l_2 of the parasitic element slightly, which will make the parasitic element to be resonant at higher frequency, thereby increasing the bandwidth.

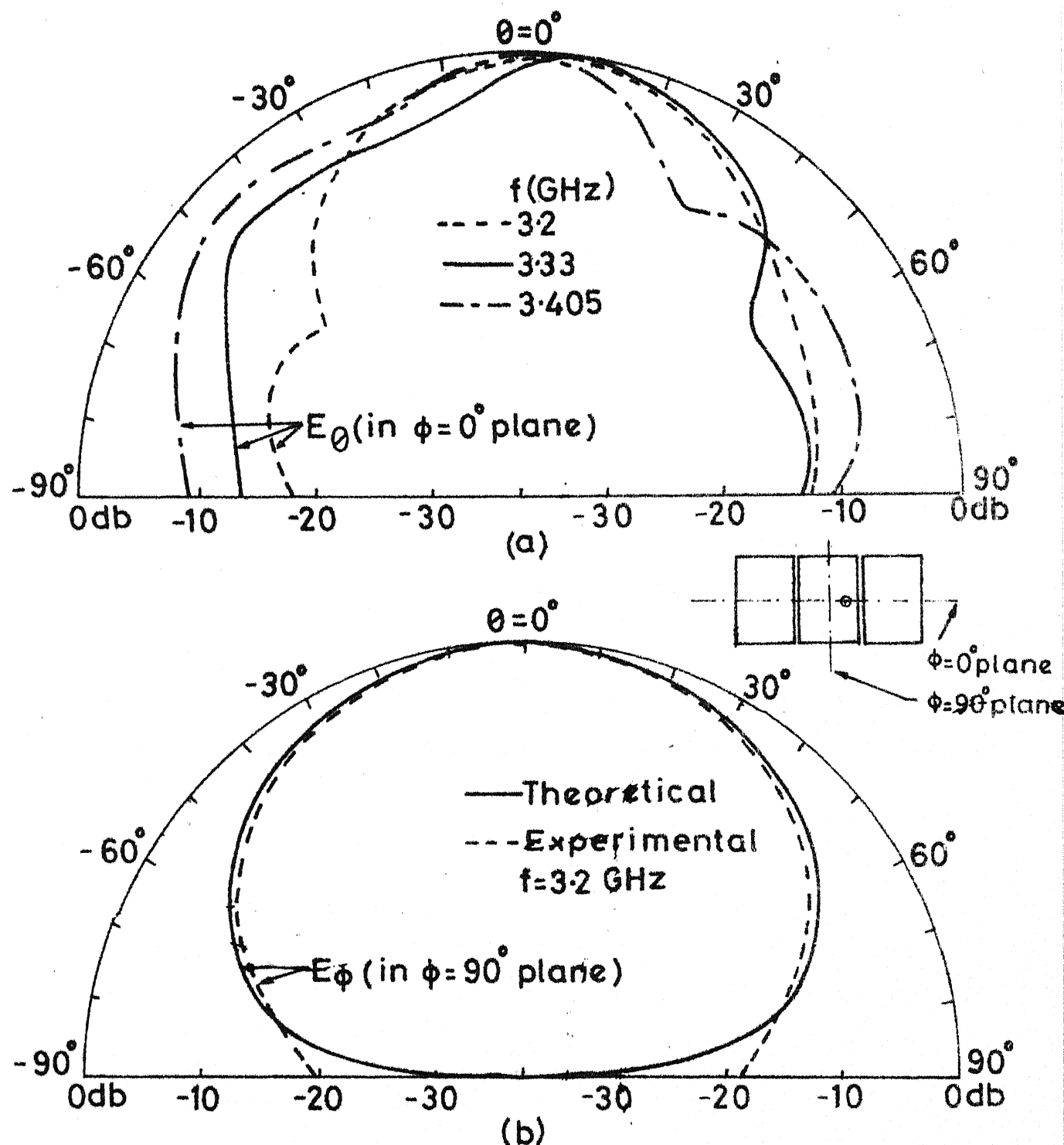


Fig.3-23 (a) Experimental E_θ in $\phi = 0^\circ$ plane and (b) theoretical and experimental E_ϕ in $\phi = 90^\circ$ plane of the REGCOMA shown in photograph 320

3.5 REGCOMA ON THICKER SUBSTRATE

As discussed in Section 2.4, for a RPA, when the thickness of the substrate is doubled, the bandwidth of the antenna also becomes nearly double for the same patch dimensions. To study the effect of doubling the substrate thickness on the bandwidth of REGCOMA, a few experiments have been performed with the substrate thickness $h = 0.318$ cm. The dimensions of the experimental antenna are shown in Fig. 3.24 (inset). The length of the central patch is considered as 2.9 cm, so that the centre frequency is around 3 GHz. The differences between the lengths of the parasitic elements and central patch are taken nearly double of that for the antenna with $h = 0.159$ cm. The widths of the resonators are reduced from 3.9 cm to 3.0 cm. The gap-widths are taken approximately equal to one and a half times the gap-widths considered in the antenna with $h = 0.159$ cm. The experimental input impedance locus and VSWR variation with frequency are plotted in Figs. 3.24(a) and (b) respectively. The bandwidth of the antenna is 485 MHz (16 percent, $f_0 = 3.04$ GHz), which is four times the bandwidth of RPA (BW = 121 MHz, $L = 2.9$ cm, $W = 3.0$ cm). The bandwidth of the RPA with $W = 3.0$ cm is interpolated from the results of RPA with $W = 4.0$ cm and 2.0 cm (BW = 133 MHz and 109 MHz respectively), given in Section 2.4.2.

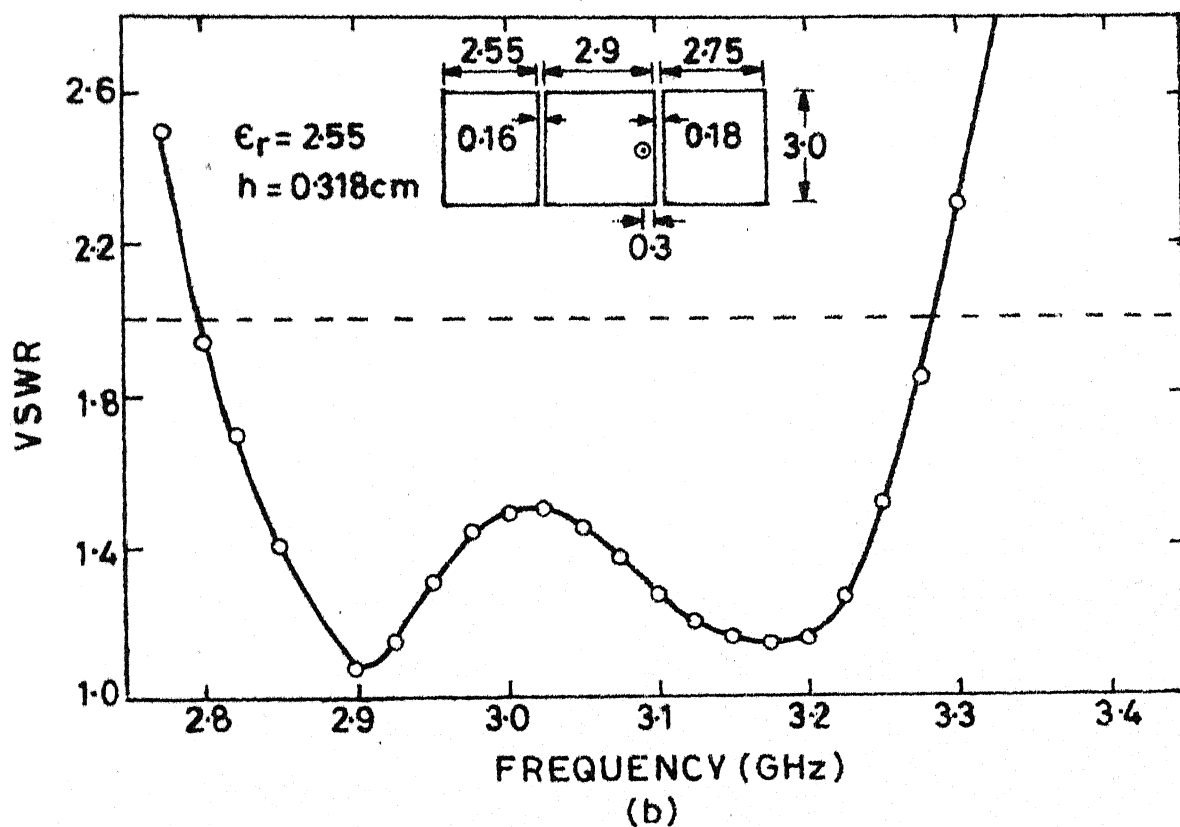
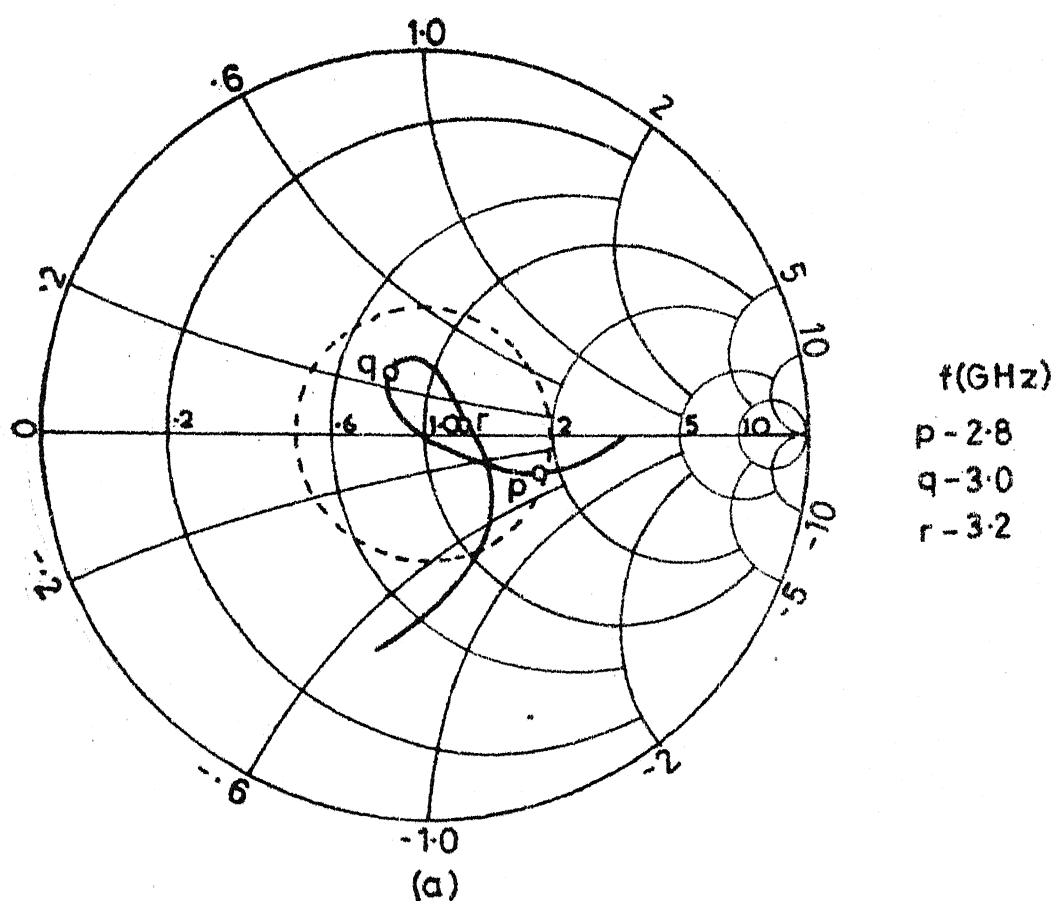


Fig.3.24 Experimental (a) input impedance locus and (b) VSWR variation with frequency of REGCOMA

Another experiment has been carried out for improving the bandwidth. The gap-widths between the resonators are reduced, which will increase the size of the loops in the impedance locus. The modified dimensions of the REGCOMA are depicted in Fig. 3.25 (inset) and the photograph of the fabricated antenna is shown in Fig. 3.26. The experiment input impedance locus and variation of VSWR with frequency are plotted in Figs. 3.25(a) and (b) respectively. The experimental bandwidth is 512 MHz (17 percent, $f_0 = 3.016$ GHz), which shows an improvement of 27 MHz in the bandwidth over the previous experiment. The ripples in the VSWR versus frequency plot remain lower than $VSWR = 1.7$. If the bandwidth is defined as the frequency range for which $VSWR \leq 1.7$, then it is equal to 470 MHz, which is five times the bandwidth of RPA ($BW = 93$ MHz for $VSWR \leq 1.7$).

Theoretical input impedance locus and VSWR variation with frequency of the REGCOMA are also plotted in Fig. 3.25. The modified values of the gap capacitances are used for analysis. The discrepancy between the theoretical and experimental results is more in the case of REGCOMA with $h = 0.318$ cm as compared to that for REGCOMA with $h = 0.159$ cm. Because with increase in the substrate thickness, the dielectric loss and losses due to the surface wave propagation increase, and since these losses have not been considered in the analysis, the discrepancy between the theoretical and experimental results increases.

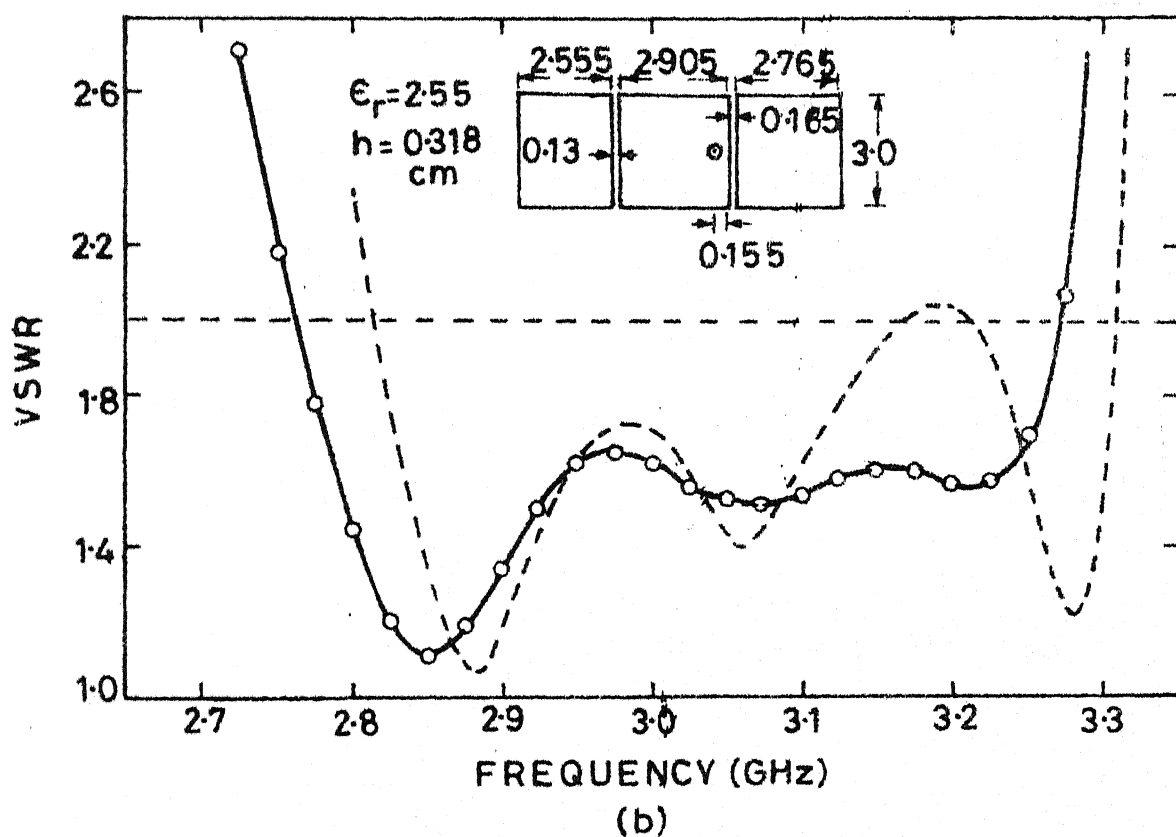
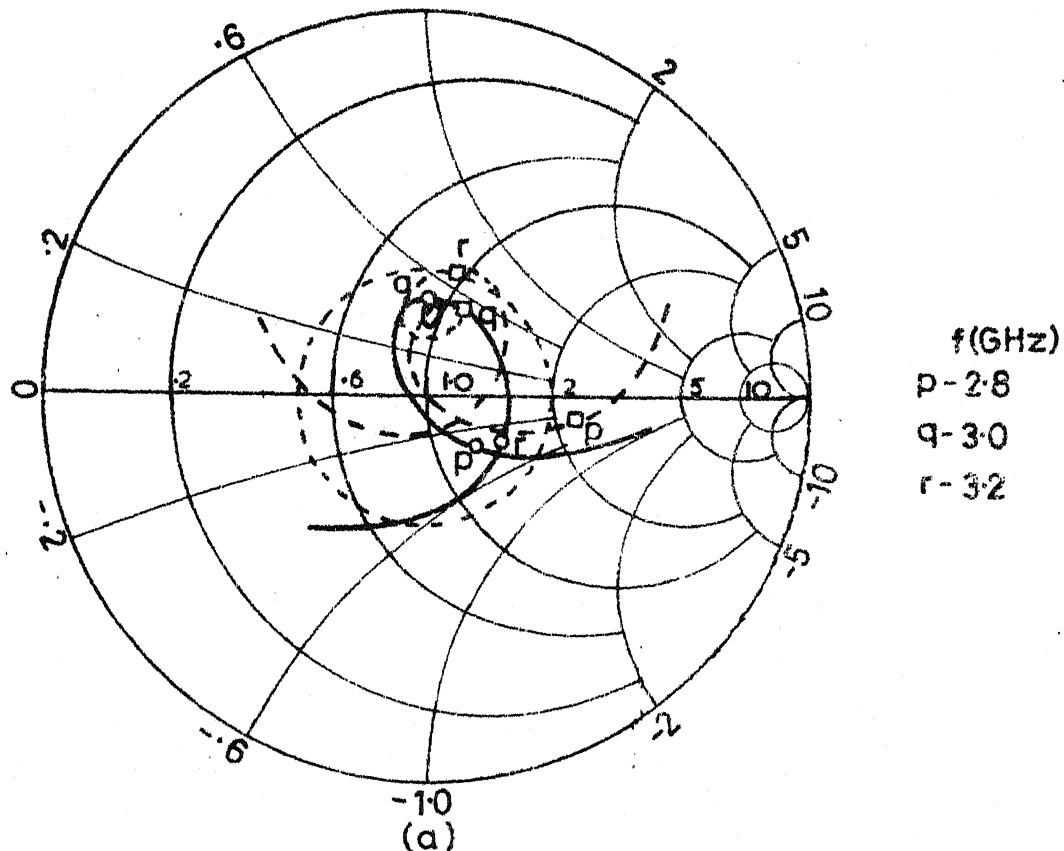


Fig.3.25 Theoretical (---) and experimental (—)
 (a) input impedance loci and (b)
 variations of VSWR with frequency of

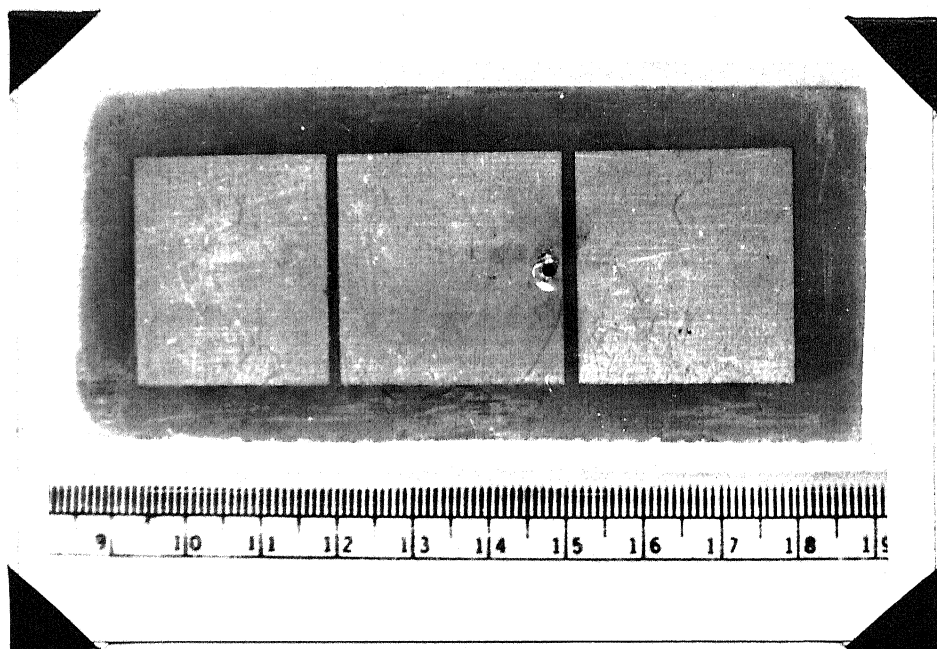


Fig. 3.26 Photograph of the REGCOMA fabricated on the substrate having thickness $h = 0.318$ cm and $\epsilon_r = 2.55$

Radiation pattern of the antenna is calculated in both $\varphi = 0^\circ$ and $\varphi = 90^\circ$ planes. The radiation characteristics are found to be similar to that of the REGCOMA with $h = 0.159$ cm (shown in Fig. 3.22), and have not been plotted.

The bandwidth of the REGCOMA shown in Fig. 3.25 (inset), can be further improved by reducing the length l_2 of the parasitic element and gap-width S_2 . Because this will shift the smaller loop in the impedance locus of Fig. 3.25(a) towards the higher frequency points on the Smith chart and also its size will be increased.

3.6 DISCUSSION

Radiating edges gap coupled microstrip antennas have been designed, analyzed and optimized around 3 GHz centre frequency using the Green's function approach and the segmentation method. The variables which have been optimized to yield broader bandwidth are : lengths of the parasitic elements, gap-widths between the parasitic elements and central rectangular patch, and the location of the feed-point. Based on these designs, experiments have been performed with two substrates having different thicknesses ($h = 0.159$ cm

and 0.318 cm) but equal dielectric constants ($\epsilon_r = 2.55$). The experimental bandwidths of the REGCOMA are found to be 331 MHz and 512 MHz for $h = 0.159$ cm and 0.318 cm respectively, which are five and four times the bandwidths of the corresponding RPA (BW = 62 MHz and 121 MHz respectively).

While the investigations on REGCOMA were being carried out, microstrip antennas with short-circuit quarter wavelength parasitic elements coupled to the radiating edges of rectangular patch antenna (shown in Fig. 1.4(c)) have been reported in the literature [58]. In this case, the bandwidth obtained is only twice of that of a RPA, whereas REGCOMA yields four to five times the bandwidth of RPA. Moreover, the shorting of the edges of the parasitic elements with the ground plane has to be done.

In the next chapter, another gap coupled antenna configurations, namely, non-radiating edges gap coupled and four edges gap coupled microstrip antennas are suggested to improve the bandwidth of RPA.

CHAPTER FOUR

NON-RADIATING EDGES GAP COUPLED AND FOUR EDGES GAP COUPLED MICROSTRIP ANTENNAS

In this chapter, analysis and design of non-radiating edges gap coupled microstrip antennas (NEGCOMA) and four edges gap coupled microstrip antennas (FEGCOMA) are discussed. These antenna structures are also analyzed by Green's function approach using segmentation method and the coupling gaps between the resonators are modelled as capacitive π -networks as described in Chapter Three.

4.1 NEGCOMA WITH IDENTICAL PARASITIC ELEMENTS

4.1.1 Analysis

Two identical rectangular resonators of length l_1 and width equal to that of the rectangular patch antenna are placed adjacent to the non-radiating edges of the patch antenna (patch dimensions : $L \times W$) as shown in Fig. 4.1(a). This structure may behave like a REGCOMA at a different frequency where the resonance is caused by the width W (i.e. when W becomes approximately half wavelength). Since the antenna structure and the feeding arrangement are symmetrical with respect to the axis XX , the fields will have an even symmetry with respect to XX . Thus only half of the structure with a magnetic wall at XX , need to be analyzed. Even-mode half section of NEGCOMA with open-end fringing fields taken into account is shown in Fig. 4.1(b).

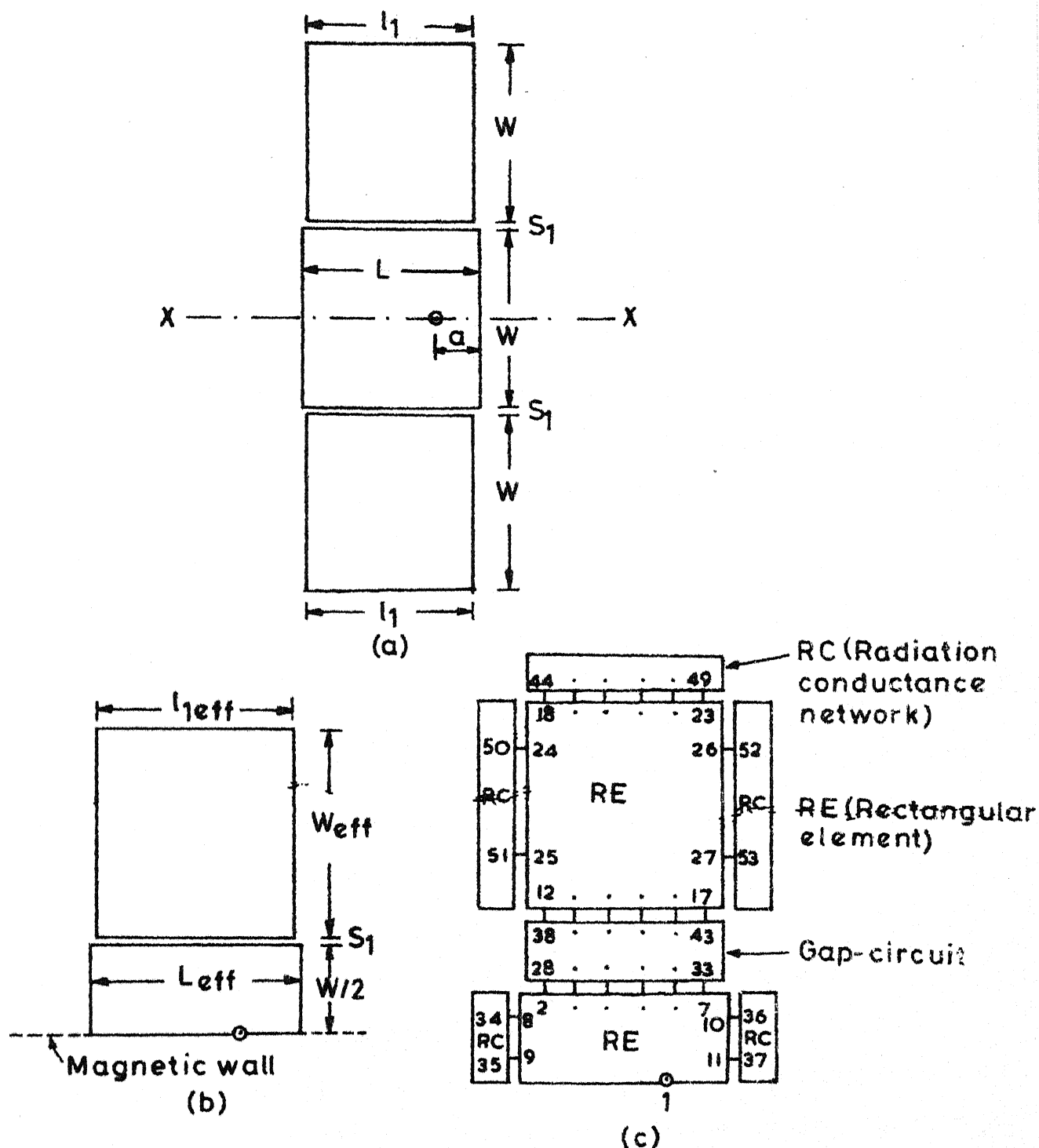


Fig. 4.1(a) NEGCOMA with identical parasitic elements and its (b) even-mode half section and (c) segmented network

To apply segmentation method for analysis, NEGCOMA is divided into various segments as shown in Fig. 4.1(c). These segments are : two rectangular elements, a gap-circuit, and five radiation conductance networks. Edges of the antenna are divided into 53 ports with c and d ports being 26 each and a single p-port which corresponds to the feed-point location. Z-matrix for the overall circuit is calculated from the Z-matrices of the individual sub-components by using (2.5). For a unit current excitation at the feed-port, voltage distribution at the various ports is obtained from (2.6). The electric vector potential is calculated by using (2.10) and radiation fields are evaluated from (2.11).

4.1.2 Effect of antenna parameters on performance

The various antenna parameters, for any given patch dimensions ($L = 2.9$ cm and $W = 4.0$ cm), substrate specifications ($\epsilon_r = 2.55$ and $h = 0.159$ cm), and the width of the parasitic element being equal to the width of the central rectangular patch, which govern the input impedance characteristics of NEGCOMA are : gap-width S_1 between the two resonators, length l_1 of the parasitic element, and feed-point location 'a'. Effects of these three parameters on the input impedance locus of NEGCOMA are discussed separately in this section.

Gap-width S_1 between the resonators

NEGCOMA is analyzed for three different values of gap-widths ($S_1 = 0.1, 0.05$ and 0.025 cm), with parasitic element length $l_1 = 2.9$ cm and feed-point location ' a ' = 0.29 cm. As discussed in Section 3.5, the values of the gap-capacitances considered in the gap-modelling (shown in Fig. 3.3) are not accurate, and have been therefore modified to match the theoretical results with the experimental results. The coefficients for the capacitances C_1, C_2 and C_g in the present case may be different from those obtained for REGCOMA, because in the case of NEGCOMA, fields are roughly sinusoidal along the coupled non-radiating edges, whereas fields are nearly uniform along the coupled radiating edges of REGCOMA. Hence, these coefficients are reevaluated. The effects of these coefficients on the input impedance locus are studied later in this section. The gap width considered here is much smaller than the gap-width required for sufficient coupling in the case of REGCOMA. This is due to the fact that coupling between the resonators will be much less when field varies sinusoidally along the coupled edges as compared to the uniform field for the same gap-width.

The impedance loci for three different values of gap-widths are plotted in Fig. 4.2 for coupling coefficients $C_{c1} = C_{c2} = 1.0$ and $C_{cg} = 0.5$. From these plots the following points are noted. A loop in the impedance locus is formed due to the presence of the parasitic elements, as in the case

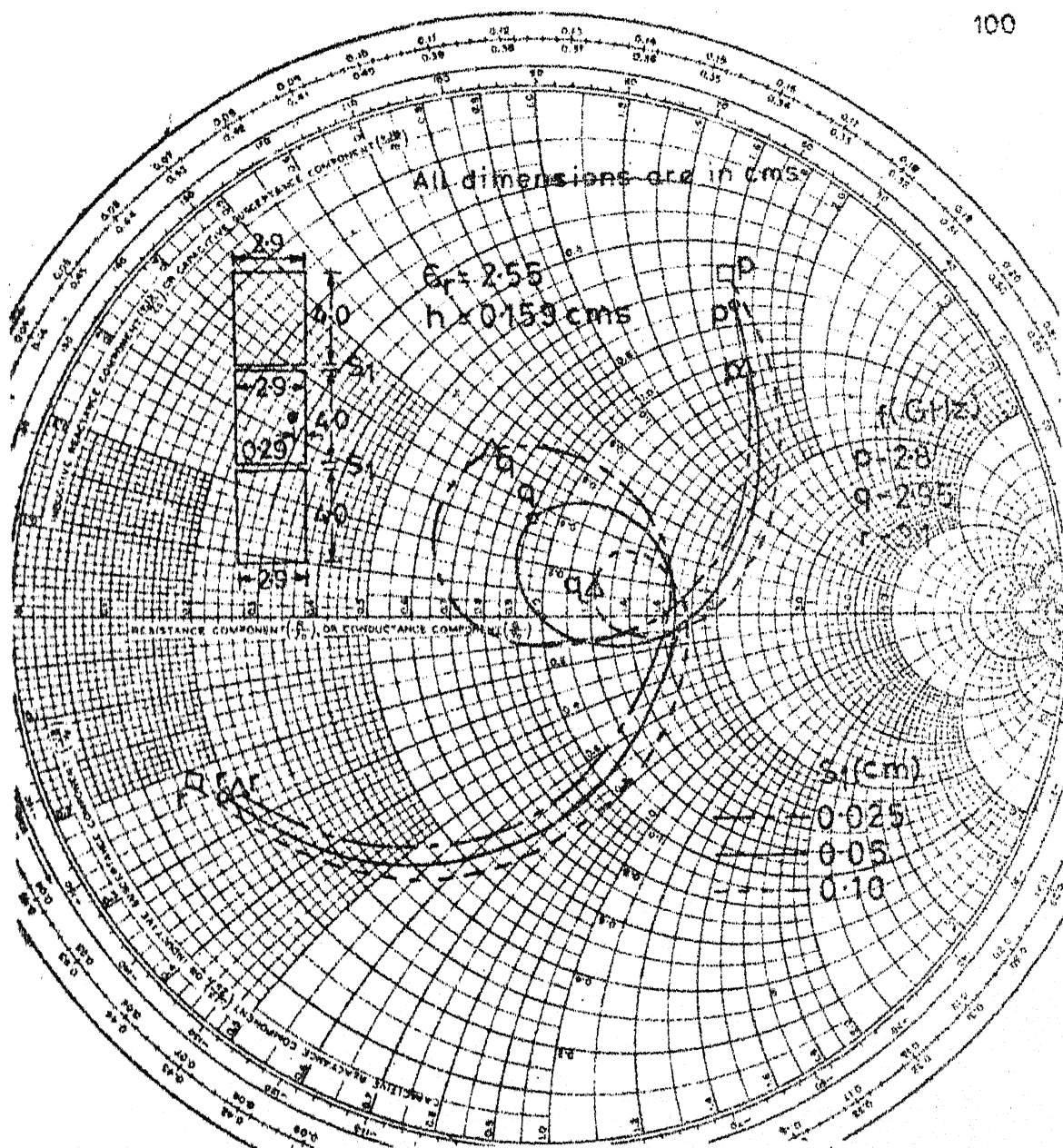


Fig.4.2 Input impedance loci of NEGCOMA for three different values of gap-width S_1

of REGCOMA. With increase in gap-width, the interaction between the resonators decreases, so the size of the loop in the impedance locus decreases. Also, the impedance locus shifts towards the right side of the Smith chart with increase in gap-width. As the gap-width is increased further, loop size will go on decreasing and finally for a considerably larger gap, the loop will disappear, and the impedance locus of NEGCOMA will become similar to that of RPA.

As discussed above, the values of the coefficients of capacitances may be different than those obtained for REGCOMA, so the effects of changing these coefficients on the input impedance locus are studied. Impedance loci for three different coefficients of capacitance C_g ($C_{cg} = 0.6$, 0.5 , and 0.4), with coefficients of capacitances C_1 and C_2 being taken as unity, are plotted in Fig. 4.3. The dimensions of the antenna are shown in Fig. 4.3. With decrease in the value of C_{cg} (from 0.6 to 0.4), the size of the loop decreases and the impedance locus shifts towards the right side of the Smith chart.

Impedance loci for three different coefficients of capacitances C_1 and C_2 ($C_{ci} = 0.6$, 1.0 and 1.4 , where $i = 1, 2$), with $C_{cg} = 0.5$ are plotted in Fig. 4.4. As the value of C_{ci} increases from 0.6 to 1.4 , the loop in the impedance locus shifts downward and towards the left side of the Smith chart. However, there is not much change in the size of the loop.

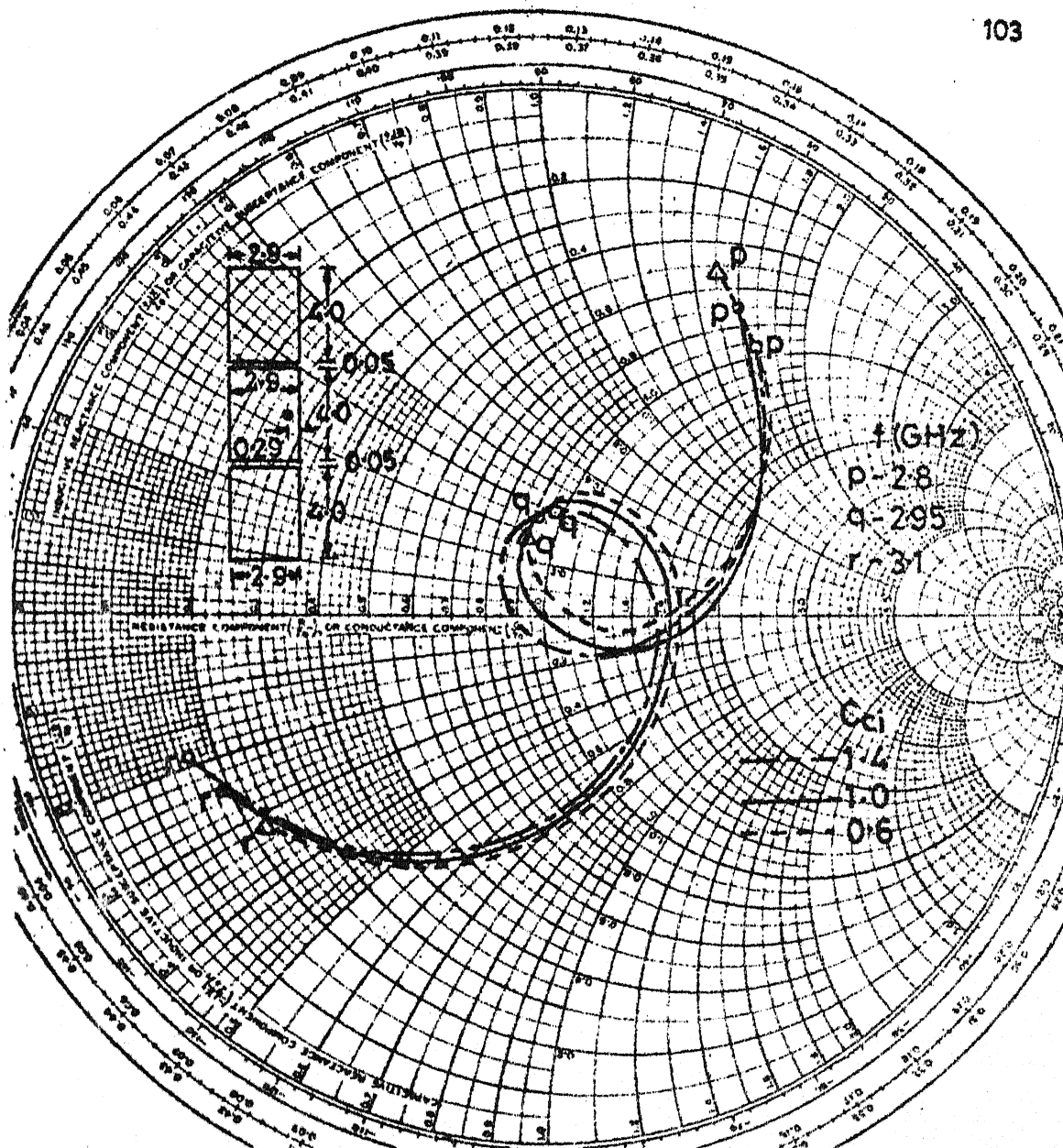


Fig. 4.4 Input impedance loci of NEGCOMA for three different values of coupling co-efficient C_{ci}

Length of the parasitic element

Impedance loci for three different lengths of parasitic elements ($l_1 = 3.0, 2.9$ and 2.8 cm) with gap width $S_1 = 0.05$ cm and feed-point location ' a ' = 0.29 cm are plotted in Fig. 4.5. As the length l_1 of the parasitic element decreases from 3.0 cm to 2.8 cm, the loop in the impedance locus shifts downward and towards the left side of the Smith chart, but there is not much change in the size of the loop. Except for the presence of the loops, the impedance loci for the three different values of l_1 follow the same pattern as the impedance locus of RPA. When the length of the parasitic element decreases, its resonance frequency increases, so the loop is formed at the higher frequency points on the impedance locus of RPA. Since the locus of RPA moves downward with increase in frequency, the loop in the impedance locus of NEGCOMA shifts downward with decrease in the length of the parasitic element.

Location of feed-point

Impedance loci for three different feed-point locations ($a = 0.435, 0.29$ and 0.145 cm) with $l_1 = 2.9$ cm and $S_1 = 0.05$ cm, are plotted in Fig. 4.6. When the location of the feed-point is shifted towards the nearer edge of the central resonator (i.e. from $a = 0.435$ cm to 0.145 cm), impedance locus shifts towards the right side of the Smith chart. However, the impedance locus shape remains unaltered. Similar shift in the impedance locus has been also observed in the case of RPA.

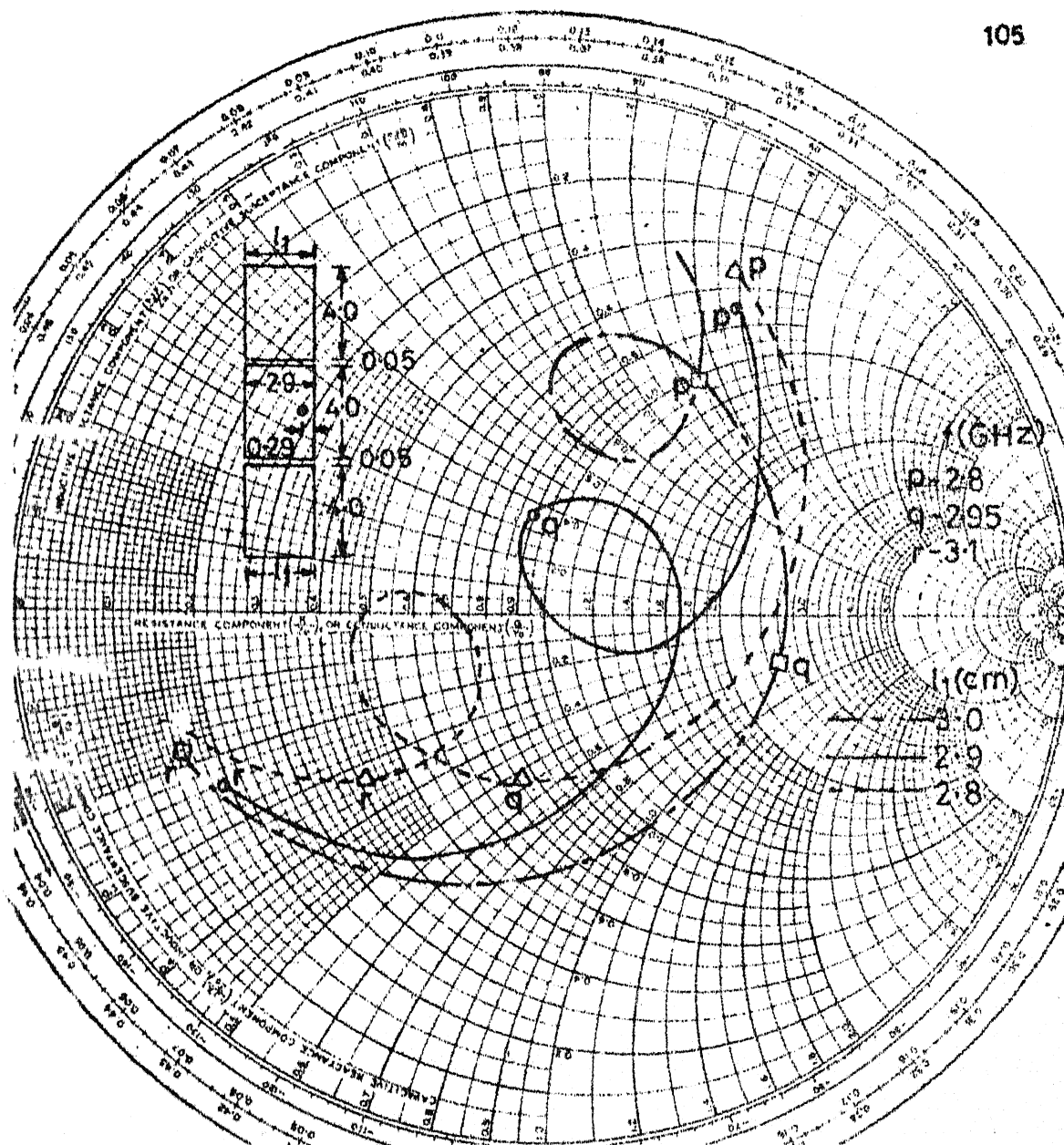


Fig. 45 Input impedance loci of NEGCOMA for three values of length l_1 of parasitic element

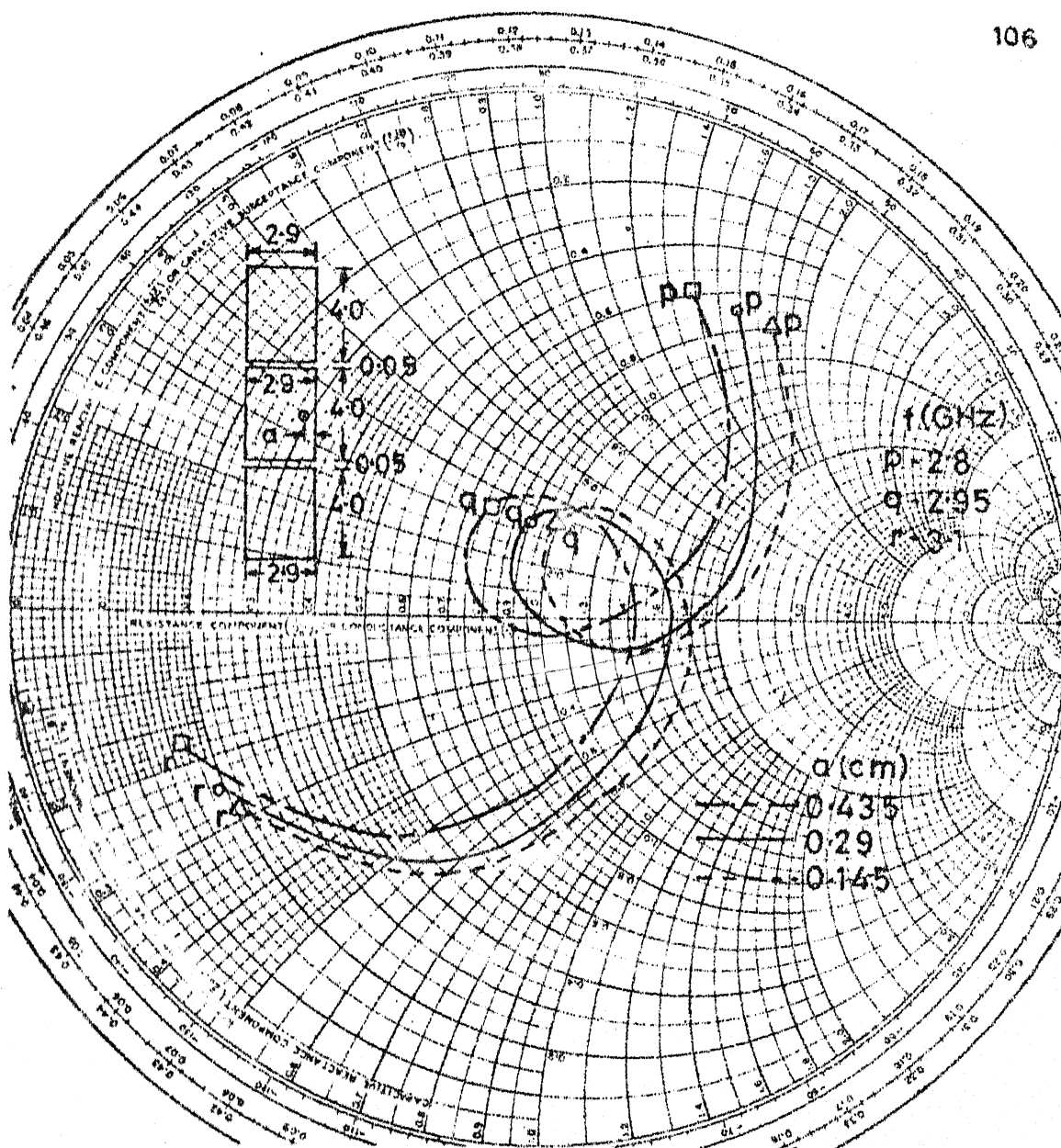
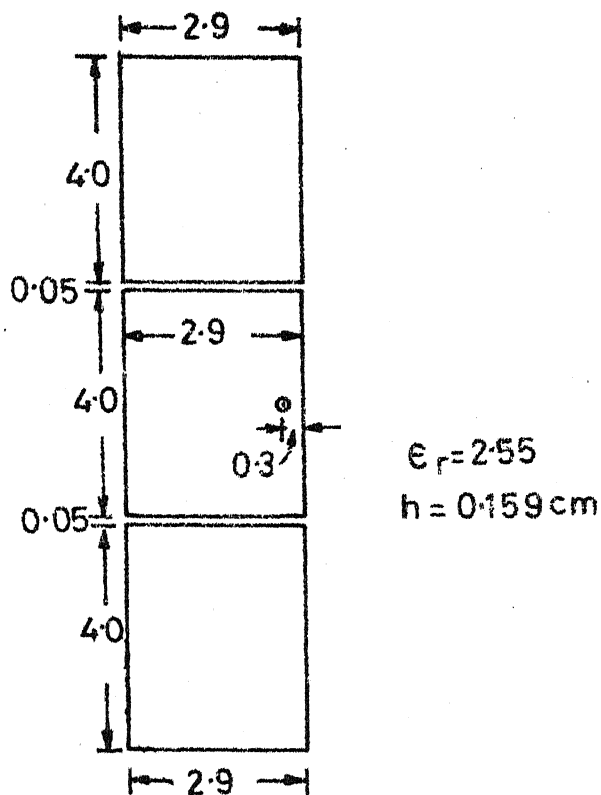


Fig. 4.6 Input impedance loci of NEGCOMA for three locations of the feed-point

4.1.3 Experiments

Experiment has been performed on NEGCOMA with parasitic element length $l_1 = 2.9$ cm, gap-width $S_1 = 0.05$ cm and feed-point location 'a' = 0.3 cm, as shown in Fig. 4.7(a). The experimental input impedance locus is plotted in Fig. 4.7(b). If this impedance locus is compared with the corresponding theoretical input impedance locus shown in Fig. 4.5 (in solid lines), it may be noted that theoretical results do not agree with the experimental results. The loop in the experimental impedance locus is shifted upward and towards the right side of the Smith chart. Similar discrepancy has been observed by other investigators also [22], [58]. In the case of REGCOMA, theoretical values were in reasonable agreement with the experimental values when the gap capacitances were modified suitably. But for NEGCOMA, theoretical values do not match with the experimental values for any combination of capacitance coefficients. However, by taking $C_{ci} = 1.0$ and $C_{cg} = 0.47$, the size of the loop in the two cases is nearly same as shown in Fig. 4.7(b).

Another experiment has been performed on NEGCOMA (the dimensions are shown in Fig. 4.8 (inset)) to bring the loop in the impedance plot of Fig. 4.7(b) inside the VSWR = 2 circle. The length of the parasitic element is reduced from 2.9 cm to 2.75 cm, because with the decrease in the length of the parasitic element, the loop in the impedance locus shifts downward and towards the left side of the Smith chart



(a)

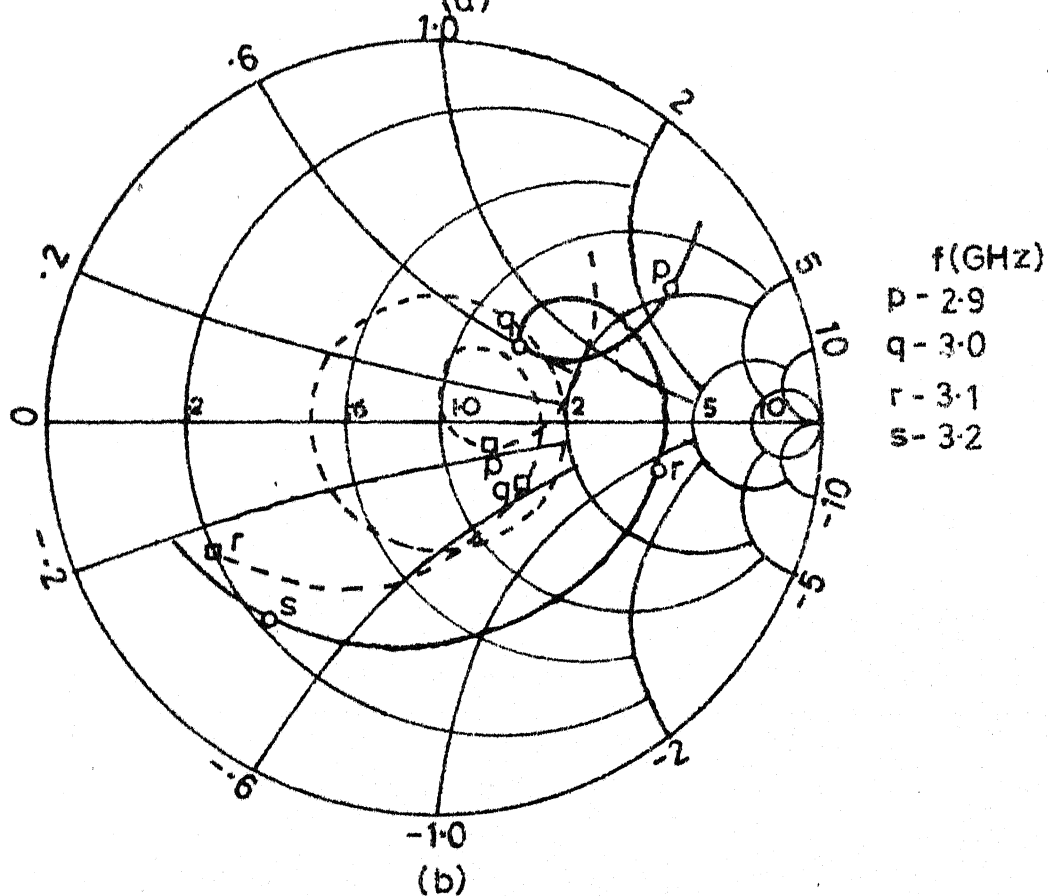
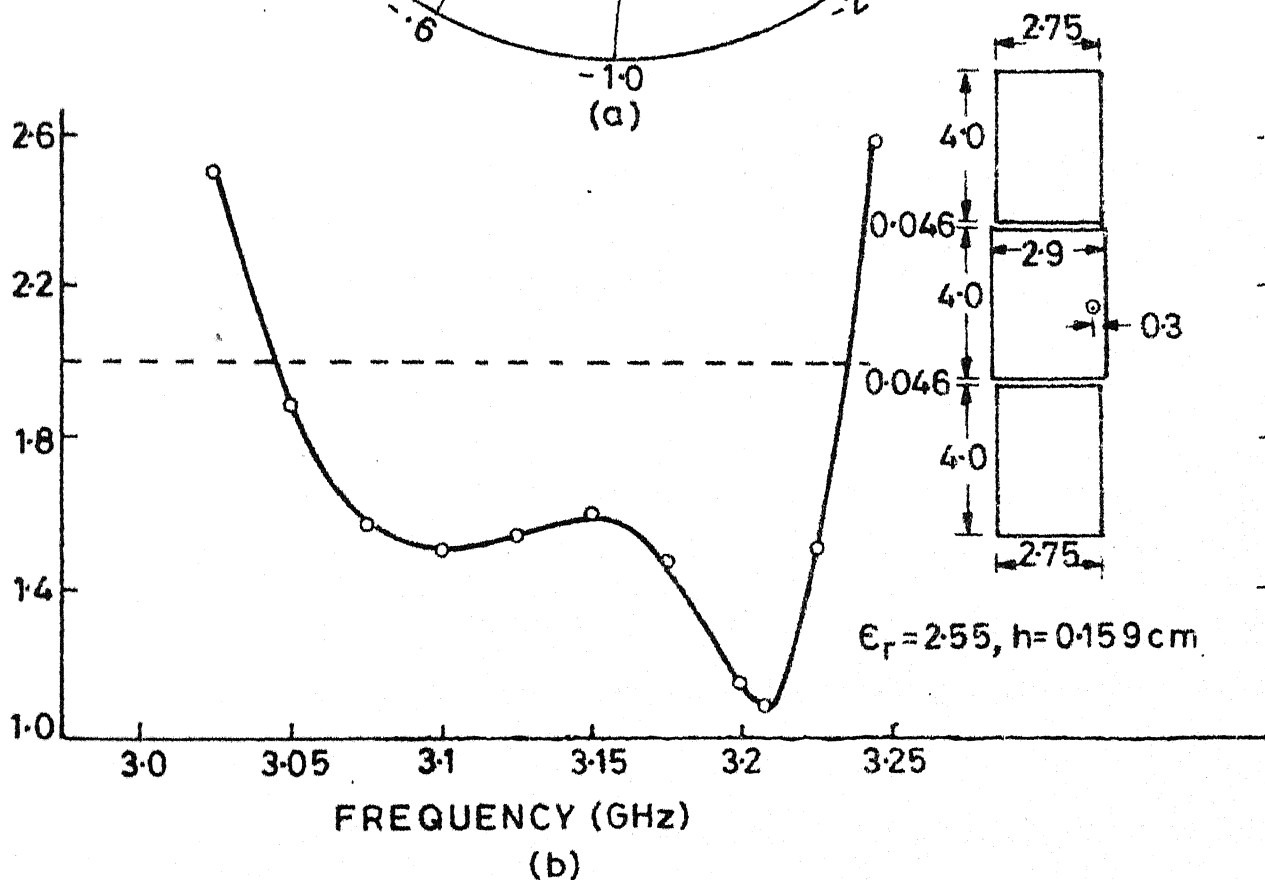
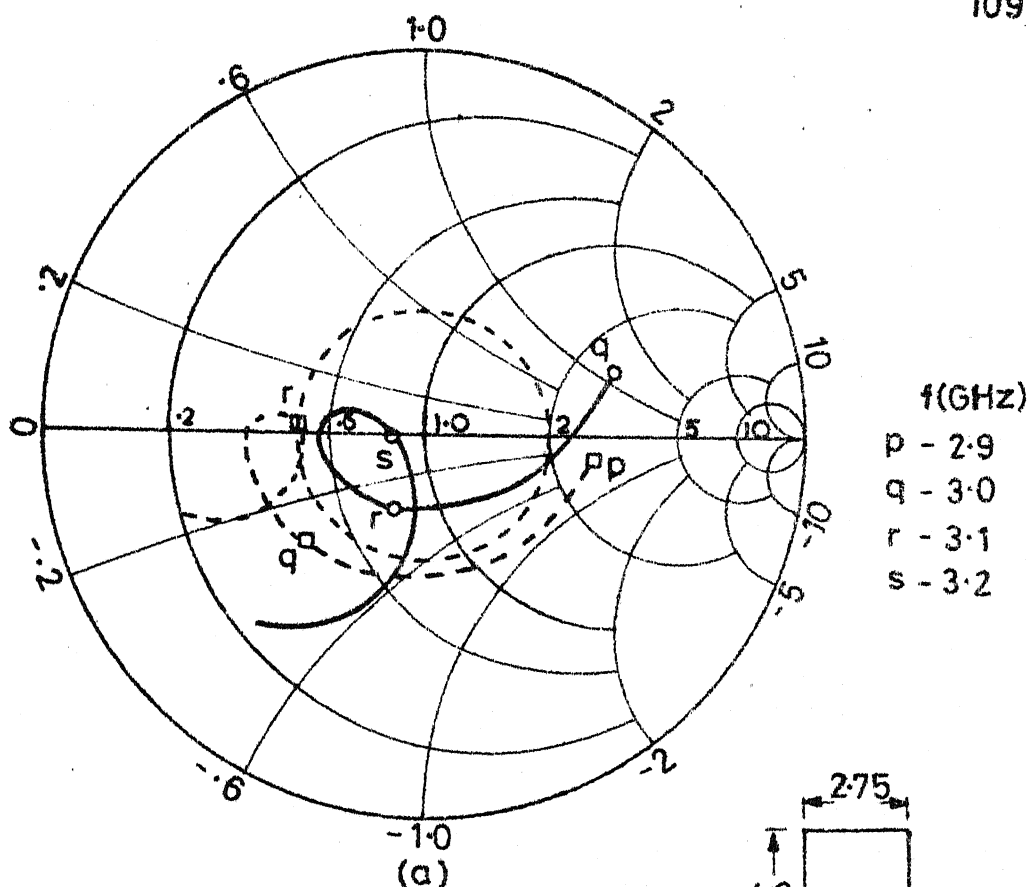


Fig.4.7(a) NEGCOMA with identical parasitic elements and its (b) theoretical (---) and experimental (—) input



g.4-8(a) Theoretical (---) and experimental (—) input impedance loci and (b) experimental VSWR variation with frequency of NEGCOMA

as discussed in Section 4.1.2. Experimental and theoretical input impedance loci and variation of VSWR with frequency are shown in Fig. 4.8. As expected, the loop in the experimental impedance locus is inside the $VSWR = 2$ circle. The bandwidth of the antenna is 192 MHz (6.1 percent, centre frequency $f_0 = 3.14$ GHz), which is three times the bandwidth of RPA. The loop in the theoretical input impedance locus is not inside the $VSWR = 2$ circle, so it is not justified if the experimental bandwidth is compared with this bandwidth, which is too low. The bandwidth is calculated for different dimensions of the antenna, for which the loop is inside the $VSWR = 2$ circle. The size of the loop should be equal to that of the loop obtained experimentally. This will give some rough idea of the theoretical bandwidth. The bandwidth is obtained from the impedance locus shown in Fig. 4.7(b) and it is 160 MHz, which is 32 MHz less than the experimental bandwidth.

The bandwidth of the antenna can be further increased by increasing the parasitic element length slightly (which will shift the loop towards the right side of the Smith chart), and by reducing the gap width (which will increase the size of the loop).

4.2 NEGCOMA WITH PARASITIC ELEMENTS OF DIFFERENT LENGTHS

In Section 4.1, NEGCOMA with identical parasitic elements have been discussed. The gap widths between the resonators were

also taken equal. In this case, central rectangular patch was resonant at one frequency and parasitic elements were resonant at a nearby frequency. When the two parasitic elements are of different lengths, their resonant frequencies will be different. So, each parasitic element will form a separate loop in the impedance locus and hence there will be two loops in the impedance locus, while only one loop was present when the parasitic elements were identical. Thus, the NEGCOMA with parasitic elements of different lengths will yield wider bandwidth than the NEGCOMA with identical parasitic elements.

The NEGCOMA with parasitic elements of different lengths l_1 and l_2 is shown in Fig. 4.9(a). The widths of these elements are taken equal to that of the rectangular patch element. The gap-widths between the parasitic element and rectangular patch need not be equal. Since the antenna structure is not symmetrical with the axis XX, the full structure is analyzed. The NEGCOMA is divided into various segments, namely, three rectangular elements, two gap-circuits and eight radiation conductance networks. In all, 97 ports are considered on the antenna edges with c ($= d$) ports equal to 48 ports and a single p-port as shown in Fig. 4.9(b). The input impedance and radiation fields of the antenna are calculated from (2.5) and (2.11) respectively.

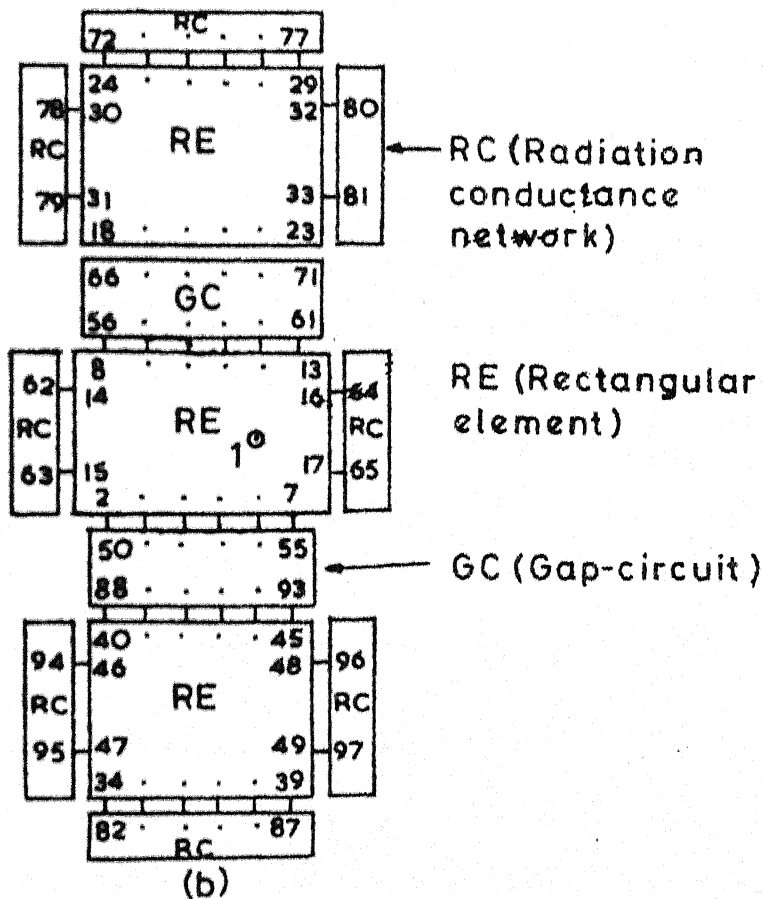
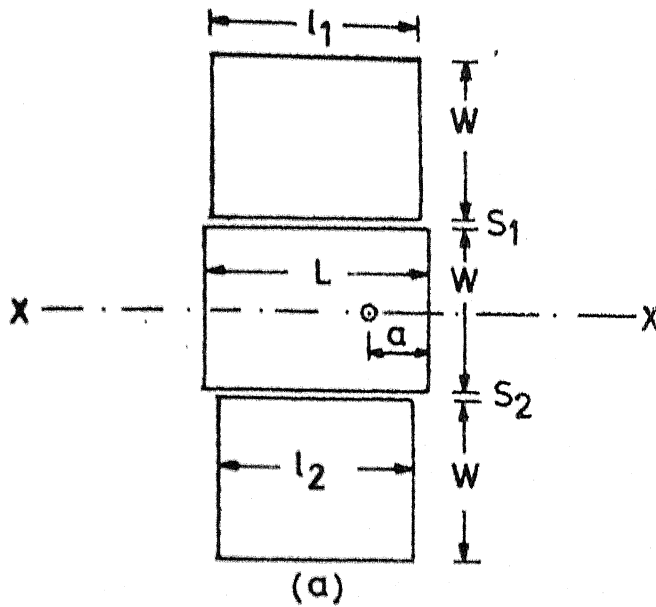


Fig. 4-9 (a) NEGCOMA with parasitic elements of different lengths and (b) its segmented network

4.2.1 Effect of antenna parameters

In this section, the effects of changing the lengths l_1 and l_2 of the parasitic elements, and the gap widths S_1 and S_2 between the central patch and the parasitic elements on the input impedance locus of the antenna are studied. These studies are useful for optimizing the antenna for wider bandwidth.

Gap-widths between the resonators

For three combinations of gap-widths S_1 and S_2 ($= (0.05, 0.05), (0.05, 0.02),$ and $(0.02, 0.02)$ cm) with $l_1 = 2.85$ cm, $l_2 = 2.7$ cm and $a = 0.14$ cm, input impedance loci of the antenna are plotted in Fig. 4.10. From the theoretical results it is observed that two loops are present in the impedance loci. Loops 1 and 2 correspond to the parasitic elements with larger and smaller lengths (l_1 and l_2) respectively. Size of the loops 1 and 2 are mainly affected by changes in S_1 and S_2 respectively. With decrease in the gap-width S_1 (or S_2), size of the loop 1 (or loop 2) increases, and also the two loops come closer.

Lengths of the parasitic elements

Impedance loci for three combinations of the parasitic elements lengths l_1 and l_2 ($= (2.85, 2.7), (2.85, 2.75),$ and $(2.9, 2.75)$ cm) with $S_1 = S_2 = 0.05$ cm and $a = 0.14$ cm, are plotted in Fig. 4.11. From these plots, the following points

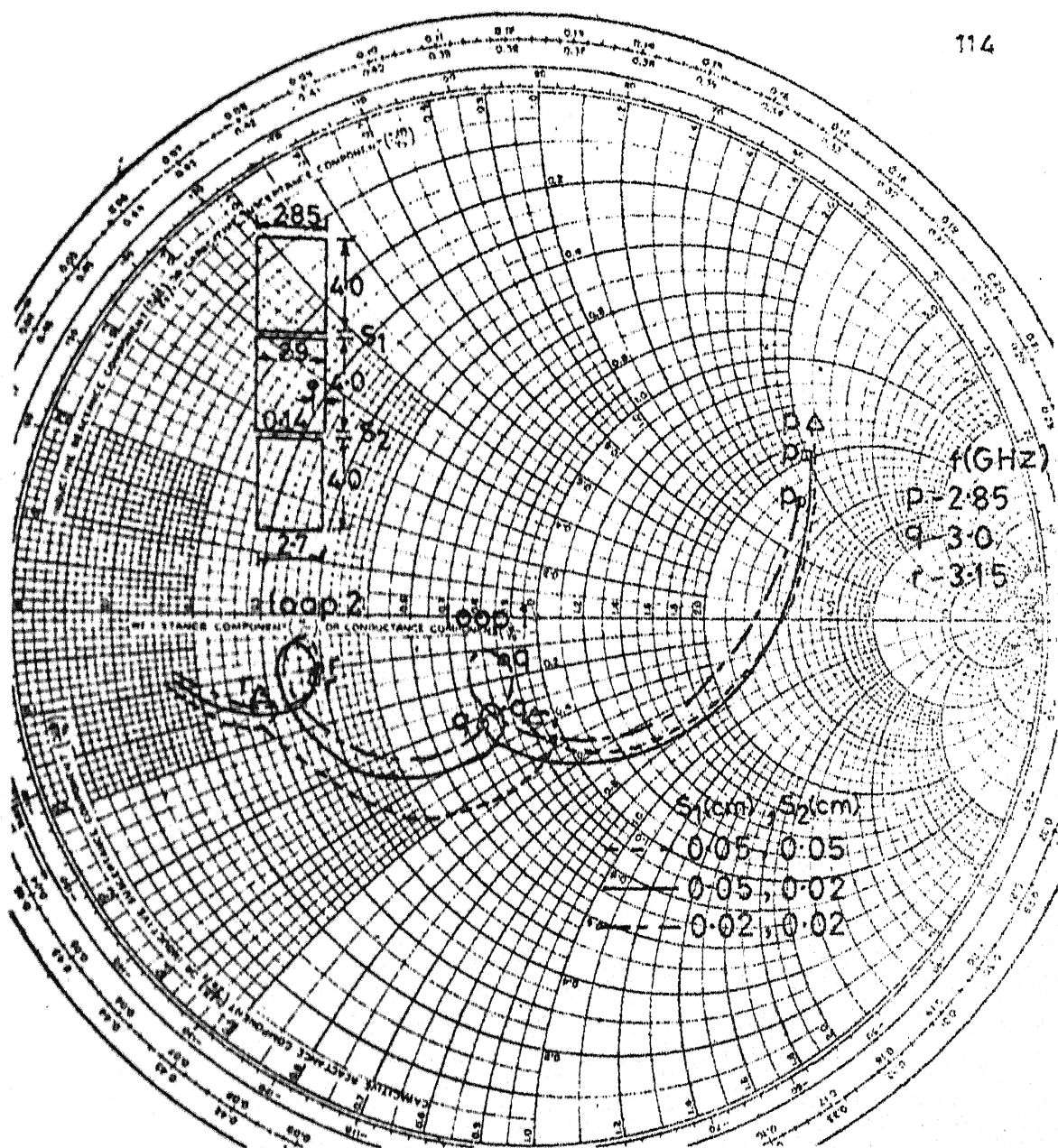


Fig.4-10 Input impedance loci of NEGCOMA for three different combinations of gap widths S_1 and S_2

may be noted. The loops 1 and 2 present in the impedance loci, correspond to the larger and smaller lengths (l_1 and l_2) of the parasitic elements respectively. As the difference between the two lengths l_1 and l_2 decreases, the two loops come nearer and nearer, and finally merge into a single loop when l_1 is equal to l_2 . When both the lengths l_1 and l_2 are increased from (2.85, 2.7) cm to (2.9, 2.75) cm, while keeping the difference between them constant, both the loops in the impedance locus shift upward and towards the right side of the Smith chart.

4.2.2 Experiment

Experiment has been performed on NEGCOMA with dimensions shown in Fig. 4.12 (inset). The theoretical input impedance locus is plotted in Fig. 4.12(a). There are two loops in the impedance locus, one of them is located inside the $V_{SWR} = 2$ circle and other is lying outside the left side of the circle. The reason for carrying out this experiment with these dimensions is that the experimental impedance locus shifts towards the right side of the Smith chart (as observed in the case of NEGCOMA with identical parasitic elements, and shown in Fig. 4.7), so the two loops will come inside the $V_{SWR} = 2$ circle. Photograph of the fabricated NEGCOMA is shown in Fig. 4.13. The experimental input impedance locus and V_{SWR} variation with frequency are plotted in Figs. 4.12(a) and (b) respectively. As expected, the experimental impedance locus is shifted towards the right side of

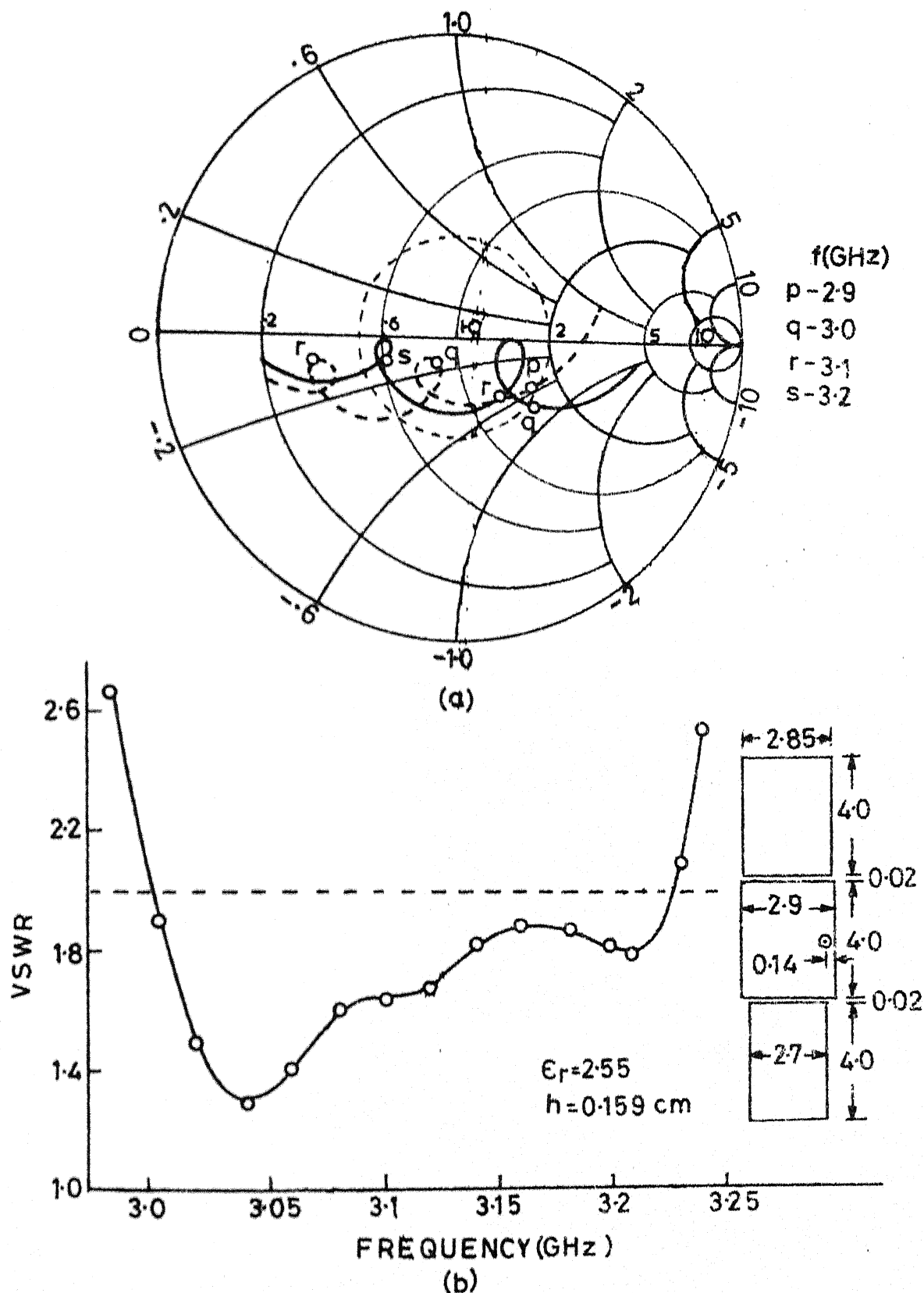


Fig.4.12(a) Theoretical (---) and experimental (—) input impedance loci and (b) experimental VSWR variation with frequency of NEGCOMA

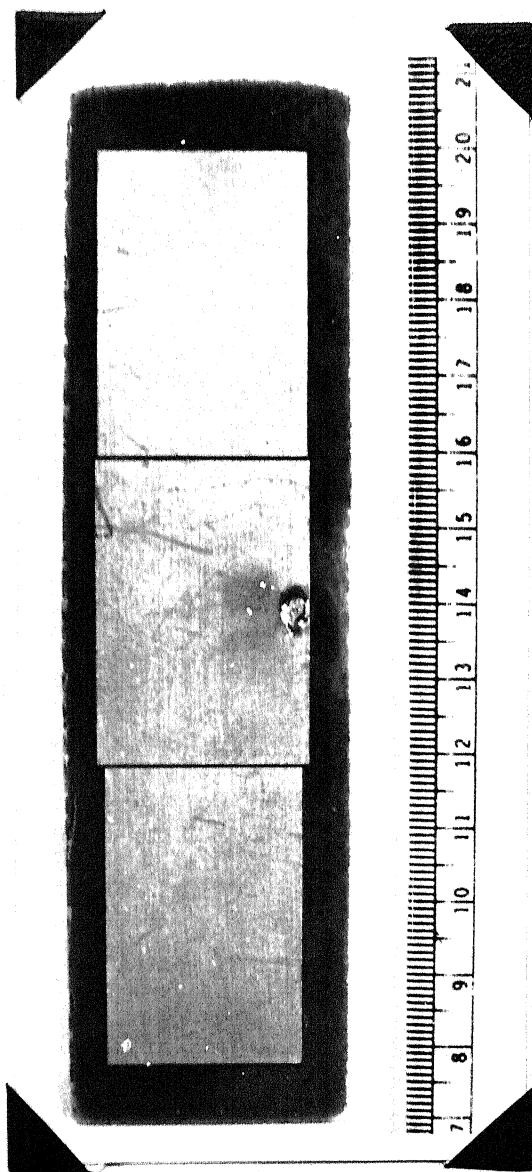


Fig. 4.13 Photograph of the NEGCOMA fabricated on the substrate having thickness $h = 0.159$ cm and $\epsilon_r = 2.55$

the Smith chart and the two loops have come inside the $VSWR = 2$ circle. The measured bandwidth of the antenna is 225 MHz (7.2 percent, $f_0 = 3.115$ GHz), which is 3.6 times the bandwidth of RPA.

The bandwidth of the antenna can be further increased by increasing the coupling between the resonators (i.e. by decreasing the gap-width from 0.02 cm to as small as possible).

4.3 NEGCOMA ON THICKER SUBSTRATE

It has been observed in Section 2.4 that when the thickness of the substrate is doubled, the bandwidth of RPA also becomes nearly double for the same patch dimensions. The effect of doubling the substrate thickness on the bandwidth of NEGCOMA is studied in this section.

It has been observed in the previous section that the gap-width between the resonators was very small to provide sufficient coupling between the resonators for yielding broader bandwidth, and the bandwidth could have been further increased by increasing the coupling between the resonators. With increase in the substrate thickness, the coupling between the resonators is increased for any specified value of gap-width. So, an improvement of more than twice in the bandwidth of NEGCOMA is expected, when the substrate thickness is doubled.

4.3.1 Identical parasitic elements

NEGCOMA with identical parasitic elements is analyzed to obtain wider bandwidth for substrate thickness $h = 0.318$ cm. Input impedance loci for two different lengths ($l_1 = 2.65$ cm and 2.5 cm) of the parasitic elements with $S_1 = 0.08$ cm and $a = 0.15$ cm, are plotted in Fig. 4.14. The theoretical bandwidth of the antenna with parasitic element length $l_1 = 2.65$ cm is 230 MHz (7.77 percent, $f_0 = 2.96$ GHz). However, experiment has been performed on NEGCOMA with parasitic element length $l_1 = 2.5$ cm, for which loop in the impedance locus is located outside the left side of the VSWR = 2 circle on the Smith chart. The reason for doing experiment on these dimensions is that experimentally the loop in the impedance locus shifts towards the right side of the Smith chart, so it may come inside the VSWR = 2 circle. The experimental input impedance locus and variation of VSWR with frequency are plotted in Fig. 4.15. For comparison, theoretical input impedance locus is also plotted in this figure. As predicted, the loop in the experimental input impedance locus is inside the VSWR = 2 circle. The measured bandwidth is 313 MHz (9.65 percent, $f_0 = 3.245$ GHz), which is 2.6 times the bandwidth of RPA (BW = 121 MHz, $f_0 = 2.94$ GHz, $L = 2.9$ cm, $W = 3.0$ cm, $\epsilon_r = 2.55$ and $h = 0.318$ cm). The bandwidth of the RPA for $W = 3.0$ cm is interpolated from its bandwidths for the widths equal to 4.0 cm and 2.0 cm (BW = 133 MHz and 109 MHz respectively), given in Section 2.4.

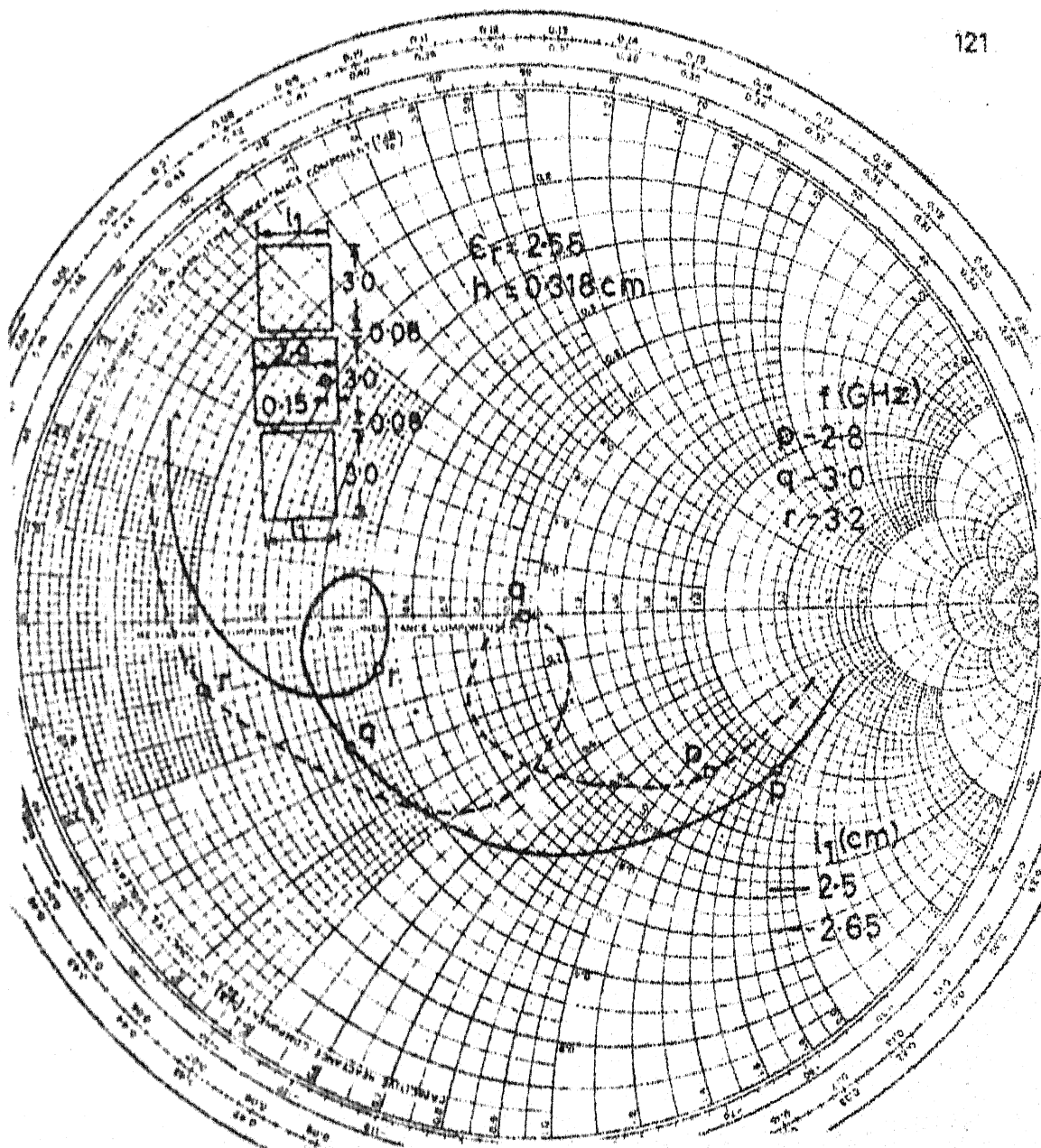


Fig. 4-14 Input impedance loci of NEGCOMA for two values of length l_1 of parasitic element

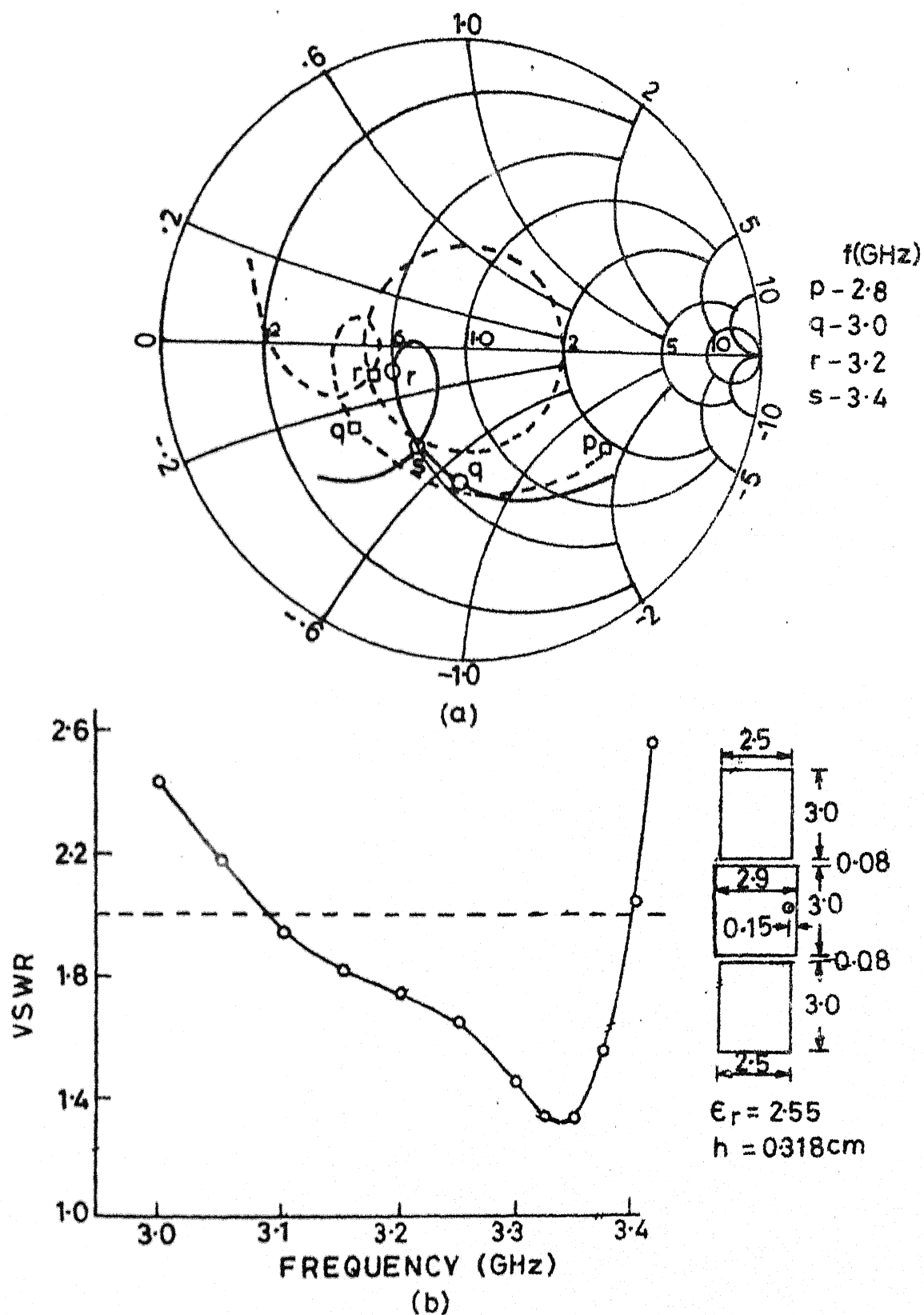


Fig. 4.15 (a) Theoretical (---) and experimental (—) input impedance loci and (b) experimental VSWR variation with frequency of NEGCOMA

4.3.2 Parasitic elements of different lengths

NEGCOMA with parasitic elements of different lengths is analyzed as discussed in Section 4.2. Impedance loci for two different combinations of lengths l_1 and l_2 ($= (2.8, 2.5)$ cm, $(2.9, 2.6)$ cm) are depicted in Fig. 4.16. Impedance locus for $l_1 = 2.9$ cm and $l_2 = 2.6$ cm, gives the theoretical bandwidth of the antenna, which is 430 MHz. Experiment has been performed on NEGCOMA with $l_1 = 2.8$ cm and $l_2 = 2.5$ cm and photograph of the antenna fabricated is shown in Fig. 4.17.

The experimental input impedance locus and variation of VSWR with frequency are plotted in Figs. 4.18(a) and (b) respectively. Theoretical input impedance locus is also plotted in Fig. 4.18(a). It can be noted from these impedance plots that the two loops in the experimental input impedance locus are shifted towards the right side of the Smith chart, and they are inside the VSWR = 2 circle. The measured bandwidth of NEGCOMA is 480 MHz (15.4 percent, $f_0 = 3.11$ GHz), which is nearly four times the bandwidth of RPA.

Voltage distribution and radiation pattern

Radiation pattern of the antenna is calculated from the voltage distribution along the periphery of the antenna by using (2.11). The voltage distribution along the periphery is obtained from (2.6). Normalized values of the real

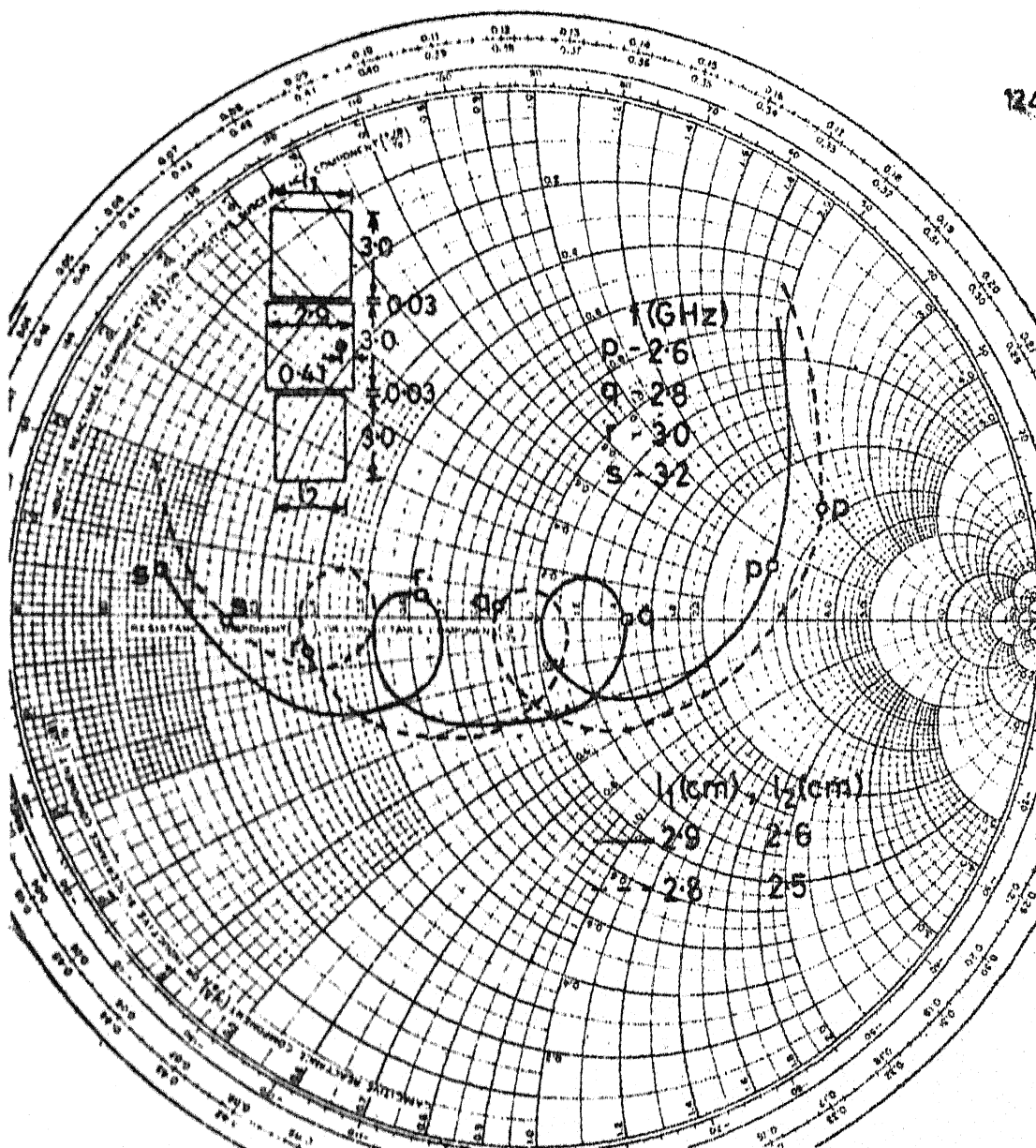


Fig. 4-16 Input impedance loci of NEGCOMA for two combinations of lengths l_1 and l_2 of parasitic elements

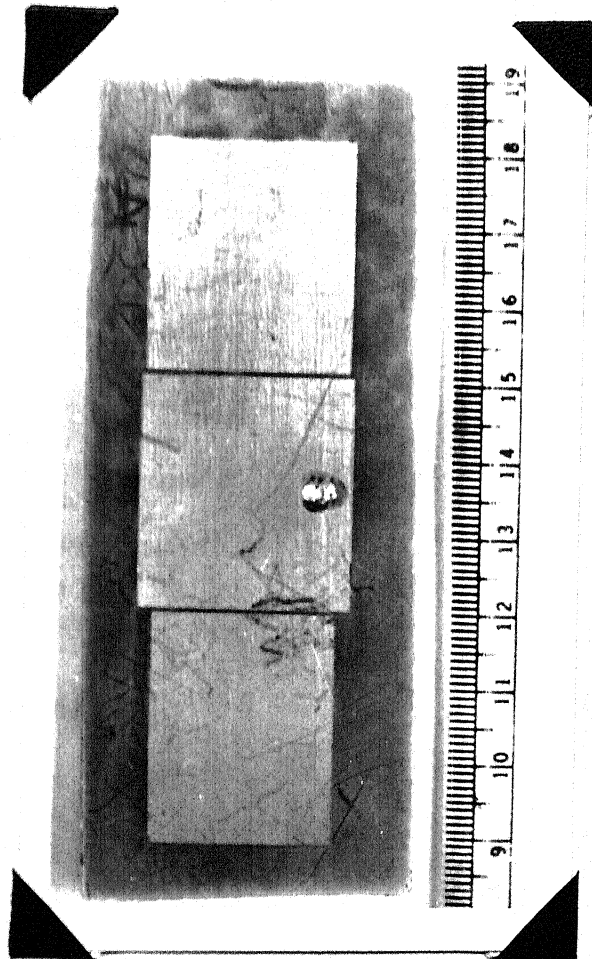


Fig. 4.17 Photograph of the NEGCOMA fabricated on $h = 0.318$ cm thick substrate with $\epsilon_r = 2.55$

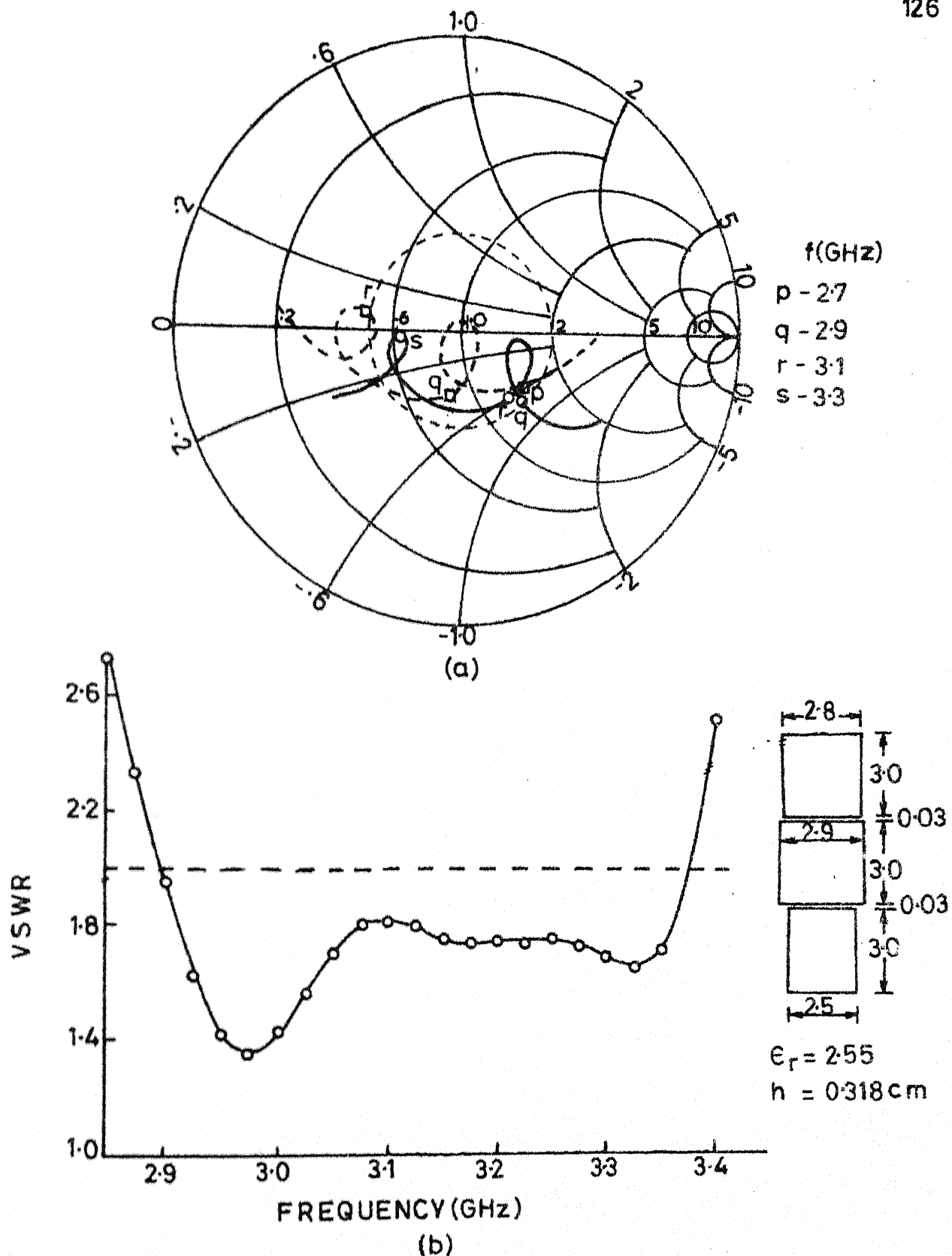


Fig. 4-18 (a) Theoretical (---) and experimental (—) input impedance loci and (b) experimental VSWR variation with frequency of NEGCOMA

and imaginary parts of the voltage along the periphery of the antenna, at three frequencies, are plotted in Figs. 4.19(a) and (b) respectively. From these plots it may be noted that the voltage distribution along the periphery of the antenna varies with frequency. The variation in the values of the voltages along the radiating edges of rectangular elements is much smaller than the variation along the non-radiating edges. As the frequency changes, the voltage across the gap (i.e. the difference of the voltages along the non-radiating coupled edges) also varies.

Since the voltage distribution along the periphery of the antenna changes with frequency, one would expect that radiation pattern will also change with frequency. Radiation pattern in both $\varphi = 0^\circ$ and $\varphi = 90^\circ$ planes is calculated at several frequencies. Only E_θ component is present in $\varphi = 0^\circ$ plane and only E_φ component is present in $\varphi = 90^\circ$ plane as in the cases of RPA and REGCOMA. E_θ component of the radiation field in $\varphi = 0^\circ$ plane is plotted for two frequencies in Fig. 4.20(a). At other frequencies of interest, E_θ varies between these two curves. 3-db beamwidth in $\varphi = 0^\circ$ plane varies between 98° and 110° in the frequency range of 2.8 GHz to 3.2 GHz. E_φ component of the radiation field in $\varphi = 90^\circ$ plane is plotted for four frequencies in Fig. 4.20(b). From these plots, following may be noted. E_φ is not symmetrical with $\theta = 0^\circ$ axis. With the increase in frequency from 2.8 GHz to 3.2 GHz, the direction of maximum radiation shifts from

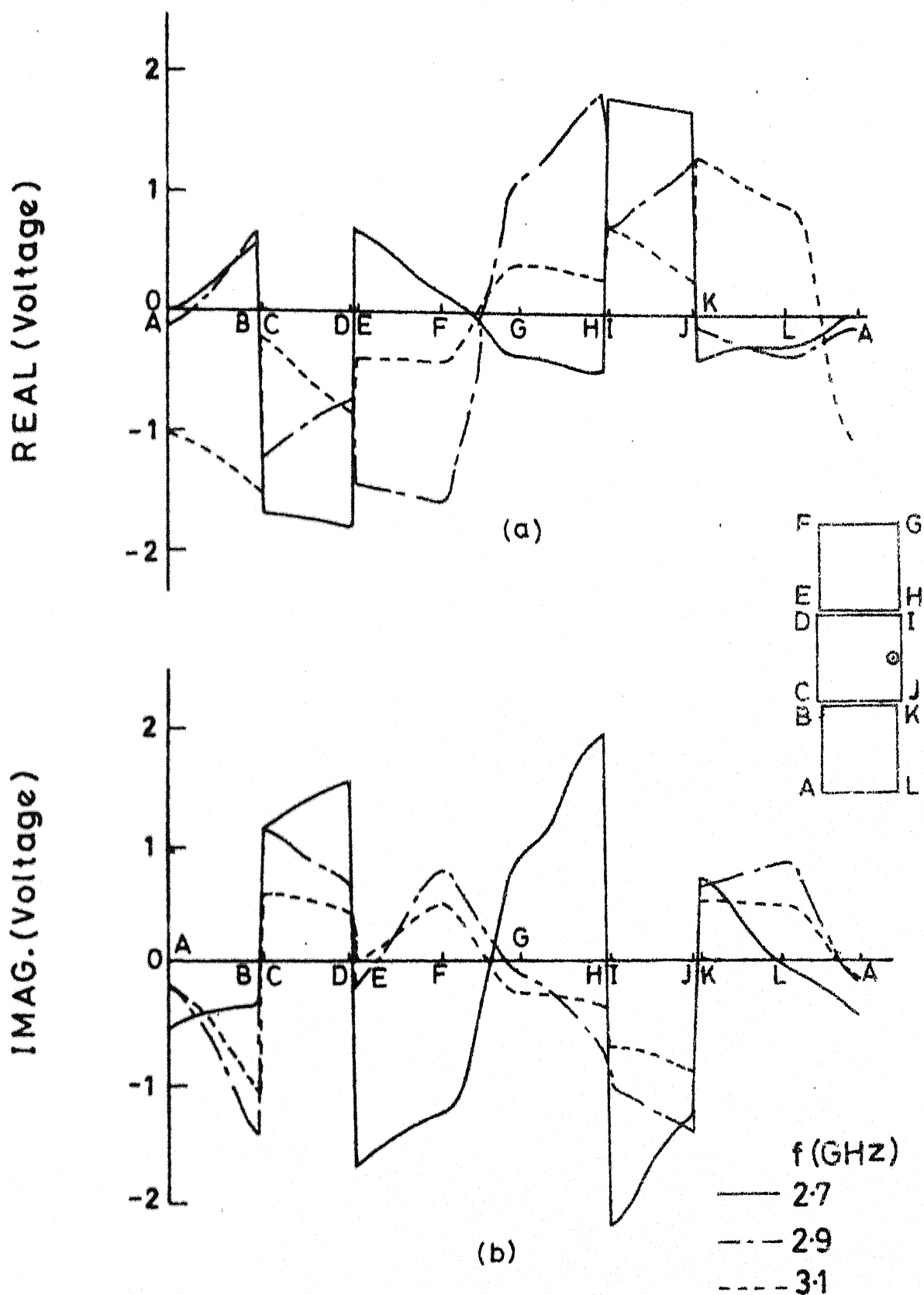


Fig.4.19 Real and imaginary parts of the voltage distribution along the periphery of the NEGCOMA at different frequencies

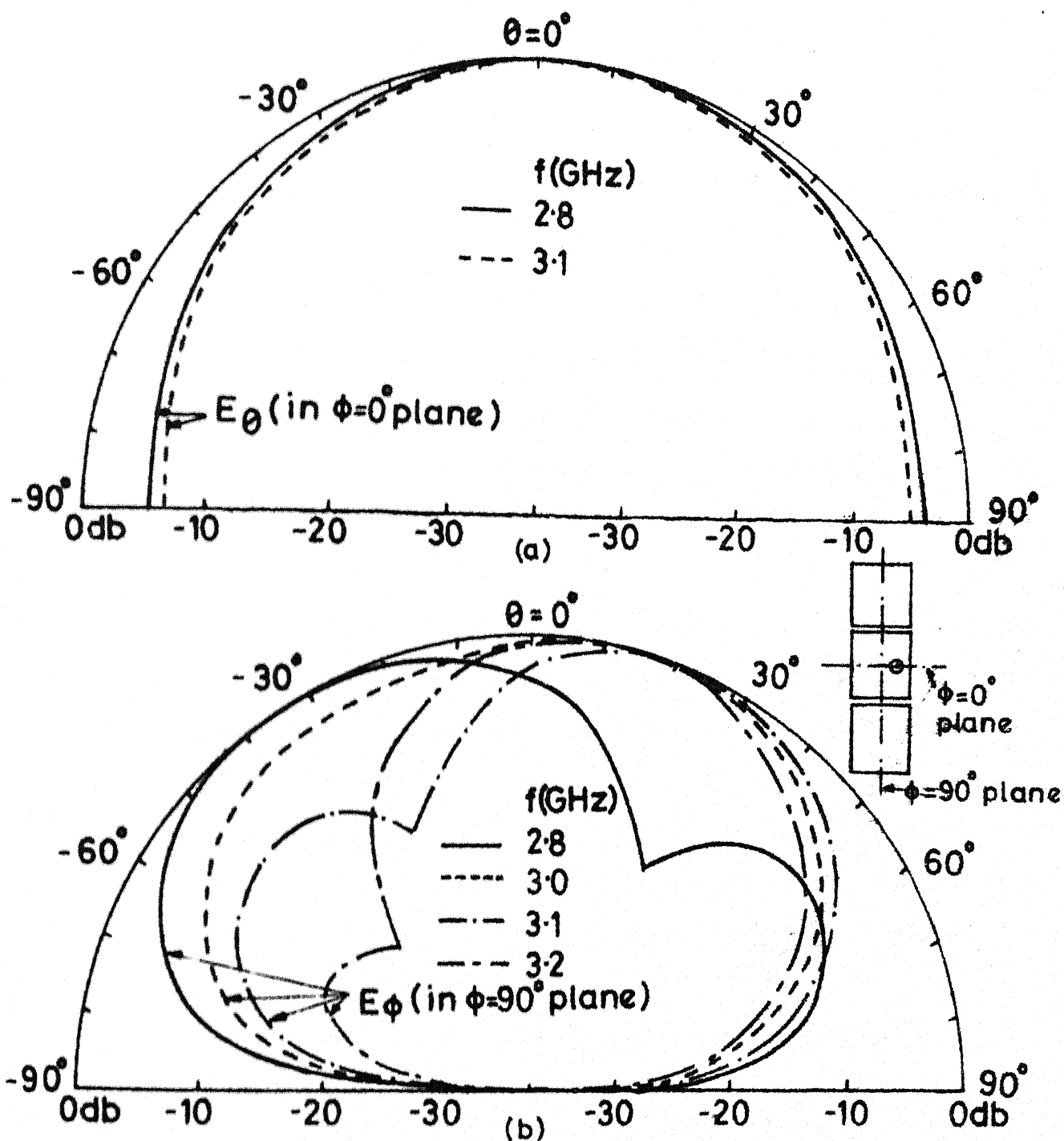


Fig. 4.20 Theoretical values of radiation fields of NEGCOMA shown in Fig. 4.17

$\theta = -30^\circ$ to $\theta = 20^\circ$. A minimum in E_φ occurs in the positive θ direction at the lower frequencies, and in the negative θ direction at the higher frequencies. 3-db beamwidth in $\varphi = 90^\circ$ plane varies between 47° and 81° in the frequency range of 2.8 to 3.2 GHz.

Radiation pattern is measured in both $\varphi = 0^\circ$ and $\varphi = 90^\circ$ planes at the various frequencies covering the entire bandwidth of the antenna. Only E_θ component is present in $\varphi = 0^\circ$ plane, and only E_φ component is present in $\varphi = 90^\circ$ plane as predicted theoretically. E_θ component in $\varphi = 0^\circ$ plane is plotted for the two extreme frequencies ($f = 2.95$ GHz and 3.325 GHz) in Fig. 4.21(a). At intermediate frequencies, E_θ remains between these two curves. 3-db beamwidth is measured as 75° at $f = 2.95$ GHz and 73° at $f = 3.325$ GHz. E_φ component of the radiation field in $\varphi = 90^\circ$ plane is plotted at four different frequencies in Fig. 4.21(b). The variation of E_φ is in accordance with the theoretical values depicted in Fig. 4.20. A minimum is present in E_φ at the various frequencies. 3-db beamwidth in $\varphi = 90^\circ$ plane varies between 38° to 63° in the frequency range of 2.95 GHz to 3.325 GHz. Experimental values of the 3-db beamwidth in the two planes ($\varphi = 0^\circ$ and 90° planes) are less than that of the theoretical values.

So, it has been observed that the bandwidth of the RPA can be increased by using NEGCOMA configuration, but its

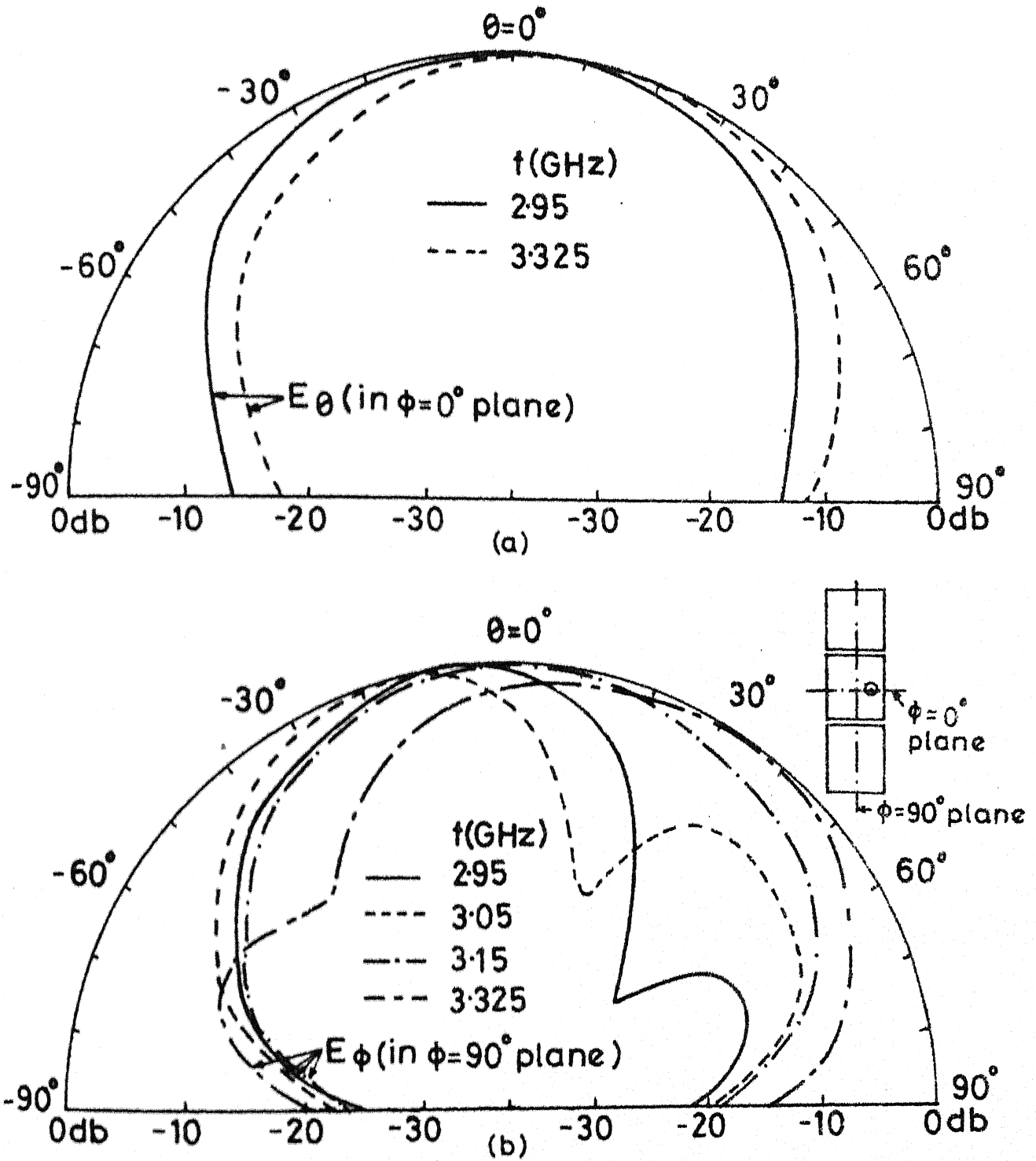


Fig.4-21 Experimental values of radiation fields of NEGCOMA shown in Fig. 4-17

radiation characteristics vary with frequency. The bandwidth of the NEGCOMA shown in Fig. 4.18, can be further improved by decreasing the gap-width between the resonators, which will increase the size of the loops present in its impedance locus.

4.4 FOUR EDGES GAP COUPLED MICROSTRIP ANTENNAS (FEGCOMA)

4.4.1 Introduction

In Chapter Three, radiating edges gap coupled microstrip antennas (REGCOMA) have been analyzed to yield wider bandwidth. In that configuration, two resonators were placed adjacent to the radiating edges of the rectangular patch antenna, and the bandwidth obtained was of the order of 510 MHz, While in case of NEGCOMA, discussed in Sections 4.1 to 4.3, two resonators were gap coupled to the non-radiating edges of the rectangular patch element yielding a bandwidth of 480 MHz. If the additional resonators are placed adjacent to all the four edges of rectangular patch element, much wider bandwidth can be obtained as compared to REGCOMA and NEGCOMA.

4.4.2 Analysis

A four edges gap coupled microstrip antenna (FEGCOMA) with four parasitic elements of different lengths, is shown in Fig. 4.22. FEGCOMA is also analyzed by using Green's function approach with segmentation method. If the two

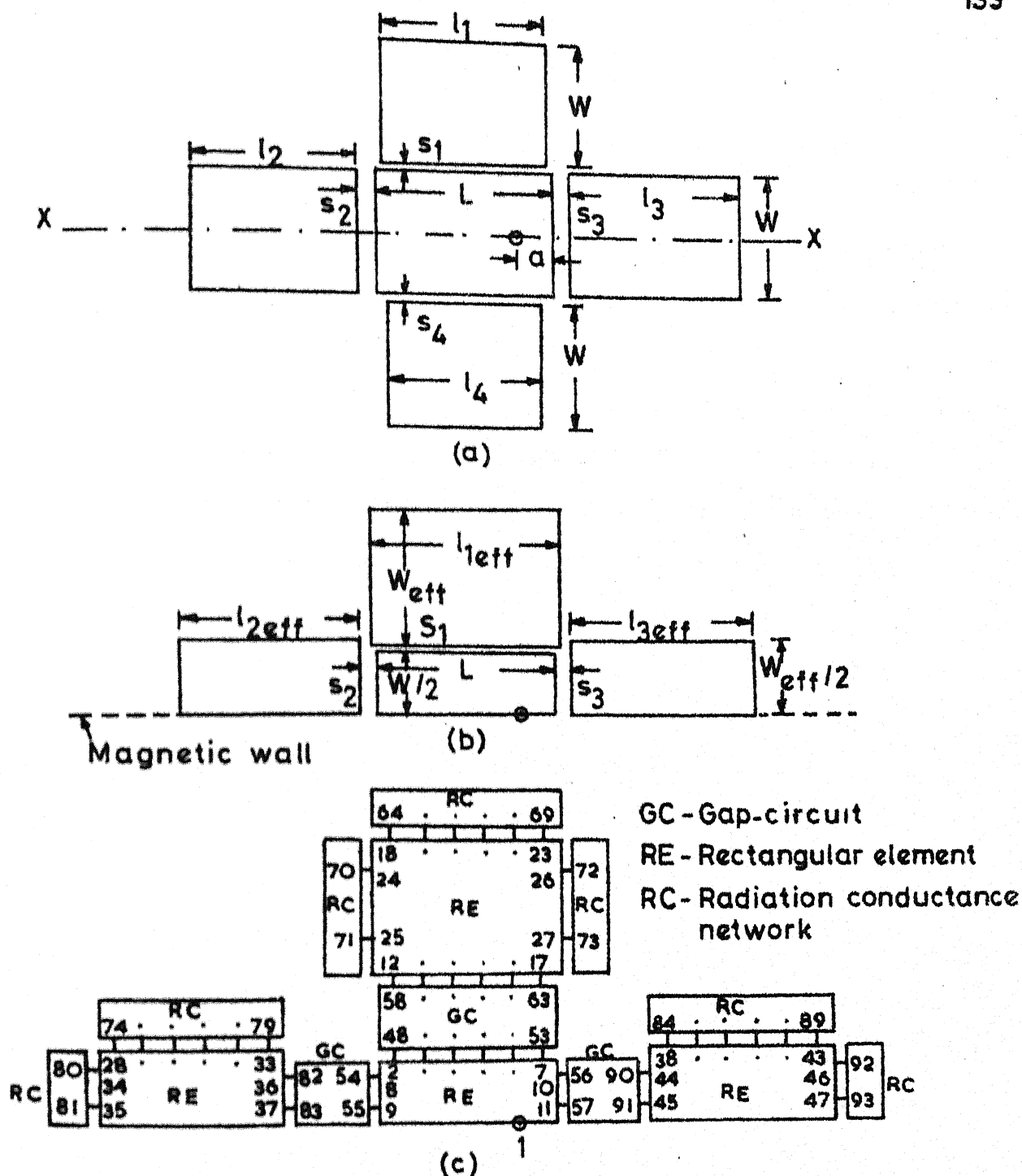


Fig. 4-22 (a) Four edges gap coupled microstrip antenna (FEGCOMA), (b) its even mode half section (for $l_1 = l_4$ and $s_1 = s_4$) and (c) segmented network

parasitic elements along the non-radiating edges are identical (i.e. $l_1 = l_4$), and gap-widths along non-radiating edges are equal (i.e. $S_1 = S_4$), then the antenna structure and feeding arrangement will be symmetrical with the axis XX. So, even-mode half section of FEGCOMA, after taking into account the open-end fringing fields as shown in Fig. 4.22(b), is sufficient to analyze. To apply segmentation method, even-mode half section of FEGCOMA is divided into various segments as illustrated in Fig. 4.22(c). These segments are: four rectangular elements, three gap-circuits and seven radiation conductance networks. The antenna edges are divided into 97 ports with connected c and d ports being 46 each and a single external p-port. Input impedance of the antenna is obtained from the impedance matrices of the individual segments by using (2.5).

A bandwidth of the order of 590 MHz (19.6 percent, $f_0 = 3.0$ GHz) is obtained for FEGCOMA with dimensions shown in Fig. 4.23 (inset). Input impedance locus of the antenna is plotted in Fig. 4.23. The value of the coefficients of gap capacitances are taken as: $C_{ci} = 1.0$ for all the gap-widths and $C_{cg} = 0.37$ for S_1 , and 0.5 for S_2 and S_3 . From Fig. 4.23, the following points may be observed. There are three loops present in the impedance locus. Loop 1 corresponds to the length l_1 of the parasitic elements placed along the non-radiating edges, and loops 2 and 3 correspond to the lengths l_2 and l_3 of the parasitic elements coupled to the

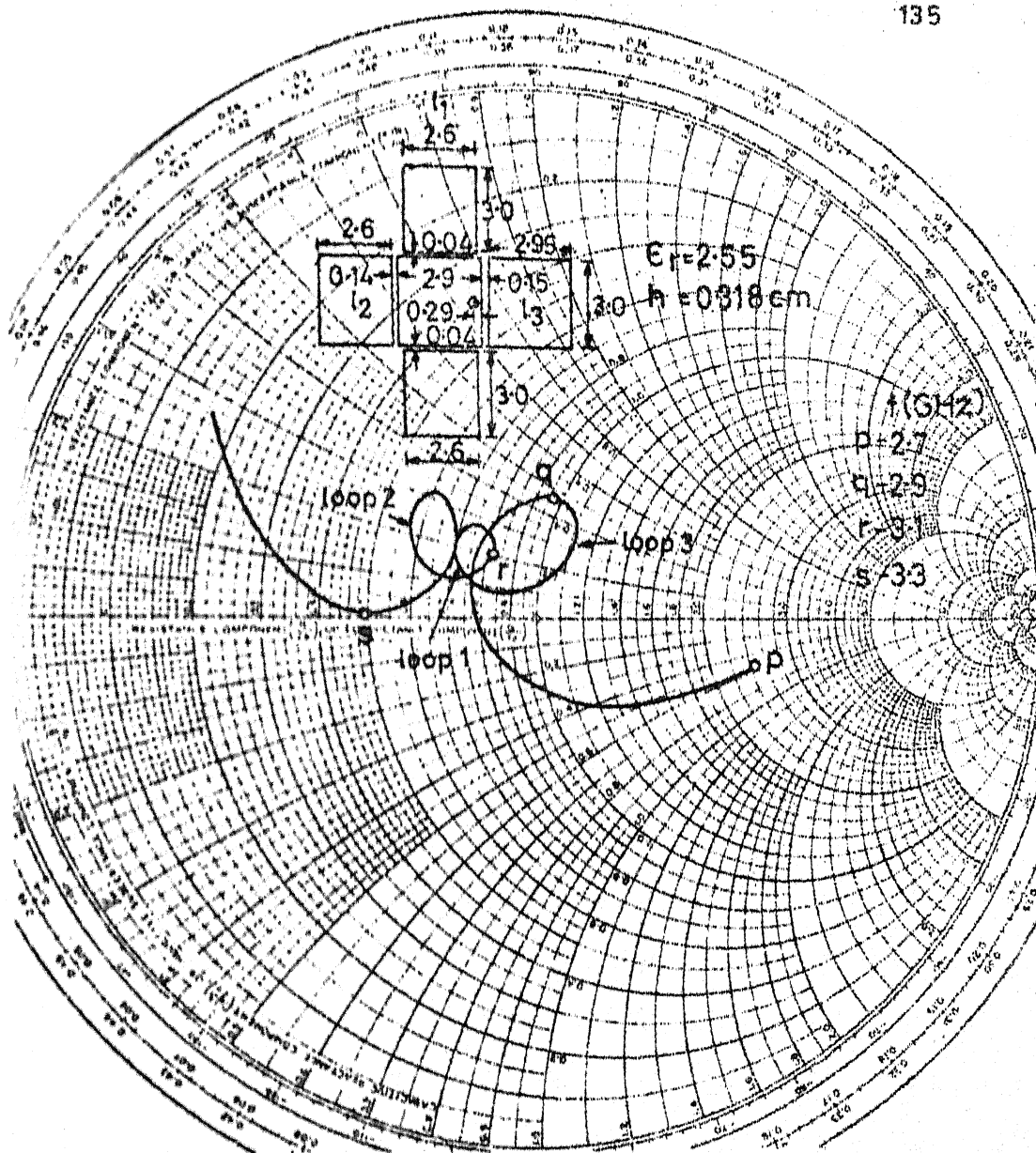


Fig.423 Theoretical input impedance locus of FEGCOMA

radiating edges of the rectangular patch element. The effects of varying the various parameters (i.e., lengths of the parasitic elements, gap-widths between the central rectangular patch and the parasitic elements, and feed-point location) on the input impedance locus of FEGCOMA are similar to that of the effects of varying the parameters in the cases of REGCOMA and NEGCOMA.

4.4.3 Experiments and optimization

Experiment has been performed on FEGCOMA with dimensions shown in Fig. 4.24(a). These dimensions are the combinations of the optimum dimensions obtained in the cases of REGCOMA and NEGCOMA separately. Experiment has not been performed on the dimensions obtained theoretically, because it has been noted in the cases of REGCOMA and NEGCOMA, that theoretical results do not agree well with the experimental results. Thus, it is more likely that the discrepancies in the two cases may add-up resulting in large deviation between the theoretical and experimental input impedance loci of FEGCOMA.

Experimental input impedance locus of the antenna is plotted in Fig. 4.24(b). From this plot it may be noted that only two loops are present in the impedance locus and one of the loop lies outside the $V_{SWR} = 2$ circle. The bandwidth of the antenna for $V_{SWR} \leq 2.2$ is 600 MHz (20 percent, $f_0 = 3.0$ GHz).

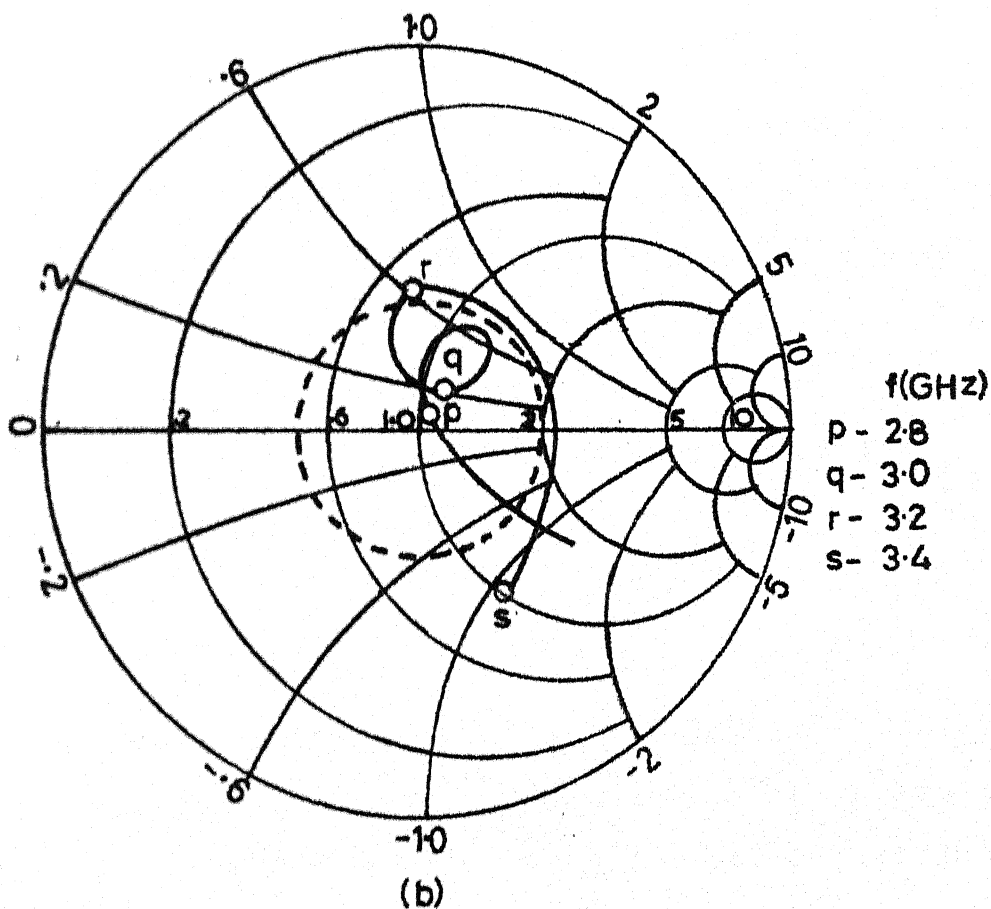
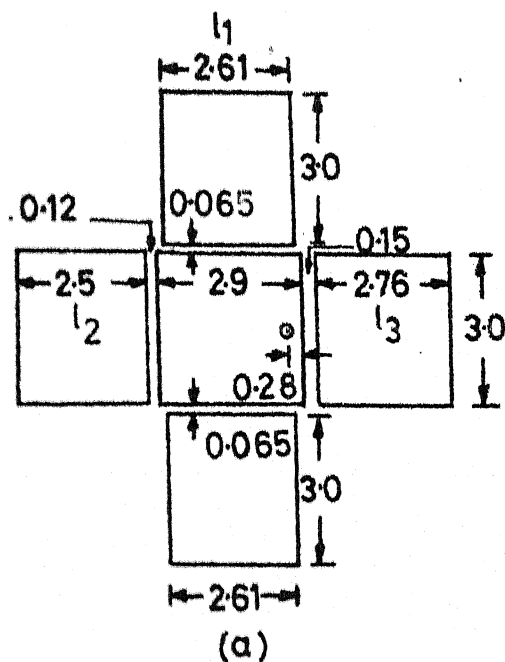
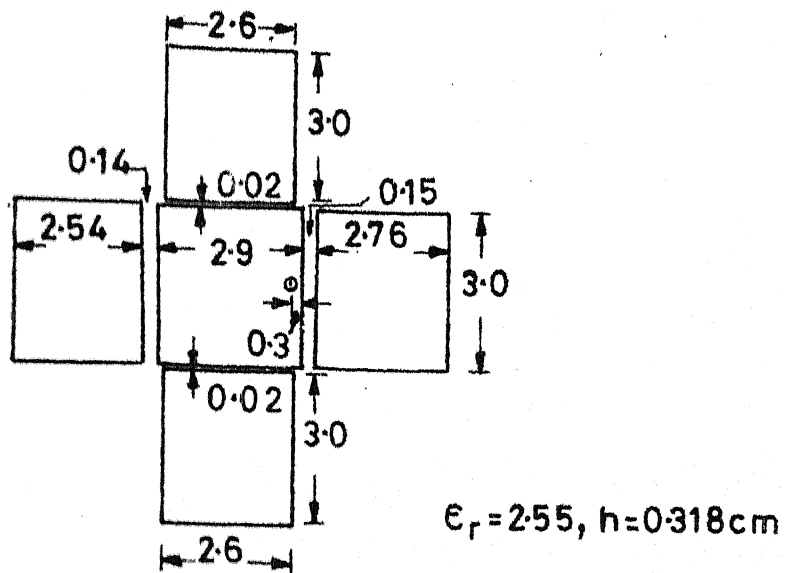


Fig.424(a) FEGCOMA and (b) its experimental input impedance locus

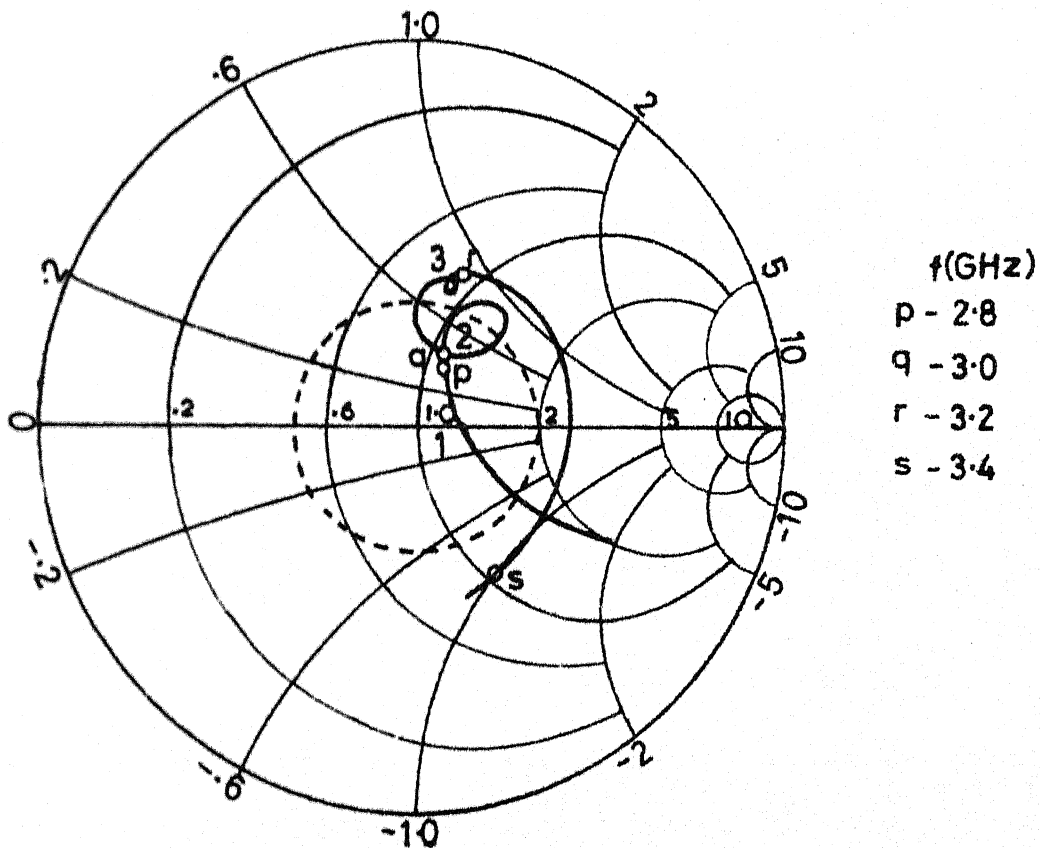
Since the lengths l_1 , l_2 and l_3 of parasitic elements are different, each length will yield a loop in the impedance locus. So, there should be three loops in the impedance locus, but only two loops are present in the impedance locus. This may be due to the reason that the coupling along the non-radiating edges is not sufficient, so the parasitic elements along the non-radiating edges are not getting properly excited. The loop inside the $VSWR = 2$ circle corresponds to the length l_3 , and the other loop is due to the length l_2 with some contribution from length l_1 .

Another experiment has been carried out on FEGCOMA with gap-width S_1 reduced from 0.065 cm to 0.02 cm. Other dimensions are nearly equal to the corresponding dimensions of the previous experiment, as shown in Fig. 4.25(a). The input impedance locus of the antenna is depicted in Fig. 4.25(b). As expected, three loops are present in the impedance locus, but these loops are not inside the $VSWR = 2$ circle. The bandwidth of the antenna for $VSWR \leq 2.5$ is 707 MHz (23.2 percent, $f_0 = 3.04$ GHz).

At a lower frequency (about $f = 2.8$ GHz), the parasitic element of length l_3 ($= 2.76$ cm) is resonant which results in a loop (i.e. loop 1) in the impedance locus. When the frequency is increased to nearly 2.95 GHz, the length l_1 ($= 2.6$ cm) becomes resonant, which yields loop 2 in the



(a)



(b)

Fig.425 (a) FEGCOMA with $S_1 = 0.02 \text{ cm}$ and
(b) its experimental input impedance locus

impedance locus. But before this loop could have been completed, the length l_2 ($= 2.54$ cm) is resonant around $f = 3.14$ GHz, which produces another loop (i.e. loop 3) in the impedance locus.

If the length l_1 is decreased (from 2.6 cm to 2.4 cm), then the length l_2 will be resonant at lower frequency than l_1 . As l_2 is less than 2.6 cm, the second loop in the impedance locus will shift downward and it may come inside the $VSWR = 2$ circle.

In order to bring the three loops in the impedance locus inside the $VSWR = 2$ circle, another experiment has been performed on FEGCOMA, whose photograph is shown in Fig. 4.26 and dimensions are depicted in Fig. 4.27(a). The length l_1 of the parasitic element is reduced from 2.6 cm to 2.4 cm, and length l_2 is decreased from 2.54 cm to 2.49 cm. Input impedance locus and VSWR variation with frequency are plotted in Figs. 4.27(b) and 4.28. As expected, the three loops in the impedance locus are inside the $VSWR = 2$ circle. The bandwidth of the antenna for $VSWR \leq 2$ is 815 MHz (25.8 per cent, $f_0 = 3.16$ GHz), which is 6.7 times the bandwidth of RPA (BW = 121 MHz). The ripples in the VSWR variation with frequency plot remain less than $VSWR = 1.8$. The bandwidth for $VSWR \leq 1.8$ is 790 MHz, which is 7.6 times the bandwidth of corresponding RPA (BW = 104 MHz for $VSWR \leq 1.8$).

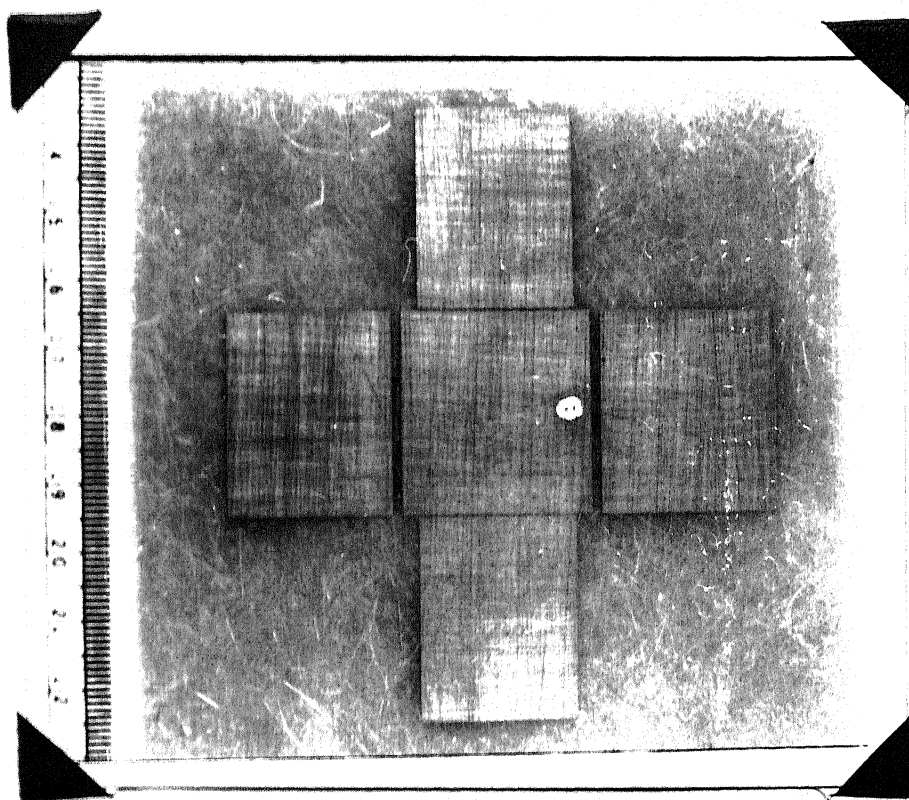
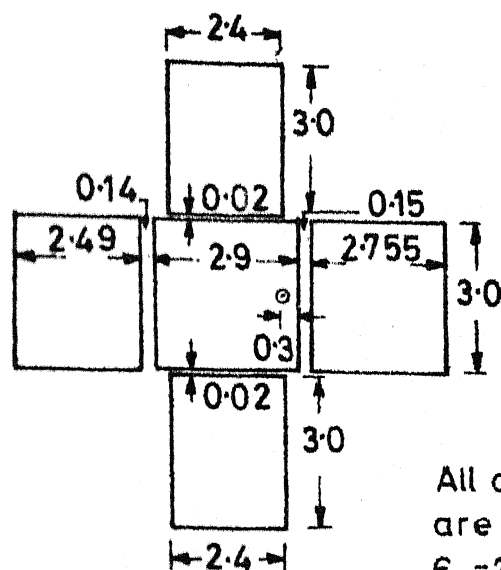


Fig. 4.26 FEGCOMA fabricated on the substrate with $h = 0.318$ cm and $\epsilon_r = 2.55$



All dimensions
are in cm
 $\epsilon_r = 2.55, h = 0.318 \text{ cm}$

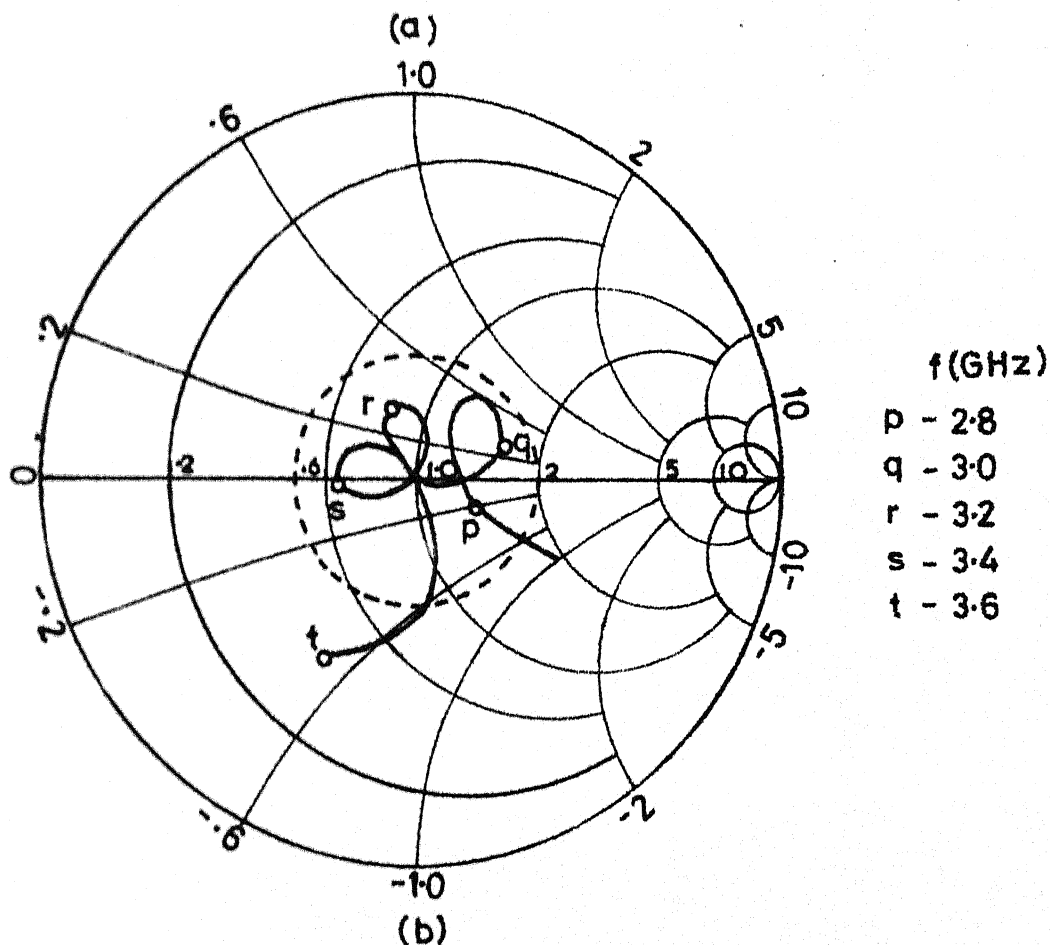


Fig. 4.27(a) FEGCOMA with $l_1 = 2.4 \text{ cm}$ and
(b) its experimental input impedance
locus

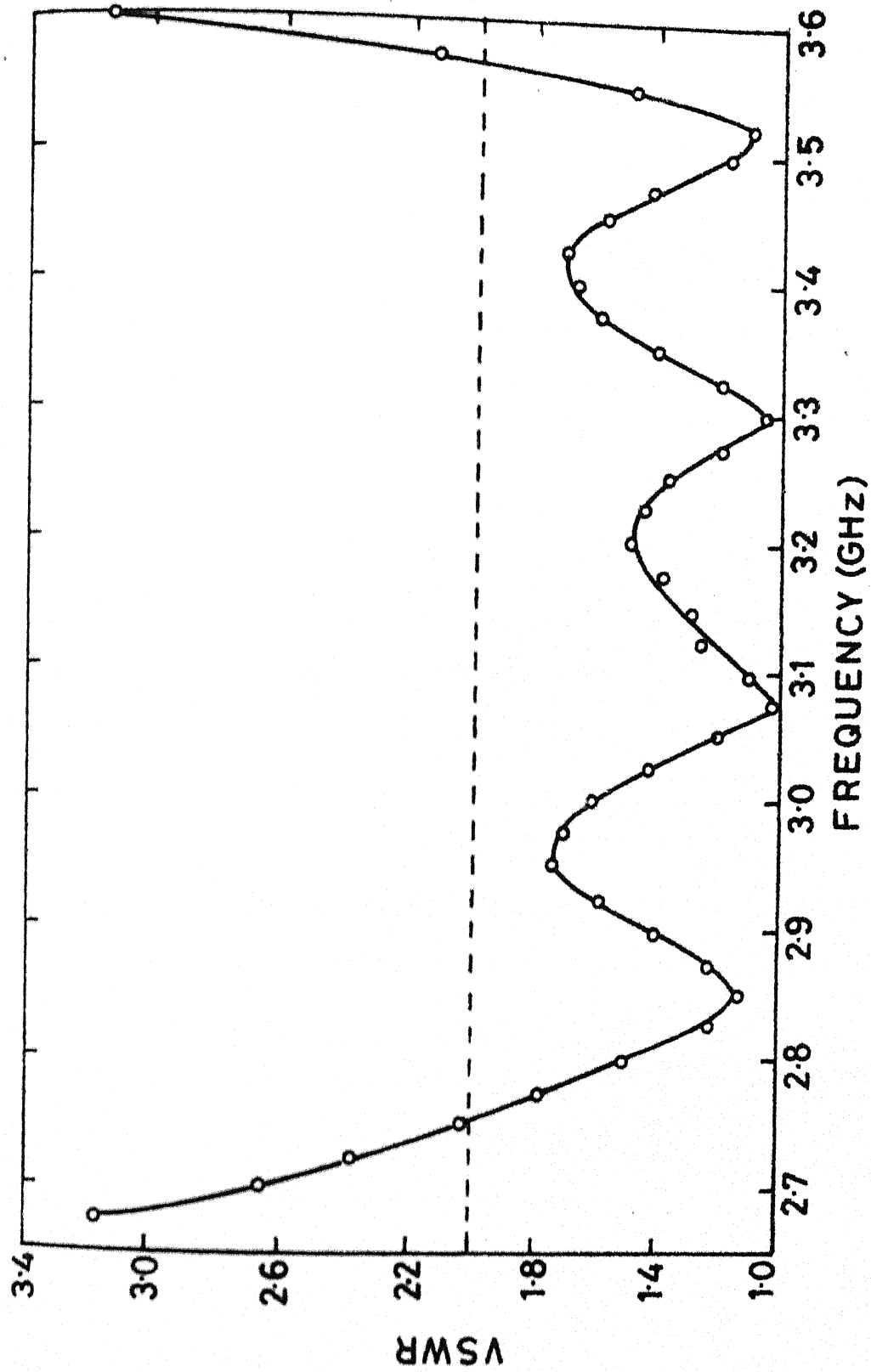


FIG.4.28 EXPERIMENTAL VARIATION OF VSWR WITH FREQUENCY
OF FEGCOMA SHOWN IN FIG. 4.27

Radiation pattern of the antenna is measured in both $\varphi = 0^\circ$ and $\varphi = 90^\circ$ planes at the various frequencies for which VSWR remains less than two. Only E_θ component of the radiation field is present in $\varphi = 0^\circ$ plane, and only E_φ component is present in $\varphi = 90^\circ$ plane as observed in the cases of RPA, REGCOMA and NEGCOMA. E_θ component in $\varphi = 0^\circ$ plane is plotted at four frequencies in Fig. 4.29(a). The 3-db beamwidth in $\varphi = 0^\circ$ plane varies between 50° and 74° in the frequency range of 2.935 GHz to 3.542 GHz. A minimum is present in E_θ , and its level at $f = 2.935$ GHz is 13 db below the corresponding maximum level.

E_φ component of the radiation field in $\varphi = 90^\circ$ plane is plotted at four frequencies in Fig. 4.29(b). The 3-db beamwidth in $\varphi = 90^\circ$ plane decreases from 68° to 33° as the frequency increases from 2.935 GHz to 3.542 GHz. Minima are present in E_φ at higher frequencies. The level of minima at $f = 3.542$ GHz is 11 db below the maximum level.

In the case of REGCOMA, only E_θ component in $\varphi = 0^\circ$ plane changes with frequency, but E_φ component in $\varphi = 90^\circ$ plane remains almost unaltered with frequency. While, in the case of NEGCOMA, there is no appreciable change in E_θ (in $\varphi = 0^\circ$ plane) with frequency but E_φ in $\varphi = 90^\circ$ plane varies with frequency. But in the case of FEGCOMA, both E_θ (in $\varphi = 0^\circ$ plane) and E_φ (in $\varphi = 90^\circ$ plane) change with frequency.

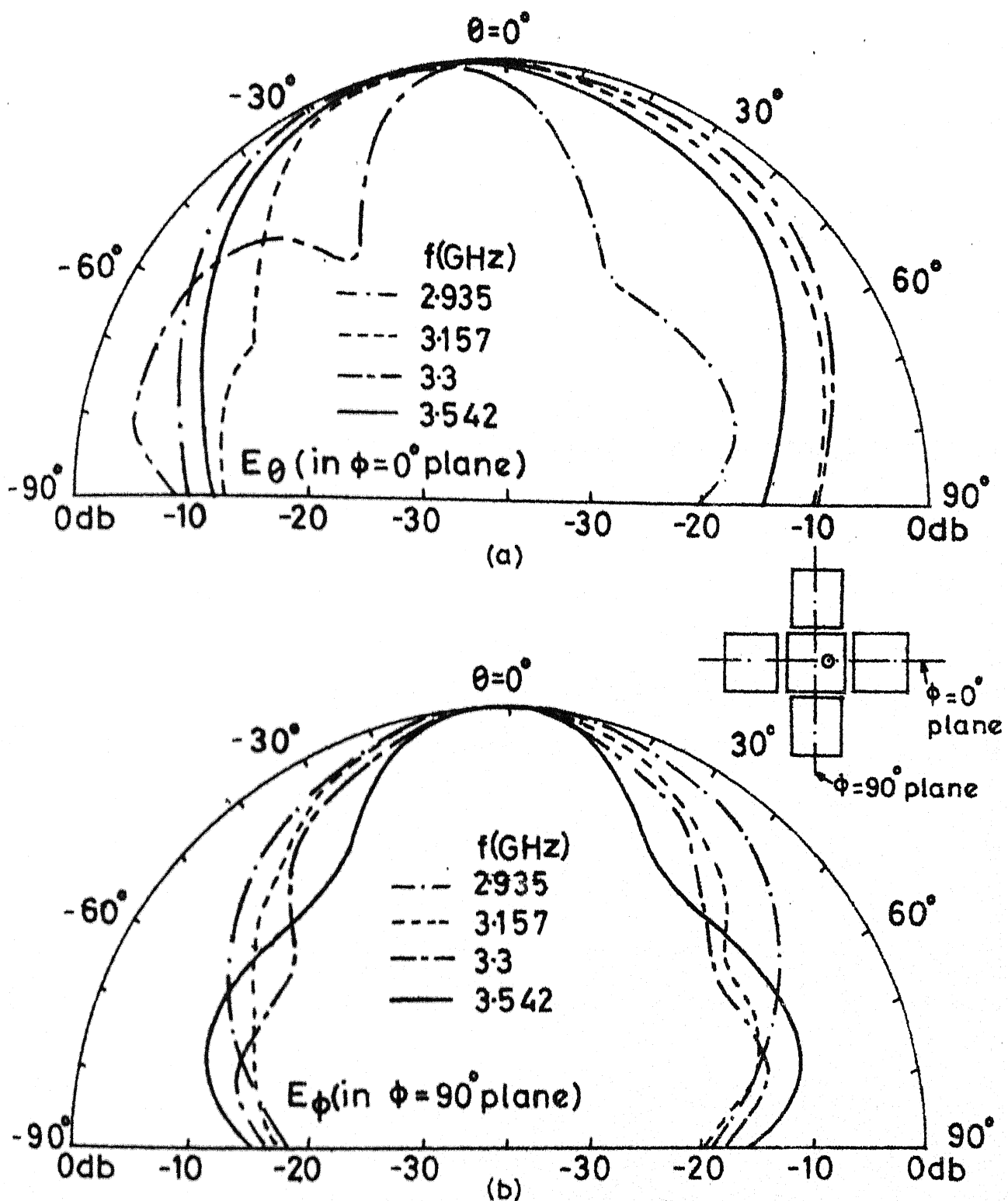


Fig.4.29 Experimental values of radiation fields of FEGCOMA shown in Fig.4.26

The experimental bandwidth of FEGCOMA, shown in Fig. 4.26, can be further improved by increasing the coupling between the resonators, which will increase the size of the loops in the impedance locus. This can be achieved by decreasing the gap-widths between the resonators and by reducing the length l_1 of the parasitic element.

4.5 DISCUSSION

Investigations have been carried out on NEGCOMA on the substrates having two different thicknesses ($h = 0.159$ cm and 0.318 cm) but equal dielectric constants ($\epsilon_r = 2.55$). The lengths of the parasitic elements, gap-width between the resonators, and feed-point location are optimized, and experiments have been performed on both the substrates, which yield broader bandwidth. The bandwidth of the antenna can be further improved by increasing the coupling between the resonators (i.e. by decreasing the gap-width between the resonators). The gap-width cannot be decreased much as it is already very small (nearly 0.02 cm to 0.03 cm). The coupling between the resonators can be increased by connecting the resonators directly through short sections of microstrip line. In the chapter Six, non-radiating edges directly coupled microstrip antennas are discussed, in which resonators are directly coupled instead of coupling through the gaps.

The experimental bandwidth of the FEGCOMA has been found to be 815 MHz (for substrate thickness $h = 0.318$ cm and $\epsilon_r = 2.55$), which is much larger than the bandwidths of the REGCOMA and NEGCOMA (510 MHz and 480 MHz respectively).

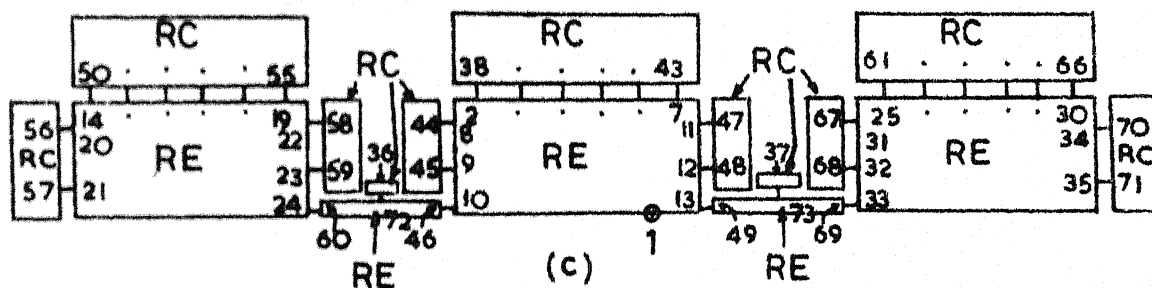
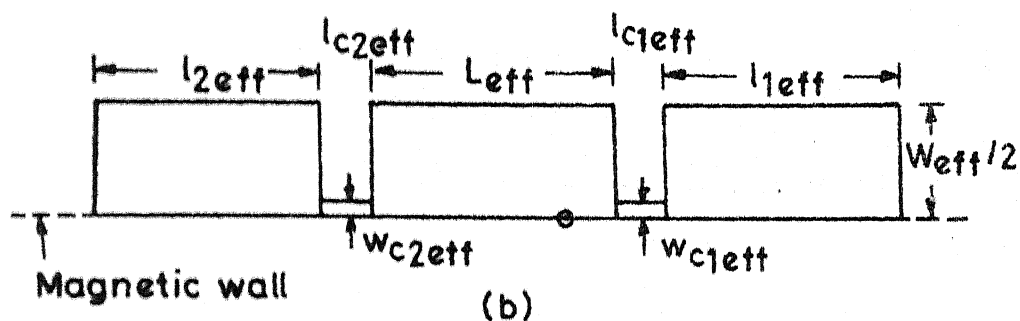
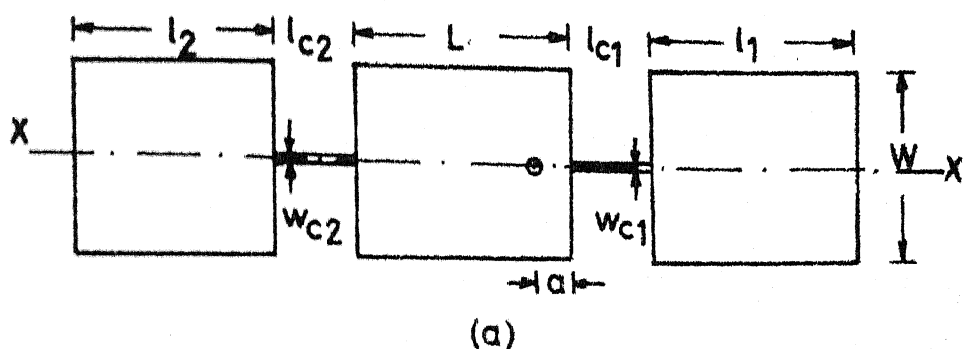
CHAPTER FIVE

RADIATING EDGES DIRECTLY COUPLED MICROSTRIP ANTENNAS (REDCOMA)

In Chapter Three, analysis and design of radiating edges gap coupled microstrip antennas (REGCOMA) have been described. In REGCOMA, two resonators have been gap coupled to the radiating edges of the rectangular patch antenna. This chapter contains the details of the investigations carried out on radiating edges directly coupled microstrip antennas (REDCOMA) using the Green's function approach. The difference between the REGCOMA and REDCOMA is that the mechanism of coupling between the resonators is gap coupling in the former and direct coupling in the latter.

5.1 ANALYSIS

Two parasitic resonators of slightly different lengths (approximately half wavelength) and widths equal to that of the rectangular patch antenna are directly coupled to the radiating edges of the rectangular patch element through short sections of microstripline as shown in Fig. 5.1(a). The lengths of these connecting strips are taken long enough (greater than twice the substrate thickness) to minimize gap coupling between the resonators. The location of the connecting strips along the radiating edges of the resonators does not change the antenna characteristics because the field is uniform along these edges. These strips are located at the



RC (Radiation conductance network)

RE (Rectangular element)

Fig. 5-1(a) Radiating edges directly coupled microstrip antenna (REDCOMA), (b) even-mode half section, and (c) segmented network

mid-point of the widths of the resonators such that the antenna structure is symmetrical with respect to axis XX. Even-mode half section of the REDCOMA with fringing fields at open-ends taken into account, is shown in Fig. 5.1(b).

To apply segmentation method for analysis, even-mode half section of REDCOMA is divided into simpler segments (rectangular elements and radiation conductance networks) as illustrated in Fig. 5.1(c). Edges of the antenna are divided into 73 ports, i.e. 36c- and 36d -ports and a single p-port corresponding to the feed-point location. Z-matrix for the multiport antenna structure is evaluated from (2.5) and the voltage distribution at the various ports is obtained from (2.6). Radiation fields are calculated from the voltage distribution by using (2.11).

5.2 EFFECT OF ANTENNA PARAMETERS ON PERFORMANCE

For any given patch dimensions ($L = 3.0$ cm and $W = 2.0$ cm), substrate specifications ($\epsilon_r = 2.55$ and $h = 0.318$ cm), and for the widths of the parasitic elements equal to the width of the central rectangular patch, the parameters which govern the input impedance characteristics of REDCOMA are : lengths of the parasitic elements, length and width of the connecting strips (the two connecting strips are considered identical i.e. $l_{c1} = l_{c2} = l_c$ and $w_{c1} = w_{c2} = w_c$) and location of the feed-point. Study of the effects of these parameters on the performance of REDCOMA helps in optimizing the bandwidth of the antenna.

5.2.1 Lengths of the parasitic elements

Input impedance loci of REDCOMA for two different values of length l_1 (2.85 cm and 2.75 cm) of parasitic element are shown in Fig. 5.2. The other dimensions of the antenna are : length $l_2 = 2.55$ cm, length and width of the connecting strips equal to 1.1 cm and 0.05 cm respectively, and feed-point location given by $a = 0.4$ cm. From this plot, the following points may be noted. Two loops are present in the impedance locus because of interaction between the rectangular patch and the two parasitic elements of different lengths. Loops 1 and 2 correspond to the lengths l_1 and l_2 of parasitic elements respectively. With decrease in length l_1 from 2.85 cm to 2.75 cm (i.e. the difference between the lengths l_1 and l_2 is decreased), the loop 1 in the impedance locus shifts downward and towards the left side of the Smith chart and loop 2 shifts upward and towards the right side of the Smith chart. Also, the size of the loops decreases and loop 2 comes inside the loop 1. If the two lengths l_1 and l_2 are made equal, the two loops in the impedance locus will merge into a single loop, as observed in the case of REGCOMA.

Impedance loci of REDCOMA for two different values of length l_2 (2.55 cm and 2.65 cm) are plotted in Fig. 5.3. Other dimensions of REDCOMA are depicted in Fig. 5.3(inset). From the impedance locus plot it may be observed that when the length l_2 is increased from 2.55 cm to 2.65 cm (i.e. the

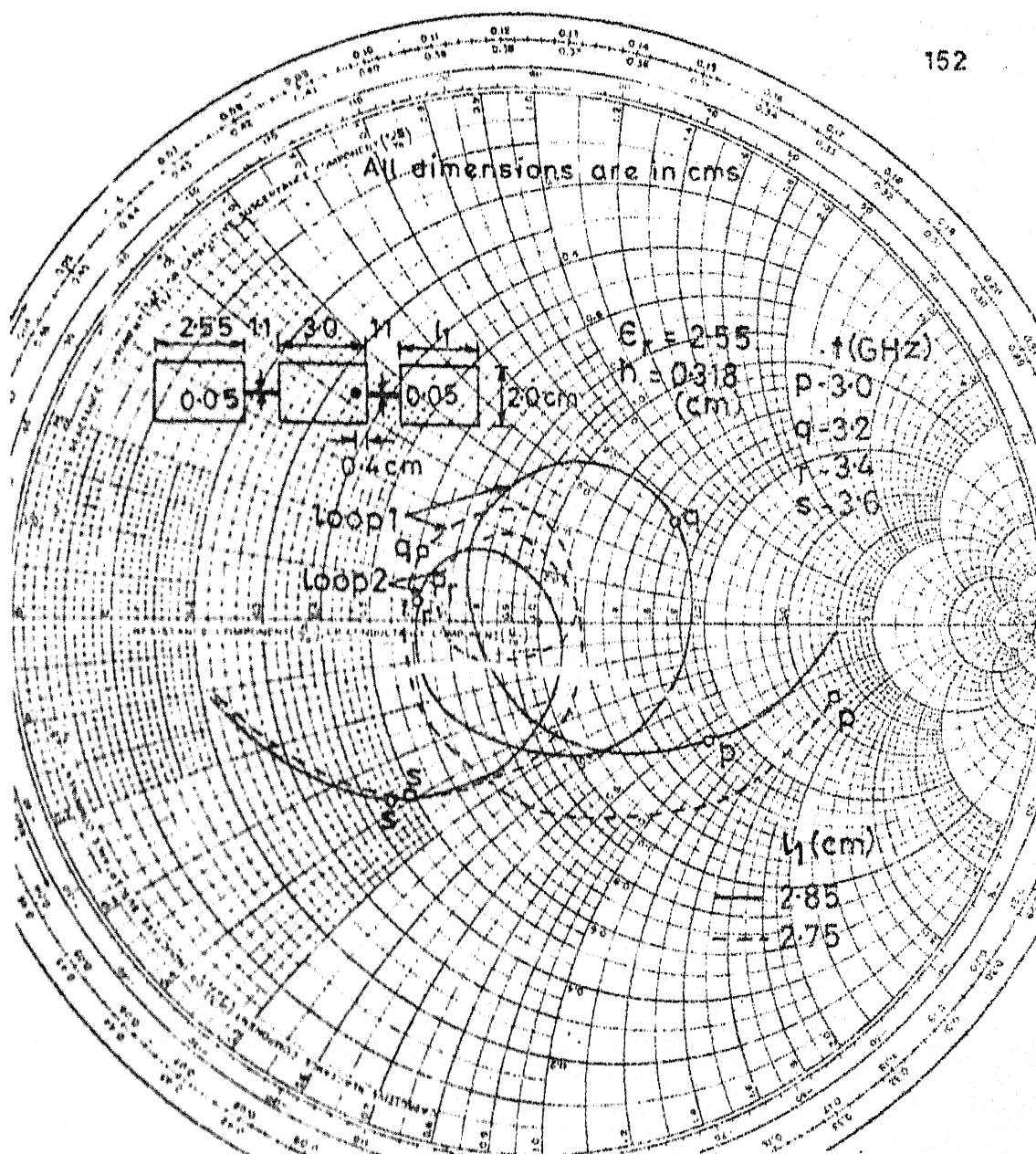


Fig.5.2 Input impedance loci of REDCOMA for two values of length l_1 of parasitic element

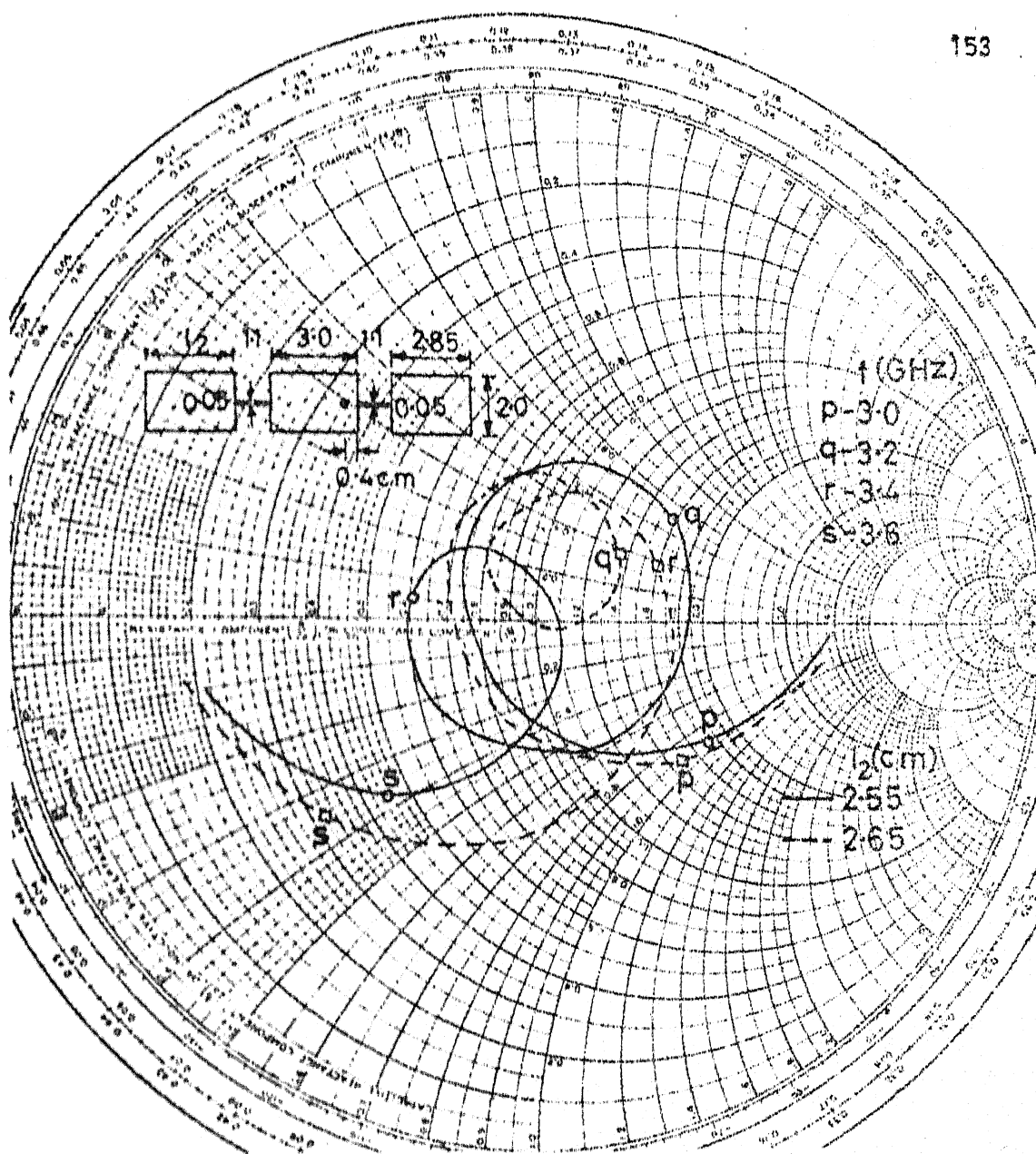


Fig.5.3 Input impedance loci of REDCOMA for two values of length l_2 of parasitic element

difference between the two lengths is decreased), loop 2 in the impedance locus shifts upward and towards the right side of the Smith chart and loop 1 shifts slightly downward. Also, the size of the loop 2 decreases slightly and it comes inside the loop 1.

5.2.2 Length and width of the connecting strips

Impedance loci of REDCOMA for two different values of length l_c (1.1 cm and 0.9 cm) of connecting strips with other dimensions shown in Fig. 5.4(inset), are plotted in Fig. 5.4, and for two different values of width w_c (0.05 cm and 0.15 cm), these are plotted in Fig. 5.5. From these plots, following may be noted. When the length l_c is decreased from 1.1 cm to 0.9 cm (or the width w_c is increased from 0.05 cm to 0.15 cm), the loops in the impedance locus shift upward and also their size is increased. This is due to the fact that with decrease in length l_c (or increase in width w_c), the coupling between the resonators is increased.

5.2.3 Feed-point location

For two different values of feed-point location 'a' (0.4 cm and 0.6 cm), input impedance loci of REDCOMA are plotted in Fig. 5.6. With the increase in the feed-point location from 0.4 cm to 0.6 cm, the impedance locus shifts upward and towards the left side of the Smith chart. However, there is no significant change in the shape of the impedance locus.

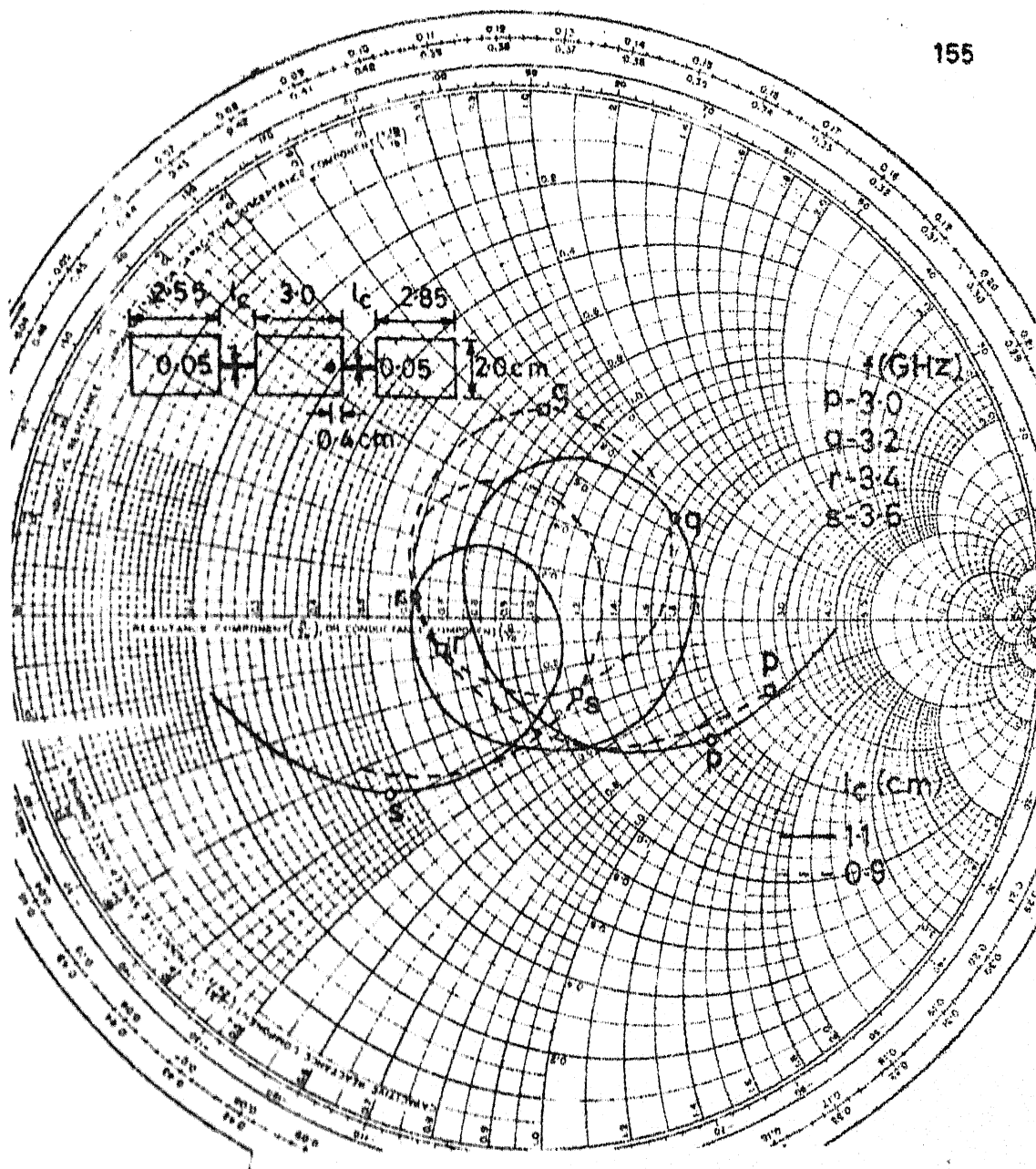


Fig.5.4 Input impedance loci of REDCOMA for different values of length l_c of connecting strips

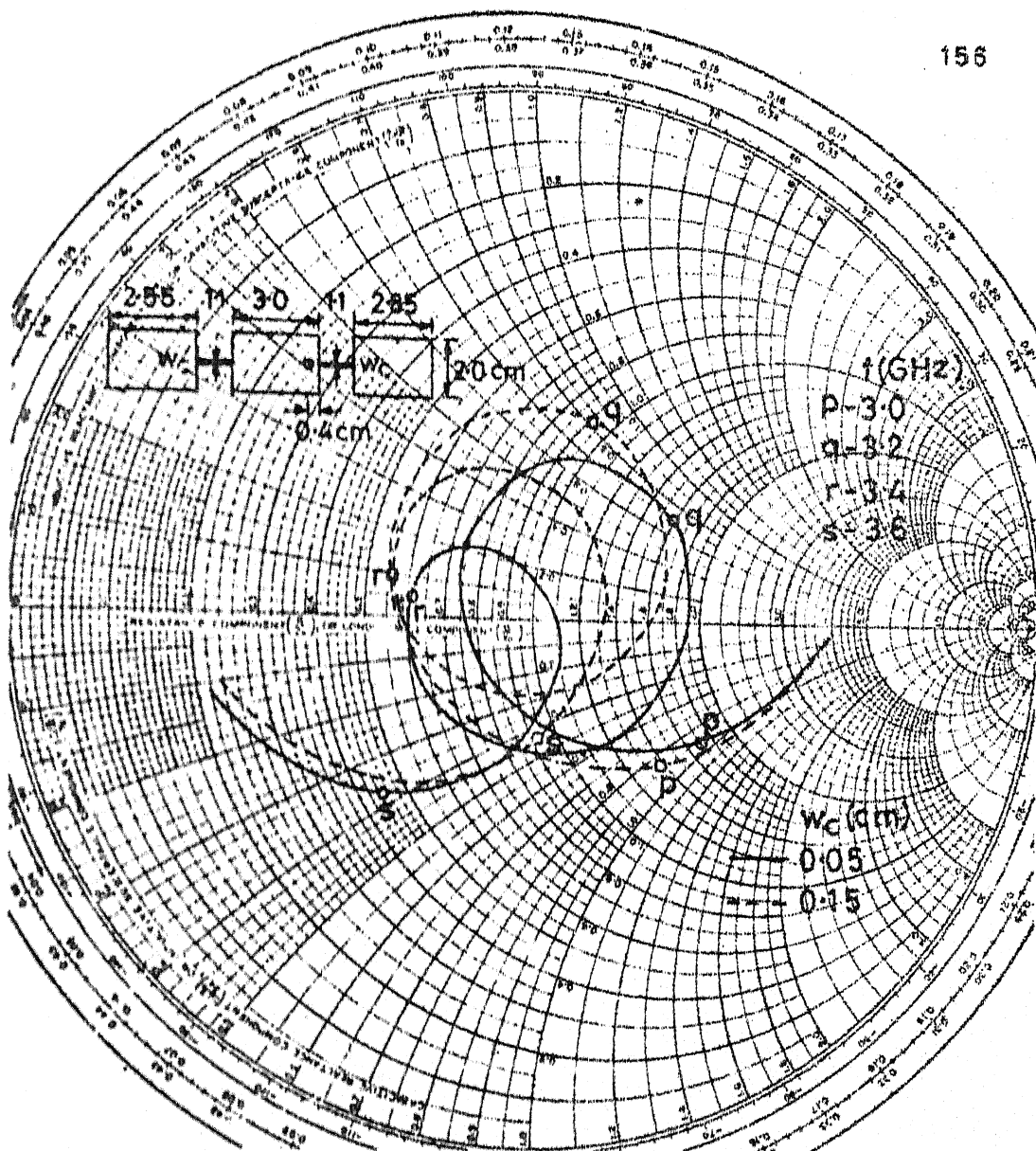


Fig.5.5 Input impedance loci of REDCOMA for two different widths w_c of connecting strips

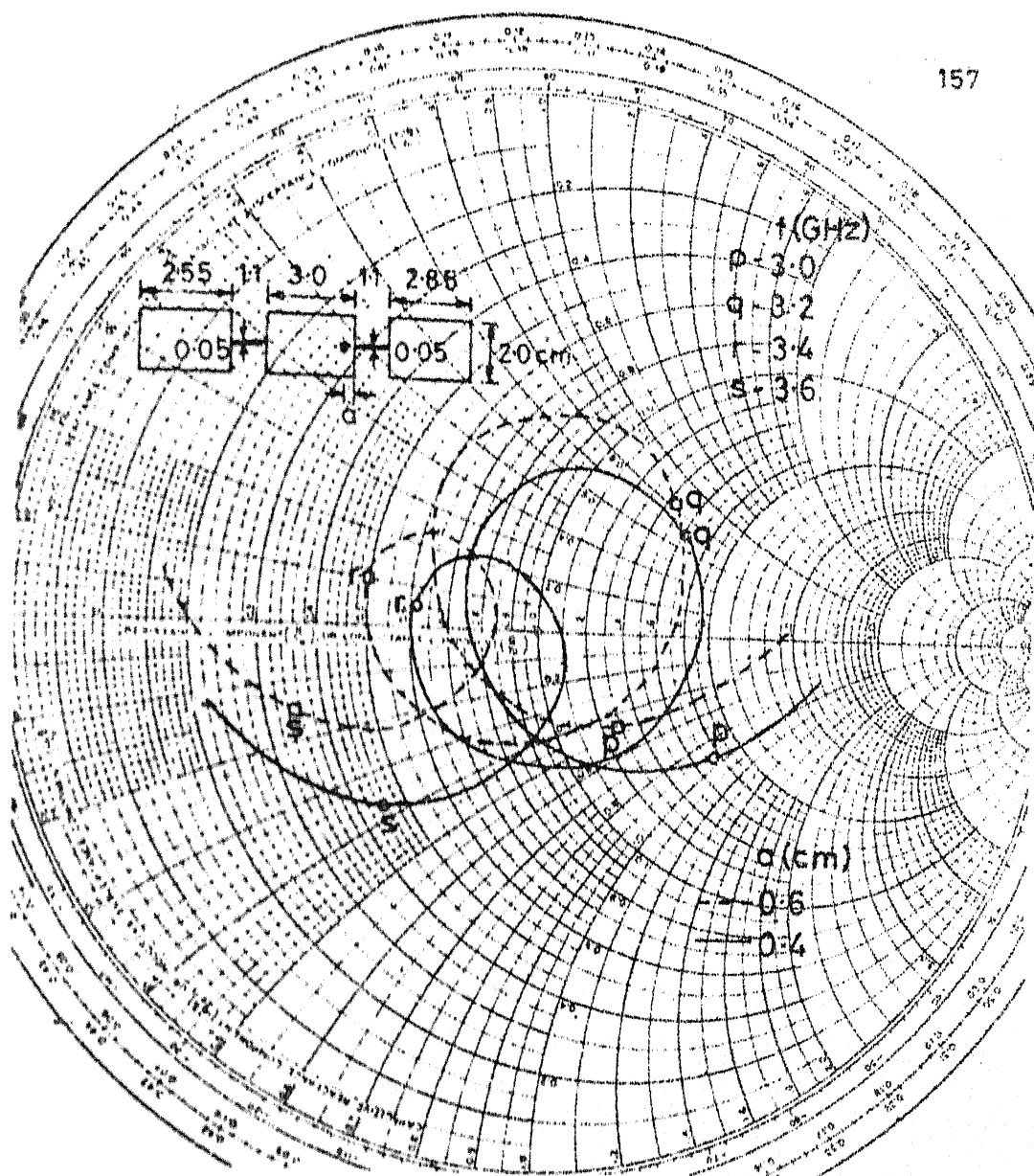


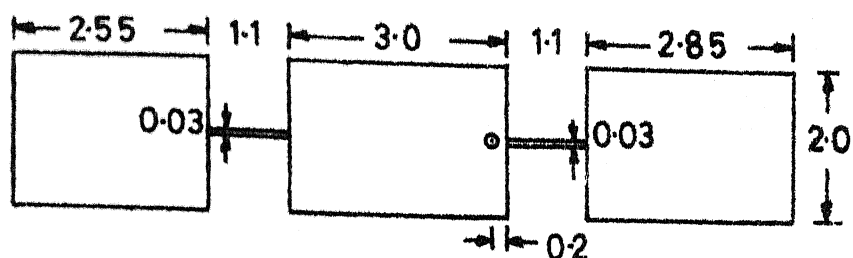
Fig.5.6 Input impedance loci of REDCOMA for two different feed-point locations

5.3 EXPERIMENTS AND OPTIMIZATION

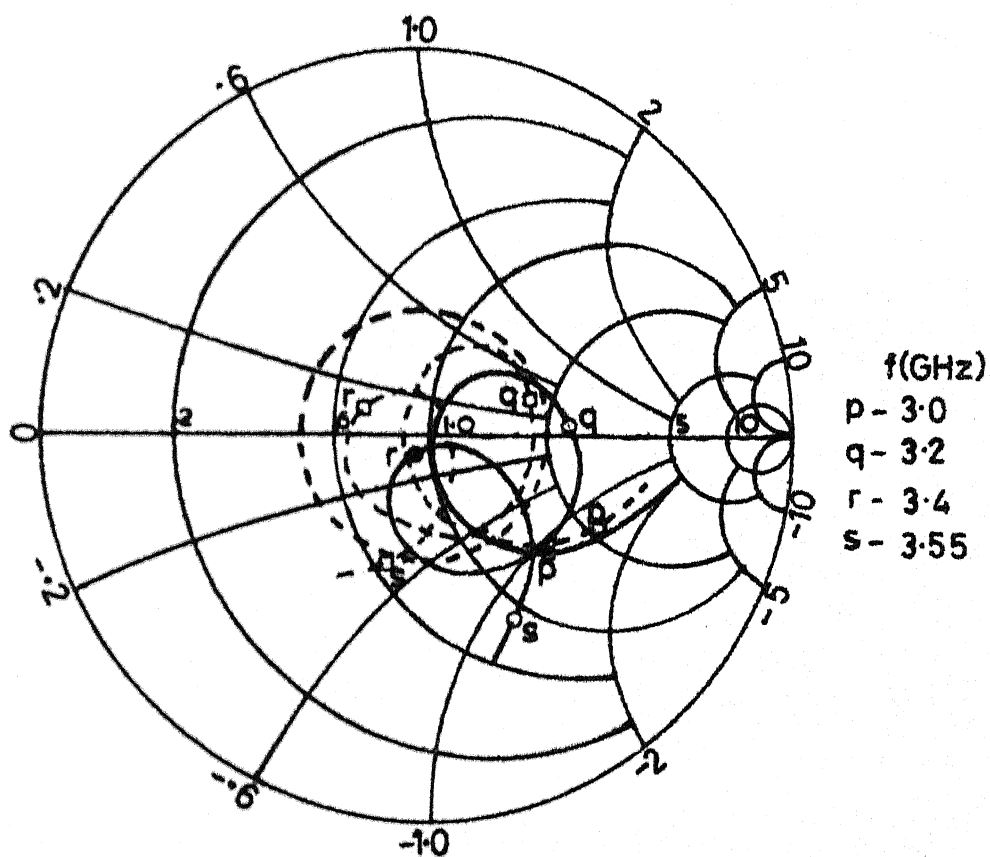
Experiment has been performed on REDCOMA (shown in Fig. 5.7(a)), for which theoretical impedance locus is plotted in Fig. 5.7(b). The bandwidth of the antenna is 515 MHz (15.6 percent, centre frequency $f_o = 3.3$ GHz), which is 4.7 times the bandwidth of RPA (BW = 110 MHz, $f_o = 2.985$ GHz, $L = 2.9$ cm, $W = 2.0$ cm, $\epsilon_r = 2.55$ and $h = 0.318$ cm).

The experimental locus of input impedance is also plotted in Fig. 5.7(b). It can be observed from this plot that the experimental impedance locus is shifted towards the **right** side of the Smith chart as compared to the theoretical impedance locus, and both the loops in the impedance locus are not inside the VSWR = 2 circle. Similar discrepancy has been observed in the case of NEGCOMA also.

Another experiment on REDCOMA (with dimensions shown in Fig. 5.8(inset)) has been carried out to bring both the loops in the impedance locus (of Fig. 5.7(b)) inside the VSWR = 2 circle. To obtain this, the spacing 'a' between the feed point and the edge is increased from 0.2 cm to 0.6 cm, which will shift the impedance locus upwards as described in Section 5.2.3. The photograph of the fabricated REDCOMA is shown in Fig. 5.9.



(a)



(b)

Fig.57(a) REDCOMA and (b) its theoretical (---) and experimental (—) input impedance loci

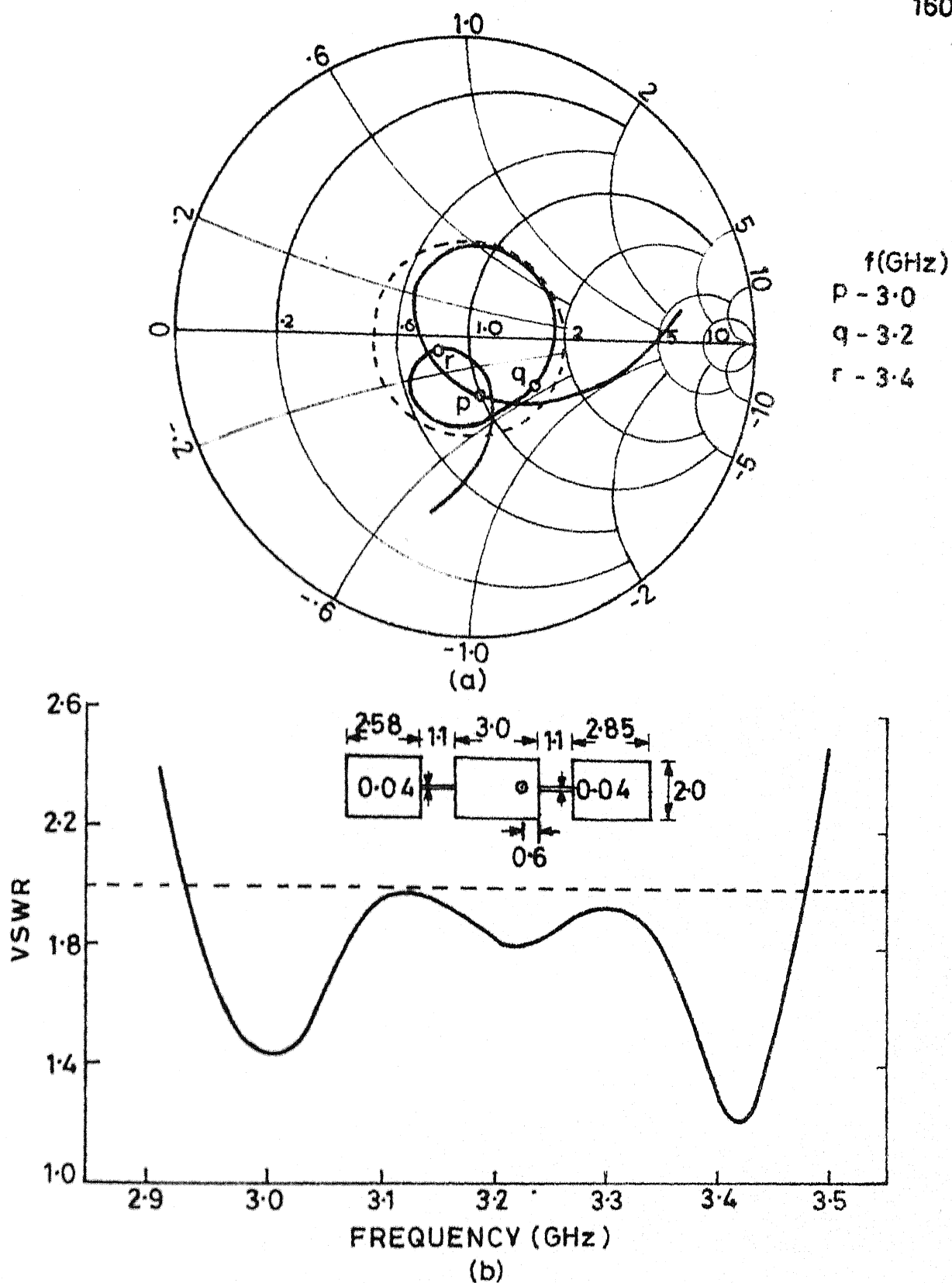


Fig.5.8 (a) Experimental input impedance locus and
(b) VSWR variation with frequency of
REDCOMA shown in inset

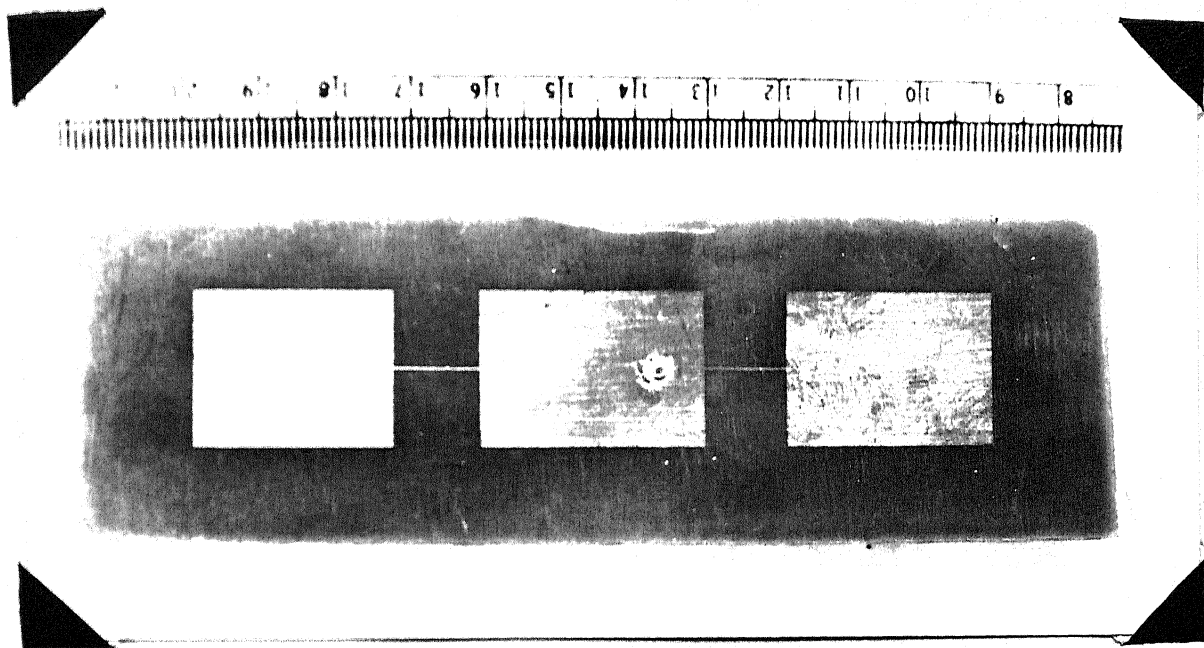


Fig. 5.9 Photograph of the fabricated REDCOMA

The experimental values of the input impedance locus and variation of VSWR with frequency are plotted in Figs. 5.8(a) and 5.8(b) respectively. As expected, the two loops in the impedance locus are shifted inside the $VSWR = 2$ circle. The measured bandwidth of the antenna is 548 MHz (17.1 percent, $f_0 = 3.2$ GHz), which is nearly five times the bandwidth of RPA.

Radiation pattern of the antenna (shown in Fig. 5.9) is calculated at various frequencies in both $\varphi = 0^\circ$ and $\varphi = 90^\circ$ planes. E_θ component of the radiation field in $\varphi = 0^\circ$ plane is plotted for three frequencies ($f = 3.05$, 3.25 and 3.45 GHz) in Fig. 5.10. A minimum is present in E_θ at all the three frequencies and its level at $f = 3.45$ GHz is 15 db below the maximum level. 3 db beamwidth in $\varphi = 0^\circ$ plane is 111° at $f = 3.05$ GHz and 40° at $f = 3.45$ GHz. Radiation is maximum along $\theta = -40^\circ$ direction at $f = 3.05$ GHz and it is 0.5 db below the maximum level along $\theta = 0^\circ$ direction. At $f = 3.25$ GHz, maximum radiation occurs along $\theta = 20^\circ$, and the level of radiation is 1.8 db below the maximum level along $\theta = -36^\circ$. Radiation is maximum along $\theta = 4^\circ$ at $f = 3.45$ GHz. With increase in frequency from 3.05 GHz to 3.45 GHz, the level of radiation along $\theta = 90^\circ$ direction (end-fire direction) decreases from 4.75 db to 12.5 db with respect to the corresponding maximum radiation levels.

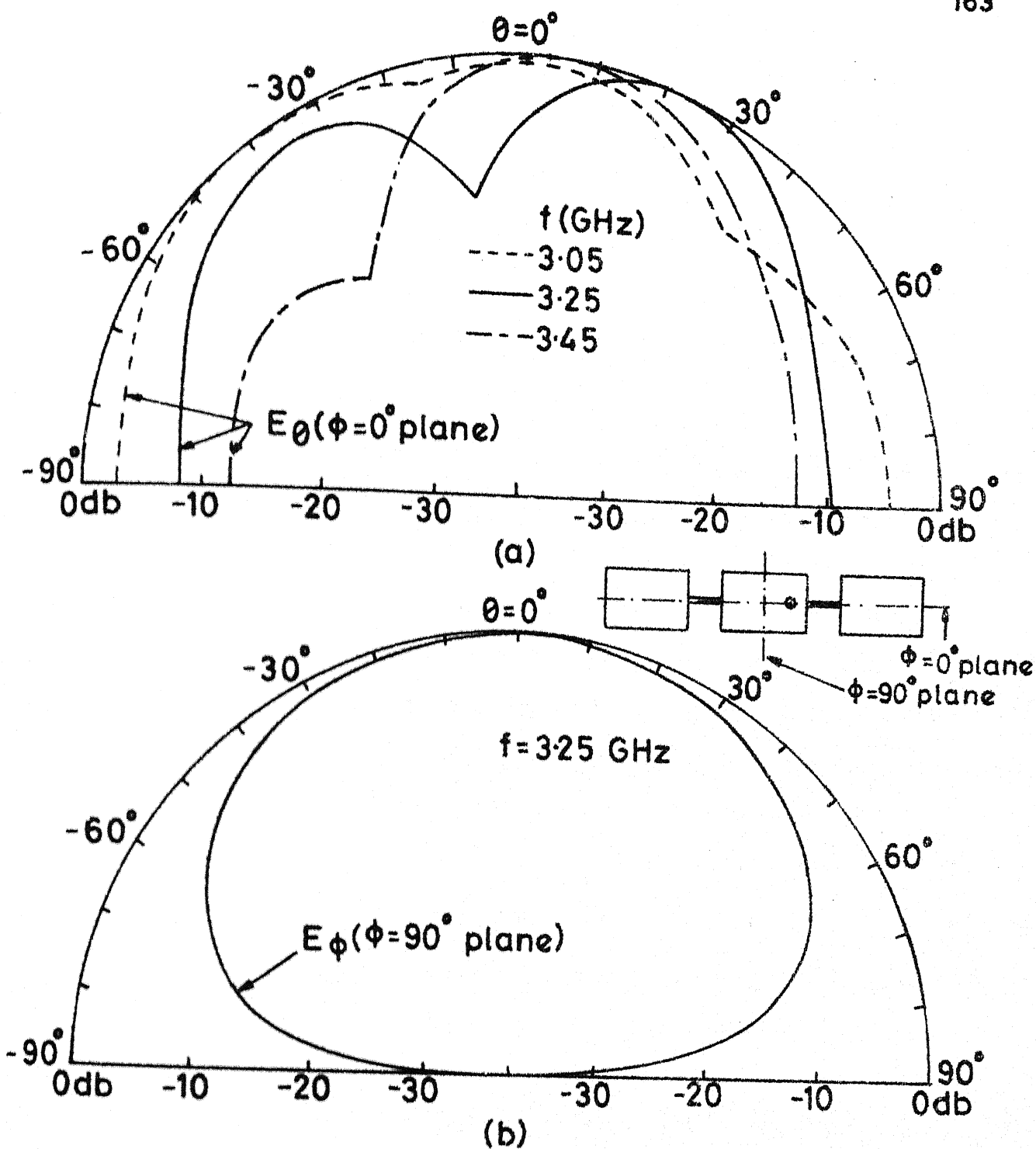


Fig. 5-10 Theoretical values of (a) E_θ (in $\phi = 0^\circ$ plane) and (b) E_ϕ (in $\phi = 90^\circ$ plane) for REDCOMA shown in Fig. 5-9

E_φ component of radiation field in $\varphi = 90^\circ$ plane is plotted for $f = 3.25$ GHz in Fig. 5.10(b). E_φ is plotted only for a single frequency because there is no appreciable change in its value with frequency. 3-db beamwidth in $\varphi = 90^\circ$ plane is 84° .

Radiation fields of REDCOMA (shown in photograph 5.9) are measured in both $\varphi = 0^\circ$ and $\varphi = 90^\circ$ planes at various frequencies covering the entire bandwidth of the antenna. Experimental value of E_θ in $\varphi = 0^\circ$ plane is plotted in Fig. 5.11(a) for three frequencies ($f = 3.015$, 3.22 and 3.42 GHz), where VSWR plot passes through minima (shown in Fig. 5.8(b)). In the frequency range of 3.015 GHz to 3.42 GHz, the direction of maximum radiation varies between $\theta = -40^\circ$ and $\theta = 12^\circ$, and 3-db beamwidth in $\varphi = 0^\circ$ plane remains between 27° and 38° . Radiation along $\theta = 0^\circ$ direction remains below 2.5 db of the corresponding maximum level at all the three frequencies.

Experimental value of E_φ in $\varphi = 90^\circ$ plane is plotted for $f = 3.25$ GHz in Fig. 5.11(b). For comparison, theoretical value of E_φ is also plotted. Experimental 3- db beamwidth is found to be 78° , which is 6° less than the theoretical value.

The bandwidth of REDCOMA (shown in Fig. 5.8(inset)) can be further improved by increasing the coupling between the parasitic element of length l_2 and the central patch

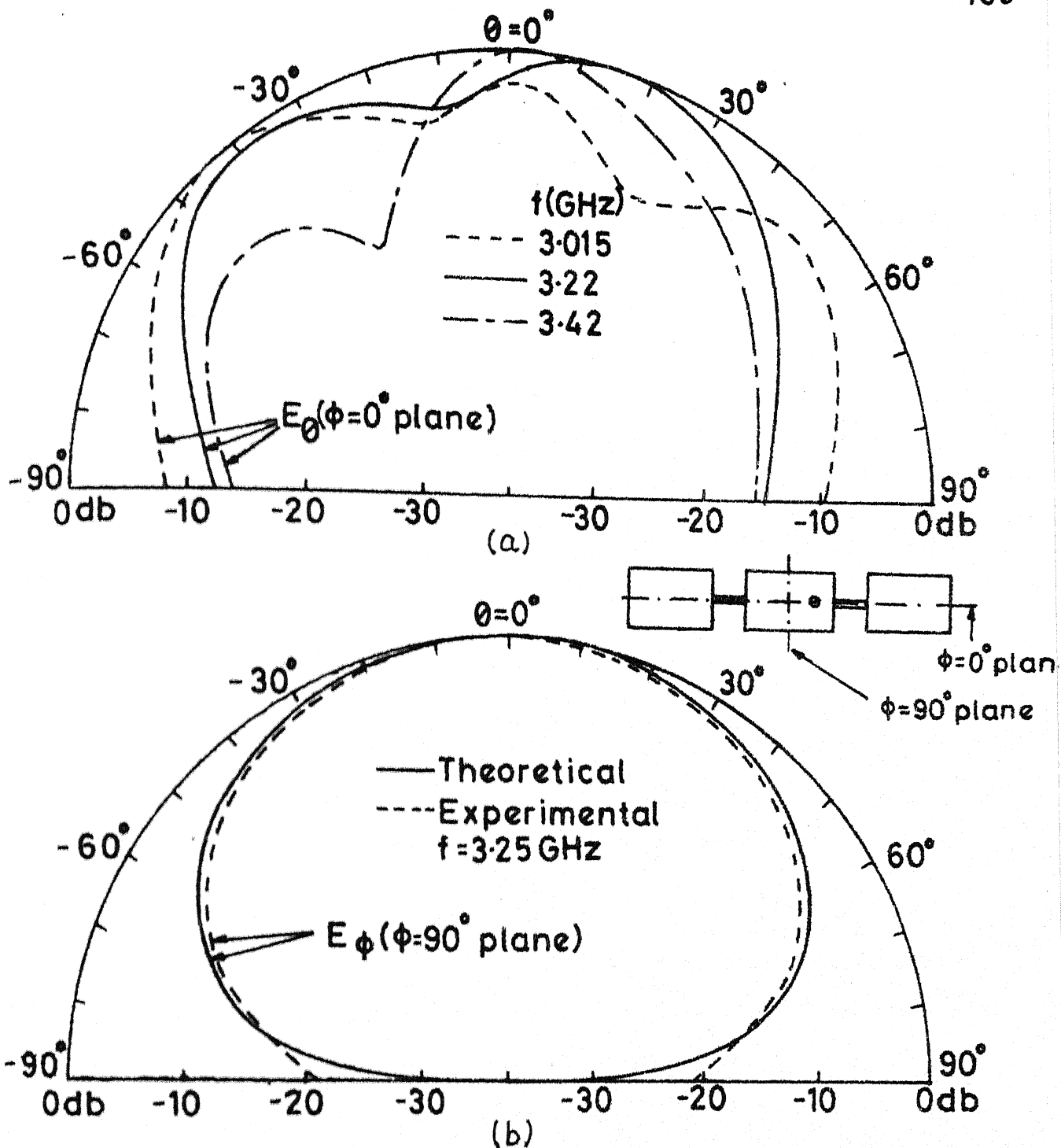


Fig.5-11(a) Experimental values of E_θ (in $\phi=0^\circ$ plane) and (b) Theoretical (—) and experimental (---) values of E_ϕ (in $\phi=90^\circ$ plane) for REDCOMA shown in Fig. 5-9

element (i.e. by decreasing the length l_c or by increasing the width w_c of the connecting strip), which will increase the size of the smaller loop in the impedance locus shown in Fig. 5.8.

5.4 DISCUSSION

Radiating edges directly coupled microstrip antennas have been analyzed and optimized (for S-band operation) by using Green's function approach and segmentation method. The bandwidth of the antenna obtained experimentally is 548 MHz (= 17.1 percent), which is nearly five times the bandwidth of RPA, and 36 MHz more than the bandwidth of REGCOMA. The width of the REDCOMA ($W = 2.0$ cm) is smaller than the width of REGCOMA ($W = 3.0$ cm). The total length of the antenna structure in case of REDCOMA is 10.6 cm, which is nearly 2.0 cm larger than the total length of REGCOMA.

Agreement between the theoretical and experimental results is better in case of REDCOMA than REGCOMA, because in REGCOMA the values of capacitances used in the gap modelling were not accurate. While in REDCOMA, coupling is only through the interconnecting microstriplines for which impedance Green's functions are accurately known.

CHAPTER SIX

NON-RADIATING EDGES DIRECTLY COUPLED AND FOUR EDGES DIRECTLY COUPLED MICROSTRIP ANTENNAS

This chapter deals with the analysis and design of non-radiating edges directly coupled microstrip antennas (NEDCOMA) and four edges directly coupled microstrip antennas (FEDCOMA) using Green's function approach. Based on these designs, experiments have been performed on these two antenna configurations to yield broader bandwidth.

6.1 NON-RADIATING EDGES DIRECTLY COUPLED MICROSTRIP ANTENNAS (NEDCOMA)

6.1.1 Analysis

A non-radiating edges directly coupled microstrip antenna is shown in Fig. 6.1(a). In this configuration, two parasitic elements are connected (directly coupled) to non-radiating edges of rectangular patch antenna via short sections of microstrip line. The lengths l_1 and l_2 of these parasitic elements are taken slightly different but nearly equal to half wavelength, and widths of the elements are taken equal to that of the central rectangular patch. The lengths l_1 and l_2 are selected to obtain the wider bandwidth. The locations of the connecting strips are chosen to yield optimum coupling, and are generally near the corners of the resonators. The lengths of these strips are taken slightly

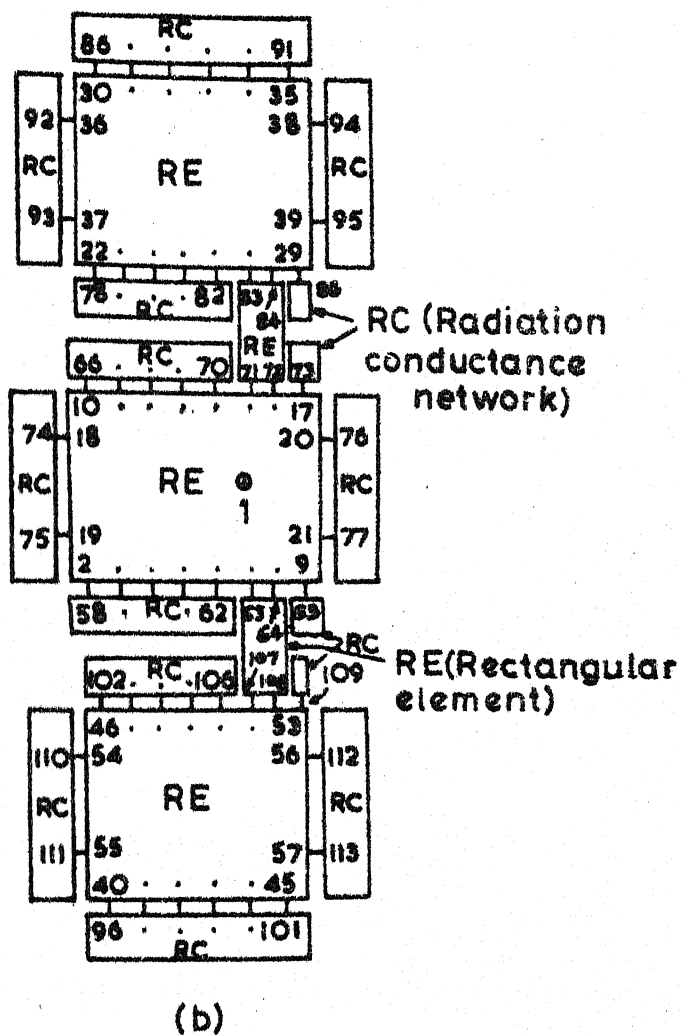
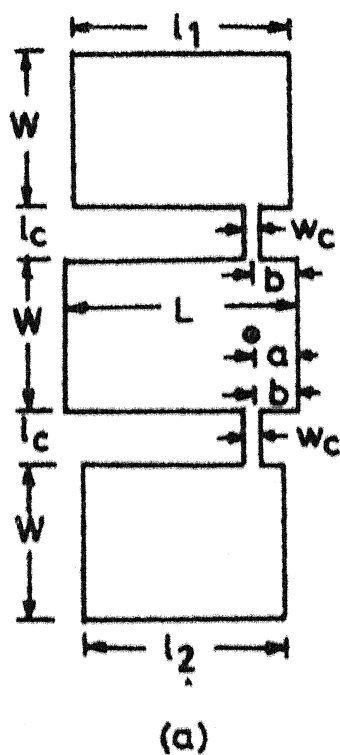


Fig.6-1(a) Non-radiating edges directly coupled microstrip antenna (NEDCOMA) and (b) its segmented network

greater than twice the thickness of the substrate so that the capacitive coupling through the gaps is negligible.

The analysis procedure for NEDCOMA is similar to that for REDCOMA of Chapter Five. The planar model, obtained by extending the physical boundary outward to account for the open-end fringing fields, is divided into simpler segments (rectangular elements and radiation conductance networks) as shown in Fig. 6.1(b). The interfaces between the various segments are divided into 105 ports : namely 52c- and 52d-ports, and a single p-port corresponding to the feed-point location. Z-matrix for the overall circuit is obtained from the Z-matrices of the individual segments by using (2.5). The radiation fields are evaluated from (2.11) after calculating the voltage distribution at various ports by using (2.6).

6.1.2 Effect of antenna parameters on the input impedance

For any specified patch dimensions ($L = 3.0$ cm and $W = 2.0$ cm), substrate parameters ($\epsilon_r = 2.55$ and $h = 0.318$ cm) and for the widths of the parasitic elements equal to the width of central rectangular patch, the input impedance of NEDCOMA is affected by the following parameters: lengths of the parasitic elements, dimensions (lengths and widths) of the connecting strips, and locations of the connecting strips and feed-point. The effects of these parameters on the input impedance locus are discussed in this section.

Lengths of the parasitic elements

For two different values of the length l_1 (2.75 cm and 2.65 cm) of the parasitic element, input impedance loci of NEDCOMA are plotted in Fig. 6.2. The other dimensions are: length $l_2 = 2.45$ cm, $l_c = 0.7$ cm, $w_c = 0.2$ cm, and locations of the connecting strips and feed-point (given by 'a' and 'b') equal to 0.6 cm each. A study of these impedance loci plots leads to the following observations. There are two loops in the impedance locus. These loops are caused by the interaction between the rectangular patch and the parasitic elements. Loops 1 and 2 correspond to the resonances of the larger length l_1 and the smaller length l_2 of parasitic elements respectively. When the length l_1 is decreased from 2.75 cm to 2.65 cm, loop 1 shifts towards the left side of the Smith chart and comes nearer to the loop 2. Also, size of the loop 1 decreases significantly. As the length l_1 is further reduced, the two loops will come nearer and nearer, and will finally merge into a single loop when length l_1 becomes equal to l_2 .

The input impedance loci of NEDCOMA for two different values of length l_2 (2.45 cm and 2.55 cm) of parasitic element, with other dimensions shown in Fig. 6.3(inset), are plotted in Fig. 6.3. With increase in length l_2 from 2.45 cm to 2.55 cm (i.e. when the difference between the two lengths l_1 and l_2 is reduced), loop 2 shifts upward and towards the right side of the Smith chart, and comes nearer to the loop 1.

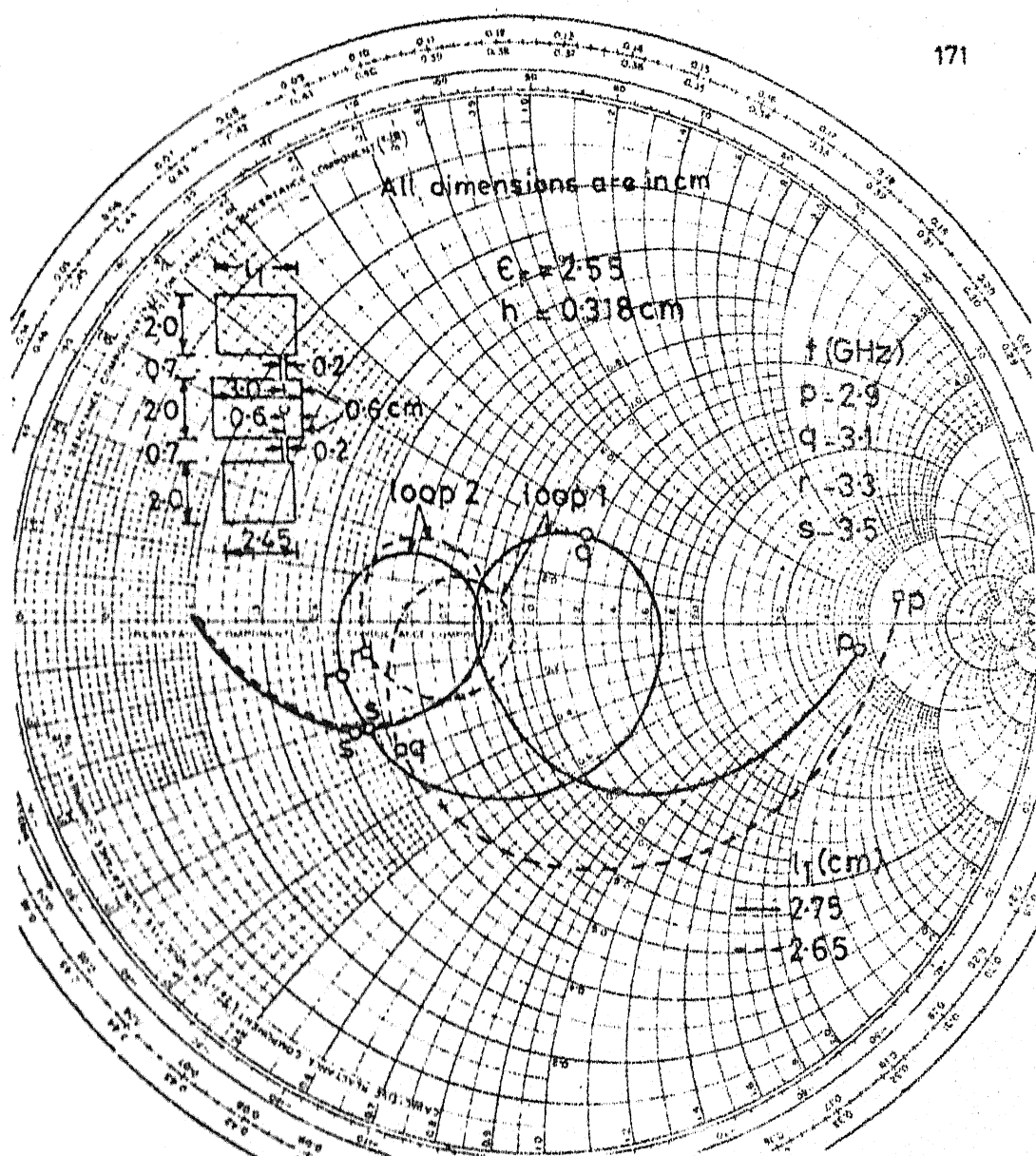


Fig.6.2 Input impedance loci of NEDCOMA for two different values of length l_1 of parasitic element

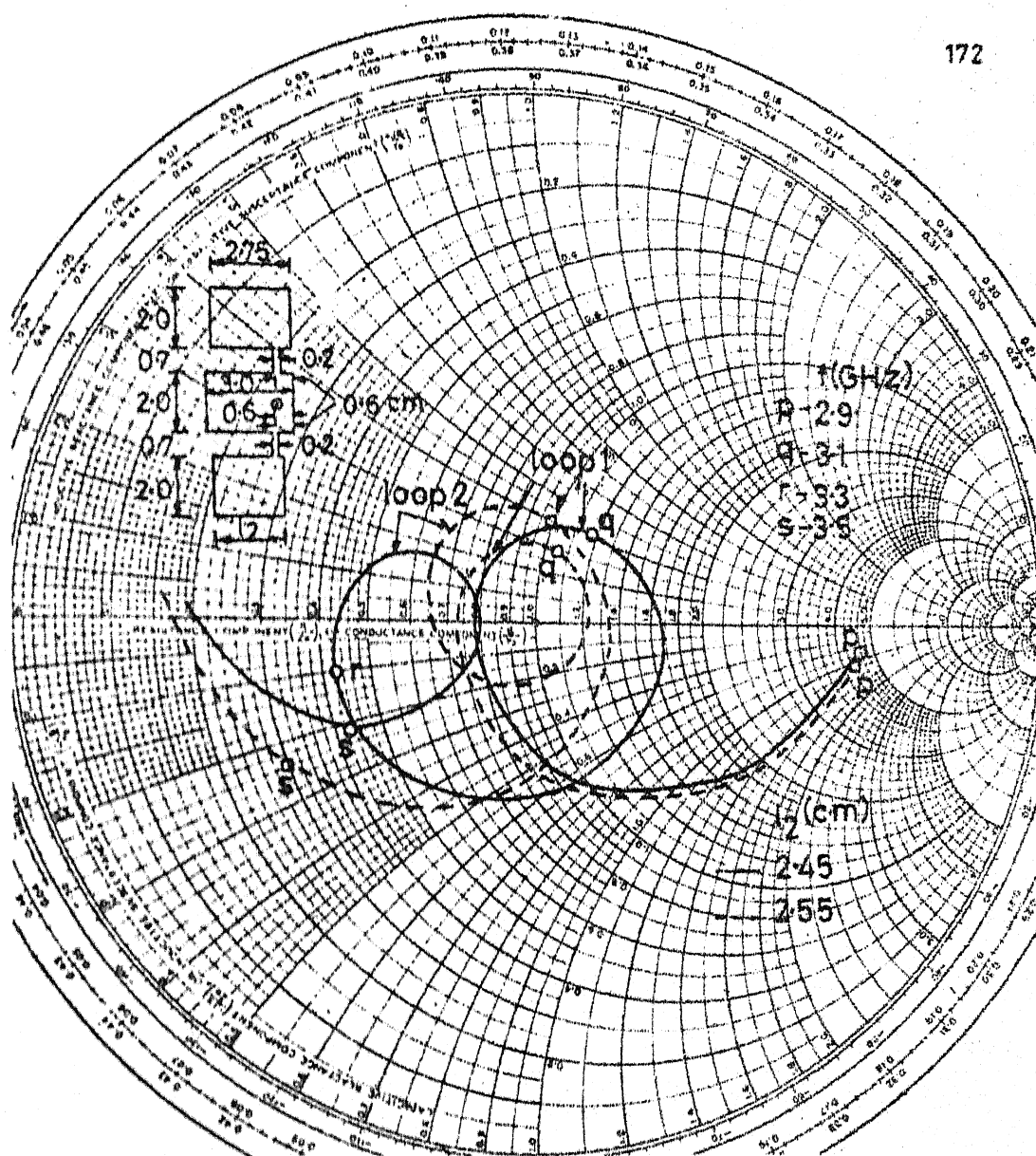


Fig. 63 Input impedance loci of NEDCOMA for two values of length l_2 of parasitic element

Dimensions of the connecting strips

Impedance loci of NEDCOMA for two different values of length l_c (0.7 cm and 0.9 cm) of connecting strips are plotted in Fig. 6.4, and for two different values of width w_c (0.3 cm and 0.1 cm), these are plotted in Fig. 6.5. With increase in length l_c from 0.7 cm to 0.9 cm (i.e. the spacing between the rectangular patch and the parasitic elements is increased), both the loops in the impedance locus shift towards the left side of the Smith chart.

When the width w_c is decreased from 0.3 cm to 0.1 cm, both the loops in the impedance locus (shown in Fig. 6.5) shift downward and also their sizes are reduced slightly because of decrease in the coupling between the resonators.

Location of the connecting strips

For two different locations of the connecting strips ($b = 0.6$ cm and 0.75 cm), input impedance loci of NEDCOMA are depicted in Fig. 6.6. With the increase in the value of b , both the loops in the impedance locus shift downward with their sizes reduced, and also the two loops shift apart.

In NEDCOMA, the field varies along the non-radiating edges and it is maximum at the corners. Thus, when the location of the connecting strip is shifted away from the corner, the field value decreases and hence the coupling between the resonators is reduced. This results in decrease in the size of the loops.

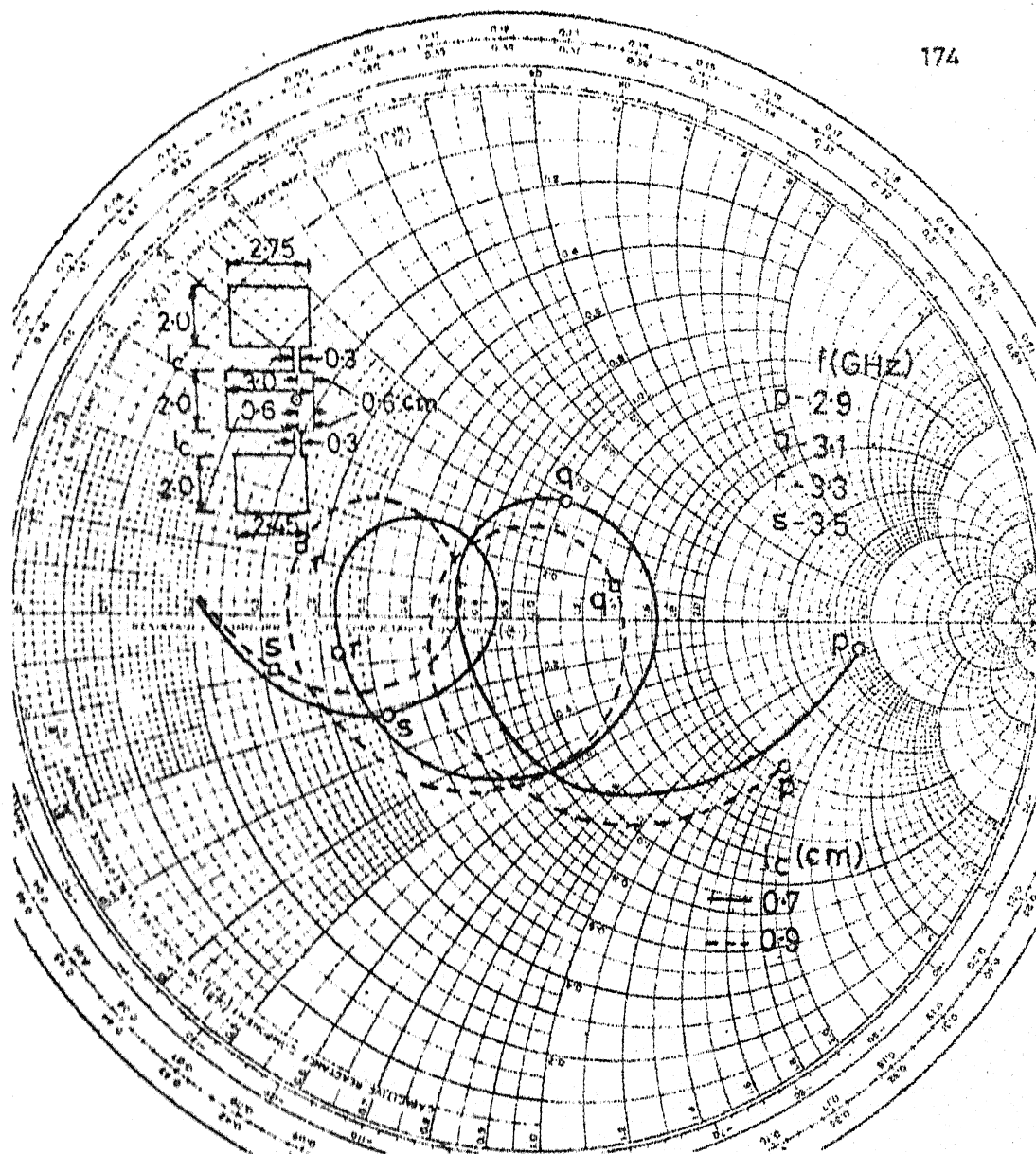


Fig.6.4 Input impedance loci of NEDCOMA for two different values of length l_c of connecting strips

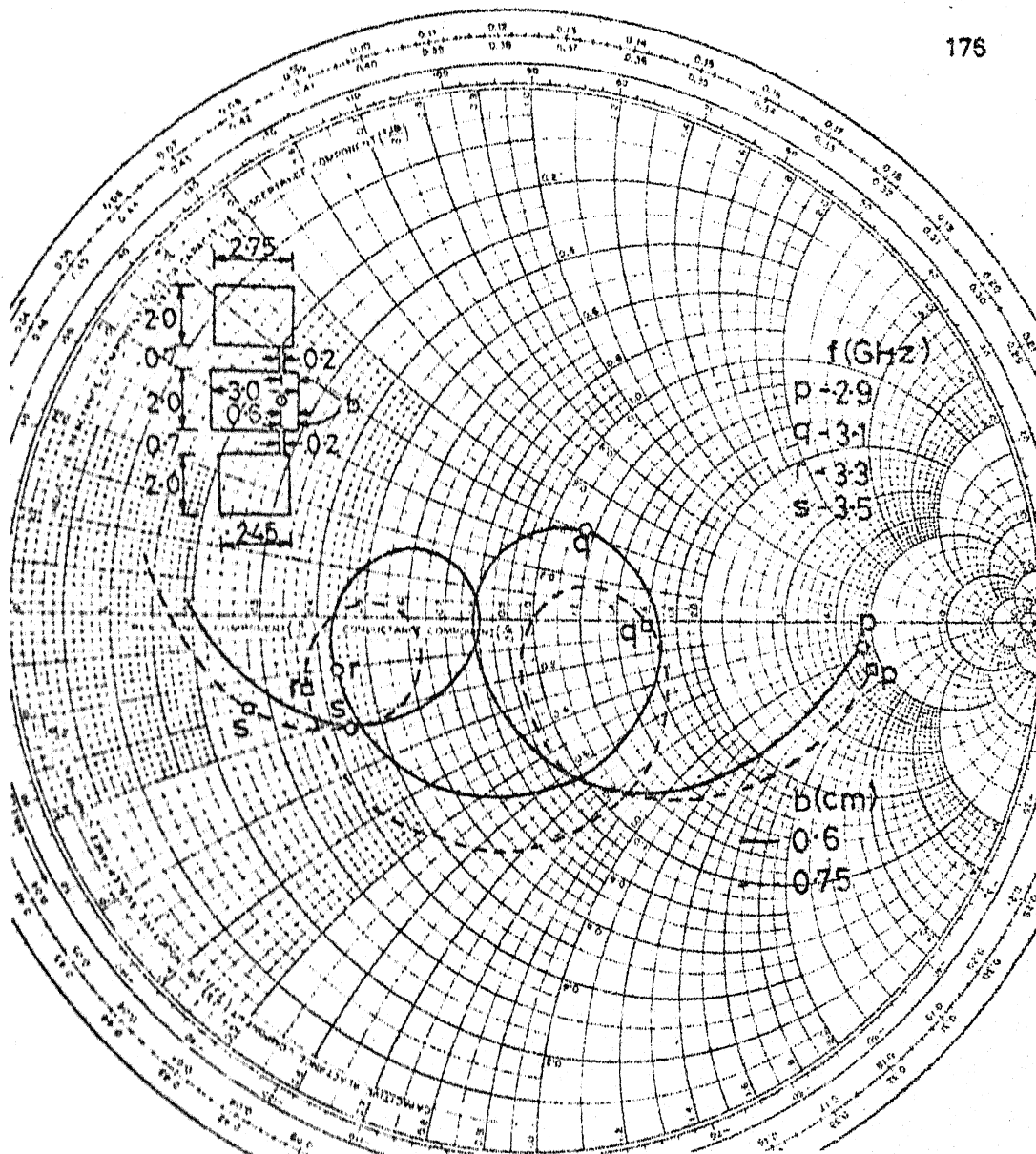


Fig.6.6 Input impedance loci of NEDCOMA for two different locations 'b' of the connecting strips

Feed-point location

Input impedance loci of NEDCOMA, for two different values of feed-point location ($a = 0.6$ cm and 0.39 cm), are plotted in Fig. 6.7. When the feed-point location is changed from 0.6 cm to 0.39 cm, the impedance locus shifts downward and towards the right side of the Smith chart, but the shape of the impedance locus remains unaltered.

6.1.3 Experiments

After studying the effects of various parameters on the input impedance, the bandwidth of the antenna is optimized (maximized) by bringing the two loops in the impedance locus inside the $VSWR = 2$ circle on the Smith chart. For the NEDCOMA shown in Fig. 6.8 (inset), the theoretical input impedance locus is depicted in Fig. 6.8. It may be noted from this plot that both the loops in the impedance locus are inside the $VSWR = 2$ circle. The bandwidth of the antenna is 485 MHz (15.1 percent, centre frequency $f_0 = 3.21$ GHz), which is 4.4 times the bandwidth of RPA ($BW = 110$ MHz for $W = 2.0$ cm).

The experiment has been carried out on NEDCOMA, with dimensions shown in Fig. 6.9 (inset), for which theoretical input impedance locus is plotted in Fig. 6.9(a). It may be observed from this plot that both the loops in the theoretical impedance locus are not inside the $VSWR = 2$ circle. One loop is located slightly outside the left side of the $VSWR = 2$ circle. The purpose of performing the experiment on these

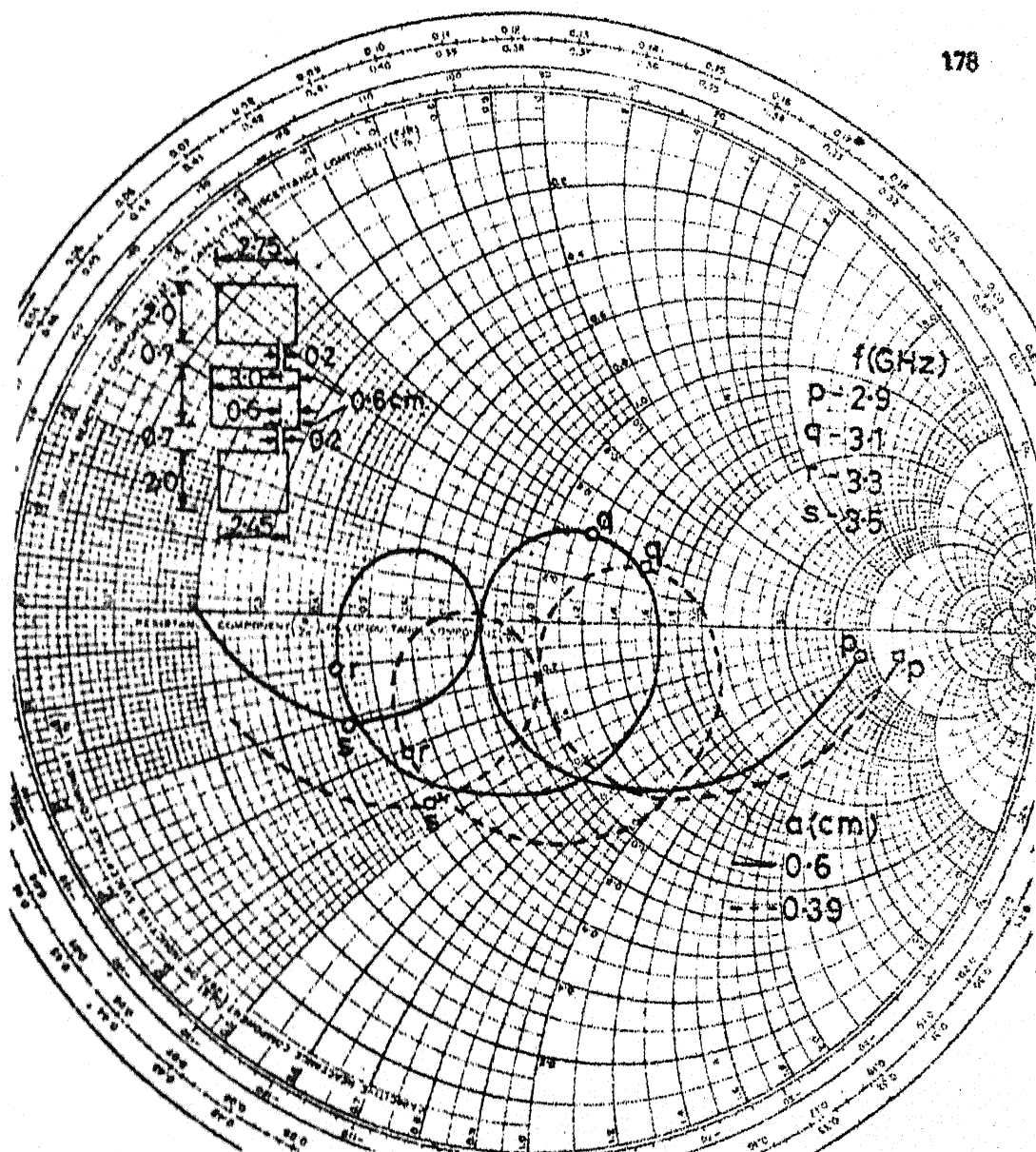


Fig.6-7 Input impedance loci of NEDCOMA for two different values of feed-point location 'a'

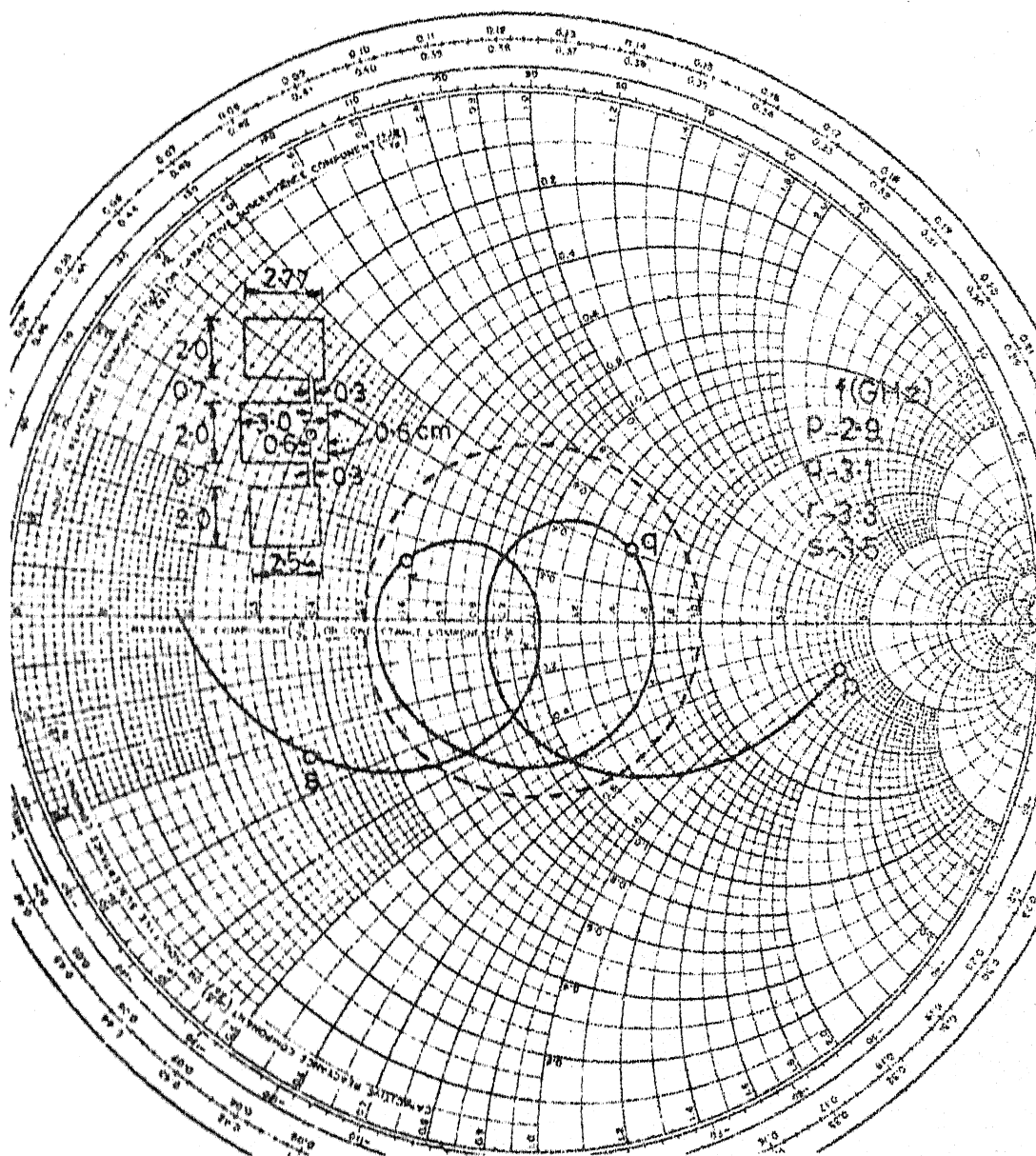


Fig.6-8 Input impedance locus of NEDCOMA shown in inset

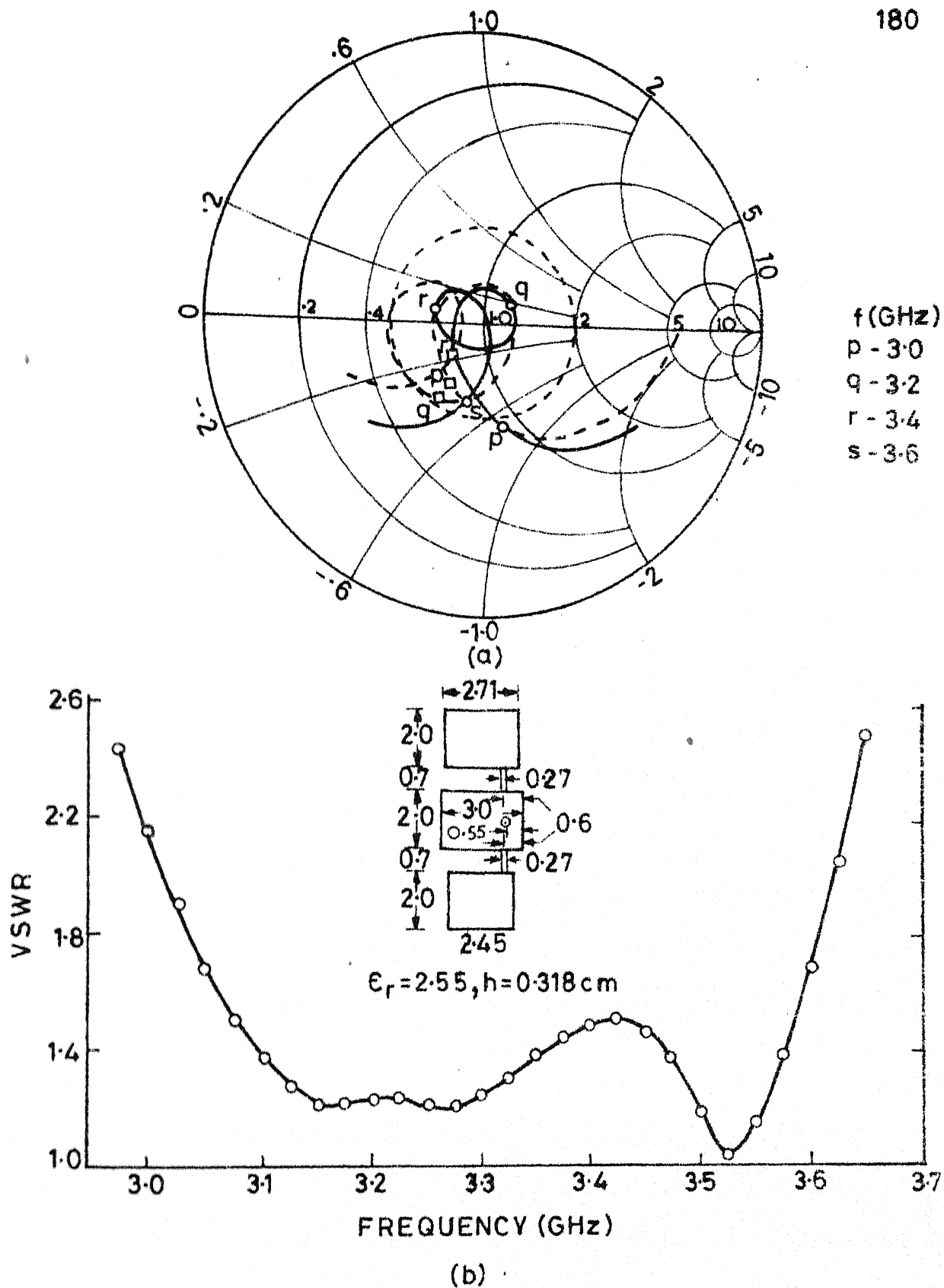


Fig. 6-9(a) Theoretical (---) and experimental (—) input impedance loci and (b) experimental VSWR variation with frequency of NEDCOMA

dimensions was to find out whether the loops in the experimental impedance locus shift towards the right side of the Smith chart as observed earlier in the cases of NEGCOMA and REDCOMA.

The photograph of NEDCOMA fabricated is shown in Fig. 6.10. The experimental input impedance locus and VSWR variation with frequency are plotted in Fig. 6.9(a) and (b) respectively. As expected, the two loops are inside the $VSWR = 2$ circle. The bandwidth of the antenna obtained experimentally is 605 MHz (18.3 percent, $f_0 = 3.31$ GHz), which is 5.5 times the bandwidth of RPA. Experimental bandwidth is more than the theoretical value because dielectric losses, conductor losses, and losses due to surface wave propagation have been ignored in the analysis.

6.1.4 Radiation pattern

Radiation pattern of the NEDCOMA shown in Fig. 6.10 has been calculated in both $\varphi = 0^\circ$ and $\varphi = 90^\circ$ planes at various frequencies of interest. Only E_θ component of the radiation field is present in $\varphi = 0^\circ$ plane and only E_φ component is present in $\varphi = 90^\circ$ plane, as in the case of RPA. E_θ in $\varphi = 0^\circ$ plane is plotted for two frequencies ($f = 3.05$ GHz and 3.45 GHz) in Fig. 6.11(a). At other frequencies, the value of E_θ varies between these two curves. 3-db beamwidth in $\varphi = 0^\circ$ plane at the two frequencies is equal to 97° . With increase in the frequency, E_θ curve becomes asymmetrical with respect to $\theta = 0^\circ$ direction.

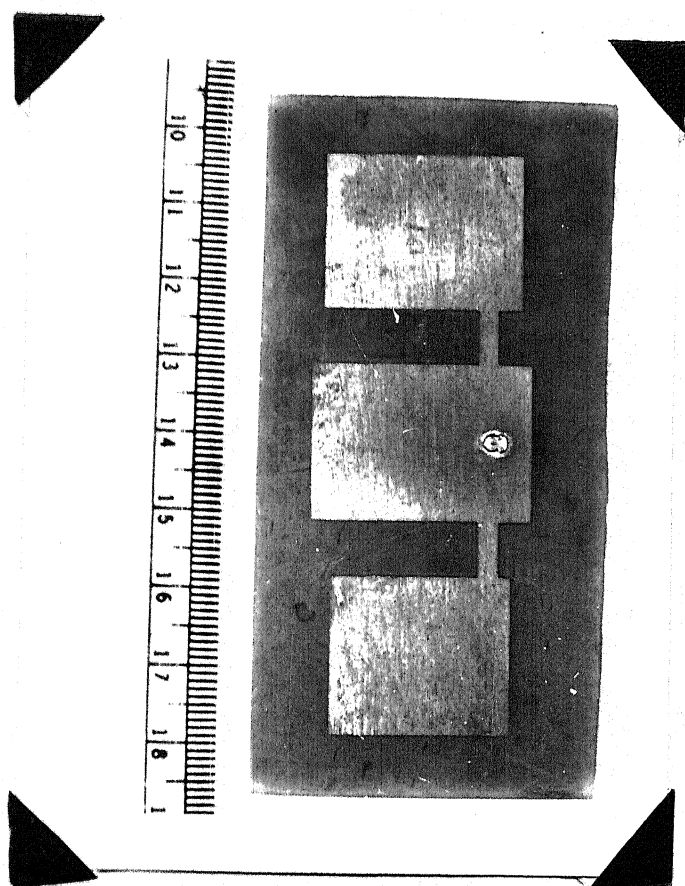


Fig. 6.10 Photograph of the NEDCOMA configuration

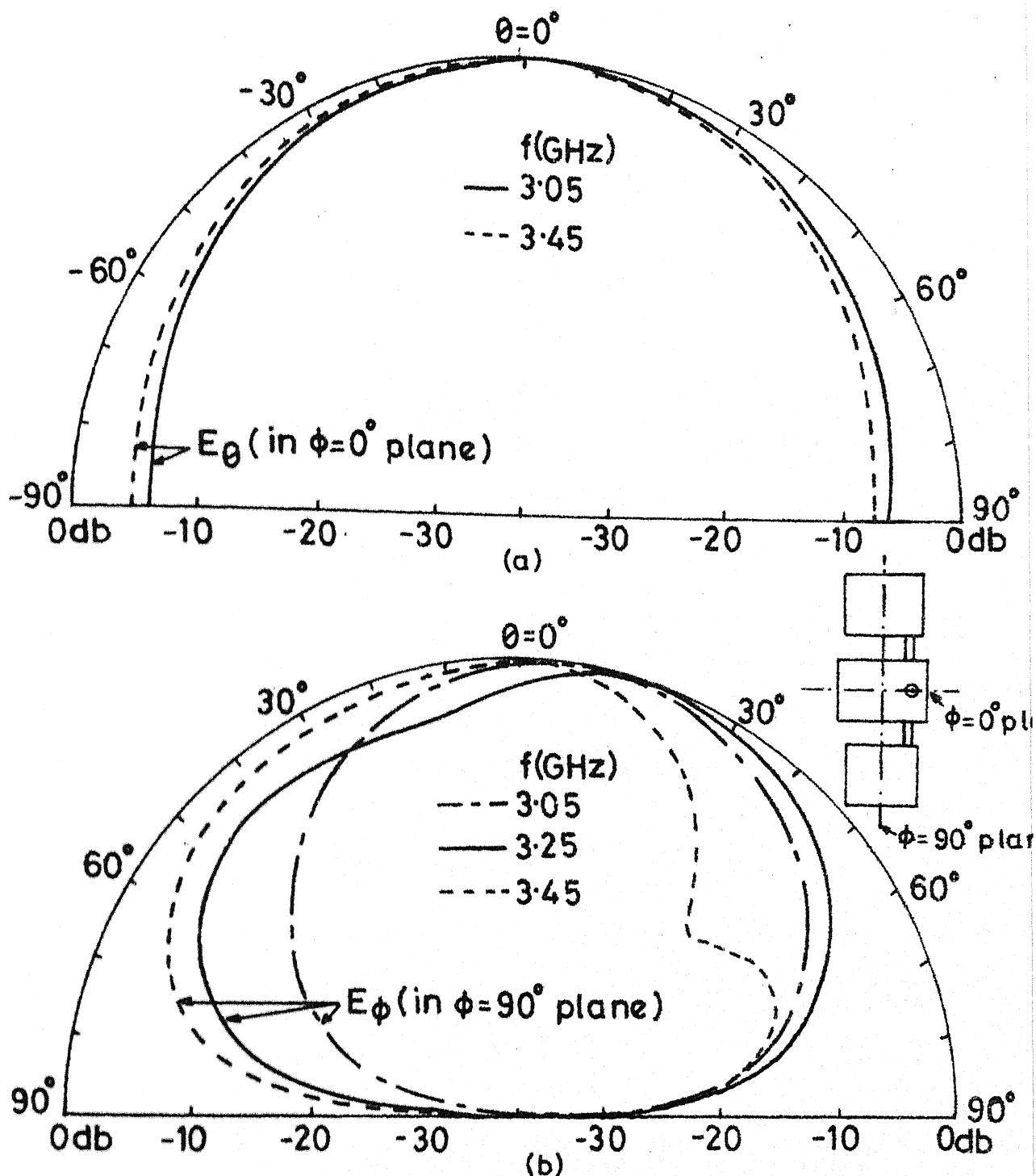


Fig. 6.11 Theoretical values of E_θ in $\phi=0^\circ$ plane and E_ϕ in $\phi=90^\circ$ plane of NEDCOMA shown in photograph 6.10

E_φ component in $\varphi = 90^\circ$ plane for three different frequencies ($f = 3.05, 3.25$ and 3.45 GHz) is depicted in Fig. 6.11(b). 3-db beamwidth at these three frequencies is $58^\circ, 52^\circ$ and 75° respectively. Direction of maximum radiation varies between $\theta = 0^\circ$ and $\theta = 20^\circ$ with the frequency. Radiation along $\theta = 0^\circ$ direction remains below 2.0 db of the corresponding maximum level. A minimum is present in E_φ at higher frequency ($f = 3.45$ GHz) and its level is 16.5 db below the maximum level.

Radiation pattern is measured in both $\varphi = 0^\circ$ and $\varphi = 90^\circ$ planes at the various frequencies for which VSWR remains less than two. E_θ component in $\varphi = 0^\circ$ plane is plotted for two frequencies ($f = 3.07$ GHz and 3.49 GHz) in Fig. 6.12(a). 3-db beamwidth in $\varphi = 0^\circ$ plane at the two frequencies is 69° and 79° respectively. At the higher frequency, E_θ is more asymmetrical with $\theta = 0^\circ$ direction.

E_φ component in $\varphi = 90^\circ$ plane is plotted for $f = 3.15$ GHz and 3.49 GHz in Fig. 6.12(b). 3-db beamwidth in $\varphi = 90^\circ$ plane at these frequencies is 65° and 59° respectively. Radiation is maximum along $\theta = 20^\circ$ at $f = 3.15$ GHz and along $\theta = -15^\circ$ at $f = 3.49$ GHz. Radiation along $\theta = 0^\circ$ direction at the two frequencies remains below 1.8 db of the corresponding maximum radiation level. The level of minimum present in E_φ at $f = 3.49$ GHz is 12 db below the maximum level.

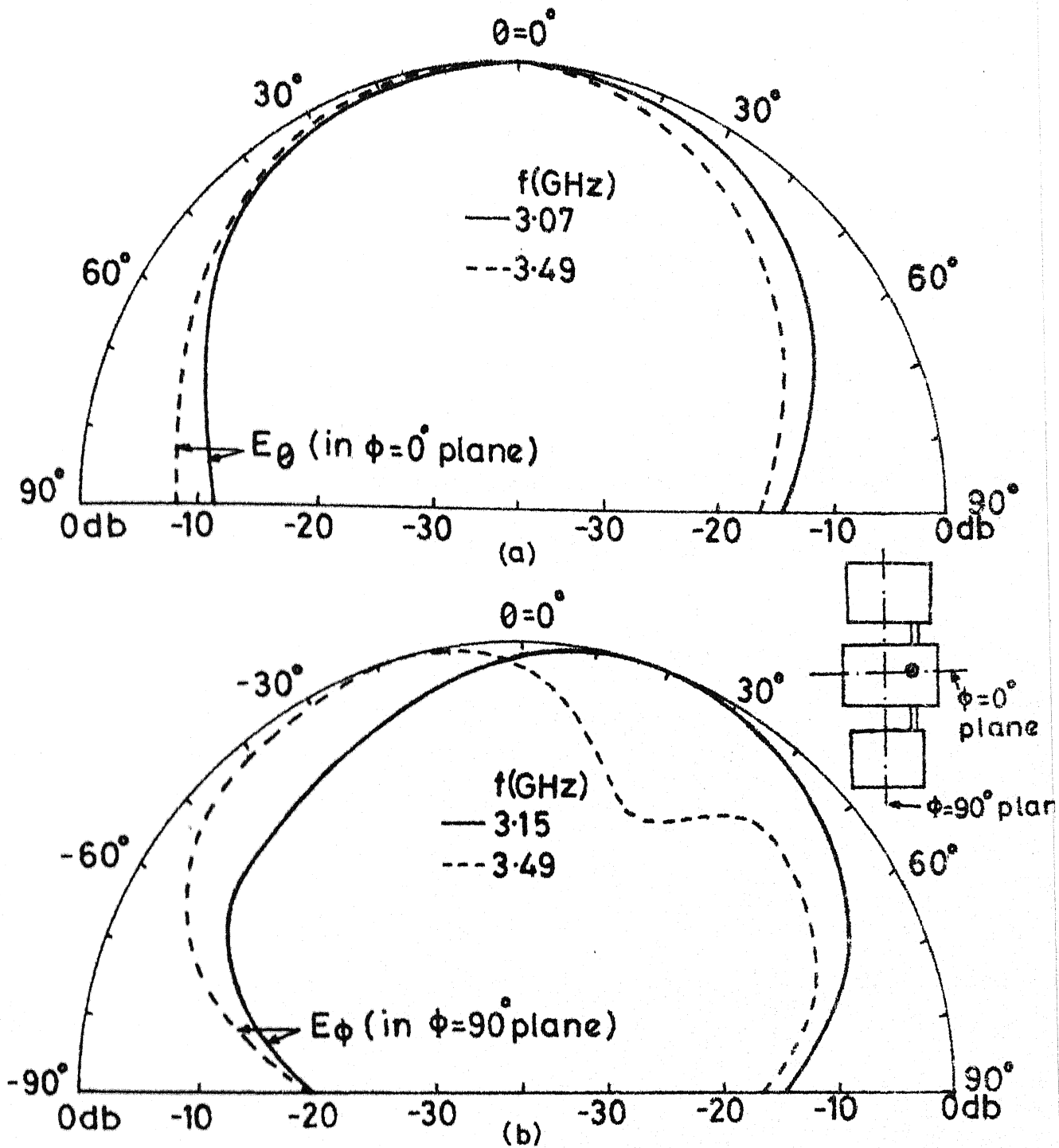


Fig. 6-12 Experimental values of E_θ in $\phi=0^\circ$ plane and E_ϕ in $\phi=90^\circ$ plane of NEDCOMA shown in photograph 6-10

The bandwidth of NEDCOMA (shown in Fig. 6.9 (inset)) can be further improved by increasing the width w_c of the connecting strips (which will increase the size of the loops in the impedance locus of Fig. 6.9(a)). Also, the length l_2 can be decreased from 2.45 cm to 2.4 cm, so the parasitic element will be resonant at higher frequency and hence the bandwidth will increase further.

6.2 FOUR EDGES DIRECTLY COUPLED MICROSTRIP ANTENNAS (FEDCOMA)

It has been pointed out in Section 4.4 that four edges gap coupled microstrip antennas yield much more wider bandwidth than the radiating edges gap coupled or non-radiating edges gap coupled microstrip antennas. Similarly, it can be expected that four edges directly coupled microstrip antennas (FEDCOMA) will also exhibit better bandwidth than REDCOMA or NEDCOMA.

6.2.1 Analysis

In FEDCOMA, four parasitic elements of slightly different lengths are directly coupled to the four edges of the rectangular patch antenna through short sections of microstrip line as shown in Fig. 6.13(a). The width W of all the parasitic elements is taken equal to that of rectangular patch element itself. If the parasitic elements coupled to the non-radiating edges are identical (i.e. $l_3 = l_4$), and the dimensions and locations of the connecting strips along the non-radiating edges are identical (i.e. $l_{c3} = l_{c4}$, $w_{c3} = w_{c4}$ and

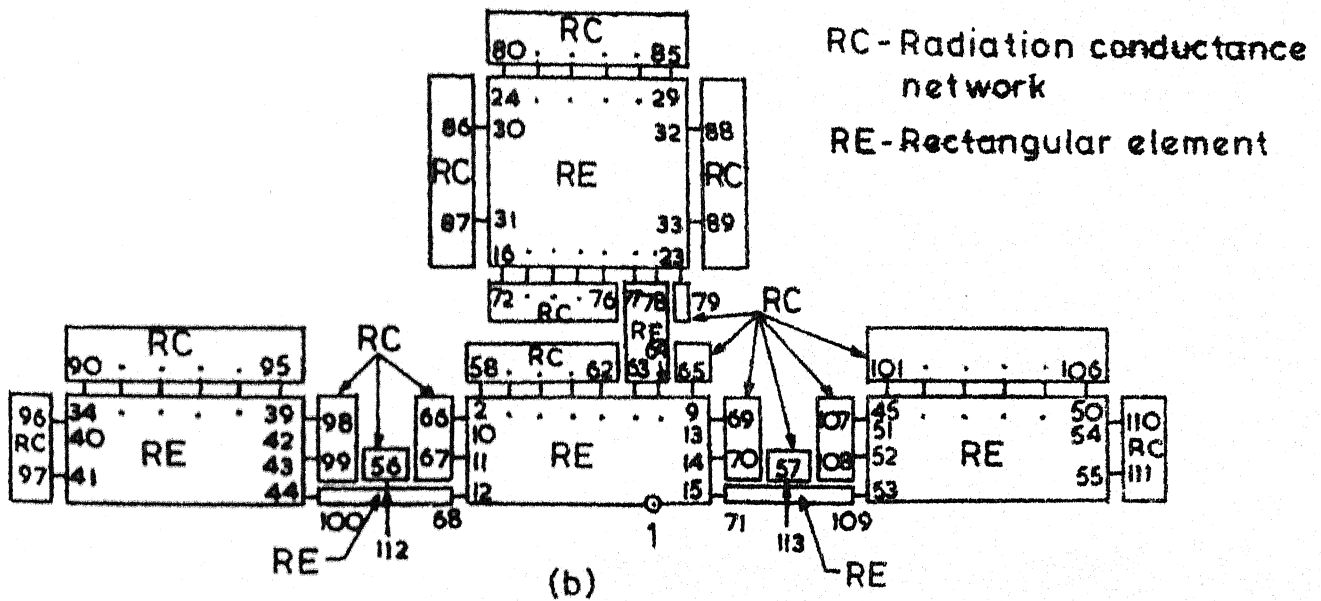
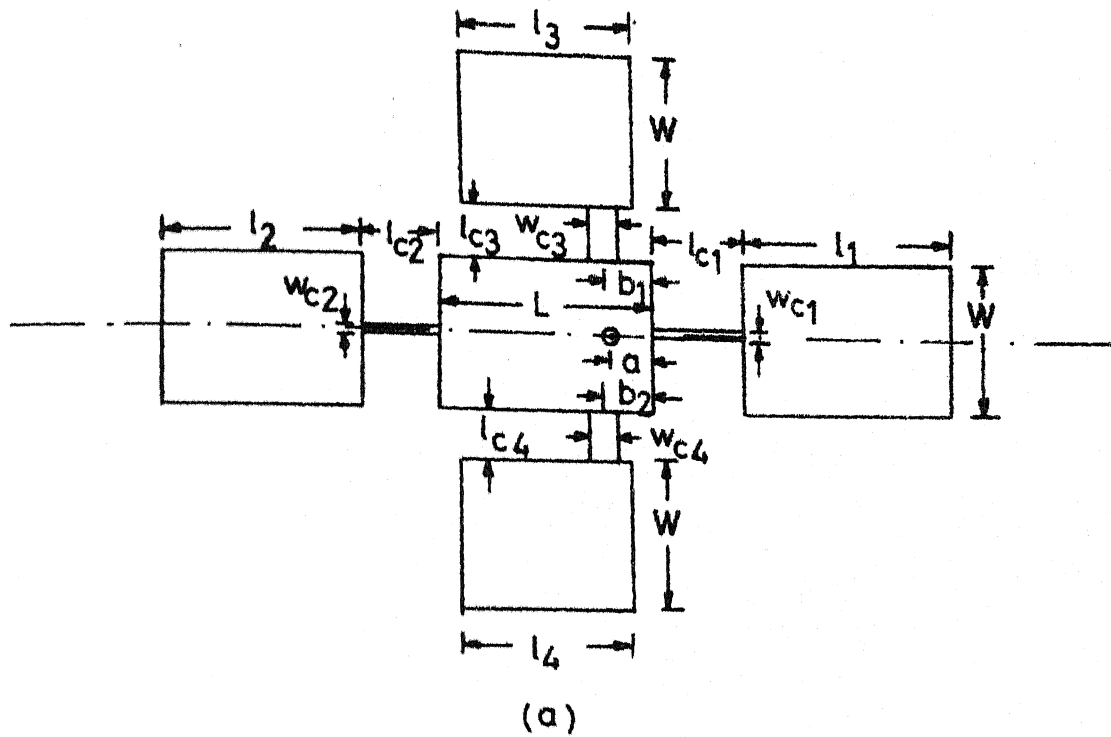


Fig. 6-13(a) Four edges directly coupled microstrip antennas (FEDCOMA) and (b) segmented network of even-mode half section of FEDCOMA

$b_1 = b_2$), then the antenna structure will be symmetrical with respect to the axis XX. Even-mode half-section of FEDCOMA, after extending the physical boundary outwards to account for the open-end fringing fields, is divided into rectangular elements and radiation conductance networks as shown in Fig. 6.13(b). As before the outer periphery of the antenna is divided into various ports. Input impedance and radiation pattern of FEDCOMA are evaluated from (2.5) and (2.11) respectively.

6.2.2 Optimization and experiment

For any given patch dimensions ($L = 3.0$ cm and $W = 2.0$ cm), substrate specifications ($\epsilon_r = 2.55$ and $h = 0.318$ cm), and widths of all the resonators being equal to 2.0 cm, the parameters which govern the input impedance characteristics of FEDCOMA are : lengths of the parasitic elements, dimensions of the connecting strips, locations of the connecting strips along the non-radiating edges of rectangular patch element, and the feed-point location. The effects of these parameters on the input impedance of FEDCOMA are similar to that in the cases of REDCOMA and NEDCOMA, discussed in Chapter Five and Section 6.1.

If the lengths l_1, l_2 and l_3 of parasitic elements are slightly different (but all approximately half wavelength), then there will be three loops in the impedance locus. Each one of these loops corresponds to the parasitic elements of

different lengths. The above mentioned parameters are optimized, to bring the three loops in the impedance locus inside the $VSWR = 2$ circle. This yields broader bandwidth than REDCOMA or NEDCOMA, because there are three loops inside the $VSWR = 2$ circle instead of two loops.

A theoretical bandwidth of the order of 630 MHz (18.9 percent, $f_0 = 3.34$ GHz) is obtained for the FEDCOMA shown in Fig. 6.14(a). Theoretical input impedance locus is plotted in Fig. 6.14(b). From the impedance plot, it may be observed that there are three loops in the impedance locus which are inside $VSWR = 2$ circle on Smith chart. Loops 1, 2 and 3 correspond to the lengths $l_1 (= 2.85$ cm), $l_2 (= 2.635$ cm) and $l_3 (= 2.35$ cm) of parasitic elements respectively.

Experimental input impedance locus and VSWR variation with frequency are plotted in Figs. 6.14(b) and 6.15 respectively. Photograph of the FEDCOMA fabricated is shown in Fig. 6.16. Some discrepancy between theoretical and experimental input impedance loci may be noted. All the three loops in the experimental input impedance locus are shifted slightly downward on the Smith chart, but they are still inside the $VSWR = 2$ circle. The experimental bandwidth of the antenna is 810 MHz (24 percent, $f_0 = 3.38$ GHz), which is 7.36 times the bandwidth of the corresponding RPA ($BW = 109$ MHz). As in the other cases the experimental bandwidth is much larger than the

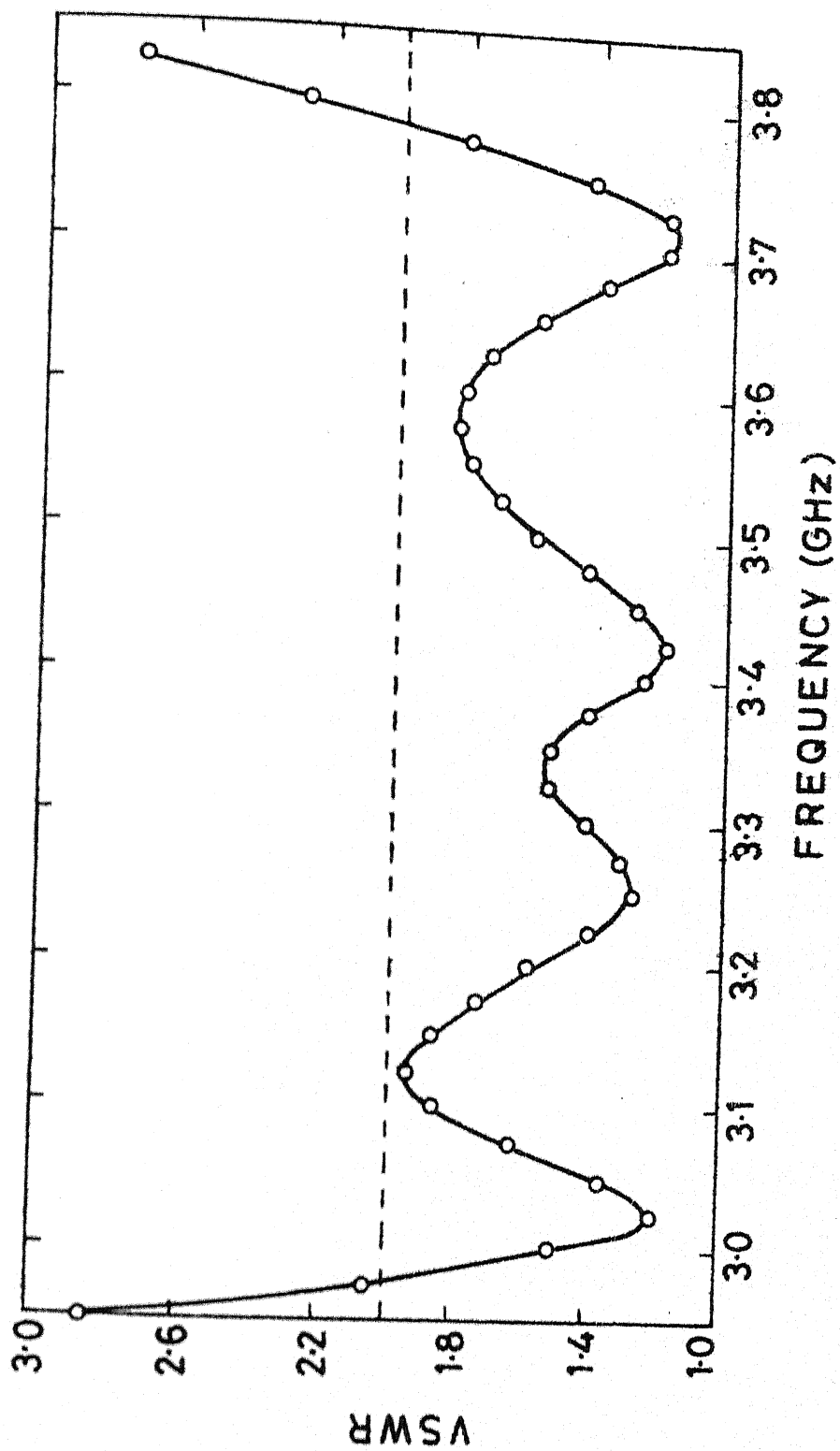


FIG. 6.15 EXPERIMENTAL VSWR VARIATION WITH FREQUENCY OF FEDCOMA SHOWN IN FIG 6.14(a)

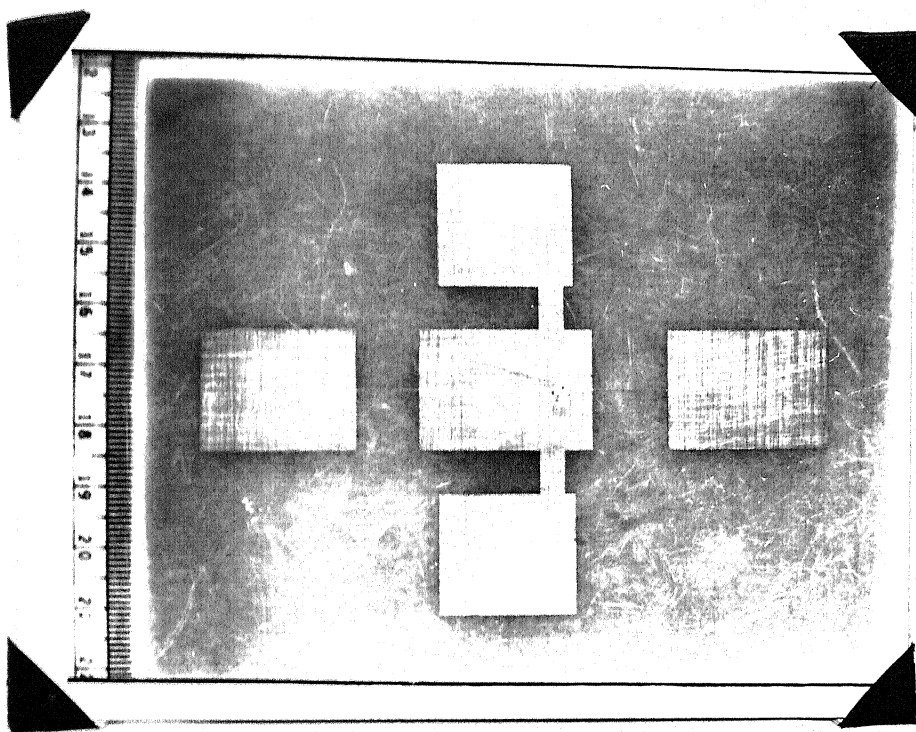


Fig. 6.16 Photograph of the FEDCOMA

theoretical bandwidth, because of the dielectric losses, conductor losses, and surface wave propagation losses associated with the configuration.

6.2.3 Radiation pattern

Radiation pattern of FEDCOMA (shown in Photograph 6.16) is calculated in both $\varphi = 0^\circ$ and $\varphi = 90^\circ$ planes at the various frequencies covering the entire bandwidth of the antenna. E_θ component of the radiation field in $\varphi = 0^\circ$ plane is plotted at four frequencies in Fig. 6.17(a). From this plot it may be noted that the direction of maximum radiation varies between $\theta = -35^\circ$ and $\theta = 24^\circ$ in the frequency range of 3.1 GHz to 3.6 GHz. However, along $\theta = 0^\circ$ direction, level of radiation remains within 2.8 db of the corresponding maximum level. A minimum is present in E_θ , and its level at $f = 3.1$ GHz is 16 db below the maximum level.

E_φ component in $\varphi = 90^\circ$ plane is plotted at three frequencies in Fig. 6.17(b). 3-db beamwidth in $\varphi = 90^\circ$ plane decreases from 87° to 43° as the frequency increases from 3.1 GHz to 3.6 GHz. E_φ is symmetrical with respect to $\theta = 0^\circ$ axis, because the parasitic elements and connecting strips along the non-radiating edges are identical.

Radiation pattern of the above FEDCOMA is measured in both $\varphi = 0^\circ$ and $\varphi = 90^\circ$ planes at the various frequencies for which VSWR remains less than two. E_θ component in $\varphi = 0^\circ$ plane is plotted at four frequencies in Fig. 6.18(a). In the

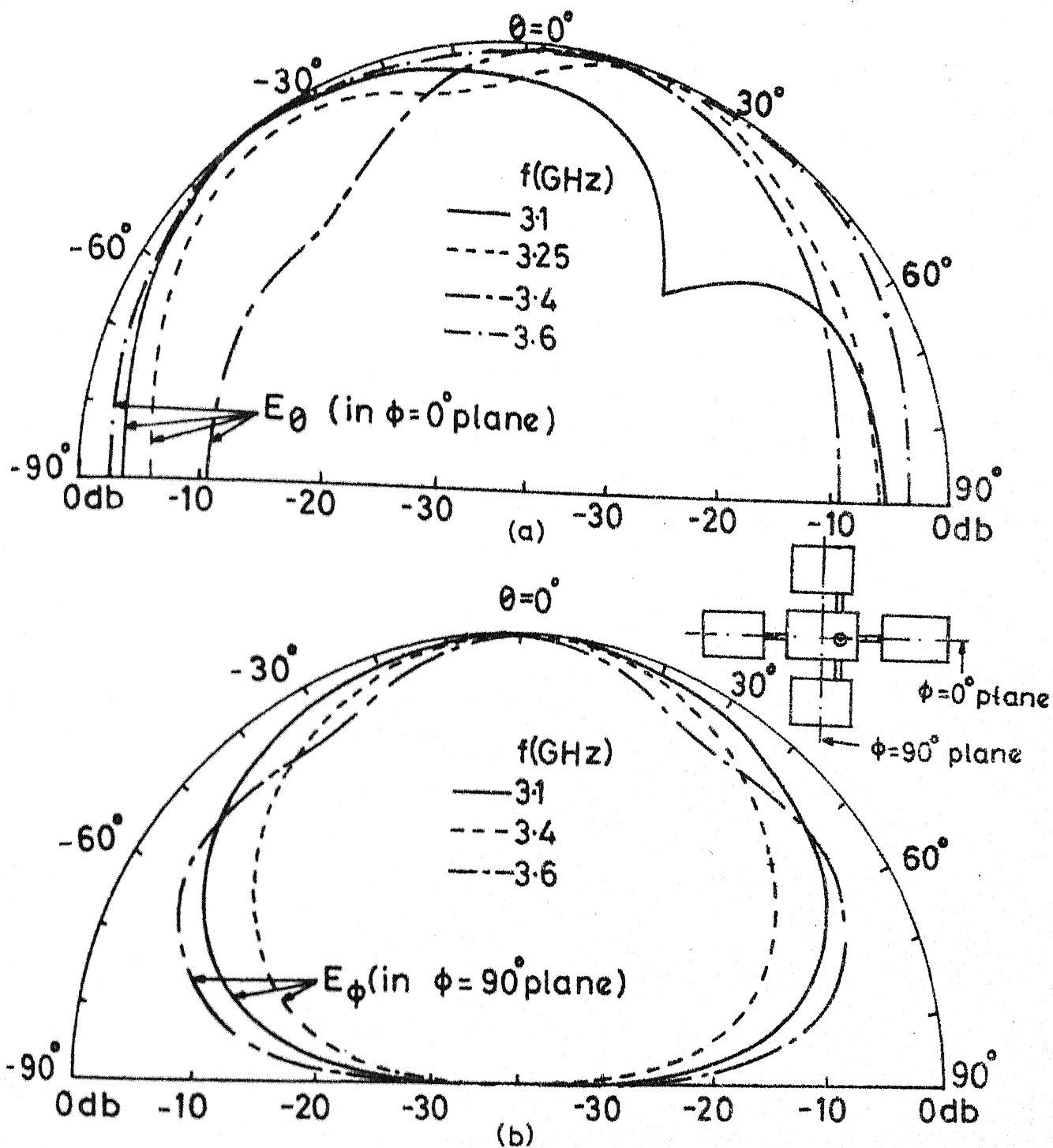


Fig.6.17 Theoretical values of (a) E_θ in $\phi=0^\circ$ plane and (b) E_ϕ in $\phi=90^\circ$ plane of FEDCOMA shown in photograph 6.16

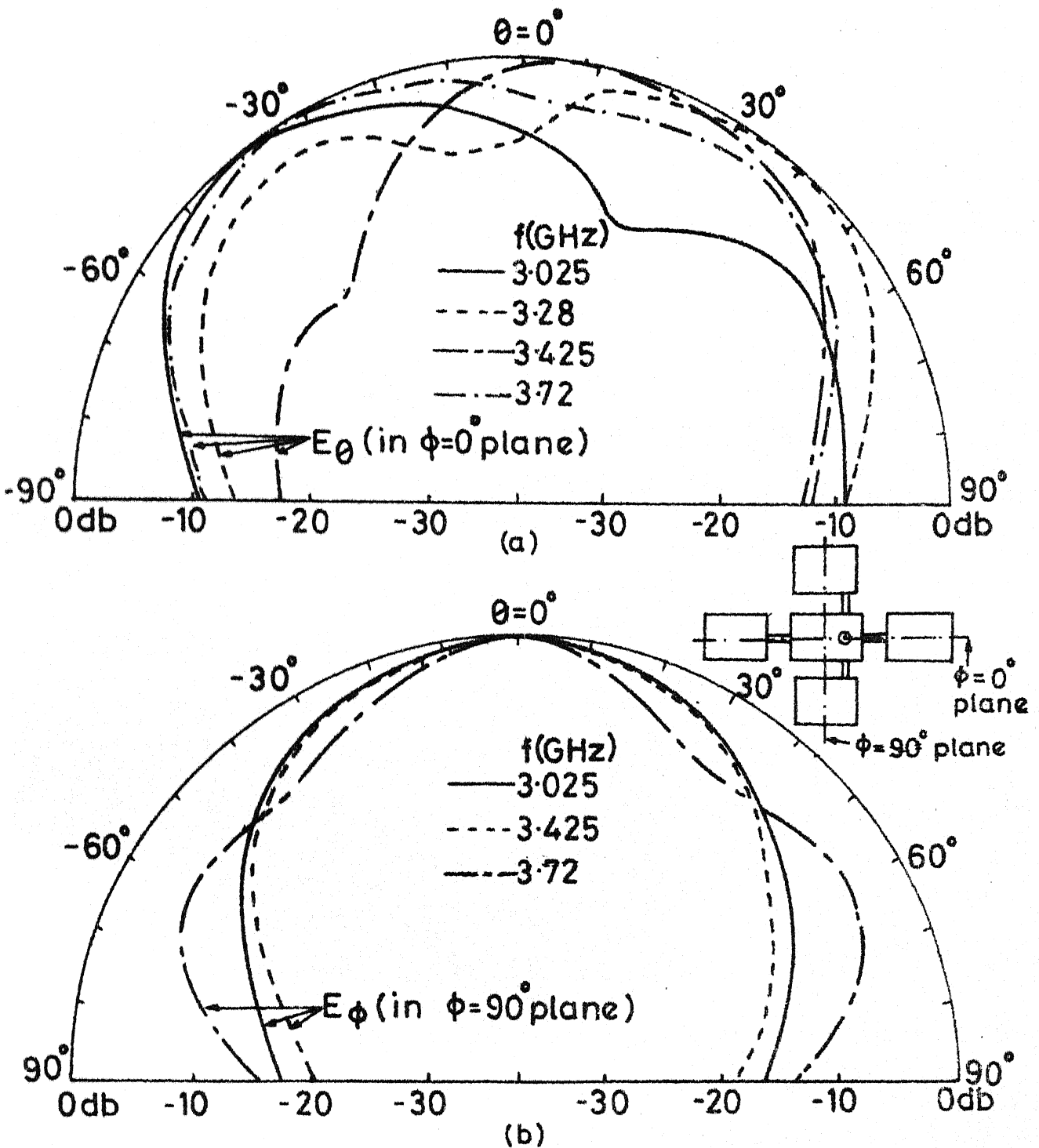


Fig.6-18 Experimental values of (a) E_θ in $\phi=0^\circ$ plane and (b) E_ϕ in $\phi=90^\circ$ plane of FEDCOMA shown in photograph 6-16

frequency range of 3.025 GHz to 3.72 GHz, direction of maximum radiation varies between $\theta = -40^\circ$ and $\theta = 35^\circ$, and 3-db beamwidth in $\varphi = 0^\circ$ plane fluctuates between 45° and 56° . A minimum is present in E_θ , and its level at $f = 3.025$ GHz is 7 db below the corresponding maximum level.

E_φ in $\varphi = 90^\circ$ plane is plotted at three frequencies in Fig. 6.18(b). With increase in the frequency from 3.025 GHz to 3.72 GHz, 3-db beamwidth in $\varphi = 90^\circ$ plane decreases from 61° to 36° . This value is less than the theoretical value. Similar discrepancy has also been observed in other antenna structures discussed in the previous chapters.

The bandwidth of the FEDCOMA (shown in Fig. 6.14(a)) can be improved further by increasing the size of the loops 2 and 3 in the input impedance locus shown in Fig. 6.14(b). This can be achieved by increasing the value of width w_{c2} and w_{c3} of the connecting strips, and by reducing the length l_3 of the parasitic element slightly.

6.3 DISCUSSION

In this chapter, the bandwidth of the rectangular patch antenna has been increased by using NEDCOMA and FEDCOMA configurations. In NEDCOMA, the various parameters which are optimized to yield broader bandwidth are : lengths of the parasitic elements, dimensions and locations of the connecting strips, and feed-point location. Based on these designs, experiments have been carried out yielding a bandwidth of

605 MHz (18.3 percent, $f_0 = 3.31$ GHz). The bandwidth obtained in this case is more than the bandwidth of NEGCOMA (BW = 480 MHz), but the number of variables to be optimized are also more. Theoretical results agree better with the experimental results in case of NEDCOMA than NEGCOMA, because in the case of NEGCOMA, the modelling of gaps was not accurate.

The bandwidth of the FEDCOMA obtained experimentally is 810 MHz (24 percent, $f_0 = 3.38$ GHz), which is nearly equal to the bandwidth of FEGCOMA. The bandwidth of FEDCOMA can be further improved by considering parasitic elements along the non-radiating edges of different lengths, which will yield four loops in the impedance locus instead of three loops. In this case, computation time for arriving at the optimum configuration will be nearly double, because the circuit is not symmetrical with axis XX (shown in Fig. 6.13(a)) and the full circuit need to be analyzed.

CHAPTER SEVEN

CONCLUDING REMARKS

This chapter contains a summary of the results reported in this thesis and some suggestions for further investigations

7.1 SALIENT RESULTS

7.1.1 General approach

In this thesis, several microstrip antenna configurations which yield broader bandwidth as compared to commonly used rectangular patch antennas, have been reported. These configurations are : radiating edges coupled, non-radiating edges coupled, and four edges coupled microstrip antennas. These antenna configurations consist of multiple resonators of slightly different resonant lengths. At some operating frequency, one of the resonators is resonant and at nearby frequencies, other resonators become resonant. This staggering of resonances yields wider bandwidth. Two types of mechanisms for coupling between the resonators have been investigated, namely, gap coupling and direct coupling. In gap coupling, two resonators are placed adjacent to each other with a narrow gap between them. In direct coupling, resonators are coupled through a short section of microstrip line.

Green's function approach and segmentation method have been used for analyzing and designing these antenna structures.

In segmentation method, the antenna configuration is divided into various simpler segments, for which impedance Green's functions are known. In the gap coupled configurations, the gap between the coupled resonators has been modelled as a capacitive π -network. The value of these capacitances has been evaluated from the expressions available for the asymmetric coupled microstrip lines. All the series capacitances in the π -networks are shunted by conductances which account for the radiation from the gap. This capacitive network model for the gap has been considered as one of the segments in the segmentation procedure. Based on these designs, more than fifty antennas have been fabricated for S-band operation on polystyrene substrate ($\epsilon_r = 2.55$) of two different thicknesses ($h = 0.159$ cm and 0.318 cm).

7.1.2 Gap-coupled antennas

In radiating edges gap coupled microstrip antennas (REGCOMA), two resonators have been placed in close vicinity of radiating edges of a rectangular patch element. Lengths of these resonators have been taken slightly different but approximately equal to half wavelength. The various parameters which have been optimized to yield broader bandwidth are : lengths of the parasitic elements, gap between the resonators, and location of the feed-point. With increase in substrate thickness h from 0.159 cm to 0.318 cm, the experimental bandwidth of the antenna increases from 330 MHz

to 510 MHz, while the bandwidth of the rectangular patch antenna increases from 62 MHz to 121 MHz.

In case of non-radiating edges gap coupled microstrip antennas (NEGCOMA), two resonators of slightly different lengths (approximately half wavelength) have been placed adjacent to the non-radiating edges of the rectangular patch element. In this configuration, the gap-width between the resonators is required to be much smaller (nearly 0.2 to 0.3 mm) than that in the case of REGCOMA. This is because of the fact that the field varies roughly sinusoidally along the non-radiating edges. So for any specified gap-width, the coupling will be less as compared to REGCOMA, where the field is nearly uniform along the coupled radiating edges. By doubling the thickness of the substrate (from 0.159 cm to 0.318 cm), the measured bandwidth of the antenna increases from 225 MHz to 480 MHz.

Four edges gap coupled microstrip antennas (FEGCOMA) contain four parasitic elements which are gap coupled to the four edges of rectangular patch element. The length of the parasitic elements placed along the non-radiating edges has been taken equal, so that only even-mode half section of the antenna is needed to be analyzed, thereby reducing the computational time to half. Experimental bandwidth of FEGCOMA is found to be 815 MHz for $h = 0.318$ cm.

7.1.3 Directly coupled antennas

In the cases of radiating edges directly coupled (REDCOMA), non-radiating edges directly coupled (NEDCOMA), and four edges directly coupled microstrip antennas (FEDCOMA), additional resonators have been coupled directly to the radiating edges, non-radiating edges and all the four edges of the rectangular patch element through short sections of microstrip lines. The lengths of these connecting strips have been taken larger than twice the substrate thickness to minimize coupling through the gaps. The parameters of the REDCOMA, which have been optimized to obtain broader bandwidth are : lengths of the parasitic elements, lengths and widths of the connecting strips, and feed-point location. In NEDCOMA and FEDCOMA, the field varies along the non-radiating coupled edges, so the coupling between the resonators is more when the connecting strip is located at a higher field point, which is near the corner. Therefore, for these two antenna configurations, locations of the connecting strips along the non-radiating edges have been taken as additional design parameters along with the other parameters of REDCOMA. In FEDCOMA, the parasitic elements along the non-radiating edges have been considered identical for economy of the limited computer time budget. The bandwidths obtained experimentally for REDCOMA, NEDCOMA and FEDCOMA are 548 MHz, 605 MHz and 810 MHz respectively.

7.1.4 Comparison

A comparison of the experimental bandwidth of the various types of antennas (for substrate thickness $h = 0.318$ cm and $\epsilon_r = 2.55$) is given in Table 7.1.

Table 7.1 Experimental bandwidth of the various types of antennas (Substrate thickness = 0.318 cm, $\epsilon_r = 2.55$)

Antenna configurations	Centre frequency (GHz)	Bandwidth in MHz	Percentage bandwidth
1. RPA*	2.985	109	3.7
2. REGCOMA	3.020	512	16.9
3. NEGCOMA	3.110	480	15.4
4. FEGCOMA	3.160	815	25.8
5. REDCOMA	3.200	548	17.1
6. NEDCOMA	3.310	605	13.3
7. FEDCOMA	3.380	810	24.0

*Rectangular patch antenna is included for reference purposes.

Radiating edges directly coupled and non-radiating edges directly coupled microstrip antennas give larger bandwidth than the corresponding gap coupled antennas. Four edges gap coupled and directly coupled microstrip antennas yield largest bandwidth.

7.2 FURTHER INVESTIGATIONS

Investigations reported in this thesis could be extended further in several directions. Some of the ideas which appear worth exploring, are summarized in this section.

7.2.1 Unsymmetrical four edges coupled antennas

In the four edges gap coupled and directly coupled microstrip antennas discussed in Chapters Four and Six respectively, the two parasitic elements coupled to the nonradiating edges of rectangular patch element have been taken identical. If these parasitic elements are of different lengths, the symmetry about the plane XX (Figs. 4.22(a) and 6.13(a)) is no longer present, and the computational time required for the analysis and the optimization will be nearly double. However, the bandwidth of the antennas will improve further. For an unsymmetrical four edges directly coupled microstrip antenna, shown in Fig. 6.13(a), when the lengths L , l_1, l_2, l_3 and l_4 are unequal, there will be four loops in the input impedance locus instead of three loops for FEDCOMA discussed in Section 6.2. Each loop in the impedance locus will correspond to the resonance of one of the parasitic elements. This configuration has not been analyzed and optimized so far because of the limitations of the computer time available.

7.2.2 Mixed (gap and direct) coupling in microstrip antennas

In directly coupled antennas discussed in Chapters Five and Six, the lengths of the connecting strips are taken larger

than twice the substrate thickness to avoid coupling because of the gap capacitances. If the lengths of these connecting strips are small, then the coupling between the resonators will be through the connecting strips as well as through the gap between the resonators. The combination of gap coupling and direct coupling can be used in the various antenna configurations described in this thesis. Number of design parameters remain the same, only the restriction that the strip length be greater than twice the thickness of the substrate can now be relaxed. This relaxes the constraint on the minimum length of the connecting strips in the directly coupled configuration and is likely to lead to a better optimized antenna configuration. Such an antenna configuration can be analyzed by combining the techniques used for gap coupled and directly coupled antennas. Segmented network model of a radiating edges mixed(gap and direct)coupled antenna configuration is shown in Fig. 7.1.

7.2.3 Arrays of broadband microstrip antennas

The broadband antenna configurations proposed in this thesis can be used in microstrip antenna arrays also. This will increase the bandwidth of the antenna arrays considerably. A few suggestions are depicted in Figs. 7.2 and 7.3. Both series-fed and corporate-fed arrays can be designed. There is a need for both theoretical and experimental investigations in this area .

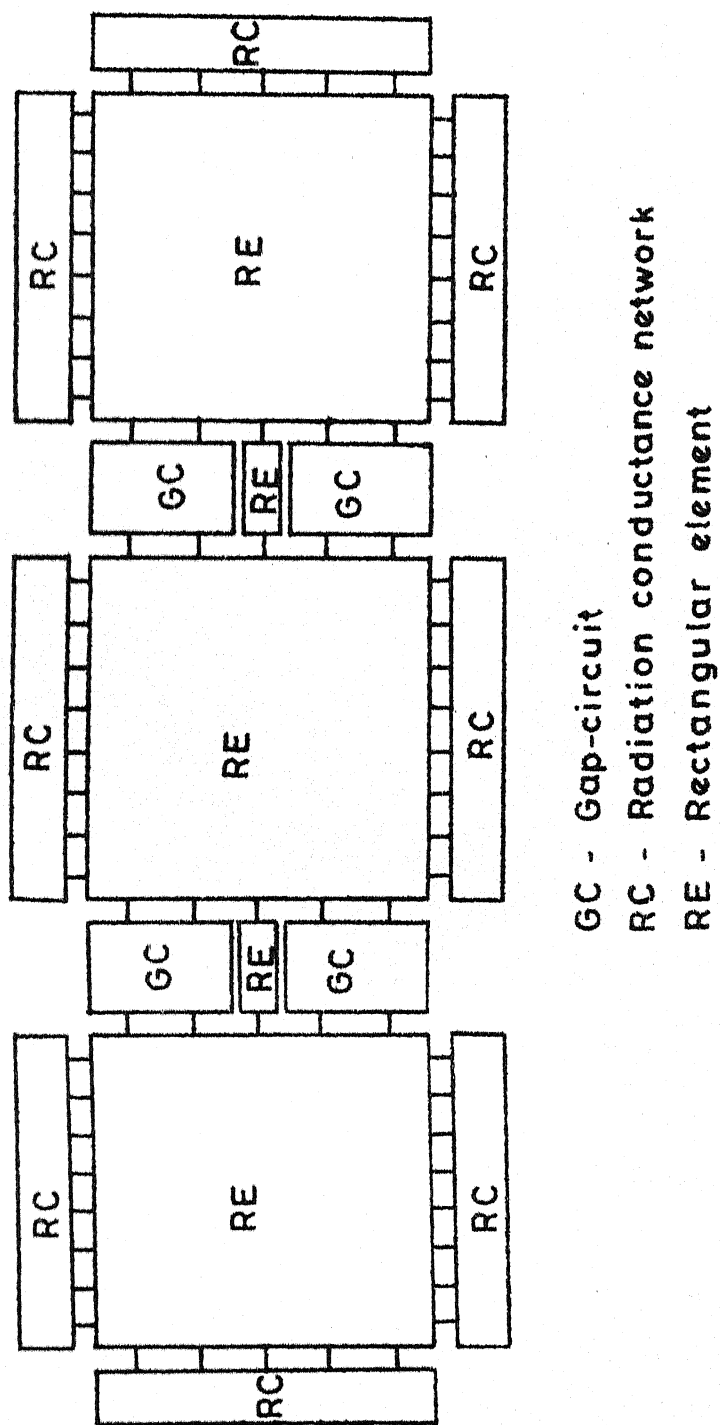


Fig. 7.1 Segmentation for analysis of a microstrip antenna with mixed coupled resonators along the radiating edges

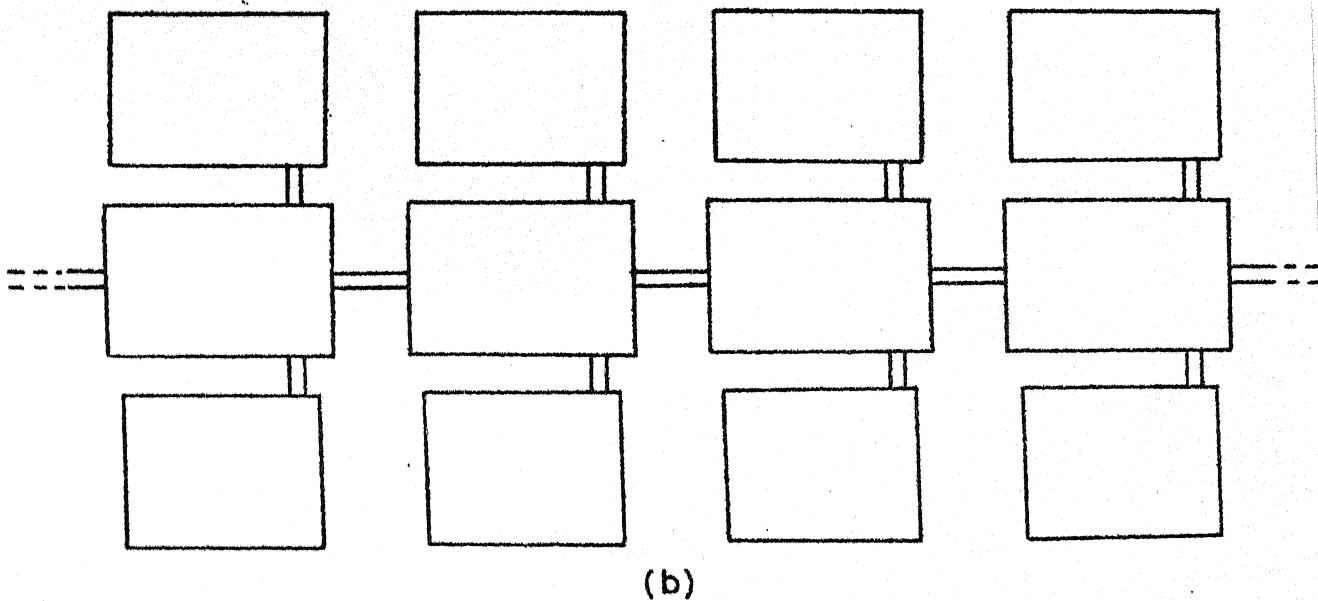
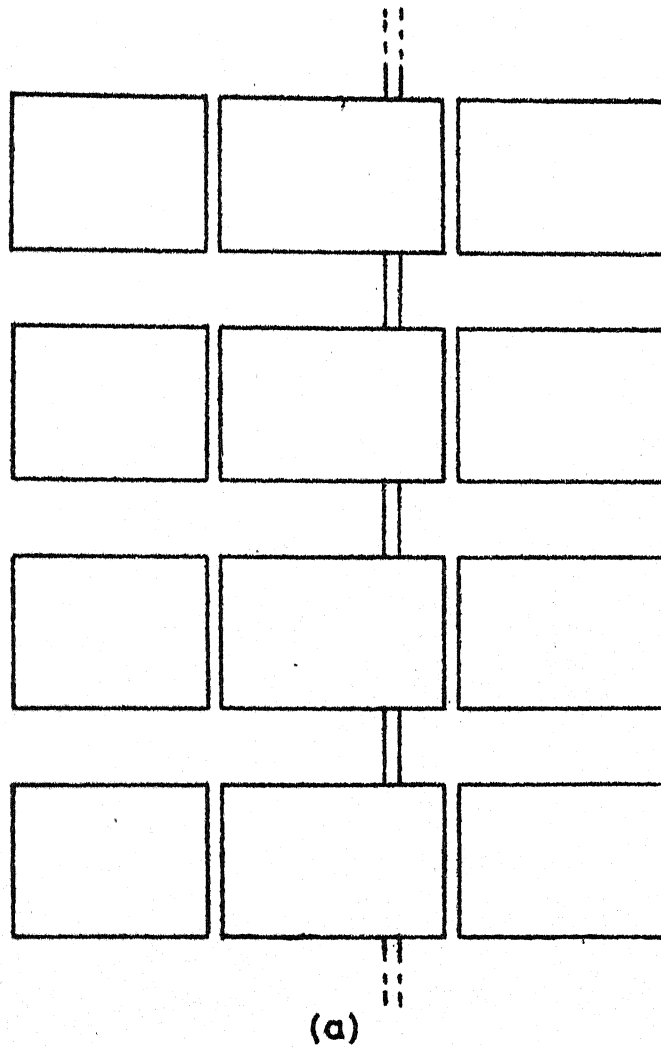


Fig.7.2 Series-fed arrays of (a) REGCOMA'S and (b) NEDCOMA'S

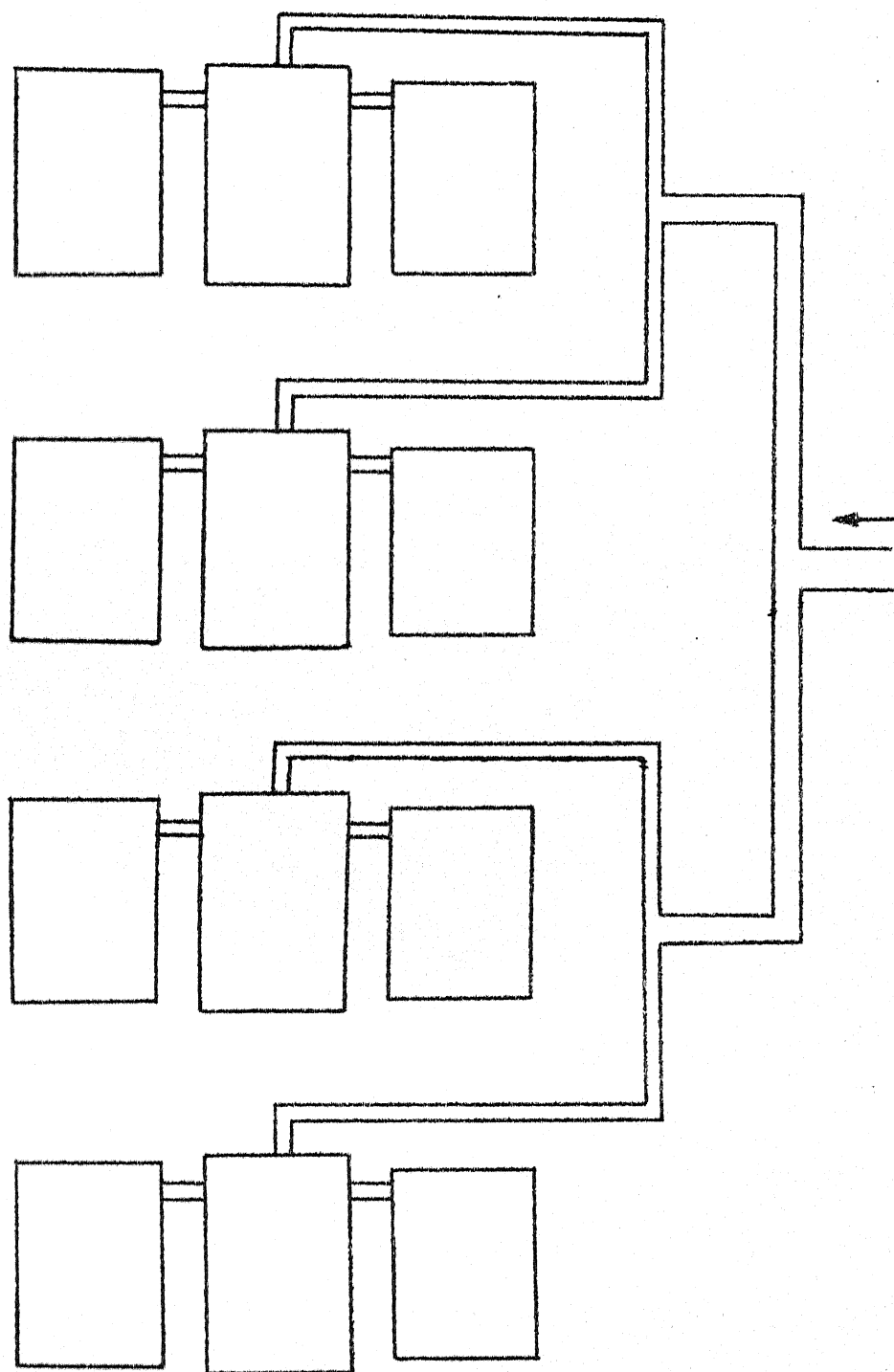
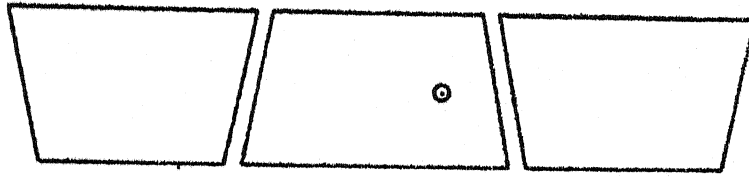


Fig. 7.3 A corporate-fed array of NEDCOMAS

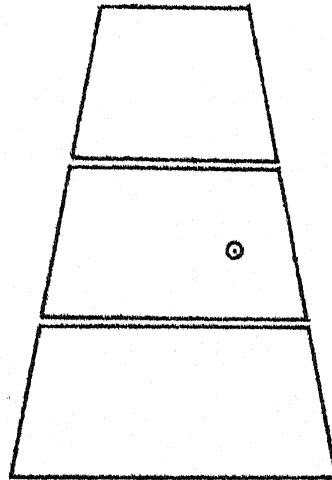
A series-fed array of rectangular elements [30] can in itself be analyzed by employing the technique used in this thesis for two-edges and four-edges directly coupled microstrip antennas.

7.2.4 Coupled trapezoidal microstrip antennas

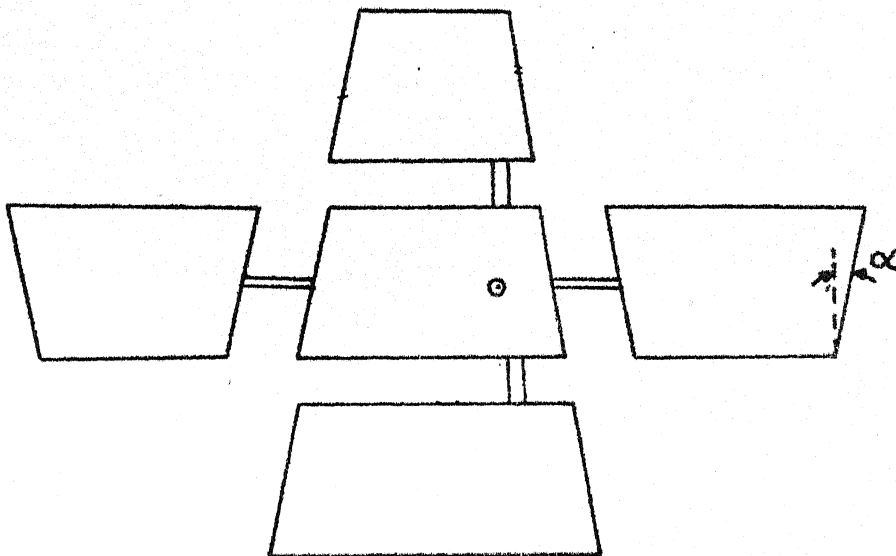
It has been discussed in Section 1.2.2 that trapezoidal structured antennas yield 20 percent more bandwidth than the commonly used rectangular microstrip antennas [57]. If these trapezoidal structures are used in place of rectangular structures used in the various broadband antenna configurations studied in this thesis, the bandwidth of the antennas will increase further because the bandwidth of each element is now 20 percent higher. Radiating edges gap coupled, non-radiating edges gap coupled, and four edges directly coupled microstrip antennas with trapezoidals instead of rectangles are depicted in Fig. 7.4. Other configurations with trapezoidals can be realized in a similar way. One of the difficulties with the analysis of trapezoidal configuration arises because of the fact that unless a very specific trapezoidal shape (with $\alpha = 30^\circ$, 45° or 60°) is selected, the segmentation method of partitioning the circuit into simpler segments is not applicable. If the angle α has a much smaller value, as in the case of results reported in [57], contour integral approach [68] can be used. This technique has been developed for the analysis of two-dimensional microwave circuits of



(a)



(b)



(c)

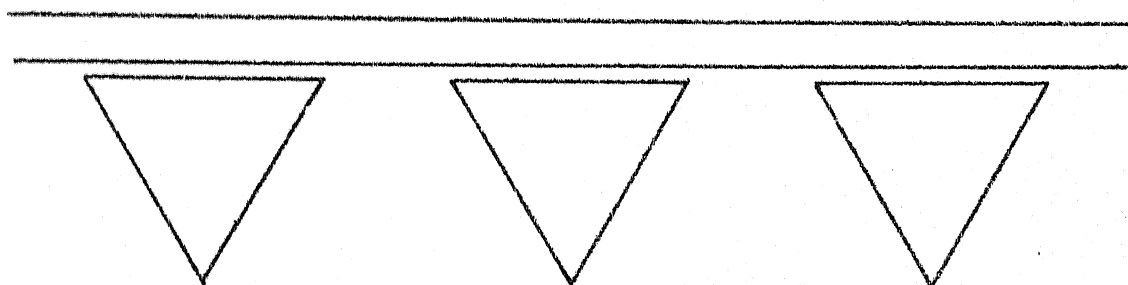
Fig.7-4(a) REGCOMA, (b) NEGCOMA and (c) FEDCOMA realized with trapezoidal structures

arbitrary shapes and can also be used for microstrip antennas of arbitrary shape.

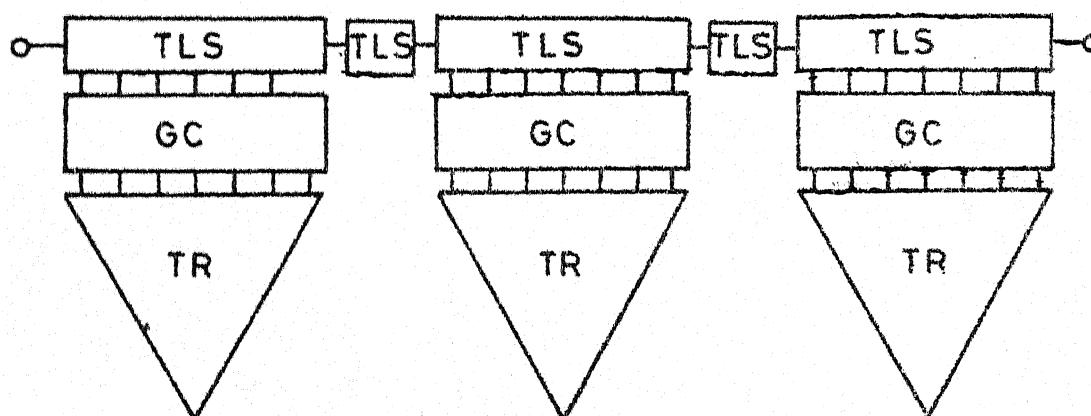
7.2.5 Gap coupled planar microwave circuits

Capacitive coupling through a gap between parallel edges of two planar components, which has been used for gap coupled antennas in this thesis, has also been recommended [69] for use in two-dimensional planar microwave circuits. Segmentation method with the gap modelled as a two-dimensional capacitive π -network, as developed in this thesis, can be used for analysis of these gap coupled circuits also. Segmentation model for the analysis of a band-stop filter using triangular resonators gap coupled to the main line is shown in Fig. 7.5. When the substrate height is small and/or the dielectric constant of the substrate is large, radiation effects can be ignored and the analysis becomes much simpler. Radiation conductance network need not be considered at the open edges of the triangular resonators. Also the capacitive π -network is now a pure capacitive network as the conductances corresponding to the radiation are not included.

Gap coupled circuits in stripline configuration can also be analyzed using a similar technique. The values of the capacitances for the capacitive π -network in this case are obtained from the formulas available for asymmetric coupled striplines [70].



(a)



TLS - Transmission line section

TR - Triangular resonator

GC - Gap-circuit

(b)

Fig.7.5(a) Band stop filter using gap coupled triangular resonators and (b) its segmented network

APPENDIX A

MEASUREMENT OF DIELECTRIC CONSTANT

The dielectric constant of the substrates, which have been used for fabricating the various microstrip antennas, was measured as follows [45].

A half-wave resonator in stripline configuration has been fabricated. The resonator is excited by a gap coupled feed-line as depicted in Fig. A.1. The widths (w) of the resonator and feed-line are taken equal to that of a 50 ohms stripline with an assumed value of dielectric constant $\epsilon_r = 2.55$. The length of the resonator is extended outward to account for the open-end fringing fields, and the extension in the length is given by

$$\delta = \frac{2h \ln 2}{\pi} \quad (\text{A.1})$$

where h is the thickness of the substrate. The resonance frequency (f_r) of the resonator is measured, from which the dielectric constant of the substrate is evaluated as

$$\epsilon_r = \left[\frac{c}{2f_r(1+2\delta)} \right]^2 \quad (\text{A.2})$$

where $c = 3 \times 10^8$ m/sec.

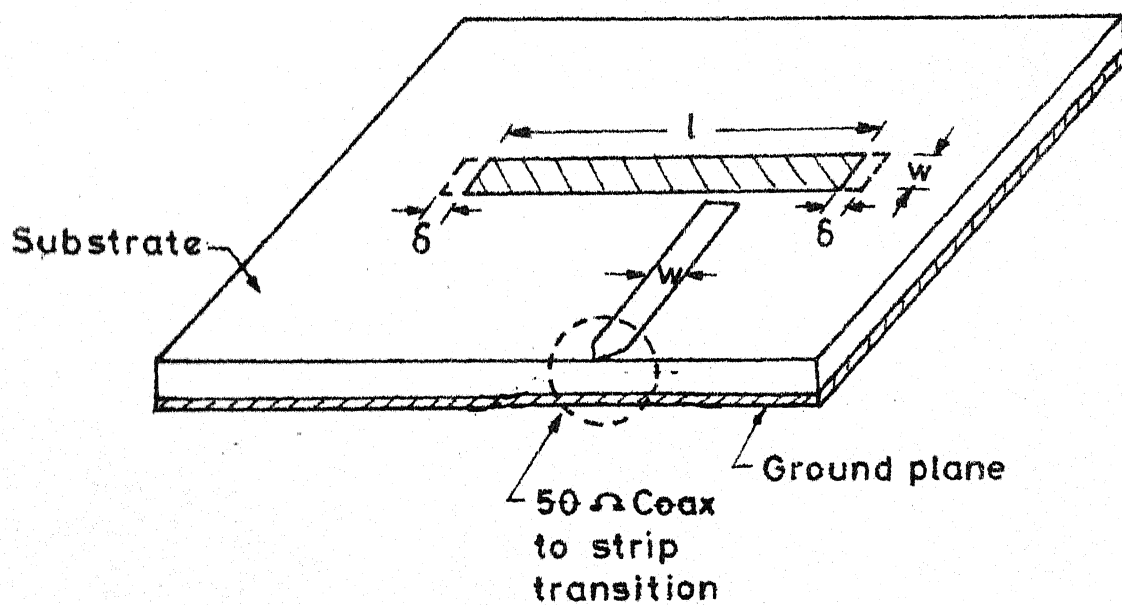


Fig.A.1 A stripline half-wave resonator with upper plane removed

APPENDIX B

EVALUATION OF GAP CAPACITANCES

In this appendix, the values of the gap capacitances are evaluated from the formulas for asymmetric coupled microstrip lines [67].

An asymmetric coupled microstrip line configuration is shown in Fig. B.1. The break-up of total line capacitance into a parallel plate and two fringing capacitances, one for each side of the strip, is also shown for even and odd mode circuits. The values of the gap capacitances shown in Fig.B.2, are obtained as

$$C_1 = C'_{f1}, \quad C_2 = C'_{f2} \quad (B.1)$$

and

$$C_g = \frac{(C_{ga} + C_{gd} - C'_{f1})(C_{ga} + C_{gd} - C'_{f2})}{2(C_{ga} + C_{gd}) - C'_{f1} - C'_{f2}} \quad (B.2)$$

where

$$C'_{fi} = \frac{C_{fi}}{1 + A_i(h/S) \tanh(12 S/h)} \sqrt{\frac{\epsilon_r}{\epsilon_{rei}}} \quad (B.3)$$

$$C_{fi} = 0.5(\sqrt{\epsilon_{rei}/cZ_{oi}} - C_{pi}) \quad (B.4)$$

$$A_i = \exp[-0.1 \exp(2.33 - 2.53 W_i/h)] \quad (B.5)$$

$$C_{pi} = \epsilon_o \epsilon_r W_i/h \quad (B.6)$$

$$\epsilon_{rei} = \frac{\epsilon_r + 1}{2} + \frac{\epsilon_r - 1}{2} \left(1 + \frac{12h}{W_i}\right)^{-\frac{1}{2}} \quad (B.7)$$

where $i = 1, 2$ mean that the corresponding capacitance expressions should be evaluated for the stripwidth W_1 or W_2 . Z_{oi}

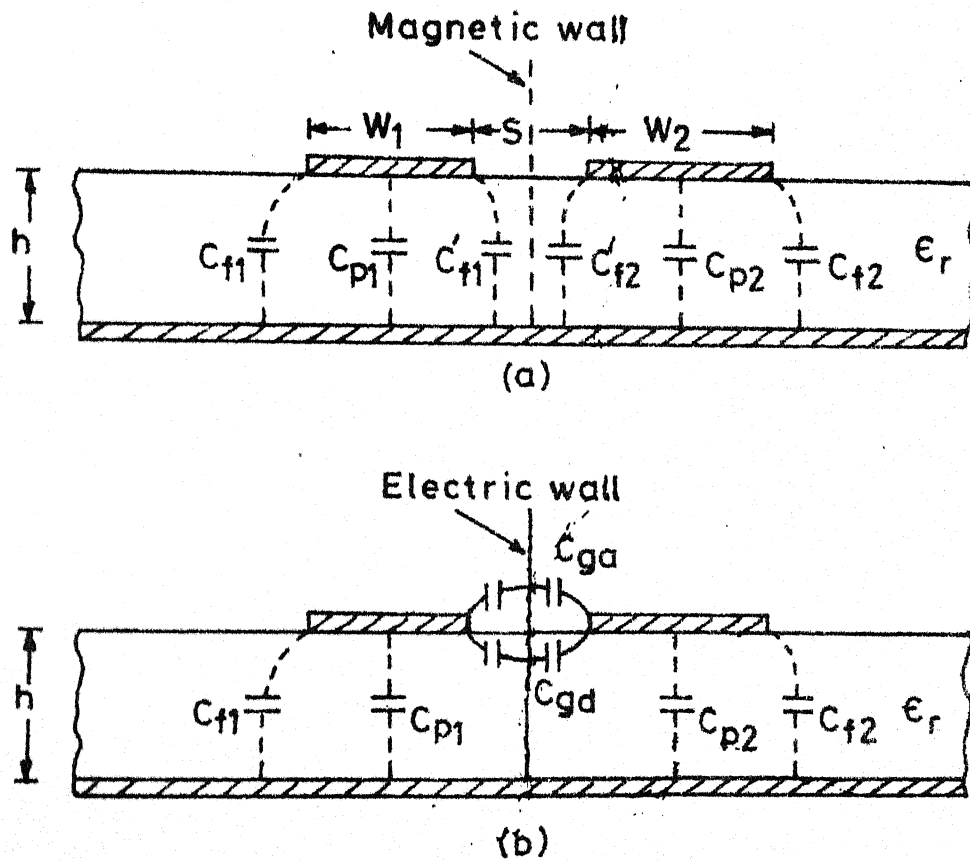


Fig.B1 Asymmetric microstrip coupled line and its (a) even-mode capacitances and (b) odd-mode capacitances

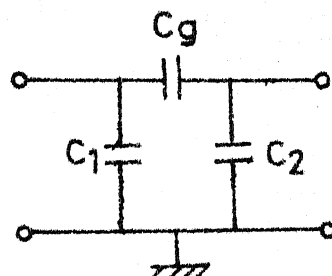


Fig.B2 Representation of gap by capacitive π -network

is the characteristic impedance of the stripwidth W_i .

C_{ga} is the odd-mode capacitance for the fringing field across the gap in the air region, and is given by

$$C_{ga} = \epsilon_0 \frac{K(k')}{K(k)}, \quad k = \frac{S/h}{S/h + 2W/h}, \quad k' = \sqrt{1-k^2} \quad (B.8)$$

where W is the mean value of the stripwidths, i.e. $0.5 \times (W_1 + W_2)$. The ratio of the complete elliptic function $K(k)$ and its complement $K(k')$ is found as

$$\frac{K(k')}{K(k)} = \begin{cases} \frac{1}{\pi} \ln \left[2 \frac{1 + \sqrt{k'}}{1 - \sqrt{k'}} \right] & 0 \leq k^2 \leq 0.5 \\ \frac{\pi}{\ln \left[2 \frac{1 + \sqrt{k}}{1 - \sqrt{k}} \right]} & 0.5 \leq k^2 \leq 1.0 \end{cases} \quad (B.9)$$

C_{gd} represents the odd-mode fringing field capacitance across the gap in the dielectric region, and is calculated as

$$C_{gd} = \frac{\epsilon_0 \epsilon_r}{\pi} \ln \left\{ \coth \left(\frac{\pi S}{4h} \right) \right\} + 0.65 C_f \left[\frac{0.02}{S/h} \sqrt{\epsilon_r + 1 - \epsilon_r^{-2}} \right] \quad (B.10)$$

The value of C_f is evaluated from (B.4) using the mean value of stripwidths.

REFERENCES

- [1] G.A. Deschamps, 'Microstrip microwave antennas', 3rd USAP Symp. on Antennas, 1953.
- [2] J.Q. Howell, 'Microstrip antennas', IEEE AP-S Int. Symp. Digest, pp. 177-180, Dec. 1972.
- [3] R.E. Munson, 'Conformal microstrip antennas and arrays', IEEE Trans. Antennas Propagat., vol. AP-22, pp. 74-78, Jan. 1974.
- [4] J.Q. Howell, 'Microstrip antennas', IEEE Trans. Antennas Propagat., vol. AP-23, pp. 90-93, Jan. 1975.
- [5] H.D. Weinschel, 'A cylindrical array of circularly polarized microstrip antennas', IEEE AP-S Int. Symp. Digest, pp. 177-180, June 1975.
- [6] C.W. Garvin et al., 'Low-profile, electrically small missile base mounted microstrip antennas', IEEE AP-S Int. Symp. Digest, pp. 244-247, June 1975.
- [7] G.G. Sanford and L. Klein, 'Development and test of a conformal microstrip airborne phased array for use with the ATIS-6 Satellite', IEE Int. Conf. on Antennas for Aircraft and Spacecraft, pp. 115-122, 1975.
- [8] L.T. Ostavald and C.W. Garvin, 'Microstrip command and telemetry antennas for communications technology satellite', ibid, pp. 217-222.
- [9] J.R. James and G.J. Wilson, 'New design techniques for microstrip antenna arrays', Proc. 5th European Microwave Conf., pp. 658-662, Sept. 1975.
- [10] A.G. Derneryd, 'Linearly polarized microstrip antennas', IEEE Trans. Antennas Propagat., vol. AP-24, pp. 846-851, Nov. 1976.
- [11] M. Cuhai and D.S. James, 'Radiation from triangular and circular resonators in microstrip', IEEE MTT-S Int. Symp. Digest, June 1977.
- [12] L.C. Shen et al., 'Resonant frequency of a circular disk printed-circuit antenna', IEEE Trans. Antennas Propagat., vol. AP-25, pp. 595-596, July 1977.

- [13] C.W. Garvin et al., 'Missile base mounted microstrip antennas', *ibid.*, pp. 604-610.
- [14] P.K. Agrawal and M.C. Bailey, 'An analysis technique for microstrip antennas', *IEEE Trans. Antennas Propagat.*, vol. AP-25, pp. 756-759, Sept. 1977.
- [15] C. Wood, P.S. Hall, and J.R. James, 'Design of wide-band circularly polarized microstrip antennas and arrays', *IEE Conf. on Antennas and Propagat.*, pp. 312-316, 1978.
- [16] A.G. Derneryd, 'A theoretical investigation of the rectangular microstrip antenna element', *IEEE Trans. Antennas Propagat.*, vol. AP-26, pp. 532-535, July, 1978.
- [17] W.F. Richards, Y.T. Lo, and D.D. Harrison, 'Improved theory for microstrip antennas', *Electron. Lett.*, vol. 15, pp. 42-44, Jan. 1979.
- [18] P. Hammer et al., 'A model for calculating the radiation field of microstrip antennas', *IEEE Trans. Antennas Propagat.*, vol. AP-27, pp. 267-270, March 1979.
- [19] A.G. Derneryd and A.G. Lind, 'Extended analysis of rectangular microstrip antennas', *ibid.*, pp. 846-849, Nov. 1979.
- [20] J.R. Mosig and F.E. Gardiol, 'The near field of a open microstrip structure', *IEEE AP-S Int. Symp. Digest*, pp. 379-381, June 1979.
- [21] N.G. Alexopoulos et al., 'Radiation by microstrip patches', *ibid.*, pp. 722-727.
- [22] Y.T. Lo, D. Solomon and W.F. Richards, 'Theory and experiment on microstrip antennas', *IEEE Trans. Antennas Propagat.*, vol. AP-27, pp. 137-145, March 1979.
- [23] K.R. Carver and E.L. Coffey, 'Theoretical investigation of the microstrip antenna', *New Mexico State Univ., Tech. Rep. PT-00929*, Jan. 1979.
- [24] K.R. Carver, 'A modal expansion theory for the microstrip antenna', *IEEE AP-S Int. Symp. Digest*, pp. 101-104, June 1979.

- [25] W.F. Richards and Y.L. Lo, 'An improved theory for microstrip antennas and applications', *ibid.*, pp. 113-115.
- [26] K.R. Carver, 'Practical analytical techniques for the microstrip antennas', *Proc. Workshop Printed Circuit Antennas*, New Mexico State Univ., pp. 7.1 - 7.20, Oct. 1979.
- [27] A. Van de Capelle, 'Theoretical investigations of microstrip antennas', *ibid.*, pp. 11.1 - 11.8.
- [28] W.F. Richards et al., 'Theory and application for microstrip antennas', *ibid.*, pp. 8.1 - 8.23.
- [29] *Proc. Workshop on Printed Circuit Antennas*, New Mexico State Univ., Oct. 1979.
- [30] I.J. Bahl and P. Bhartia, *Microstrip antennas*, Dedham, MA: Artech House, 1981.
- [31] K.R. Carver and J.W. Mink, 'Microstrip antenna technology', *IEEE Trans. Antennas Propagat.*, vol. AP-29, pp. 2-24, Jan. 1981.
- [32] W.F. Richards et al., 'An improved theory for microstrip antennas and applications', *ibid.*, pp. 38-46.
- [33] *IEEE Trans. Antennas Propagat.*, 'Special Issue on Microstrip Antennas', vol. AP-29, Jan. 1981.
- [34] T. Okoshi and T. Miyoshi, 'The planar circuit - an approach to microwave integrated circuitry', *IEEE Trans. Microwave Theory Tech.*, vol. MTT-20, pp. 245-252, April 1972.
- [35] R.F. Harrington, *Time-Harmonic Electromagnetic Fields*, McGraw-Hill Book Co., NY 1961, p. 183.
- [36] K.C. Gupta and P.C. Sharma, 'Segmentation and desegmentation techniques for analysis of planar microstrip antennas', *IEEE AP-S Int. Symp. Digest*, pp. 19-22, June 1981.
- [37] T. Okoshi et al., 'Planar 3-db hybrid circuit', *Electron. Commun. Japal*, vol. 58-B, No.8, pp.80-90, Aug. 1975.

- [38] R. Chadha and K.C. Gupta, 'Green's functions for triangular segments in planar microwave circuits', IEEE Trans. Microwave Theory Tech., vol. MTT-28, pp. 1139-1143, Oct. 1980.
- [39] R. Chadha and K.C. Gupta, 'Green's functions for circular sectors, annular rings and annular sectors in planar microwave circuits', ibid., vol. MTT-29, pp. 68-71, Jan. 1981.
- [40] R. Chadha, 'Triangular segments and two-dimensional analysis for microwave integrated circuits', Ph.D. thesis, Department of Electrical Engineering, Indian Institute of Technology, Kanpur, India, May 1981.
- [41] T. Okoshi et al., 'The segmentation method - an approach to the analysis of planar microwave Theory Tech., vol. MTT-24, pp. 662-668, Oct. 1976.
- [42] R. Chadha and K.C. Gupta, 'Segmentation method using impedance matrices for analysis of planar microwave integrated circuits', IEEE Trans. Microwave Theory Tech., vol. MTT-29, pp. 71-74, Jan. 1981.
- [43] P.C. Sharma and K.C. Gupta, 'Design of a diagonal fed rectangular microstrip antenna for circular polarization', Int. Conf. on Commun. Circuits and Systems, Calcutta (India), p.3, Dec. 1981.
- [44] K.C. Gupta, 'Two-dimensional analysis of microstrip circuits and antennas', JIETE, India, vol. 28, pp. 346-364, July 1982.
- [45] P.C. Sharma, 'Desegmentation method and its application to circularly polarized microstrip antennas', Ph.D. Thesis, Department of Electrical Engineering, Indian Institute of Technology, Kanpur, India, April 1982.
- [46] P.C. Sharma, and K.C. Gupta, 'Analysis and design of a corners-chopped circularly polarized square microstrip antenna', Int. Symp. on Microwaves and Commun., Kharagpur (India), pp. 117-120, Dec. 1981.
- [47] P.C. Sharma and K.C. Gupta, 'Design of a circularly polarized square patch microstrip antenna with a diagonal slot', Int. Conf. on Commun. Circuits and Systems, Calcutta (India), p.3, Dec. 1981.

- [48] J.H. Richmand, 'A wire-grid model for scattering by conducting bodies', IEEE Trans. Antennas Propagat., vol. AP-14, pp. 782-786, Nov. 1966.
- [49] E.L. Newmann, 'Strip antenna in dielectric slab', ibid., vol. AP-26, pp. 647-653, Sept. 1978.
- [50] T. Itoh and R. Mittra, 'A method for computing edge capacitance of finite and semi-infinite microstrip lines', IEEE Trans. Microwave Theory Tech., vol. MTT-20, pp. 847-849, Dec. 1972.
- [51] T. Itoh and R. Mittra, 'A new method for calculating the capacitance of a circular disk for microwave integrated circuits', ibid., vol. MTT-21, pp. 431-432, June 1973.
- [52] Y. Rahmal-Samii, T. Itoh and R. Mittra, 'A spectral domain analysis for solving microstrip discontinuity problems', ibid., vol. MTT-22, pp. 372-378, April 1974.
- [53] A.K. Sharma, 'Spectral domain analysis of microstrip resonant structures', Ph.D. Thesis, Department of Electrical Engineering, Indian Institute of Technology, New Delhi, India, 1979.
- [54] T. Itoh and W. Menzel, 'A full-wave analysis method for microstrip structures', IEEE Trans. Antennas Propagat., vol. AP-29, pp. 63-68, Jan. 1981.
- [55] K. Araki and T. Itoh, 'Hankel transform domain analysis of open circular microstrip radiating structures', ibid., pp. 84-89.
- [56] S. Yano and A. Ishimaru, 'Broadbanding of microstrip antennas by orthogonal polarizations', IEEE AP-S Int. Symp. Digest, pp. 363-365, June 1981.
- [57] Girish Kumar and K.C. Gupta, 'Trapezoidal shaped microstrip antennas for wider bandwidth and beamwidth', Int. Conf. on Commun. Circuits and Systems, Calcutta (India), p.7, Dec. 1981.
- [58] C. Wood, 'Improved bandwidth of microstrip antennas using parasitic elements', IEE Proc., MOA, vol.127, No.4, pp. 231-234, Aug. 1980.

- [59] D.H. Schaubert and F.G. Farrar, 'Some conformal printed circuit antenna designs', Proc. Workshop Printed Circuit Antennas, New Mexico State Univ., pp. 5.1 - 5.21, Oct. 1979.
- [60] Y.T. Lo et al., 'Study of microstrip antennas, microstrip phased arrays, and microstrip feed networks', Tech. Rep. RADC-TR-77-406, Univ. of Illinois, Urbana, Oct. 1977.
- [61] P.S. Hall, 'New wideband microstrip antenna using log-periodic technique', Electron. Lett., vol.16, No.4, pp. 127-128, Feb. 14, 1980.
- [62] H. Pues et al., 'Wideband quasi-log-periodic microstrip antenna', IEE Proc., MOA, vol. 128, No.3, pp. 159-163, June 1981.
- [63] P.S. Hall, C. Wood and C. Garrett, 'Wide bandwidth microstrip antennas for circuit integration', Electron. Lett., vol. 15, No.15, pp. 458-460, July 19, 1979.
- [64] H. Pues et al., 'Broadband microstrip resonator antennas', IEEE AP-S Int. Symp. Digest, pp.268-271, 1978.
- [65] I. Wolff and N. Knoppik, 'Rectangular and circular microstrip disc capacitors and resonators', IEEE Trans. Microwave Theory Tech., vol.MTT-22, pp. 857-863, Oct. 1974.
- [66] H. Pues and A. Van de Capelle, 'A simple accurate formula for the radiation conductance of a rectangular microstrip antenna', IEEE AP-S Int. Symp. Digest, pp. 23-26, June 1981.
- [67] Ramesh Garg, 'Design equations for coupled microstrip lines', INT. J. Electronics, vol.47, No.6, pp.587-591, 1979.
- [68] K.C. Gupta, et al., Computer-aided design of microwave circuits, Dedham, MA: Artech House, pp 253-256, 1981.
- [69] J. Helszajn and D.S. James, 'Planar triangular resonators with magnetic walls', IEEE Trans. Microwave Theory Tech., vol. MTT-26, pp. 95-100, Feb. 1978.
- [70] S.B. Cohn, 'Shielded coupled-strip transmission line', ibid., MTT-3, No.5, Oct. 1955.